CONCRETE CRACK WIDTH UNDER COMBINED REINFORCEMENT CORROSION AND APPLIED LOAD

SHANGTONG YANG

A thesis submitted in partial fulfilment of the requirements
of the University of Greenwich for the
Degree of Doctor of Philosophy

November 2010

DECLARATION

I certify that this work has not been accepted in substance for any degree, and is not concurrently being submitted for any degree other than that of Doctor of Philosophy (PhD) being studied at the University of Greenwich. I also declare that this work is the result of my own investigations except where otherwise identified by references and that I have not plagiarised another's work.

---------- ----------

Shangtong Yang Date

(Student)

---------- ----------

Prof. Chun-Qing Li Date

(Supervisor)

ACKNOWLEDGEMENTS

The author is extremely indebted to his supervisor Prof. Chun-Qing Li. He has guided the author through every stage of this research and contributed many ideas to its development. His constant encouragement and unwavering support are greatly appreciated and his guidance has proved invaluable.

Grateful thanks are extended to Dr. Ouahid Harireche, who gave me his time and expert advice without hesitation.

Thanks to the technical staff in the Civil Engineering laboratory for their eagerness to assist me throughout my research.

Thanks also to colleagues and friends within the research unit who provided the laughs and social relief through the years.

Specifically, and finally, the author wishes to express his greatest appreciation to his parents, for their support, throughout the course of this work. This would not have been possible without them.

ABSTRACT

For reinforced concrete structures subjected to chlorides, carbon dioxide laden and other aggressive environments, corrosion of the reinforcing steel is seen as a global problem. Maintenance and repairs resulting primarily from premature concrete cracking and spalling have an estimated cost running to $100 billion per annum world-wide. The continual demands for greater load carrying capacity of existing infrastructure only exacerbate the problem. In practice, concrete crack width propagation is seen as one of the most important criteria for design and assessment of the long term serviceability of concrete structures. It is therefore economically beneficial to have a fundamental understanding of the growth of the crack width over time so that better informed decisions can be made regarding the carrying out of any repairs. This research attempts to examine the process of concrete cracking and determine the surface crack width of concrete structures under the combined effects of reinforcement corrosion and applied load in both an analytical and numerical manner. In the analytical method, a model for stiffness reduction of cracked concrete has been derived based on the concept of fracture energy and an analytical solution has been obtained. In the numerical method, an interfacial element has been developed to predict concrete crack width under combined effects based on a cohesive crack model in conjunction with finite element codes. To help accurate prediction of crack width in the numerical method, a realistic constitutive relationship for concrete under direct tension has been obtained from the laboratory experiments. It is concluded in this thesis that both the analytical and numerical methods are one of very few available theoretical methods that can predict with reasonable accuracy concrete crack width of reinforced concrete structures under the combined effects of reinforcement corrosion and applied load. This research focuses on concrete cracking caused by reinforcement corrosion and applied load without considering other factors, e.g., weathering, freeze-thaw and chemical attack. Both methods can be used as a tool to assess the serviceability

of corrosion affected concrete infrastructure if reinforcement corrosion and applied load are the main causal factors of concrete cracking. For this type of concrete structures, therefore, scientific information can be provided for asset managers in decision making regarding possible interventions. Timely interventions have the potential to prolong the service life of reinforced concrete structures.

CONTENTS

LIST OF FIGURES

LIST OF TABLES

NOTATION

A	Diffusion coefficient	$[B]$	Geometric matrix
$C(x, t)$	Chloride ion content	C_s	Equilibrium chloride content
C_2S	Dicalcium silicate	C_3S	Tricalcium silicate
$C_3S_2H_3^{'}$	Calcium silicate hydrates	D	Stiffness degradation parameter for cohesive element
$\dot{D}$	Viscous stiffness degradation parameter	D_0	Diffusion constant
D_c	Chloride diffusion coefficient	$[D_r]$	Constitutive matrix
E	Young's modulus of concrete	E_{ef}	Effective modulus of Elasticity
E_r	Residual modulus of elasticity of cracked concrete	F_a	Faraday constant
F	External work done by applied loads	G	Energy release rate
G_e	Elastic energy release rate prior to peak stress	G_f	Fracture energy
G_{Ic}	Energy rate consumed in creating two cracked faces	G_q	Energy release rate for Mode I quasi-brittle crack
G_r	Energy release rate after peak stress	G_σ	Energy rate to overcome the cohesive pressure between the two cracked faces

$H^{'}$	Water	I	Current
K_{I}	Mode I stress intensity factor	K_{Ic}	Fracture toughness
K_p	Penalty stiffness	$[K_r]$	Stiffness matrix
L	Length of a structure	M	Atomic weight of metal
P	Probability of an event	$P(t)$	Internal pressure on concrete
$P_1(t)$	Corrosion-induced pressure on concrete	P_2	Applied load induced pressure on concrete
P_a	External applied load	P_w	Equivalent force introduced by self-weight of a concrete beam
$R(t)$	Structural resistance	R_0	Original structural resistance
R_p	Polarization resistance	T	Tension vector
U	Strain energy	U_d	Elastic energy density
W	Energy available for crack formation	$W_{rust}(t)$	Total amount of corrosion products
W_c	Amount of rust in the band $d_c(t)$	W_0	Amount of rust filling the porous band d_0
W_s	Amount of rust replacing the corroded steel	a	Inner radius of the cylinder
b	Outer radius of the cylinder	d_0	Thickness of the porous band
d_a	Maximum aggregate size	$d_c(t)$	Thickness of the rust in concrete
d_p	Radial displacement of concrete induced by applied load	$erf(x)$	Error function

f_c	Concrete strength in compression	$f_{c,0}$	Strength of zero porosity
$f_t^{'}$	Tensile strength of concrete	h	Geometric thickness of cohesive element
h_c	Thickness of crack band	h_t	Theoretic thickness of cohesive element
$i_{corr}(t)$	Corrosion current density	l_{ch}	Characteristic length
m	Mass of steel consumed	p_a	Minimum acceptable probability
r	Radius	r_0	Radius at the crack tip
s_n	Stress of rust	t	Time
t_2	Surface cracking time of concrete	w_c	Crack width of concrete
x	Depth of carbonation/chloride penetration	z	Ionic charge
α	Stiffness reduction factor of concrete	α_{rust}	Coefficient related to corrosion products
δ	Tensile displacement of cohesive interface	$\overline{\delta}$	Average displacement from the transducers
δ_0	Tensile displacement at peak stress of cohesive interface	δ_{ef}	Effective displacement
δ_1	Displacement of cohesive element in normal direction	δ_2	Displacement of cohesive element in shear direction
$\overline{\delta_p}$	Average displacement at the peak stress from the transducers	$\varepsilon_1, \varepsilon_2$	Normal strain and shear strain of cohesive element
$\varepsilon^{'}$	Strain of the bulk concrete	ε_0	Strain at the maximum stress
ϵ_{cor}	Strain of rust	ε_{cu}	Ultimate concrete strain

ε^f	Inelastic fracturing strain	$\overline{\varepsilon_\theta}$	Average residual tangential strain
ε_θ	Tangential strain	$\overline{\varepsilon_\theta^{e,m}}$	Average maximum elastic tangential strain
θ	Angle between bond stress and rebar	μ	Viscosity paramter
υ_1	Poisson's ratio in the radial direction	υ_2	Poisson's ratio in the tangential direction
ν_c	Poisson's ratio	$\prod$	Potential energy
ρ_{rust}	Density of corrosion products	ρ_{st}	Density of steel
σ	Tensile stress of cohesive interface	σ_1, σ_2	Normal stress and shear stress of cohesive element
$\sigma^{'}$	Stress of the bulk concrete	σ_f	Failure stress
σ_p	Peak value of tensile stress	σ_r	Radial stress
σ_s	The stress in the reinforcing bar due to the applied load	σ_u	Undamaged stress
σ_θ	Tangential/hoop stress	τ	Longitudinal bond stress
$\varphi(t)$	Deterioration function	φ_a	Acceptable limit
$\Re$	Crack growth resistance		

CHAPTER 1

INTRODUCTION

1.1 Background

Reinforced concrete (RC) structures have been the most common type of structures used in the civil engineering construction since middle nineteenth century. RC structures have been widely used for building, bridges, retaining walls, tunnels, and indeed any physical infrastructure built on and under the ground. The extensive application of reinforced concrete in construction stems from the unique feature of versatility, durability and economy of reinforced concrete as a building material. Thus far, almost anything built is related to reinforced concrete (Bentur *et al.* 1997; Bhatt *et al*. 2006).

Reinforced concrete has been considered as a durable material until about 1950s when it emerged that some reinforced concrete structures failed prematurely. Among many examples, the bridges in the USA (Raina, 1995) which were subject to sea salts or deicing salts were found to have failed prematurely and the failure was attributed to reinforcement corrosion. Furthermore, in some areas of Europe and the Middle East, sea water was used for concrete mixing until 1970s with the misunderstanding that chlorides would be bounded in the cement and would not cause corrosion, which has been proven to be an expensive error (Broomfield 1997).

Since 1970s, it has become an accepted knowledge that the concrete cover has its limitation on protecting the reinforcing steel from corrosion. As a result, a series of research has been initiated on improving the understanding of the corrosion of steel in concrete (Wilkins and Lawrence 1980), such as the Concrete in the Oceans research programme in the UK in the 1970s. Furthermore, it appears to be inevitable that RC structures will suffer from reinforcement corrosion in chloride (Cl^-) and carbon dioxide (CO_2) laden environment. Practical experience and experimental observations (Andrade *et al.* 1993; Li 2003 and 2005; Otsuki *et al.* 2000) suggest that corrosion affected RC structures deteriorate faster in terms of serviceability (e.g., cracking or deflection) than safety (e.g., strength) as shown in Fig. 1-1. The reason for this is attributed to the nature of the problem; the corrosion products exert an

expansive pressure on concrete. The deterioration rate in Fig. 1-1 is represented by a deterioration function $\varphi(t)$ which is defined in Li (2003) as the residual structural resistance divided by the original structural resistance. This makes sense that the lower the deterioration rate, the smaller the residual structural resistance and thus the more severe the deterioration of the concrete structure. Due to the low tensile strength of concrete, this expansive pressure results in concrete cracking, spalling and de-bonding between the reinforcing bar and concrete. All these effects are prominent once corrosion actively propagates in concrete and subsequently reduces structural serviceability. The situation can be exacerbated when applied load adds more internal pressure to concrete. Consequently, this leads to more cracks in concrete, destroying the structural integrity and incurring costly repairs and inconvenience to the public.

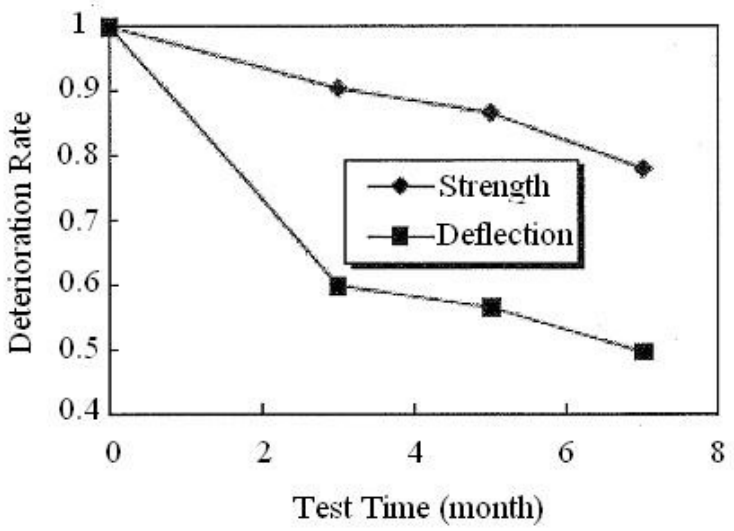

Figure 1-1 Structural deterioration under different limit states (from Li 2005)

Considerable research has been carried out on reinforcing steel corrosion in RC structures in general (Li *et al*. 2003; Melchers and Li 2006; Parrott, 1994; Tuutti 1982). Numerous studies have also been undertaken on corrosion-induced concrete cracking (Dagher and Kulendran 1992; Liu and Weyers 1998). Liu and Weyers (1998) examined the time from corrosion initiation to cracking of the cover concrete both theoretically and experimentally. They developed a model to calculate the critical amount of corrosion products. Li *et al.* (2006) established an analytical model for corrosion-induced crack width which gives

quantitative relationships between the critical factors affecting cracking and crack width. Ueda *et al*. (1998) used finite element methods to examine the factors that affect corrosion-induced cracking in concrete and found that the tensile strength and creep of the concrete are important factors that affect concrete surface cracking. Andrade *et al*. (1993) carried out experiments on small corroded reinforced concrete beams and established a relationship between the surface crack width and the reduction of the cross-section of the steel reinforcement. However, in their experiments, impressed direct current (DC) was applied to induce the corrosion process which is different from that under a natural environment. Moreover, the corrosion characteristics, i.e., corrosion products and distribution, of the steel reinforcement can be different for the corrosion process induced by DC and under natural agents. Tests on corrosion induced structural deterioration, under more realistic environments, e.g., simultaneous salt water spray and service load, has also been conducted (Li 2001). A more detailed literature survey shows that most of the research appears to focus on surface cracking of concrete rather than on direct determination of crack width over time with very limited exception of Li *et al.* (2006) perhaps.

In comparison, research on load-induced concrete longitudinal cracking, i.e., parallel to the reinforcing steel bar has been accorded little attention (Colotti and Spadea 2004; Coronelli 2002; Goto 1971; Tepfers 1979). Goto (1971) conducted an experiment on the characteristics of internal cracks, transverse cracks and longitudinal cracks around tensile reinforcing bars and found that the longitudinal cracks are more likely when primary (transverse) crack spacing is near the maximum. Tepfers (1979) investigated the cracking resistance of cover concrete due to bond stress and the stress distribution in concrete for both elastic and plastic stages and found a quantitative relationship between the load-carrying capacity of the concrete ring and the thickness of concrete cover. Coronelli (2002) combined the corrosion-induced pressure with the pressure (stress) produced by bond action in determining the stress distribution in concrete but the focus was on modifying the bond strength between the concrete and steel bar rather than on concrete cracking.

As for the longitudinal cracking induced by combined effects of reinforcement corrosion and applied load, there has been very little research. Noghabai (1996), Coronelli (2002) and Maaddawy *et al*. (2005) are perhaps the only few studies that have been carried out in the relevant areas. Noghabai (1996) and Coronelli (2002) both focused on predicting bond strength between the steel reinforcement and its surrounding concrete with consideration of steel corrosion. However, only the effect of corrosion on the bond strength was investigated and the combined effects of corrosion and applied load on the surface crack width were not examined. Maaddawy *et al*. (2005) carried out a series of tests to investigate the combined effects of corrosion and sustained loads on the structural performance of reinforced concrete beams. They observed both vertical (flexural) cracks and longitudinal cracks for the reinforced concrete beams under reinforcement corrosion and sustained load. Based on the test results, they proposed an empirical relationship between the corrosion (longitudinal) crack width and the percentage of the steel mass loss from the measurements under accelerated corrosion conditions.

A comprehensive literature survey undertaken in this research shows that, with regard to the whole process of concrete longitudinal cracking and crack width under the combined effects of reinforcement corrosion and applied load, no models have been proposed thus far, neither analytical nor numerical. This gives rise to the need of the present research which will investigate the whole process of concrete cracking and crack width for reinforced concrete structures subject to steel corrosion and applied load.

1.2 Significance of the research

Although the bare steel tends to corrode, the reinforced concrete structures are generally durable because the steel reinforcement is encased by the concrete. The concrete cover works as a physical barrier which prevents the aggressive agents from the steel reinforcement. This protection fundamentally ensures the good performance of reinforced concrete structures. However, corrosion of steel reinforcement in concrete has become a considerable durability problem in the

past three decades for reinforced concrete structures (Bentur *et al.* 1997). For reinforced concrete structures subjected to both reinforcement corrosion and sustained load, it has been found (Maaddawy *et al*. 2005) from experiments that all the specimens failed the serviceability limits of crack width specified by design Codes and Standards when they reached the degree of corrosion of 4% to 5% (percentage of steel mass loss). This demonstrates the severity of corrosion problem to the serviceability of reinforced concrete structures.

Since corrosion of steel reinforcement is inevitable for steel reinforced concrete structures, maintenance of the corrosion-affected reinforced concrete structures is a very serious issue during the service life of the structures which is always tedious and costly. Even with protective measures to the steel reinforcement, e.g., paint systems and cathodic protection, maintenance can still not be avoided and the costs of these protections themselves can be quite high (Bentur *et al.* 1997; Keesler and Power 1988). It is reported that corrosion of steel reinforcement in concrete has cost around $100 billion per annum world-wide for the maintenance and repairs primarily of premature concrete cracking and spalling (Chen 2004). According to the Federal Highway Administration (1997) in USA, of the 581862 bridges in and off the USA federal-aid system, about 101518 bridges were rated as structurally deficient. Whilst corrosion of reinforcing steel was not the only cause that contributes to the deficiencies, it was considered as the significant one (Federal Highway Administration 1997).

Concrete crack width is one of the most important parameters for the design and assessment of reinforced concrete structures. For example, Eurocode 2 BS EN 1992-1-1:2004 specifies that crack control needs to be considered as one of the serviceability limit states and recommends the limiting calculated crack width for various conditions. Also demands on service load are likely to increase which, combined with corrosion effect, will escalate concrete cracking. These combined effects justify the need for a thorough investigation on concrete cracking to ensure the serviceability of RC structures. It is therefore imperative to have the knowledge of the growth of the crack width over time. It is also desirable to have a method to directly calculate the crack width so that better informed decisions can be made for the maintenance and repairs of reinforced

concrete structures due to concrete cracking. It is in this regard that the present research is undertaken to develop both analytical and numerical models for concrete crack width of concrete structures subjected to reinforcing steel corrosion and applied load.

1.3 Aims and objectives

The overall aim of this research project is to examine the process of concrete cracking of reinforced concrete structures under the combined effects of reinforcement corrosion and applied load and to develop a method, both analytical and numerical, to predict the concrete crack width of the structure. The main objectives are as follows:

- Develop a full understanding of the concrete cracking process under the combined effects of steel corrosion and applied load.
- Develop a model for the combined pressure of corrosion products and applied load.
- Develop a model for stiffness reduction of cracked concrete.
- Develop a program to execute the computations in the analytical method.
- Develop a finite element model based on cohesive crack model to simulate cracking process in concrete.
- Develop a step-by-step procedure for direct application of the developed numerical method.
- Determine the realistic constitutive relationship for concrete under direct tension.

- Investigate the sensitivity of various affecting factors on the concrete cracking and crack width.

1.4 Scope of the thesis

This thesis consists of 7 chapters which are outlined as follows:

Chapter 1 presents the background and significance of the research, aims and objectives and the scope of the thesis.

Chapter 2 is the literature review. In this chapter, basic theories, methods and state-of-the-art in the relevant research, including steel corrosion in concrete, material and mechanical properties of concrete, theory of fracture mechanics, numerical modelling of concrete cracking and experimental methods in obtaining the fracture parameters are critically reviewed.

Chapter 3 develops an analytical method to determine the concrete crack width under the combined effects. A mathematical model is formulated and a stiffness reduction model is derived. Examples are presented to demonstrate the application of the developed method which is followed by analysis and discussions, and further refinement of the method.

Chapter 4 develops a numerical method to determine the concrete crack width under the combined effects. Cohesive crack model is firstly presented including constitutive relationship and material properties. It is followed by the formation of an interfacial element and damage criteria used. In addition, fundamentals of nonlinear finite element analysis, material nonlinearity and viscous regularization are discussed. An example is also presented to demonstrate the application of the developed method.

Chapter 5 presents an experiment programme to obtain the real fracture properties of plain concrete, i.e., the complete stress-displacement curve, under uniaxial tension. The chapter starts with introduction of materials used, design

and casting of specimens, test set-up and test procedure. The results are then presented and analysed followed by discussions and suggestions.

Chapter 6 presents analysis and discussions for this study. Verification of the analytical and numerical methods is firstly provided by comparing the models and results with the use of the same inputs. Parametric study is then followed to investigate the effects of the various factors that affect the cracking and crack width. Discussions on the results and suggestions for the analytical and numerical modelling are also provided.

Chapter 7 concludes the thesis with future work recommended.

CHAPTER 2

LITERATURE REVIEW

2.1 Introduction

In order to predict concrete crack width induced by corrosion and applied load, knowledge of a broad area is necessary, e.g., chemistry (corrosion), mechanics (elasticity and fracture), numerical modelling (finite element method) and experimentation (material fracture property). This review critically examines all the aspects that are needed in determining the crack width under these combined effects. As the cause of concrete cracking, the corrosion of reinforcing steel in concrete is firstly discussed. It is followed by description and analysis of properties of concrete since it is the concrete that cracks. To analyse the cracks, fracture mechanics is required which is then reviewed. Numerical techniques on how to deal with cracks in finite element method is also evaluated. The testing methods proposed to obtain the material fracture parameters for different nonlinear fracture models are finally presented.

2.2 Steel corrosion in concrete

Reinforced concrete structures should be designed to be durable over the period of service life. The service life is defined as the assumed period for which a structure or part of it is to be used for its intended purpose with anticipated maintenance but without major repair being necessary (BRE Digest 455 2001; Eurocode 0 BS EN 1990:2002). The durability of RC structures, however, is subjected to decrease depending on either various environmental conditions or its internal degradation. Amongst these factors, corrosion of reinforcing steel in concrete is perhaps the most significant one to contribute to the long term deterioration of reinforced concrete structures. In this section, the fundamentals of corrosion science and their applications to steel corrosion in concrete are critically reviewed. Two main types of deterioration mechanisms, carbonation and chloride attack, are then examined. Methods of corrosion condition evaluation are finally discussed.

2.2.1 Basics of corrosion science

In order to understand corrosion-induced concrete cracking, it is essential to know what the corrosion is and how it is applied to reinforced concrete. Steel corrosion in concrete is an electrochemical process, which includes general corrosion and pitting corrosion. These two forms of corrosion are also known as macro-cell corrosion and micro-cell corrosion respectively, in terms of the separation between the anode and the cathode. The details are discussed in the following.

2.2.1.1 General corrosion

Corrosion of steel in concrete is a process in which a refined metal reverts back to its natural state by an oxidation reaction (Broomfield 1997). In simple terms, the process is of oxidation by which iron dissolves into various oxides, known collectively as rust (Pantazopoulou and Papoulia 2001). Although chemical attack can cause steel corrosion, the most common form of that in an aqueous medium is electrochemical (ACI Committee 222 1985). The corrosion products, according to Liu and Weyers (1998), depend on such conditions as pH of the solution, the oxygen supply, and moisture content and can be expressed as $m \cdot Fe(OH)_2 n \cdot Fe(OH)_3 p \cdot H_2O$, where m , n and p are coefficients and varying significantly. Details of corrosion products will be discussed later.

The steel corrosion in concrete is an electrochemical process which involves four basic parts: an anode, where electrochemical oxidation takes place; a cathode, where electrochemical reduction occurs; an electrical conductor, which is steel itself; and an aqueous medium, which lies in concrete (ACI Committee 222 1985). The chemical reactions of steel corrosion are as follows:

$$\text{The anodic reaction: } Fe \rightarrow Fe^{2+} + 2e^{-} \tag{2.1}$$

$$\text{The cathodic reaction: } 2e^{-} + H_2O + \frac{1}{2}O_2 \rightarrow 2OH^{-} \tag{2.2}$$

The anode produces electrons which are transported via aqueous concrete to the cathode where they are consumed with oxygen and water. Ferrous and hydroxyl ions flow within the concrete so that they can react with each other and with further dissolved oxygen and water:

$$Fe^{2+} + 2OH^{-} \rightarrow Fe(OH)_2 \tag{2.3}$$

$$4Fe(OH)_2 + O_2 + 2H_2O \rightarrow 4Fe(OH)_3 \tag{2.4}$$

$$2Fe(OH)_3 \rightarrow Fe_2O_3 \cdot H_2O + 2H_2O \tag{2.5}$$

The motivation of the reaction of Eq. 2.4 is due to the property of chemical instability of $Fe(OH)_2$ which is susceptible to oxidation and becomes $Fe(OH)_3$. $Fe(OH)_3$ is also instable and will break down into hydrated ferric oxides and water soon after its formation. The corrosion process is schematically shown in Fig. 2-1.

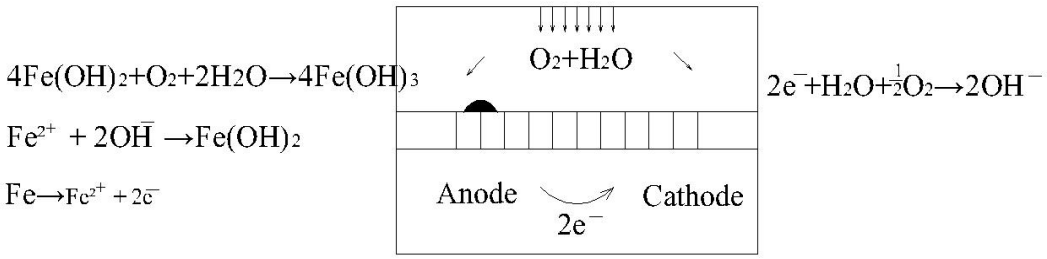

Figure 2-1 Schematic of corrosion process

In general, good quality concrete of suitable mix proportion, compacting and curing provides an excellent protective environment for steel. Thus the steel in concrete does not usually corrode. Such protections include physical and chemical means. The physical protection is offered by the concrete cover which works as physical barrier to the ingress of aggressive agents. The chemical protection is provided by the high alkalinity of concrete due to high concentrations of soluble oxides, such as calcium oxides in the pore solution. Under such an alkaline condition, a thin passive layer forms on the steel surface

which prevents the oxidation from steel. The passive layer is self-repairing and consists partially of metal oxide or hydroxide and partially of mineral from the cement (Broomfield 1997). The steel in concrete will not normally corrode as long as the passive environment is maintained. Two processes can, however, destroy the steel passivity namely carbonation and chloride ingression. Once the passive layer breaks down corrosion initiates.

There are two types of steel corrosion in concrete – macro-cell corrosion and micro-cell corrosion. They are defined by the distance between the locations of anode and cathode. If the anode and cathode are separated, macro-cell corrosion is formed. However, if they are immediately adjacent, micro-cell corrosion is formed (Bentur *et al*. 1997). For macro-cell corrosion, large areas of the steel become corroding anodes and other areas become non-corroding cathodes. The rebar acts as an electrical pathway, conducting electrons from the anode to the cathode. Macro-cell corrosion leads to uniform steel dissolution over the entire surface of the rebar and thus produces rust on the surface of the steel, causing cracking or delaminating of surrounding concrete. This kind of corrosion is usually caused by carbonation or sometimes by high chloride content at the rebar. Pitting is due to micro-cell corrosion and will be examined in the following section.

Corrosion rate is an important parameter to evaluate corrosion and to calculate mass of corrosion products. It is considerably affected by the availability of dissolved oxygen surrounding the cathodic areas. For instance, if the cathodic area is lack of oxygen the corrosion may be retarded. Since the steel is surrounded by concrete cover which slows down the diffusion of dissolved oxygen, the rate of corrosion becomes “diffusion controlled” (Broomfield 1997). Therefore, if the rate of flow of ions is slow the corrosion will also proceed at a slow rate. Since the flow of ions in concrete is directly related to the electrical resistance of the concrete, it gives rise to the need for measuring the electrical resistance to assess the corrosion rate (Bentur *et al*. 1997).

The corrosion of reinforcing steel depends on the alkalinity of the surrounding concrete as measured by pH and electrical potential (Pourbaix 1966). This

relation has been summarized schematically by Pourbaix (1966) as shown in Fig. 2-2 in simplified form. This diagram is designated for general corrosion which may be caused by carbonation. Pourbaix diagram of chloride-induced corrosion will be discussed in the next section.

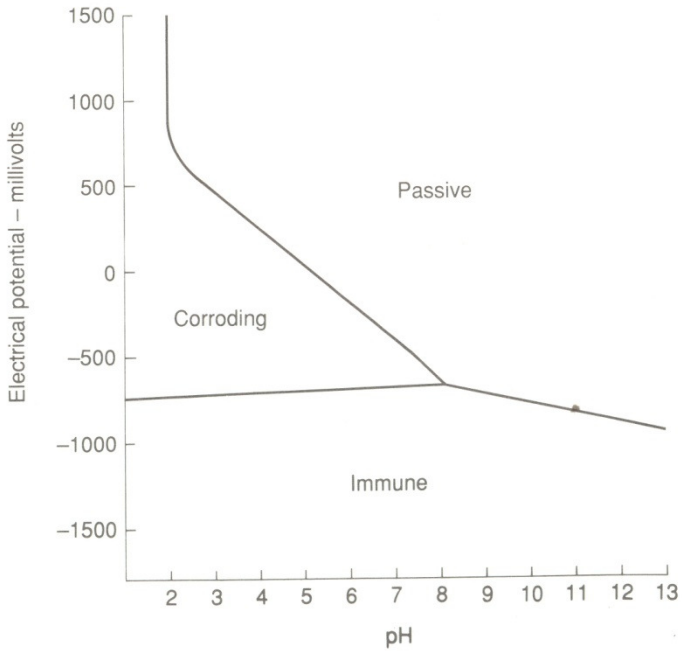

Figure 2-2 Pourbaix diagram for steel in concrete (Kay 1992)

The three regions in the Pourbaix diagram, namely “Passive”, “Corroding” and “Immune”, which provide guidance to the stability of a metal under specific conditions. “Immune” means the metal is not attacked and “Passive” means there is a stable passive layer formed on the surface of the metal (Jones 1992). From Fig. 2-2, it can be seen that at high pH the steel in concrete is in passive condition. The steel starts to corrode when pH drops to 8 and when certain electrical potential is available. The steel may however not corrode at very low pH if the electrical potential is very large.

2.2.1.2 Pitting corrosion

Under certain circumstances, when relatively high concentration of chlorides is present, a localized form of corrosion of steel, known as pitting corrosion, occurs. Pitting corrosion is an extremely dangerous and vicious type of deterioration of steel because it is localized and can be intensively developed

which may cause sudden failure. Fig. 2-3 shows the pitting corrosion process where the pit functions as the anode and the adjacent steel surface functions as the cathode. Chloride ions are intensively involved in this process which is thus called autocatalytic process. This is because, for any possible reason, when the rate of steel dissolution increases at some point, it will attract more chloride ions due to more positive charge is produced. In the meantime, high concentration of hydrogen ions at the adjacent surface is also present as a result of electric balance. Both of the chloride and hydrogen ions are able to accelerate the rates of dissolution of steel (Fontana, 1986). It is, therefore, called autocatalytic or accelerating process.

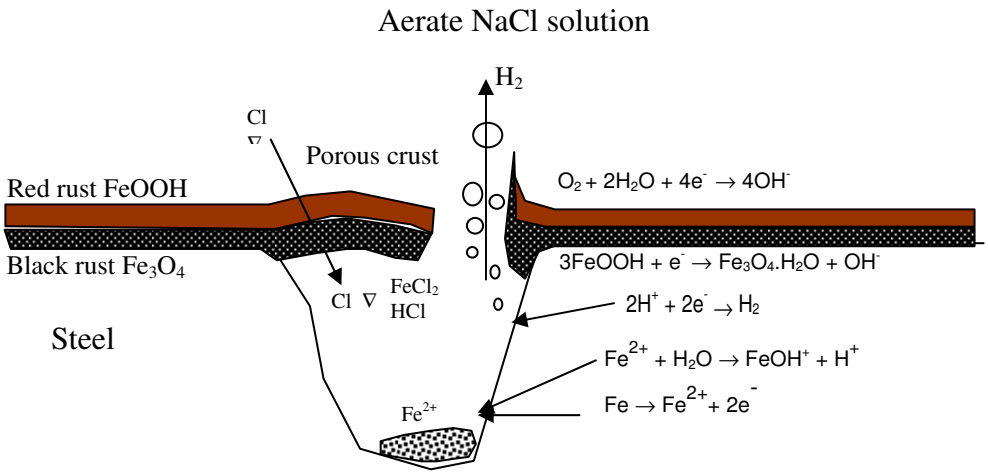

Figure 2-3 pitting corrosion process (Broomfield 1997)

There are two primary characteristics of pitting corrosion. One is that the corrosion is localized and the adjacent surface to the pit is shielded from corrosion due to cathodic protection. This is because anodic reaction which consumes the steel only takes place within the pit. The other is since oxygen is not soluble in concentrated solutions, the ferrous ions will stay in the solutions in the pit and will not be oxidised to ferric ions.

Corrosion of steel in concrete normally starts from the pitting corrosion which increase in number, expands to the generalized corrosion (Broomfield 1997). Pitting corrosion occurs over the pit which is generally located at the steel surface with a void in the adjacent cement. The passive layer of the reinforcement near to the void is most likely destroyed by the process of pitting

corrosion. Fig. 2-4 shows the Pourbaix diagram for steel in concrete when chlorides are present. It clearly demonstrates that pitting corrosion occurs even at very high pH when chlorides are involved. For the general corrosion to occur, however, the pH values have to be substantially decreased to certain levels, as shown in Fig. 2-2. The meanings of "Passive" and "Immune" are identical to those terms in Fig. 2-2.

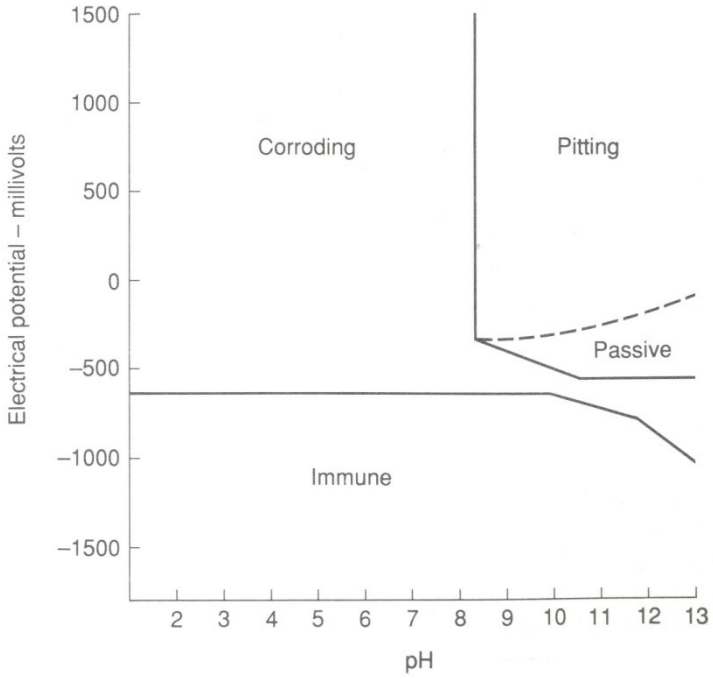

Figure 2-4 Pourbaix diagram for steel in concrete with chlorides (Kay 1992)

Pitting can be regarded as the intermediate form of generalized corrosion and no corrosion. Riggs *et al*. (1960) have carried out a series of tests on investigating the pH effects on the corrosion of steel. In this study, it was found that as the pH value was decreased from 12 to 2, the corrosion progressed from localized pitting to general corrosion, in the environment of 5% *NaCl* solution after 24 hours and given oxygen pressure. It has also been concluded that strong hot chloride environment will cause severe and overall corrosion, while dilute, cold chloride environment will relatively rarely induce corrosion.

2.2.1.3 Corrosion products

As mentioned in preceding discussions, corrosion products can be expressed in general as

$$m \cdot Fe(OH)_2 n \cdot Fe(OH)_3 p \cdot H_2O \tag{2.6}$$

where m, n and p are coefficients. According to the oxidation state, there are two kinds of steel ions: Fe^{2+} and Fe^{3+}. They are corresponding to FeO, Fe_2O_3 and Fe_3O_4 respectively in terms of oxides where Fe_3O_4 is a mixed oxides of FeO and Fe_2O_3. Unhydrated ferric oxide Fe_2O_3 and hydrated ferric oxide $Fe_2O_3 \cdot H_2O$ are the normal rusts which are red/brown brittle and flaky. It is known that oxide Fe_2O_3 has a volume of about twice of the consumed steel. However, $Fe_2O_3 \cdot H_2O$ can swell up to ten times of the original steel volume and is porous. This means that the rust will exert a pressure on the concrete and lead to the cracking and spalling of concrete. However, if the anode is starved of oxygen there is another form of rust called "black/green" rust which will not expand therefore will not incur any cracking or spalling (Broomfield 1997). It means that if the anode is short of oxygen, the reaction of Eq. 2.4 will not take place any more so that Fe^{2+} stays in solution which does not expand. In this case the corrosion products will be FeO or hydrated ferrous oxide $FeO \cdot nH_2O$. Other forms of rusts like magnetite Fe_3O_4 or hydrated magnetite $Fe_3O_4 \cdot H_2O$ may also present. Therefore, the oxygen and water are crucial not only at cathode for cathodic reaction but also at anode for oxidation of Fe^{2+} to become Fe^{3+}. Since it doesn't provide surface indication of corrosion, e.g., stains or cracking or spalling, it is particularly dangerous for black/green rust as it may seriously weaken the steel reinforcement.

Thus, different oxidation and hydration states will produce various corrosion products, which have different densities, volume and colours. Table 2-1 shows the volumes of the corrosion products relative to the uncorroded steel and their colours. The volume increase is solid in nature which is based on the same

amount of moles of steel. For example, if 1 mol of steel (Fe) is completely converted to ferrous oxide (FeO), the volume will be increased to 1.7 times of it. The composition of the rust is varying and depends considerably on circumstantial factors and therefore it cannot be credibly postulated.

Table 2-1 Volumes of corrosion products relative to uncorroded steel (Liu and Weyers, 1998)

Corrosion product	Colour	Volume increase
FeO	black	1.7
Fe_3O_4	black	2.2
Fe_2O_3	red/brown	2.3
$Fe(OH)_2$	blue/green	3.8
$Fe(OH)_3$	red/brown	4.2
$Fe(OH)_3 \cdot 3H_2O$	red/brown	6.4

The density of the rust ρ_{rust} is a significant parameter to affect the volume of expansion which is used to predict the time to cracking and crack width. According to some literature, ρ_{rust} is usually taken between ¼ and ½ of steel density for macro-cell corrosion (Andrade *et al*. 1993) and ¼ and 1/8 for micro-cell corrosion (Gonzalez *et al*. 1995). As for the mechanical behaviour of the rust, little research has been conducted. This is probably due to the difficulties in carrying out tests on the rusts. Nevertheless, Petre-lazar and Gerard (2000) managed to determine the mechanical property of rusts by using scratching tests. They described the rusts as cohesionless assemblage of incompressible crystals. Karin (2002) has further developed the stress-strain relation of the rusts based on Petre-lazar and Gerard's findings as in the equation below

$$s_n = K_{cor} \bullet \varepsilon_{cor}^{p} \tag{2.7}$$

where ϵ_{cor} is the strain, s_n is the stress, and the parameters K_{cor} and p are chosen to give reasonable agreement with the test results. Karin (2002) used 7.0GPa as the value of K_{cor} and 7.0 as that of p.

2.2.2 Mechanisms of steel corrosion in concrete

There are widely accepted two mechanisms for corrosion by which the alkalinity of concrete and the passivity of the steel surface may be destroyed:

- Reduction in alkalinity, neutralized through reaction with carbon dioxide or other acidic materials, known as carbonation.
- Reaction of chlorides with the passive film covering the surface of the rebar due to high concentration of chlorides.

2.2.2.1 Carbonation

Carbonation is the result of the interaction of carbon dioxide gas in the atmosphere with the alkaline hydroxides in the concrete (Anstice *et al.* 2004; Broomfield 1997; Castellote and Andrade 2008). The carbon dioxide in the air dissolves in water and forms carbonic acid which reacts with calcium hydroxide in the concrete pores and neutralizes the alkalis in the concrete:

$$CO_2 + H_2O \rightarrow H_2CO_3 \tag{2.8}$$

$$H_2CO_3 + Ca(OH)_2 \rightarrow CaCO_3 + 2H_2O \tag{2.9}$$

Concrete will maintain its alkaline environment at a certain level at the beginning of carbonation although the carbonation process consumes calcium hydroxide. However, the local calcium hydroxide will eventually be not enough to sustain the alkaline environment and thus the pH falls to a level (normally at 11) where the steel corrodes. Therefore, carbonation can lead to corrosion in the way that it reduces the pH values of concrete. Since the maintenance of the passive layer really relies on a high pH local environment around it, the pH drop can act as guidance for determining if the rebar is corroded, given the moisture and oxygen are adequate. Papadakis *et al.* (1992) postulated that the pH can drop from about 13 to about 9 or even 8.3 when it is fully carbonated.

The carbonation penetration depth is an important parameter to assess if the surrounding concrete of the embedded steel is carbonated. Due to the presence of coarse aggregates and sometimes cracks, however, the carbonation penetration depth varies at different positions. In order to quantify the penetration, a general/uniform condition is considered. Eq. 2.10 shows that the carbonation front proceeds into concrete roughly following the laws of diffusion. It is expressed in terms of the rate which is inversely proportional to the cover concrete thickness (Broomfield 1997).

$$dx / dt = D_0 / x \tag{2.10}$$

where x is the depth carbonation penetrates, t is time and D_0 is the diffusion constant which is dependent on concrete quality.

The solution of differential equation 2.10 gives a square root law that can be used to estimate the movement of the carbonation front which shows how deep the concrete has been carbonated, provided in a steady hygrometric environment.

$$x = A\sqrt{t} \tag{2.11}$$

where A is the diffusion coefficient and t is the time. The value of A varies for different concrete, e.g., A equals 3 or 4 $mm/\sqrt{year}$ for low strength concrete (Currie 1986). Some researchers proposed other forms of estimation of carbonation front which were summarized in Parrott (1987). It should be noted that Eq. 2.11 is only applicable when the exposure conditions are steady (Neville 1995). If the concrete is exposed to variable humidity, with periodic wetting, the carbonation rate will be decreased.

From Eq. 2.10, it can be deduced that the concrete cover is a crucial factor for preventing corrosion. Good concrete cover is essential to resist carbonation. There are also other factors influencing carbonation in concrete such as the relative humidity, the concentration of CO_2, the temperature, the permeability

and alkalinity of concrete (Lo *et al.* 2007). The permeability of concrete, considerably based on permeability properties of cement paste, can be a major factor affecting carbonation of concrete as the CO_2 penetrates through porous concrete more rapidly (Mehta and Monteiro 1993)

2.2.2.2 Chloride attack

The other main cause of corrosion of the steel in concrete is chloride attack which is a different depassivation mechanism from the carbonation. Chlorides act as catalysts to corrosion when there is sufficient concentration of chlorides at the steel surface to break down the passive layer. As most catalysts, chlorides are not consumed in the reactions although they help the reactions (corrosion process) to occur and proceed rapidly.

There are two sources of chlorides in concrete: chlorides cast in concrete and those diffused from the outside. For cast-in chlorides, there might be three possible origins: use of sea water in the mix, contaminated aggregates and deliberate addition of chloride set accelerators. Contaminated aggregates are usually sea dredged aggregates which are not adequately washed or even unwashed. It needs to be noted that in modern concrete construction, these sources of chlorides are eliminated. In addition, chlorides can diffuse into concrete from a few of external sources such as de-icing salts, sea water splashes and air binding salts near marine environment. Normally, the diffusion of chlorides is more likely to be a problem than the cast-in chlorides, however, the cast-in chlorides must not be ignored for old structures.

Diffusion of chlorides is the process where chlorides ions migrate through concrete via fluid-filled pores under the action of a concentration difference (Kumar *et al*. 1987). Some chlorides are bound with hydrated cement which are not available to move. Only free chlorides can migrate and diffuse. However, there is a state of equilibrium between the bound and remaining free chlorides (Neville 1995).

Alternate drying and wetting allows for deeper chloride penetration. When concrete is dry, salt water is rapidly absorbed by capillary suction, until the concrete is saturated. If for any reason the external environment becomes dry again, the water evaporates from the pores. However, the salts left behind. Further wetting will result in more chloride ions being taken into the concrete and the previously depositions will be sucked into a deeper depth due to the action of concentration difference. Therefore, the mechanism of drying and wetting works together with the action of concentration difference to mainly contribute to the migration of chlorides in concrete.

Chloride content at the depth of a steel bar in concrete is an important parameter to determine corrosion onset (Vidal *et al.* 2007). The concept of a chloride threshold level (CTL), therefore, is proposed and defined as the content of chloride at the steel depth that is sufficient to breakdown the local passive film and hence to initiate the corrosion process (Schiessl and Raupach 1990). According to Ann and Song (2007), the determination of the CTL is a key element in predicting corrosion initiation in the exposure of chlorides and it is usually presented in the forms of the ratio of chloride to hydroxyl ions, the free chloride content or the total chloride content relative to cement by weight. In practice, it is relative to concrete by weight. The following figures searched in some literature may help to make a good sense of CTL. Haussman (1967) firstly measured the CTL by using a synthetic concrete solution with a chloride to hydroxyl ions ratio of 0.6. The British Standard limits the chloride content to less than 0.4% by weight of cement for reinforced concrete and 0.1% for prestressed or heat cured reinforced concrete (Eurocode 2 BS EN 206-1:2000). As for the ratio to the concrete weight, the reference threshold for chloride content is 0.06% (ASTM C 876 1991; Thomas 1996). However, there are an extremely wide range of the measured values of CTL because of, referring to Ann and Song (2007), the method of measurement, method of presentation of CTL, condition of the steel-concrete interface and the influence of environmental factors.

Measurement of the chloride content or profile is normally performed to determine corrosion initiation. It consists of two stages namely: sampling and

analysis. Sampling is taking cores of concrete which have approximately equal portion of cement paste at various depths and then grinding the concrete or using impact drilling equipment. When the samples are obtained, there are several methods to analyse the chloride content. One is boiling the extracted dust sample in water (ASTM C 1218 1999). This method is to determine the free chloride concentration and is dependent on the fineness of the pulverised sample, amount of added water, temperature, agitation method and time allowed for extraction (Arya and Newman 1990). Another method is the pore press method which extracts the pore solution from the cement paste under high pressure. This is also a method to measure the free chloride content but is more accurate than the first one. Acid soluble extraction is the most widely used method for measuring the total chloride content where both the free chlorides and bound chlorides are assumed to be soluble in acid. The representation of the CTL as the total chloride content as a percentage by weight of cement is favoured because it is relatively easy to determine and it involves the corrosion risk of bound chloride and the inhibitive effect of cement hydration products (Ann and Song 2007). The total chloride can be measured by adopting a chloride ion sensitive electrode or by titration (British Standard 1881-124 1988). X-ray fluorescence is a much more costly method and confined to specialist laboratories due to high expertise required to operate it.

The rate of chloride ingress is often approximated by diffusion theory. Fick's second law is hence used to estimate the chloride content at a distance from the concrete surface x for a given time t (Crank 1975):

$$\frac{\partial C(x,t)}{\partial t} = D_c \frac{\partial^2 (x,t)}{\partial x^2} \tag{2.12}$$

where $C(x, t)$ is the chloride ion content at the distance x from the surface of concrete at the time t and D_c is the apparent diffusion coefficient, which is a property of concrete. A solution to Eq. 2.12 can be obtained for one-dimensional diffusion in a homogenous, semi-infinite medium (concrete) as follows (for example, Roberts *et al*. 2000; Bamforth 1999):

$$C(x,t) = C_s\left[1 - erf\left(\frac{x}{2\sqrt{D_c t}}\right)\right] \tag{2.13}$$

where C_s is the equilibrium chloride content on the surface of concrete and $erf(x)$ is error function. It should be noted that there are some other cases in which Fick's second law may not be accurate. For instance,

- D_c is not constant.
- Chloride binding of hydrated cement is nonlinear.
- Fick's second law is not capable of the cases in which ionic interaction between diffusing ions may take place, e.g., pore solution in concrete.

2.2.2.3 Corrosion process

The corrosion of reinforcement in RC results in cracking, spalling or delamination of the cover of concrete and thus reduces the serviceability of RC structures. To examine the corrosion process, a whole life serviceability of RC structures should be studied. In whole life assessment of corrosion-affected RC structures, each life cycle of service needs to be determined. A life cycle is a time period during the whole service life at the end of which actions of maintenance or repairs are required (Li 2003). In each life cycle of service, certain criteria, e.g. degree of corrosion, should be defined to evaluate the deterioration. Tuutti's model (1982) is perhaps the first model to predict the service life of corrosion-affected RC structures based on the degree of corrosion, which is shown in Fig. 2-5.

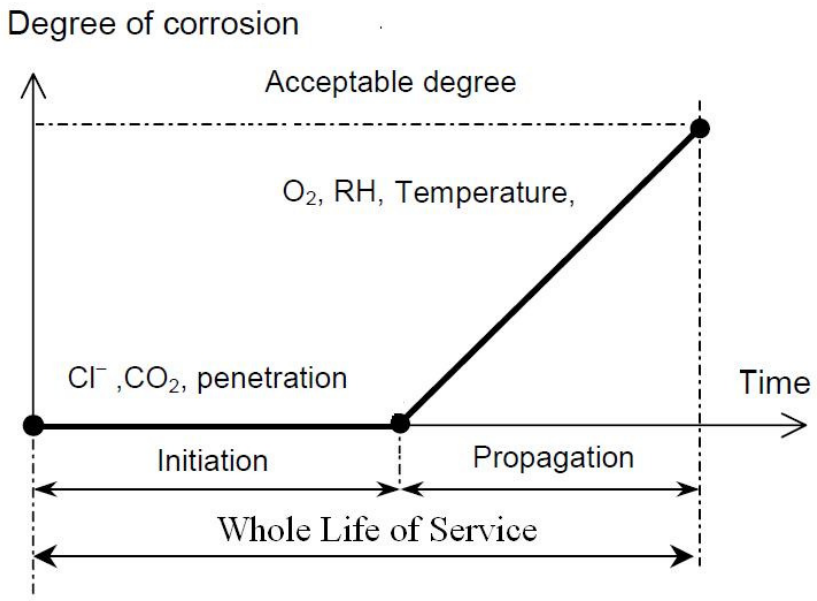

Figure 2-5 Service life model for corrosion-affected RC structures (reproduced from Tuutti 1982)

In Fig. 2-5, the initiation stage is the first life cycle of corrosion-affected RC structures which is the period of time when the ingressive agents, i.e. chlorides, penetrate into the concrete but are not sufficiently enough to initiate corrosion of the steel reinforcement. This stage has been intensively researched during past decades (e.g., Bamforth 1999; Li 2000). The Propagation stage is the period of time when corrosion products accumulate and cause unserviceability of the structure, such as, corrosion-induced cracking, spalling etc.

Tuutti's model, however, uses only degree of corrosion to indicate the service life. Even though the degree of corrosion closely corresponds to the deterioration of the structure, it is not straightforward to convert the degree of corrosion to structural deterioration, i.e. stiffness degradation of concrete. In this regard, Li (2003) proposed a performance-based model of life cycles of corrosion-affected RC structures, with the focus on the effect of corrosion propagation on structural deterioration. In Li's model (2003), a deterioration model was developed in the form of

$$R(t) = \varphi(t) R_0 \tag{2.14}$$

where $\varphi(t)$ is the deterioration function, R_0 is the original structural resistance and $R(t)$ is the structural resistance varying with time, i.e., deterioration.

Based on probabilistic methods, the performance-based assessment criterion was established as follows (Li 2003)

$$P[\varphi(t) \geq \varphi_a] \geq p_a \tag{2.15}$$

where P is the probability of an event, φ_a is the acceptable limit for the deterioration function and p_a is the minimum acceptable probability of structural failure. With this criterion, a life cycle can be determined.

To demonstrate the application of the proposed model, Li (2003) carried out flexural tests on full-scale beams under simultaneous loading and salt spray in a large corrosive chamber. It has been found that the flexural beams deteriorate at different rates with stiffness deteriorating faster than strength. Li (2003) divided the service life of corrosion-affected reinforced concrete structures into three stages: corrosion initiation (start of service life to initiation of corrosion), serviceability (initiation of corrosion to corrosion-induced unserviceability of structure) and safety (loss of serviceability to ultimate failure of the structure). It has also been observed that the initiation of corrosion starts at first 5.6% of the total service life of a beam, but less than 15% of the service life is left once the beam deteriorates to such an extent as to be unserviceable due to cracking or spalling (as also implied in Fig. 1-1). This information can be significant to engineers regarding the maintenance or strengthening of the structure, since the period from unserviceability (i.e., cracking) to ultimate failure of the structure is particularly important.

The concentration of hydroxyl ions at the reinforcement has been recognised to change with time (Page and Treadaway 1982; Sagues *et al*. 1997). However, the changing content (and nature) of hydroxyl ions with time has not been considered in most of those modern corrosion models (Bamforth *et al.* 1997; Melchers and Li 2006). Melchers and Li (2006) developed a phenomenological

model for reinforcement corrosion in concrete as shown in Fig. 2-6. This phenomenological model describes a comprehensive process of reinforcement corrosion in concrete. Specifically, Melchers and Li (2006) proposed two steps in reaching the stage of initiation of significant corrosion: the time t_i for the chlorides to reach certain critical concentration and the time t_{ac} to reach significant low level of pH by leaching out the hydroxyl ions. This explains the delay, as observed in the fields, between the chloride content reaching certain criterion and the initiation of active corrosion, which is consistent with the empirical model proposed by Liu and Weyers (1998).

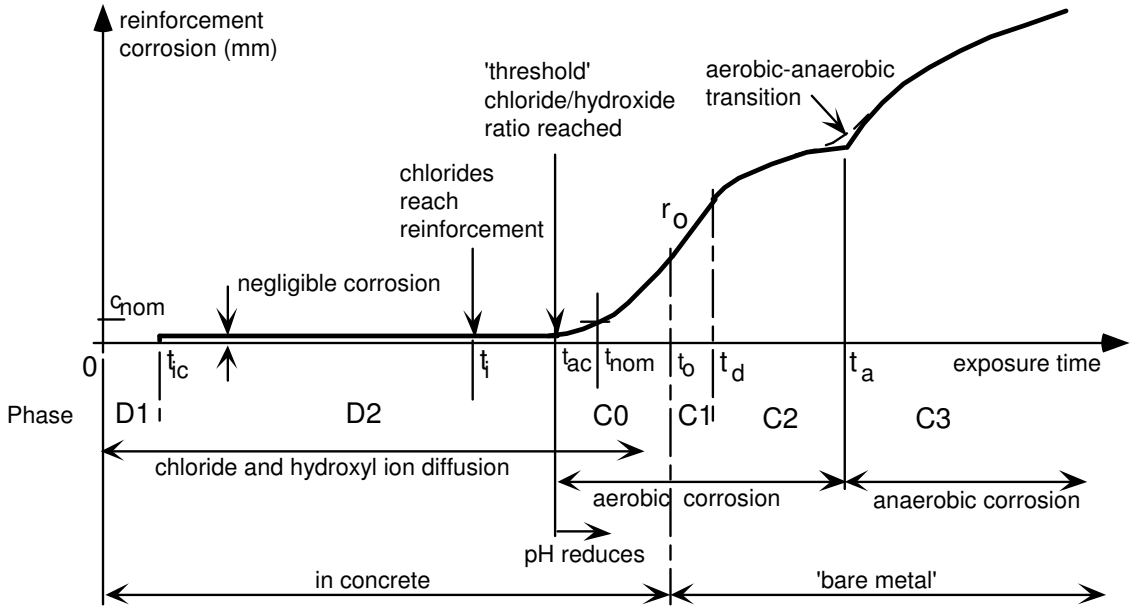

Figure 2-6 Phenomenological model for reinforcement corrosion in concrete (Melchers and Li 2006)

2.2.3 Corrosion condition evaluation

It is of importance to evaluate the condition of corroding or corroded reinforced concrete structures. There is considerable number of approaches available for identifying corrosive environments and active corrosion of steel in concrete. In general, there are destructive and non-destructive methods. Gravimetric technique, also known as weight loss method, is a destructive method. It involves weighing the specimen rebars before and after being embedded into the concrete to be tested. The difference in weight is a quantitative average of the

corrosion attack. Although gravimetric technique is suitable to laboratory studies, it cannot be used to measure the instantaneous corrosion rate and be applied to the structures in use. Therefore, non-destructive methods are appealing. Several electrochemical techniques are successfully used for monitoring corrosion of steel in concrete, such as, half cell potential measurement and linear polarisation measurement.

2.2.3.1 Visual condition assessment

The visual inspection of the structure and the environment is the first step in any investigation (ACI Committee 222 1985; BRE Digest 444 – Parts 1-3 2000). The purpose of the visual inspection is to give a first indication of the extent and severity of the damage and then make a decision on which technique should be used at next step. The main tools are the human eyes and brain, possibly a notebook and a computer, and a camera. Sometimes microscope is needed when cracks are just initiated and not visible to human eyes. In some case, visual inspection is the easiest way to know whether or not the steel corrodes if the concrete can be broken open (Broomfield 1997). A systematic visual survey should be planned in advance and should normally record the date, time and weather conditions when the survey is carried out. The interpretation usually relies on the knowledge and experience of the engineers or technicians conducting the survey. The visual inspection is also acknowledged to be time consuming and costly, and it does not provide the type of information that is required for scheduling of maintenance (ACI Committee 222 1985).

2.2.3.2 Half cell potential measurement

The half cell potential measurement is commonly employed to determine the initiation of steel corrosion, in the way that it measures the corrosion potential. The half cell, in electrochemical term, is a piece of metal in solution of its own ions, such as, copper in copper sulphate solution. When a half cell is connected to another half cell, there will be a difference in potential. The Daniell cell, shown in Fig. 2-7, can well explain this theory.

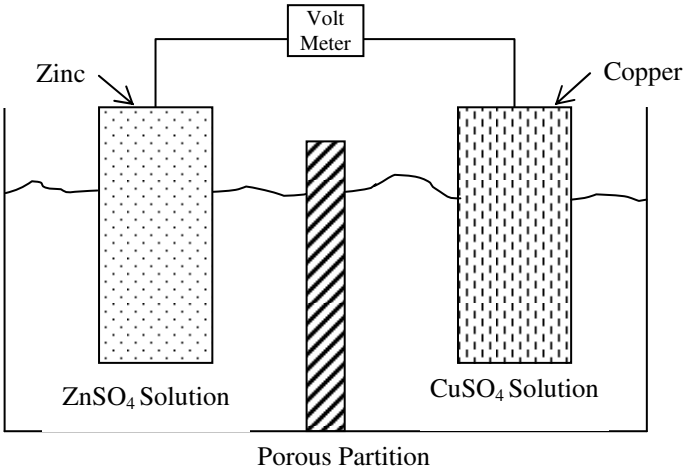

Figure 2-7 the Daniell cell

Two half-cells in the Daniell cell are zinc (Zn^{2+}) in $ZnSO_4$ solution and copper (Cu^{2+}) in $CuSO_4$ solution. When these are connected, in this case by a semi permeable membrane, it allows a charge to pass through it. A voltage is generated due to the difference in the rest potential of the zinc and copper half-cells. Table 2-2 gives the standard metal half cell potentials. From this table, the cell voltage of the Daniell cell can be known as 1.10v (0.34-(-0.76) =1.10v). This theory can be used to measure the half-cell potential of steel corrosion in concrete by placing a half cell (e.g. copper in copper sulphate solution) on the reinforced concrete surface and connecting them with a voltmeter.

Table 2-2 Different metal half cell potentials

Metal	Half cell potentials
$Zn \rightarrow Zn^{2+} + 2e^-$	-0.76v
$Fe \rightarrow Fe^{2+} + 2e^-$	-0.44v
$Cu \rightarrow Cu^{2+} + 2e^-$	+0.34v

When steel reinforcement is corroded, there is another half cell – steel in ferrous hydroxide solution. Fig. 2-8 demonstrates how the half cell measurement works. The reference electrode is working as the standard half cell, which is usually copper in copper sulphate solution. A voltmeter is connected positively to the steel and negatively to the reference electrode. When moving the reference electrode along the concrete surface, different readings of the voltmeter reveals different corrosion conditions of the steel below the moving half cell.

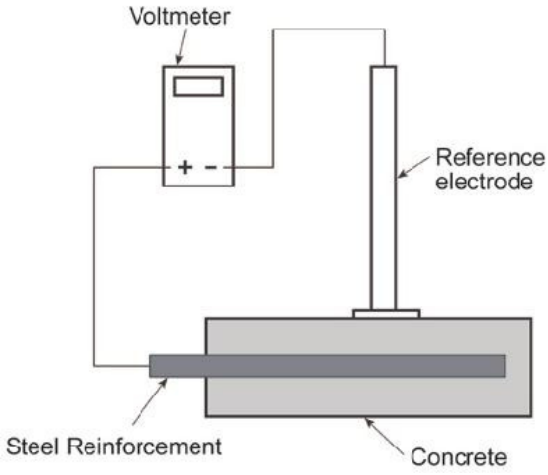

Figure 2-8 Schematic of hall cell potential measurement

In order to interpret the measured potentials, ASTM C 867 (1991) proposed a criterion which was developed empirically from salt induced corrosion of cast-in-place bridge decks in the USA, listed in Table 2-3. For instance, the steel is passive when the reading is between zero and -200 mV against a copper in copper sulphate and the steel is corroding actively when the reading is more negative than -350 mV. Between these two values, it indicates intermediate corrosion. The reason that the risk/possibility of corrosion is used is because when little oxygen is presented, i.e., concrete is saturated, the corrosion potentials measured can be very high in negative but without initiation of corrosion.

Table 2-3 Corrosion potentials for different standard half cells

Corrosion condition	$Cu/CuSO_4$	Ag/AgCl 4M KCl	Standard H^+ Electrode	Calomel (SCE)
10% risk of corrosion	> -200	> -106	> + 116	> - 126
Intermediate corrosion risk	-200 ~ -350	-106 ~ -256	+116 ~ -34	-126 ~ -276
< 90% risk of corrosion	< -350	< -256	< - 34	< -276
Severe corrosion	< -500	< - 406	< - 184	< -426

When investigating large structures, a potential map is normally drawn to reflect a comprehensive corrosion condition. The map is a printout of the readings where lines are drawn separating the levels of potential which is like the contour lines in geography (Broomfield 1997).

Half cell potential measurement is a simple way to determine the initiation of steel corrosion with reasonable accuracy. However, there are some limitations to this method:

- No indication on corrosion rate.
- Only active corrosion can be detected.
- Thickness of concrete cover affects the reading considerably.

It is, therefore, suggested for the engineers to use more than one test method to evaluate corrosion conditions.

2.2.3.3 Linear polarization

The linear polarization measurement is currently widely employed to obtain the corrosion current and thus the corrosion rate in terms of metal loss. This method is based on the relationship between the metallic dissolution and the current generated both in anodic reaction. The process is explained by Faraday's law (Mangat and Molloy 1992).

$$m = \frac{M.I.t}{z.F_a} \tag{2.16}$$

where m is the mass of steel consumed (g), I is the current (amperes), t is the time (s), F_a is Faraday constant equals to 96500 C mol^{-1}, z is the ionic charge, M is the atomic weight of metal.

For iron with $M = 56g$, density $\rho_{st} = 7.85g\ cm^{-3}$ and $z = 2$ and with definitions that A is surface area of reinforcement covered by the device in cm^2, i_{corr} is corrosion current density in $\mu A \cdot cm^{-2}$, $I = i_{corr}\ A$, x is metal loss in cm, Eq. 2.16 becomes

$$\rho Ax = \frac{M \times i_{corr} A \times t}{z \times F_a} \tag{2.17}$$

$$x = \frac{56 \times i_{corr} \times t}{2 \times 96500 \times 7.85} = 3.69 \times 10^{-5} i_{corr} t \tag{2.18}$$

Corrosion rate (μm / year)

$$= \frac{\mathrm{x}}{t} = 3.69 \times 10^{-7} \times 365 \times 24 \times 60 \times 60 i_{corr} = 11.6 i_{corr} \tag{2.19}$$

Once i_{corr} is known, the corrosion rate is determined. To obtain i_{corr}, linear polarization technique is employed. This technique polarizes the steel with an electric current and monitors its effect on the half cell potential, as illustrated in Fig. 2-9. The corresponding potential change of the half cell is measured while the applied small current is passed from the electrode to the reinforcement. The gradient of the potential and the current is R_p , expressed in Eq. 2.20:

$$R_p = \frac{Change\ in\ potential}{applied\ current} \tag{2.20}$$

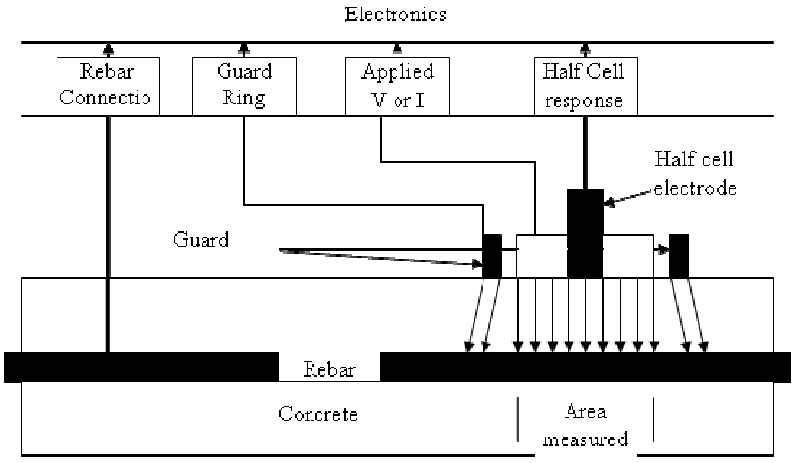

Figure 2-9 Schematic of linear polarization measurement

With the polarization resistance R_p (in ohms) being obtained, the corrosion current i_{corr} can be calculated as:

$$i_{corr} = B / R_p \tag{2.21}$$

Where B is a constant (26 to 52 mV depending on the passive or active condition of steel).

It should be noted that the term "linear polarization" refers to the linear regions of the polarization curve, therefore, the change in potential should be kept below 20mV.

Some guidelines are proposed in Broomfield (1997) and Clear (1989) on the degree of corrosion in terms of corrosion current density. These guidelines provide interpretation to the corrosion rate monitored. Table 2-4 lists the criteria developed for the devices with the sensor controlled guard ring system (shown in Fig. 2-9).

Table 2-4 Criteria for corrosion with linear polarization measurement (Broomfield 1997)

Corrosion condition	Corrosion current density i_{corr}
Passive condition	$i_{corr} < 0.1$ μA/cm^2
Low to moderate corrosion	0.1 μA/cm^2 < i_{corr} <0.5 μA/cm^2
Moderate to high corrosion	0.5 μA/cm^2 < i_{corr} <1 μA/cm^2
High corrosion rate	$i_{corr} > 1$ μA/cm^2

Linear polarization measurement is generally used by engineers to assess the corrosion rate of steel in concrete. However, there are a few limitations for this measurement. Firstly, the corrosion rate detected is instantaneous so it changes with time due to changes in temperature, relative humidity and so on; secondly, the surface area is extremely difficult to define and measure which will lead to huge error especially when the corrosion rate is low. What needed in calculating corrosion products is the average corrosion rate. In this case, some assumptions have to be made or multiple measurements are needed to obtain the average corrosion rate.

2.3 Properties of concrete

Properties of concrete are to be examined mainly due to two reasons within the scope of this research: (1) concrete protects the reinforcement from deterioration of external environment, such as, chloride ingress, carbonation, temperature, humidity and so on; and (2) the derivation of the crack width induced by either corrosion or applied loads, relies on the process of concrete cracking, which largely depends on its material properties. In this section, the basics of concrete including their effects on reinforcement corrosion are reviewed. Since corrosion-induced cracking results from the tensile failure, factors affecting concrete tensile strength are also discussed. Finally, a porous interfacial transition zone between reinforcement and surrounding concrete is examined, in terms of its alkalinity, porosity and mechanical behaviour.

2.3.1 Basics of concrete technology

In order to understand how corrosion induces concrete cracking, it is important to investigate the composition of concrete, as well as physical and mechanical properties of concrete. Concrete is known as a construction material composed of cement, aggregates, sand and water. With different mix design, concrete can have various properties.

2.3.1.1 Composition of concrete

Concrete is of alkaline rich environment (Neville 1995). This is contributed by the hydration of cement. Cement is a material with adhesive and cohesive properties which make it capable of bonding mineral fragments into an entity. Cement is hydraulic and can be classified in various types, such as, Portland cement and high-alumina cement (Neville 1995). Portland cement is the most common and frequent-used type of cement all over the world. Depending on the particular properties it exhibits, the Portland cement can also be divided into various types by changing the chemical composition such as rapid hardening Portland cement, low heat Portland cement, sulphate resisting cement and so on. This section will mainly focus on Portland cement and discuss how such an alkaline rich environment is produced.

The raw materials used in the manufacture of Portland cement, according to Neville (1995), are calcareous materials such as limestone or chalk, clay or shale containing alumina and silica, and marl, a mixture of calcareous and argillaceous materials. The raw materials consist mainly of lime, silica and alumina. Iron oxides are also included. The main compounds of Portland cement are as follow: tricalcium silicate $3CaO \cdot SiO_2 (C_3S)$, dicalcium silicate $2CaO \cdot SiO_2 (C_2S)$, tricalcium aluminate $3CaO \cdot Al_2O_3 (C_3A)$ and tetracalcium aluminoferrit $4CaO \cdot Al_2O_3 \cdot Fe_2O_3 (C_4AF)$. In addition, some minor compounds such as MgO, TiO_2, K_2O, Na_2O and Mn_2O_3 also exist. It should be noted that Na_2O and K_2O are known as alkalis which will react with aggregates (known as alkalis-aggregates reaction) and the products of reaction cause disintegration of concrete.

'Bogue composition' (Bogue 1955) is known as the equation to calculate the composition of Portland cement. He established quantitative relationships between these compounds and their comprising oxides such as CaO, SiO_2 *et al.* For the oxide composition, however, Neville (1995) and Orchard (1979) point out that CaO presents in the largest amounts which takes 60 to 70 per cent of cement content, SiO_2 takes 17 to 25 per cent, Al_2O_3 occupies 3 to 8 per cent and Fe_2O_3 ranges from 0.5 to 6 per cent. For the compound compositions, the largely depends on the proportions of the oxide composition and the influence is quite sensible. A series of figures in Neville (1995) show that when CaO content of a typical rapid-hardening cement drops by 3 per cent, with corresponding increases in other oxides, the C_3S / C_2S ratio exhibits a considerable change from 65/8 to 33/38.

In the presence of water, the cement compounds are hydrated and cement paste forms. The products of hydration of the cement are chemically the same as the products of hydration of individual compounds under similar condition (Neville 1995). Amongst these cement compounds described above, the hydrated

products of tricalcium silicate (C_3S), dicalcium silicate (C_2S) and tricalcium aluminate are the main hydrates. The hydration processes (non-stoichiometric) are described below.

$$2C_3S + 6H^{'} \rightarrow C_3S_2H_3^{'} + 3Ca(OH)_2 \quad (2.23)$$

$$2C_2S + 4H^{'} \rightarrow C_3S_2H_3^{'} + Ca(OH)_2 \quad (2.23)$$

where $H^{'}$ represents water. These reactions assume $C_3S_2H_3^{'}$ is the final product of hydration of calcium silicates, however, the lime/silica ratio is changed with time and the presence of other compounds, and it is not always 1.5 as represented in $C_3S_2H_3^{'}$. Therefore, it is more appropriate to use the form of $C-S-H^{'}$ to describe the calcium silicate hydrates with the ratio of $C:S$ to be probably near 2 (Diamond 1976). It is also considered that $C-S-H^{'}$ contains some small amounts of Al , Fe , Mg and others.

As discussed before, the reason why steel reinforcement in concrete does not corrode is because of the high alkalinity of the chemical environment of concrete. The calcium hydroxide provides and maintains such a high alkaline environment, where a protective passive layer on the steel can be sustained. However, the amount of calcium hydroxide varies depending on different types of cement used. A well-hydrated Portland cement may contain from 15 to 30 per cent calcium hydroxide by weight of the original cement (Pressler *et al.* 1961). This is normally enough to maintain the pH at 13 in concrete.

Cement composition/type has effect on the initiation stage of corrosion process. Some types of cement have chloride-binding capabilities and/or control the chloride mobility. Page *et al.* (1986) postulates that the chloride diffusion speed varies in different types of cement, in the order of high to low were: Sulphate-resisting cement, normal Portland cement, fly-ash blended cement, blast furnace slag blended cement. They have also found out that certain types of cement containing blast furnace slag or fly-ash have a high capacity to restrict the

mobility of chloride ions due to the involvement of a portion of chloride into chemical reaction (especially with C_3A) producing stable compounds.

Moreover, as discussed in preceding chapter, the best measure of corrosivity of concrete is its electrical conductivity which expresses the capacity of the concrete to allow corrosion (Broomfield 1997). In particular, the conductivity is inversely proportional to the resistivity of the concrete. High resistivity of concrete will have low corrosive activity. An increase in cement content of concrete leads to a decreased resistivity, since at a constant water/cement ratio but higher cement content there are more electrolytes available for the current to pass on.

2.3.1.2 Physical property

Concrete is a porous material. It contains capillary pores, gel pores and air voids produced by various sources. The capillary pores represent the part of the gross volume which has not been filled by the products of hydration. Capillary pores are an interconnected system randomly distributed throughout the cement paste (Verbeck 1955) and are considered to be responsible for the permeability of the hardened cement paste (Neville 1995). The gel pore can contain large amount of evaporable water which occupies about 28 per cent of the total volume of the gel. The gel pores are also interconnected but they are much smaller than the capillary pores: about one or two orders of magnitude smaller. Different from the capillary pores, the gel pores are independent of the progress of the hydration. In terms of water presence in cement paste, it is of three types: non evaporable water, gel water and capillary water (Power and Brownyard 1947). The non-evaporable water is the part chemically combined with the cement and cannot be removed until application of enough heat. In addition to these voids, imperfect compaction can also introduce air voids. The extent to which the aggregates will produce a minimum void content is also dependent on its particle shape (Orchard 1979). In general rounded aggregates create fewer voids than the irregular ones.

The effect of the porosity to corrosion could be considerable since it directly affects the penetration of carbon dioxide and chloride ions, and the electrical

resistivity of the concrete. It should be clear that if the concrete has an open pore structure, it would be much easier for the carbon dioxide and sea water containing chloride ions to diffuse in. Therefore, the permeability of concrete is perhaps one of the most significant single parameters affecting the corrosion of reinforcement in concrete. However, porosity is not really equivalent to permeability. This is because only interconnected pores can contribute to the transportation of fluids. This means even through the porosity is high, the permeability of concrete can be low as long as the pores are not well interconnected.

Provided that the cover of concrete is of certain thickness, the permeability of the cover concrete largely controls the penetration of chlorides, moisture, acid gas and oxygen. Concrete of low permeability normally has a high electrical resistivity which reduces the flow of electric current within the concrete. Such an improvement of the electrical resistivity depends also on the water content in the pores. More water in the pores will lead to higher electrical conductivity, but not definite corrosion rate. This is due to saturated water can significantly reduce the supply of oxygen. Thus, with the increase in water content in the pores of the concrete, the corrosion rate will initially increase due to the improved conductivity but then decrease because of limited delivery of oxygen.

Some measures can be taken to physically prevent the formation of an open pore structure in concrete. On the macroscopic scale, there should be good compaction of the concrete; while on a microscopic scale, the concrete has to be well cured to have smaller and fewer pores and lower connectivity of pores (ACI Committee 222 1985).

2.3.1.3 Mechanical property

To a certain degree, concrete can be regarded as elastic material. The general stress-strain relation of concrete in compression is shown in Fig. 2-10 which normally exhibits linear relationship at the beginning followed by nonlinear behaviour. The straight part of or the tangent to the curve is termed as modulus of elasticity which is also called initial tangent modulus. The secant modulus can be observed in the trend that it decreases as the corresponding stress

increases. In Fig. 2-10, it is of interest to point out both cement paste and aggregate exhibit linear stress-strain relation when individually subjected to load prior to the peak stress (Neville 1995), although some researchers suggested a nonlinear stress-strain relation for hardened cement paste (Attiogbe and Darwin 1987). It should be noted that the cement paste and concrete will have gradually decreasing strengths after their peak values, which are not demonstrated in Fig. 2-10. There are two main reasons for the nonlinear behaviour of concrete: the existence of interfaces between the aggregates and cement paste, and the development of microcracks (Shah and Winter 1968).

For the first reason, concrete is traditionally modelled as a two-phase material but more recently is modelled as three-phase material (Li *et al.* 1999, 2003; Lutz *et al.* 1997; Ramesh *et al.* 1996). In three-phase assumption, concrete consists of aggregate, cement paste and interface which is considered to be the weakest link in the matrix system (Hu and Stroeven 2004; Scrivener *et al.* 2004). The second reason can be interpreted as that the presence of the microcracks alter the stress distribution and magnitude around them locally and the local stress becomes much higher than the nominal stress. This implies the strain increases at a faster rate than the nominal stress and thus the stress-strain relation continues to bend over in concave shape.

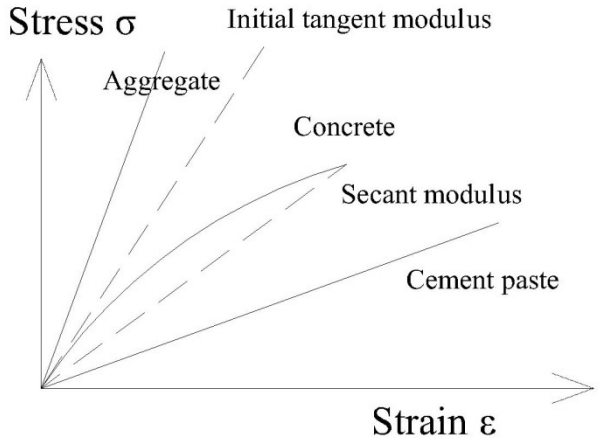

Figure 2-10 Stress-strain relations for aggregate, cement paste and concrete (Neville 1995)

Considerable effort has been made to develop the expressions for stress-strain curve of concrete by standard mathematical functions such as a parabola, hyperbola, ellipse, cubic parabola and so on. Desayi and Krishnan (1964) proposed an equation for the entire stress-strain curve as in Eq. 2.24.

$$\sigma = \frac{E\varepsilon}{1+\left(\frac{\varepsilon}{\varepsilon_0}\right)^2} \tag{2.24}$$

where σ is the stress, ε is the strain, E is the initial tangent modulus (Young's modulus) assumed to be twice the secant modulus at maximum stress, and ε_0 is the strain at the maximum stress.

Another widely acknowledged and often quoted stress-strain curve was developed by Hognestad (1951):

$$\sigma = f_c^{'}\left[2\left(\frac{\varepsilon}{\varepsilon_0}\right)-\left(\frac{\varepsilon}{\varepsilon_0}\right)^2\right] \qquad \text{for } 0 < \varepsilon \le \varepsilon_0 \tag{2.25a}$$

$$\sigma = f_c^{'} - 0.15 f_c^{'}\left[\frac{\varepsilon-\varepsilon_0}{\varepsilon_{cu}-\varepsilon_0}\right] \qquad \text{for } \varepsilon_0 < \varepsilon \le \varepsilon_{cu} \tag{2.25b}$$

where $f_c^{'}$ is the peak concrete stress and ε_{cu} is the ultimate concrete strain.

The pre-peak shape of the stress-strain relation depends on the compressive strength of concrete as well as the rate of application of stress. A number of researchers have tried to worked out a precise form of the relationship between the secant modulus of elasticity and the compressive strength, and ACI 318-02 (2001) and ACI 363R-92 (1992) have summarized the relations for normal strength concrete and high strength concrete respectively and will not be repeated here. It needs to be noted that the curvature of the relation and the modulus of elasticity of these suggested expressions are also affected by the rate

of applied load. When the load is applied promptly, the modulus increases thus concrete becomes tough to be deformed and the curvature of the stress-strain curve becomes small. However, when the load is applied with a rate in a range of 2 to 10 minutes, this effect is very small. It should be noted that the modulus of elasticity discussed is for compression only although it can be simply assumed that the modulus of elasticity in tension is equal to the modulus in compression (Galloway and Harding 1976; Lydon and Balendran 1986).

2.3.2 Factors affecting concrete tensile strength

Concrete is known to be strong in compression but weak in tension, which is why concrete structures are susceptive to cracks. Failure of concrete structures typically initiates with stable crack growth or formation of large fractures before the structure fails ultimately. No matter what theory of fracture mechanics is used for the crack propagation in concrete, the criterion of crack initiation is always based on tensile strength, that is, a crack will initiate once the tensile strength exceeds the tensile strength. Therefore, it is important to discuss the effects of various factors on the tensile strength. Since very little information about material property is available directly on tensile strength, and the compressive strength is closely related to the tensile strength (Neville 1995), some effects on compressive strength are focused from the literature. In this section, water-cement ratio, porosity and aggregate-cement paste interface are reviewed based on their effects on the strength of concrete. Some other factors which affect the compressive strength much but little in tension, such as shape and texture of aggregate, are not discussed.

2.3.2.1 Water-cement ratio

Water in concrete is known to function in two ways – to enable the hydration of cement and to lubricate the mixture to make it workable. The water required to hydrate cement is always definite, and for Portland cement it is usually 0.25 portions compared with 1 portion cement by weight. When this water-cement ratio is applied, however, it will become impossible to compact it. Therefore, extra water is needed to make the fresh concrete workable. This amount of

water will evaporate later when concrete is hardened and leaves voids inside the concrete which will be discussed in next section.

Water-cement ratio is one of the most important factors influencing the strength of concrete. When concrete is fully compacted, the strength of concrete is inversely proportional to the water-cement ratio which was proposed by Abrams (1919)

$$f_c = \frac{K_1}{K_2^{\,w/c}} \tag{2.26}$$

K_1 and K_2 are constants, w/c is water-cement ratio.

In terms of the quantitative relationship between compressive strength and water-cement ratio of Eq. 2.26, Fig. 2-11 could be drawn to reflect the relation more sensibly since it is coupled with the effect of compaction. It can be found that for fully compacted concrete, the compressive strength decreases as the water-cement ratio increases. Although water-cement ratio is not the only factor influencing concrete strength, it is the largest single factor for the strength of fully compacted concrete. Neville (1995) stated that the water-cement ratio is more important than ratio of cement to aggregate and maximum size of the aggregate when usual aggregates up to 40 mm maximum size are employed. Furthermore, Cordon and Gillespie (1963) pointed out there were three factors need to be considered: (1) the quality of the cement paste which varies with the water-cement ratio; (2) the bond strength (adhesion) between the cement paste and the aggregate particles which is influenced by the quality of the cement paste, the surface area, and surface texture of the aggregates; and (3) the angle of friction in test cylinders which varies with the size and shape and quantity of the aggregate particles and the quality of the cement paste.

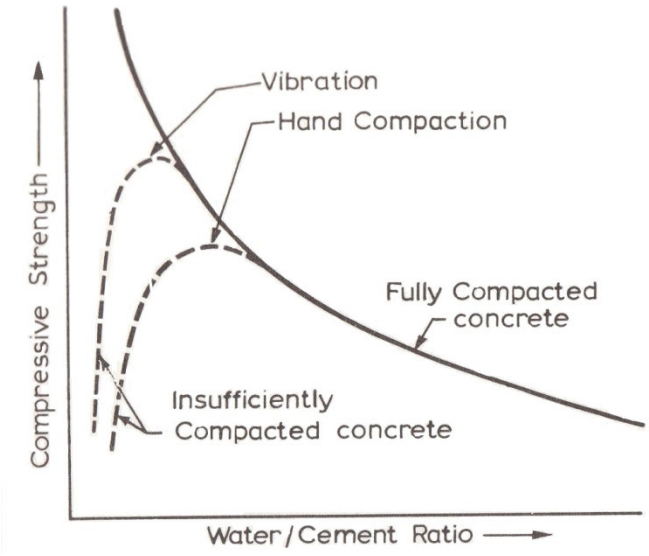

Figure 2-11 The relation between strength and water-cement ratio (Neville 1995)

2.3.2.2 Porosity

Although the porosity is closely related to water-cement ratio, it is sensible to discuss the effect of porosity on the strength of concrete separately. Strictly speaking, all the voids in concrete, which are normally capillary pores, gel pores and entrapped air, significantly influence the strength of concrete (Ward *et al.* 1969). The relationship between volume of pores and strength of concrete can be described as:

$$f_c = f_{c,0}(1-p)^n \tag{2.27}$$

f_c is the compressive strength of concrete with porosity p, $f_{c,0}$ is the strength of zero porosity, and n is a coefficient. Like many other materials with pores, Eq. 2.27 expresses the strength of concrete as a fraction of the strength with respect to zero porosity. It quantitatively shows the strength of concrete decreases as the volumes of pores increases.

Considerable research has been carried out on the exact form of relationship between the logarithm of porosity and the strength. This is expected to be linear relation since the strength of concrete is in power function of the porosity as can

be found in many text books, e.g., Neville (1995). However, there is still no confirmation, although Beaudoin and Ramachandran (1992) have found the linear relationship concerning the strength of individual cement compounds. It is certain, however, that the strength of concrete decreases while the porosity increases.

In addition to the volume of the voids, the pore size and shape also affect the strength of concrete. The pore size is usually appraised by the diameter of the pore. The effect of pores smaller than 20nm in diameter has been found not significant (Odler and Rossler 1985). Given the water/cement ratio and certain temperature, the increase in pore diameter leads to decrease in cumulative volume and thus decrease in strength of concrete. It should be noted that the term "diameter" does not imply the pore is spherical. The real shape and the sphere assumed share the same ratio of volume to surface area.

In general, the effects of the volumes and pore size on the strength of concrete are fundamental. Nevertheless, there are some other aspects which influence the strength. Sersale *et al*. (1991) considered the relation between the strength and gypsum which was found to affect the hydration and thus pore distributions. Coarse aggregates were also found to greatly influence the porosity of concrete (Winslow and Liu 1990) as there exists an interfacial transition zone between cement paste and aggregates which contains considerable voids.

2.3.2.3 Aggregate-cement paste interface

One important factor that influences concrete strength is the existence of aggregate-cement paste interface. Concrete is known as three-phase material which consists of cement paste, aggregates and the aggregate-cement paste interface also known as interfacial transition zone (Li and Zheng 2007). The properties of the interface are quite different from those of either the cement gel or aggregate. It is observed to be where the microcracking is initiated. As microcracking is regarded as the fundamental cause of concrete failures it affects both the strength and modulus of elasticity of concrete. Therefore, understanding the properties and behaviour of this interface is essential when studying the properties of concrete.

The interfacial zone is formed with hydrated cement paste but its microstructure is different from the bulk cement paste. The reason is that the existence of relatively large aggregates influences the packing of cement paste and the cement particles are unable to get as close to the aggregates as possible. The consequence of this is that more pores are produced between the cement paste and aggregates and there is a larger porous band at the interface between them. The microstructure of the interface has been investigated by various researchers using means like scanning electron microscope, such as, Barnes *et al.* (1978), Diamond (1986) and Horne *et al.* (2007). It has been found that the surface of an aggregate is covered with a layer of oriented crystalline $Ca(OH)_2$ with thickness of about $0.5\,\mu m$, over which, a thin layer of $C-S-H$ (cement gel) forms with the same thickness. Away from is the duplex film, there is a main interface zone (normally $50\,\mu m$ in thickness) consisting of the hydration products of cement – less $C-S-H$ and more $Ca(OH)_2$ with larger size. Horne *et al.* (2007) and Scrivener *et al.* (1988) have conducted some quantitative analysis on the transition zone by using backscattered electron imaging. They both found that the porosity at the interface was relatively high and decreased towards the bulk cement paste. Also, decreased level of unhydrous cement has been found at the interface although Larbi (1993) pointed out there was not any unhydrated cement.

The mechanical properties of aggregate-cement paste interface are of particular interest to investigate the strength of concrete because it is the weakest link in concrete. Usually the modulus of the interface is assumed to be uniform and less than that of the cement paste by a constant factor between 0.2 and 0.8 (Li *et al.* 1999; Sun *et al.* 2007). Lutz *et al.* (1997) have proposed a conceptual model to determine the elastic modulus of the transition zone in the form of a power-law function of radial distance from the centre of spherical (assumed) aggregate and the effective modulus of mortar. To measure the strength of the interface, a variety of tests have been carried out via flexure tests (Alexander 1959; Wang *et al.* 1986; Kosaka *et al.* 1975), direct tensile tests (Hsu and Slate 1963; Shah and Slate 1968; Su *et al.* 1991; Zimbelmann 1987), compressive tests and shear

bond test (Taylor and Broms 1964). Mitsui *et al.* (1994) developed a new aggregate pushout test to investigate the mechanical behaviour of the aggregate-cement paste interface. In their test, a closed-loop setup was used to measure the bond-slip relationship between aggregate and cement paste which was analysed to obtain the mechanical properties of the interface, such as interfacial stiffness, shear bond strength, and interfacial surface energy. They also pointed out two effective methods to reduce porosity of the transition zone: one is incorporating silica fume into the cement paste and the other is precoating the aggregates with cement and silica fume slurry. The essence of these methods is based on the fact that silica fumes will react with calcium hydroxide in concrete and make the structure denser through pozzolanic reaction. Some recent researches have been focusing on nanoscale characterization of the interface (Mondal *et al.* 2008). They used nanoindentation along with imaging to determine the mechanical properties of different phases of cement paste micro- and nano-structure.

2.3.3 Steel-cement paste interface

Like the interface between the aggregate and cement paste, there also exists interface between the steel reinforcement and cement paste. In some literature (Zhu and Bartos 2000), it is also called interfacial transition zone (ITZ). ITZ is porous and has different properties from bulk cement paste. Moreover, since ITZ is the transition area between the steel and concrete, it is the place where the corrosion products first occupy and its properties significantly influence the corrosion process of the steel reinforcement. It is, therefore, necessary to thoroughly investigate the ITZ, which may include alkalinity, porosity and mechanical behaviour.

2.3.3.1 Calcium hydroxide content

Steel reinforcement in concrete is protected from corrosion by the passive layer as long as the high alkaline environment is maintained, particularly in the region close to the steel (ACI Committee 222 1985; Broomfield 1997; Pourbaix 1974). It is, therefore, of importance to characterize the steel-cement paste interface and to examine quantitatively the presence of calcium hydroxide at the interface (Horne *et al.* 2007). A number of researchers have confirmed that a larger

amount of calcium hydroxide present at the interface than that in the bulk cement paste (Al Khalaf and Page 1979; Moreau 1973; Page 1975; Yue and Shuguang 2001). Moreau (1973) explained that the possible reason for the richness of calcium hydroxide in the interface was that at the early stage of curing, considerable amount of water is present around the steel which would enable Ca^{2+} ions moving from outside to inside the interface zone. Horne *et al.* (2007) undertook quantitative study on the microstructure of the steel-cement paste interface using backscattered electron imaging. In their research, the correlation of the area fraction of calcium hydroxide and the distance from the vertically cast steel was quantitatively described as shown in Fig. 2-12 with water/cement ratio of 0.49 and 0.7 respectively at four different curing times.

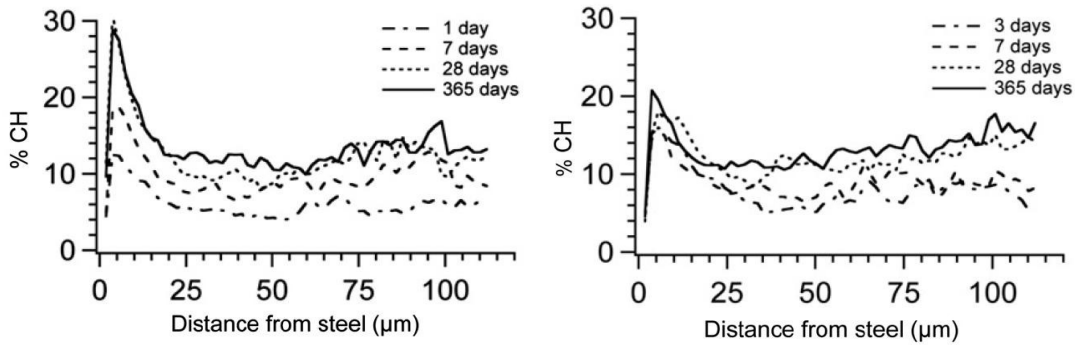

Figure 2-12 Calcium hydroxide gradients in steel-cement paste interface with w/c ratio of 0.49 (left) and 0.7 (Horne *et al.* 2007)

It can be seen from Fig. 2-12, taking curing time of 365 days and water/cement ratio of 0.49 as an example, that there is 30% calcium hydroxide close to the steel and usually this value falls to around 12% in the bulk paste. This implies that the local alkaline environment is enhanced by extra calcium hydroxide and the steel is protected better than otherwise. Additionally, water/cement ratio significantly influences the content of calcium hydroxide which deceases about 10% when the w/c ratio increases from 0.49 to 0.7.

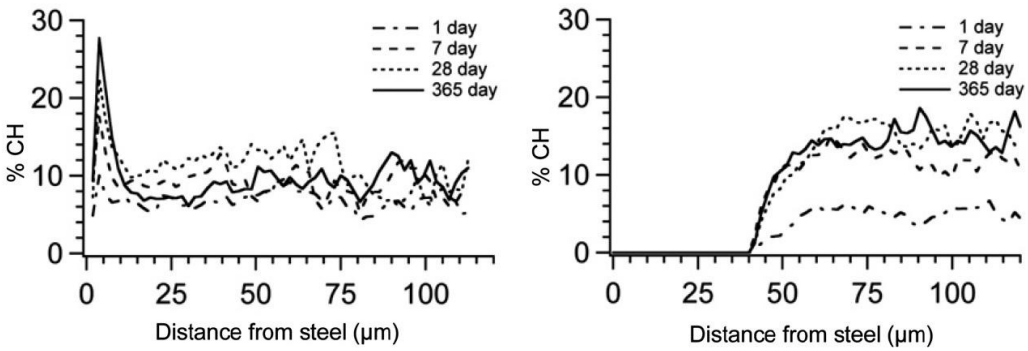

Figure 2-13 Calcium hydroxide gradients between cement paste and topside (left) and underside (right) of the steel with w/c ratio of 0.49 (Horne *et al*. 2007)

For a horizontally cast rebar, the interface at the top of the rebar has completely different profile of calcium hydroxide from that of the bottom due to existence of bleed-water zone (Horne *et al.* 2007). As shown in Fig. 2-13, up to about 40 μm, there is no calcium hydroxide at the bottom of the rebar and thereafter its content is slightly more than that at the top. This situation is not favourable for protection of steel from corrosion since passive film is maintained mainly by its surrounding concrete. This might also be the reason of the fact that corrosion initiates and accumulates at one side of the reinforcing bar (Yuan *et al.* 2007).

2.3.3.2 Levels of porosity

Same as the aggregate-cement paste interface, the steel-cement paste interfacial zone is rather porous. The porosity of ITZ significantly affects the thickness of such a porous band, which is denoted as d_0 in Chapter 3. Fig. 2-14 shows the porosity in percentage at different distance from the vertically cast steel (Horne *et al.* 2007). At 1 day the porosity reaches almost 35% close to the steel while only 12% in the bulk paste as reported by Horne *et al.* (2007). The effect of water/cement ratio on porosity is apparent. For curing times of 7 days and 28 days, the porosity with w/c ratio of 0.7 is several times larger than that with w/c ratio of 0.49. Horne *et al.* (2007) has also reported that the reinforcement orientation significantly influence the porosity of the interface as it does the content of calcium hydroxide because of the existence of the bleed-water zone. Fig. 2-15 shows extremely different porosity in the interfacial zone between top/bottom of the steel and cement paste. It should be noted that the porosity

and the content of calcium hydroxide continue to change until 365 days as shown in Figures 2-12, 2-13, 2-14, 2-15. As the curing condition is maintained, the porosity and content of calcium hydroxide are usually unchanged after 28 days in practice.

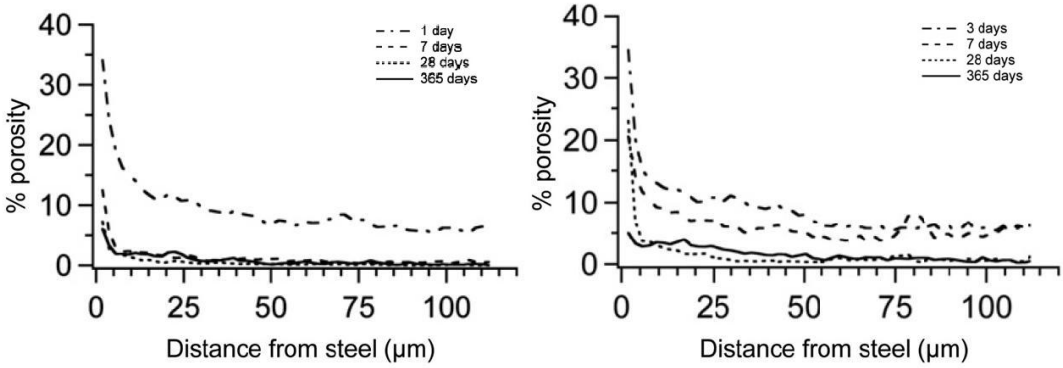

Figure 2-14 Porosity gradients in steel-cement paste interface with w/c ratio of 0.49 (left) and 0.7 (Horne *et al.* 2007)

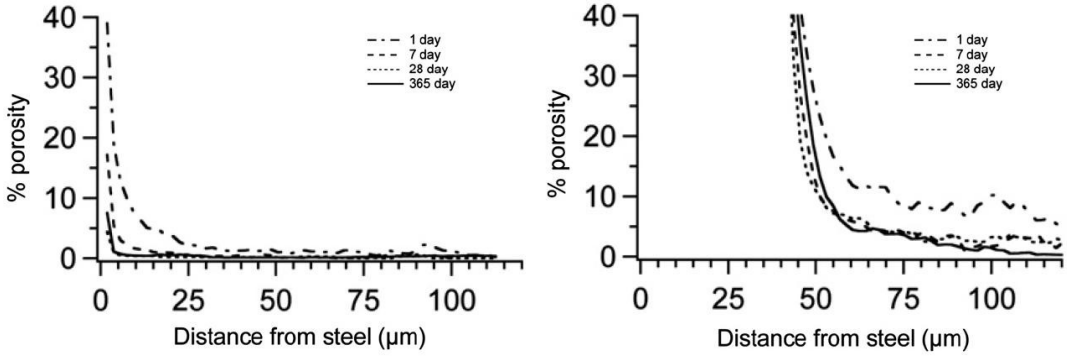

Figure 2-15 Porosity gradients between cement paste and topside (left) and underside (right) of the steel with w/c ratio of 0.49 (Horne *et al*. 2007)

Since d_0 is normally assumed as 12.5μm (Li *et al.* 2006; Liu and Weyers 1998), it can be found from Fig. 2-14 that for w/c ratio of 0.49, the porosity of ITZ after 28 days is between 7% and 2%. For w/c ratio of 0.7, the porosity of ITZ after 28 days is between 23% and 3%. The porosity of ITZ for w/c ratio of 0.7 is considerably influenced by the time since 28 days. Moreover, it is of particular interest that for horizontal casted beam, the porosity of ITZ at the bottom of the rebar is far beyond the measured range and can be considered as voids. It can be concluded that for a vertically cased structural element of concrete, e.g. column,

the porosity of the ITZ is constant at the same distance from the steel rebar but changes with the distance. However, for a horizontally casted structural element of concrete, e.g. beam, the porosity of the ITZ varies significantly at the top and bottom of the steel rebar. This may leads to a non-uniform distribution of the expansive pressure induced by corrosion products, because that the more voids available the more corrosion products the ITZ can accommodate and thus the longer time is required for the corrosion products to initiate pressure to concrete.

2.3.3.3 Mechanical behaviour

As steel-cement paste interface is rather porous, it is thus regarded as the weakest link in reinforced concrete structures, in the same manner as the aggregate-cement paste interface. To understand the mechanical properties of this interface, the modulus of elasticity and micro-strength are particularly of interest. Some researchers have carried out a series of tests using micro/nano-indentation testing method to investigate these mechanical parameters (Oliver and Pharr 1992; Trtik and Bartos 1999; Zhu and Bartos 2000). Zhu and Bartos (2000) has summerized the advantages of this new method against the conventional Vickers microhardness testing in such aspects as elastic modulus involved, load and indentation continuously monitored. The indenter can be made smaller and sharper. A typical outcome of the microindentation testing is the indentation load versus its depth hysteresis curve. Detailed apparatus arrangement and loading procedure can be found in Zhu and Bartos (1997, 2000), while herein only results are presented and discussed.

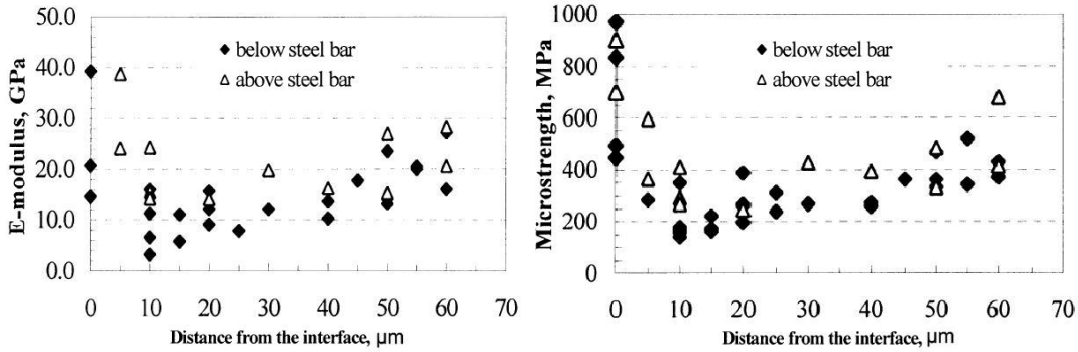

Figure 2-16 A typical set of results of micro-mechanical properties within the ITZ (Zhu and Bartos 2000)

Fig. 2-16 shows the micro-mechanical properties such as modulus of elasticity and microstrength with the relation of distance from a horizontally cast steel rebar. The elastic modulus of the interface close to the steel at both below and above the steel bar is about 40 GPa and then decreases to an average value of 17.6 GPa (above steel) and 9.8 GPa (below steel) respectively in the region of 10-30 μm. In the region of 35-60 μm, the average elastic modulus increases to 21.5 GPa (above steel) and 17.6 GPa (below steel). The microstrength follows the same trends as that of elastic modulus, and in the first region it is 329 MPa (above steel) and 229 MPa (below steel) and in the second region, it is 462 MPa (above steel) and 372 MPa (below steel). It is found that the interference of steel exists in the region of 0-10 μm and further than 60 μm the effect of bulk cement paste dominates. As the existence of bleed-water zone, the interfacial properties differ for that below and above the steel rebar as discussed. A quantitative relationship for the differences between the interfaces below and above the steel is plotted in Fig. 2-17 (Zhu and Bartos 2000). In the region of 10-35 μm, the elastic modulus below the steel is no more than 60% than that above the steel, and only 70% for the microstrength.

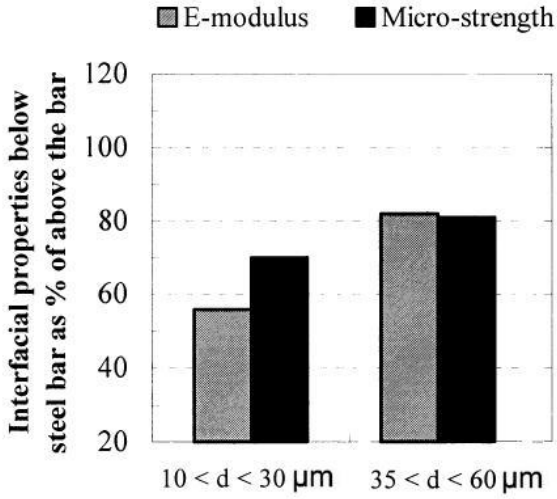

Figure 2-17 Interfacial properties below steel bar relative to above steel bar (Zhu and Bartos 2000)

2.4 Basics of fracture mechanics

Fracture mechanics, generally speaking, is a branch of mechanics that deals with the initiation and propagation of cracks in materials. It has been applied to field of concrete cracking since the first nonlinear fracture mechanics model was developed by Hillerborg *et al.* (1976), although the linear fracture mechanics – simple form of fracture mechanics – has been developed far earlier which can be used for concrete dams. To determine the crack propagation and crack width of concrete structure/element, fracture mechanics is essential no matter which method is adopted, e.g. analytical or numerical method. In this section, the rationale that fracture mechanics is used for concrete cracking is firstly presented. It is followed by the theory of linear fracture mechanics. Nonlinear fracture mechanics is then discussed including a few widely accepted nonlinear fracture models proposed in last 30 years. Fracture resistance curves are finally reviewed.

2.4.1 Application of fracture mechanics to concrete cracking

In the theory of elastic mechanics, when a crack is present it alters the stress distribution and results in the stress at the crack tip approaching infinity. The strength-based elastic mechanics, therefore, cannot be applied to cracking problems. In order to solve this problem, Griffith (1921) proposed an energy criterion of failure which could be viewed as a balance of energy – energy released equal to energy required to crack a unit surface. Bažant and Planas (1998) state that fracture mechanics is a failure theory that determines material failure by energy criteria, possibly in conjunction with strength or yield criteria, and considers failure to be propagating throughout the structure rather than simultaneous throughout the entire failure zone or surface. The classical theory of fracture mechanics, not just for concrete, is concerned with the residual strength (with respect to crack size), the critical crack size, the crack size with respect to whole life time, and initial permitted crack size (Broek 1986; Shah *et al.* 1995). Fracture mechanics may also be defined as a set of ideas or concepts that describe the transition from continuous to discrete behavior when separation of a material occurs (ACI Committee 446.3R 1997).

However, to relate the energy release rate to the elastic stress and strain fields of a body, Griffith's theory is applicable only for a particular case. This situation has not changed until 1968 when Rice derived the famous J-integral (Rice 1968a, b). J-integral is an integration performed on any closed contour counterclockwisely from the crack tip in a stressed body to relate the energy release rate to the stress and strain fields around the crack tip on much more general grounds. Apart from the energy approach for Linear Elastic Fracture Mechanics (LEFM) problems, there is another method called stress intensity factor K which is a parameter for the intensity of stresses close to the crack tip accounting for singularity of the stress field. The stress intensity factor is a function of loads, element geometry, boundary condition, and crack size, and can serve as a fracture criterion. Irwin (1957) proposed a quantitative relationship between Griffith's energy approach and stress intensity factor. In comparing these two approaches, Bažant and Planas (1998) stated that, the stress intensity factor was additive while Griffith's energy release rate was not. Besides, the stress intensity factor approach was limited to linear elastic materials, while the concept of energy release rate can be extended to nonlinear materials.

2.4.1.1 Strength degradation

Failure of structures is greatly influenced by the performance of material used. In terms of tensile stress-elongation relationship, most of engineering materials can be categorized into brittle, ductile, or quasi-brittle (Shah *et al.* 1995). For a brittle material, the tensile stress will suddenly reduce to zero when it reaches the material tensile strength and this leads to failure of the structure, as shown in Fig. 2-18a. For a ductile material, the tensile stress will stay constant after the peak stress so that the structure will not fail until the whole section reaches the tensile strength (Fig. 2-18b). For a quasi-brittle material, however, the tensile stress will be gradually decreasing after the peak value when the structure could still maintain the applied loads. The decrease of stress is called "softening". The softening part can be modelled by a number of forms such as linear, bilinear, exponential, power and so on. Fig. 2-18c shows the response of a quasi-brittle material response with exponential softening behaviour. It is clear that the

failure characterization of structures is attributed to not only by structural geometry but also from the material performance. The reason that the strength of quasi-brittle materials, e.g., concrete and ceramics, degrades is that there is an inelastic zone developed ahead of the crack tip which is also referred to as fracture process zone. When a crack propagates in concrete, the crack surfaces may be in contact to each other and are tortuous in nature (Mindess and Diamond 1982). Therefore, the cracked surfaces may still be able to sustain the tensile stress which is characterized by the softening degradation curve. Regarding the failure criterion, the strength based failure criterion can be simply used for ductile materials as its failure is yield strength dependent only. For a perfectly brittle material, however, the maximum stress depends not only on this material property but also on the structural geometry and boundary condition which means it is influenced by its size. Therefore, the strength based criterion is not applicable any more and an energy criterion in terms of dissipation of elastic energy needs to be applied. As for quasi-brittle materials, besides the elastic energy release, the failure is governed by the inelastic energy released in the fracture process zone at the tip of crack. Thus the energy failure criterion is suitable for quasi-brittle material, but it needs to consider more energy criteria which will be discussed in 4.3.

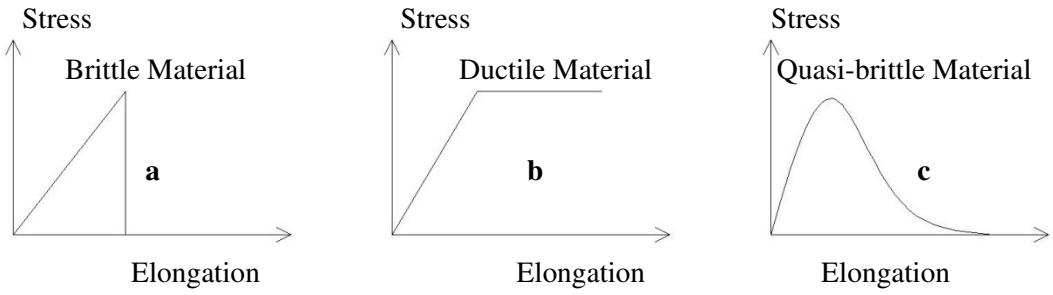

Figure 2-18 Different structural performances due to different types of materials

2.4.1.2 Size effect

As a general convention, the material criterion that is expressed in terms of stress or strain is said to exhibit no size effect. Size effect is normally considered as the deviation in terms of its dependence on strength and other material parameters (Bažant and Planas 1998). Size effect is usually defined

through a comparison of geometrically similar structures of different sizes and is conveniently characterized in terms of the nominal stress at maximum load (ACI Committee 446.1R 1991). In simple words, size effect can be described as the decrease in average stress at failure with increasing member size (ACI Committee 446.3R 1997). Figure 2-19 shows the size effect on the strength and brittleness/ductility of three similar structures with different geometric size under four-point bending. The size effect can be interpreted in two aspects. Firstly, the failure strength of the beam decreases as the structure size increases; secondly, the structure becomes more brittle when the structure size is increased.

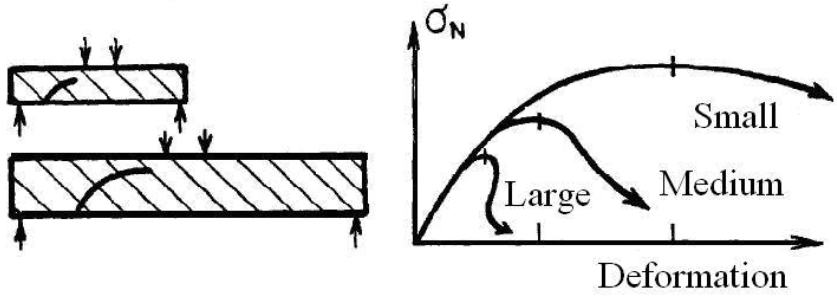

Figure 2-19 Size effect on strength and ductility of similar structures with different size (ACI Committee 446.1R 1991)

To explain the size effect, the classical failure theories such as strength criterion and yield criterion seem to be lack of ability as employing such a theory exhibits no size effect. Fracture mechanics can be employed to explain the size effect more properly in view of energy release as seen in Fig. 2-20. By approximation, the existence of the crack band of thickness h reduces the strain energy in both the crack band and the cross-hatched area (two triangles above and below the crack band) to zero. When the crack band extends by Δa at no boundary displacement, the strain energy released comes from the cross-hatched strip (outer envelope). Therefore, the larger the size of the panel is, the more area of the strip thus the more energy is released by the same extension of the crack. It can be postulated that the size effect is due to the fact that in a larger structure more strain energy is available to drive the propagation of the failure zone (Bažant and Planas 1998).

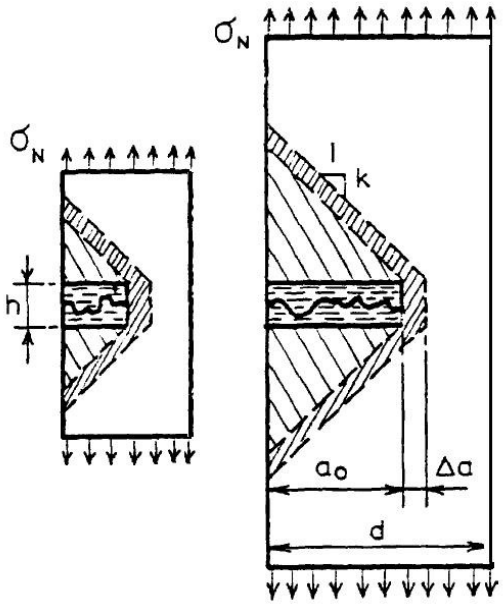

Figure 2-20 Explanation for size effect – area of energy release for similar structures with different size (ACI Committee 446.1R 1991)

2.4.2 Linear Elastic Fracture Mechanics

Linear Elastic Fracture Mechanics (LEFM) is the fundamental theory of fracture mechanics, which was firstly developed by Griffith (1921). Griffith found that in the presence of a crack the stress value cannot be used as failure criterion and hence proposed an energetic approach to solve the problem of crack propagation. The fracture mechanics became mature in its essential aspects by Irwin (1957) who introduced the concept of stress intensity factor and related it to Griffith's energy release rate. Rice (1968a, b) developed the J-integral and later related to the energy release rate.

LEFM can be applied to any materials as long as the assumption is met, that is, the whole material is elastic except in the vanishing small region ahead of the crack tip. Some kind of inelasticity occurs around the crack tip as the stress there is inevitably high. The size of this region, however, must be very small regarding its perturbation to the linear performance of the whole structure to apply LEFM.

2.4.2.1 Griffith's Energy Approach

The concept of energy release rate proposed by Griffith can be generalized by introducing the strain energy release rate for crack propagation (Shah *et al.* 1995). The energy release rate is not defined as the first-order derivative of energy with respect to time but crack extension as to be explained below.

Consider any structure with an initial crack subjected to tension, the total potential energy $\prod$ in this structure can be expressed as

$$\prod = U - F + W \tag{2.28}$$

where U is the strain energy of the structure, F is external work done by applied loads, and W is energy available for crack formation or fracture. In terms of energy conservation, the potential energy must keep as a constant and its first-order derivative with respect to crack extension is zero.

$$\frac{\partial(U - F + W)}{\partial a} = 0 \tag{2.29}$$

It is convenient to work with specific energy which is the energy per unit area of crack growth and is also called energy release rate. In this regards, Eq. 2.29 can be rewritten as:

$$\frac{\partial F}{\partial a} - \frac{\partial U}{\partial a} = \frac{\partial W}{\partial a} = Gb \tag{2.30}$$

where G is the energy release rate.

By introducing the crack growth resistance $\Re$, which is the energy required for a unit advance of the crack, the energy failure criterion to describe the condition of quasi-static crack propagation can be expressed as

$$G = \Re \tag{2.31}$$

Thus, the basic problem in fracture mechanics could be formulated as to find the amount of energy available for crack growth and compare with the energy required to do so. The crack growth resistance $\Re$ can be measured for particular materials and situations, while the energy release rate G needs to be calculated and the basic theory will be discussed as follows. Kinetic energy can be introduced as the fracture criterion for dynamic crack growth which can be found in Bažant and Planas (1998) and will not be reviewed herein. It should be pointed out that the crack growth resistance $\Re$ has a number of alternative notations in the literature depending on different applications and conditions. $\Re$ is expressed as G_R when it is self history dependent, and as G_c, $G_{\mathrm{I}c}$ or G_f when it is a material property. The notations for the later case are all called critical energy release rate or specific fracture energy.

2.4.2.2 Stress Intensity Factor Approach

The stress intensity factor method was developed by Irwin (1957) who reformulated LEFM problem in terms of the stress states around the crack tip rather than energy. It can be found in many references, for example, Bažant and Planas (1998) and Shah *et al.* (1995), that the stresses at the crack tip have the same distribution for all cracks and under all applied loads, with only the intensity of the stress concentration varying. Therefore, for the same intensity, the stresses distributions ahead of the crack tip are identical. This is illustrated in Fig. 2-22a and leads to

$$\sigma(r) = C_F r^{-\frac{1}{2}} \tag{2.32}$$

where

$$C_F = \frac{K_{\mathrm{I}}}{\sqrt{2\pi}} \tag{2.33}$$

Then the stress expression becomes

$$\sigma(r) = \frac{K_{\mathrm{I}}}{\sqrt{2\pi r}} \tag{2.34}$$

It should be noted that in this research, only Mode I fracture is discussed. There are three deformation modes of fracture, which are opening mode (Mode I), in-

plane shear mode (Mode II) and out-of-plane shear or tear mode (Mode III), as shown in Fig. 2-21. Mode I fracture only considers pure tension case without any shear is included. Mode II focuses on pure in-plane shear problems and Mode III concentrates on out-of-plane shear problems. For some applications, part or all of these three modes are combined together to form a mix-mode problem. Mode I, II and mix-mode are beyond the scope of this research and will not further discussed herein.

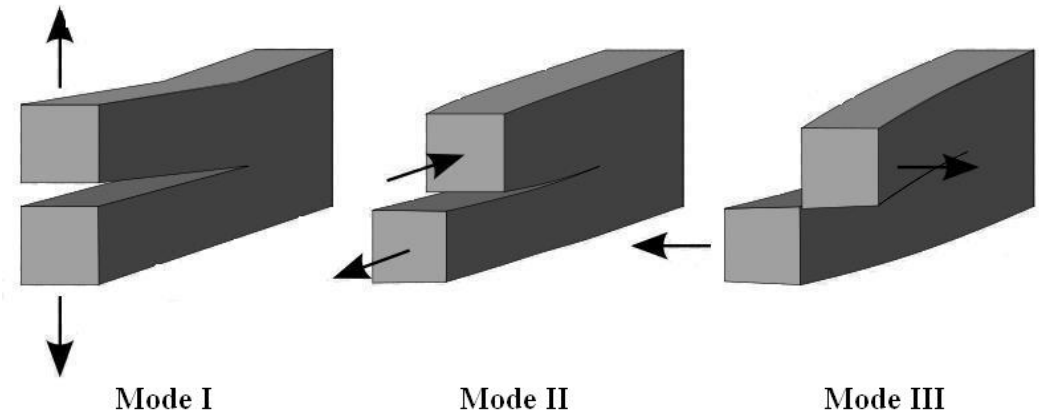

Figure 2-21 Schematic of three deformation modes of fracture

The coefficient K_{I} is the opening mode (Mode I fracture) stress intensity factor. This factor is considered to be a function of load, crack length and structural geometry and accounts for singularity of the stress field at the crack tip. For an infinite plate like the one in Fig 2-22a, the value of K_{I} can be given by

$$K_{\mathrm{I}} = \sigma\sqrt{\pi a} \tag{2.35}$$

When the plate is loaded to its failure stress σ_f , the above expression becomes

$$K_{\mathrm{Ic}} = \sigma_f\sqrt{\pi a} \tag{2.36}$$

K_{Ic} is a material fracture property called the fracture toughness. Once this toughness is available the failure stress is then known. The stress intensity factors can also serve as a fracture criterion which is

$$K_I = K_{Ic} \tag{2.37}$$

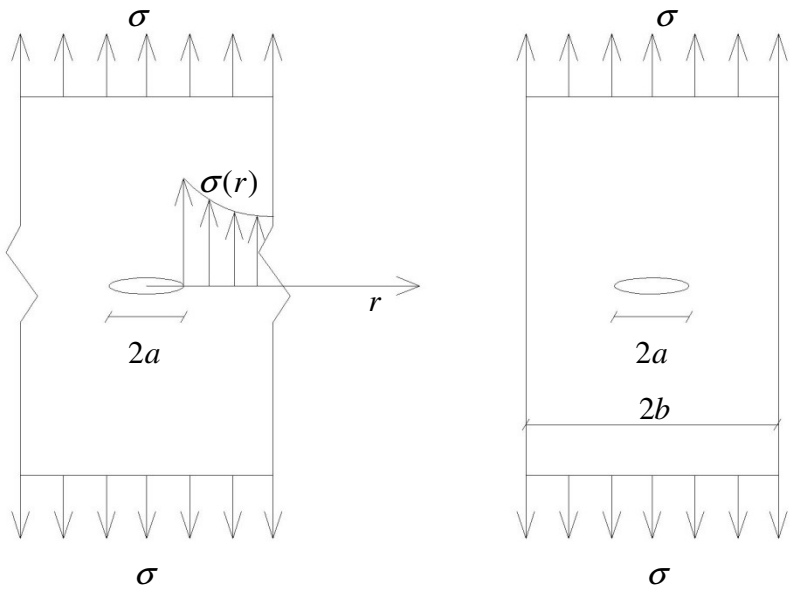

Figure 2-22 Uniaxial tension of a centre crack (a) in a infinite plate (b) in a finite plate

The stress intensity factors in Eqs. 2.35 and 2.36 are independent of structural geometry because it is assumed that the plate is infinitely wide. For most of real structures, however, the effect of structural geometry must be considered. Murakami (1987) and Tada *et al.* (1985) have presented the stress intensity factors and crack opening displacement for some commonly used geometries and loading conditions in an exact solution. Considering the uniaxial tensile plate in Fig. 4-5b, the stress intensity factor is expressed as

$$K_I = \sigma\sqrt{\pi a}\, g_1(\frac{a}{b}) \tag{2.38}$$

where

$$g_1(\frac{a}{b}) = \sqrt{\sec(\frac{\pi a}{2b})} \tag{2.39}$$

The crack opening displacement at the centre ($CODC$) is

$$CODC = \frac{4\sigma a}{E} g_2(\frac{a}{b}) \tag{2.40}$$

where the exact solution to function $g_2(\frac{a}{b})$ is

$$g_2(\frac{a}{b}) = 1 + 0.065\frac{a}{b} - 0.241(\frac{a}{b})^2 + 3.76(\frac{a}{b})^3 - 6.63(\frac{a}{b})^4 + 4.93(\frac{a}{b})^5 \tag{2.41}$$

Besides the above geometry condition, Murakami (1987) and Tada *et al.* (1985) have calculated the stress intensity factors and crack opening displacement for some other common situations such as uniaxial tensile plate with single-edge crack and double-edge crack respectively, three point beams and centre-crack plate subjected to wedge forces.

This stress intensity factor method has been acknowledged to be essentially equivalent to the Griffith energetic approach. The relationships between the stress intensity factor and energy release rate can be found in many references, like Irwin (1957) and Shah *et al.* (1995), which for Mode I fracture reads as

$$G_{\mathrm{I}} = \frac{K_{\mathrm{I}}^{\ 2}}{E} \tag{2.42}$$

This equilibrium is valid for all geometry conditions under plane stress. For plane strain problem, it only needs to replace the E with $(1-\mu^2)/E$.

2.4.2.3 J-integral

Since Rice (1968b) found that the J-integral was equal to G, the J-integral has been treated as a particular form of expressing the energy release rate. J-integral is expressed as (Bažant and Planas 1998; Shah *et al.* 1995)

$$J = \int_{\Gamma}\left[U_d dy - \mathrm{T}\frac{\partial \mathrm{u}}{\partial x} ds\right] \tag{2.43}$$

where Γ is any closed contour following a counterclockwise path surrounding the crack tip in a stressed body, U_d is elastic energy density, T is the tension vector acting on the boundary, u is the displacement vector and *ds* is the differential of arc-length along the contour Γ. It is acknowledged that the J-integral is independent of selection of the path and is equal to the energy release rate G (Bažant and Planas 1998), only if (1) the nonelastic zone reduces to a point in the interior of Γ, (2) the crack faces are traction-free, and (3) the crack is plane and extends in its own plane. In another word, the J-integral can be used as a fracture criterion due to its path-independence when the materials used exhibit elastic stress-strain behaviour, that is, a linear elastic material (Shah *et al.* 1995). For quasi-brittle materials like concrete, the presence of the inelastic fracture process zone perturbs the path-independence of the J-integral. Therefore, the J-integral can only account for partial effect and is not equal to the real energy release rate G .

2.4.3 Nonlinear Fracture Mechanics for Mode I

Concrete is known as quasi-brittle material which means that strain softening after peak load is reached. The strain softening phenomenon takes place in the region ahead of the crack tip which is normally termed as Fracture Process Zone (FPZ). For LEFM to be applicable, the size of the FPZ must be zero or vanishingly small compared to the structure size. Since the size of FPZ of concrete is not negligible, Nonlinear Fracture Mechanics (NFM) is more applicable.

2.4.3.1 Fracture Process Zone and toughening mechanisms

As LEFM allows the stress at the crack tip to approach infinity, there must be an inelastic zone developed ahead of the tip. For metallic materials this inelastic zone is known as yielding zone, while for quasi-brittle materials like concrete, it is termed as Fracture Process Zone which is dominated by complicated mechanisms. The FPZ is the cause that requires the Nonlinear Fracture

Mechanics as this inelastic zone consumes energy which cannot be calculated by LEFM.

There have been a number of researchers working on toughening mechanisms which includes microcrack shielding, crack deflection, aggregate bridging, friction between crack faces, crack tip blunted by void, and crack branching (Shah *et al.* 1995). Kachanov (1986) investigated the interaction of a crack with the microcracks ahead of the crack and found that the microcracking shielding process consumed a little amount of external energy. One of the most vital toughening mechanisms in concrete is aggregate bridging which is also called grain bridging. Van Mier (1991) examined the discontinuous crack growth process and the mechanism of grain bridging, and suggested that the aggregates would still transfer stresses across the cracked faces when the crack had progressed beyond the aggregates. For the rest of mechanisms, although they vary in their kinds, they all consume additional energy for a crack to propagate.

The influence of FPZ on fracture behaviour of concrete has been regarded as significant. This is the reason that the nonlinear fracture mechanics rather than linear elastic fracture mechanics is applied to solving concrete cracking problems. In the view of Shah *et al.* (1995), the presence of the FPZ results in stable crack growth before the ultimate load since the FPZ consumes a substantial amount of the energy produced by applied loads. As some parts of crack faces may still be in touch and thus transfer stresses, the stresses gradually decrease after the peak loads and a softening behaviour of the stress-strain or stress-displacement relationship can be observed.

Some experimental evidences have also shown that the quasi-brittle materials, such as concrete, mortar or cement paste do not follow LEFM (Higgins and Bailey 1976; Ohgishi *et al.* 1986; Walsh 1976). In these researches, the critical stress intensity factor calculated by using LEFM demonstrated size effect. The reason is that LEFM does not consider the stable crack growth associated with the FPZ. This means LEFM accounts for only the energy required to create two cracked faces. For elastic materials, that is all needed since the stress will suddenly drop to zero and catastrophical failure occurs. For quasi-brittle

materials, however, additional energy should be taken into account to separate the two cracked faces as the stress between the two faces will be decreasing continuously. This leads to the fundamental theory of energy balance of Mode I quasi-brittle crack which can be expressed as (Shah *et al.* 1995)

$$G_q = G_{\mathrm{I}c} + G_\sigma \tag{2.44}$$

where G_q represents the energy release rate for Mode I quasi-brittle crack, $G_{\mathrm{I}c}$ is the energy rate consumed in creating two cracked faces which is equivalent to the material surface energy and can be calculated based on LEFM, and G_σ is the energy rate to overcome the cohesive pressure between the two cracked faces. A few researchers have proposed models based on Eq. 2.44 to describe fracture of concrete (Cook *et al.* 1987; Cox and Marshall 1994; Jenq and shah 1985; Kobayashi *et al*. 1991). However, either mechanism can be approximately used individually to describe the fracture of quasi-brittle materials. Based on Eq. 2.44, there are two individual mechanisms, namely, Griffith-Irwin mechanism by assuming $G_\sigma = 0$ and Dugdale-Barenblatt mechanism by assuming $G_{\mathrm{I}c} = 0$. These two mechanisms are also called equivalent-elastic or effective-elastic crack approach and fictitious crack approach respectively.

2.4.3.2 Fictitious Crack Approach

The fictitious crack approach postulates that the energy required to create the new surfaces is vanishingly small compared to that required to separate them. Under this assumption, the energy dissipation in fictitious approach is completely characterized by cohesive stress-separation relationship in the FPZ. Based on such an approach, two models are widely recognised and they are fictitious crack model proposed by Hillerborg *et al*. (1976) and crack band model orientated by Bažant and Oh (1983).

In the early 1960s, Dugdale (1960) introduced a “strip-yield” model and Barenblatt (1962) proposed a cohesive force model, both of which were used to represent different nonlinear processes in the front of a pre-existent crack. Soon after, Hillerborg *et al.* (1976) extended the concept of “cohesive” for concrete to

allow the crack to develop anywhere – no pre-cracking is needed for crack propagation.

Hillerborg's cohesive crack model is characterized by cohesive stress-elongation relationship which is shown in Fig. 2-23. The stress-elongation relationship is obtained from a uniaxial tensile test of a concrete plate. In Fig. 2-23a, the tensile stress starts from zero and increase simultaneously with the elongation of the concrete plate until it reaches the tensile strength when the crack initiates. Then, the stress ahead of the crack tip decreases with continuous increase of the elongation, while unloading occurs outside the crack region. Denoting G_f as specific fracture energy, it can be obtained from $G_f = \int_0^{wc} \sigma(w)dw$.

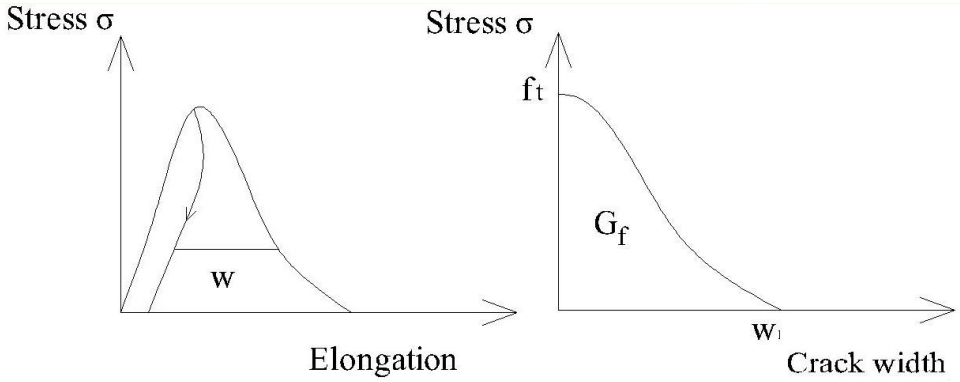

Figure 2-23 Fictitious crack model by Hillerborg (a) a complete tensile stress-elongation curve (b) stress-crack width curve

For the cohesive crack model, there are three governing parameters: material tensile strength f_t, specific fracture energy G_f and the shape of the $\sigma(w)$ curve. Most research literature simplifies the pre-cracking concrete mechanical property to isotropic linear elastic. It is assumed in the cohesive crack model that, a crack will be initiated whenever and wherever the tensile stress exceeds the tensile strength. After crack initiation, stable crack propagation requires an energy balance, i.e., the strain energy release rate is equal to the fracture resistance, which is shown as follows

$$G_\sigma = G_f \tag{2.45}$$

The curve of $\sigma(w)$ depends on concrete composition and should be determined by experiments (Bažant and Planas 1998). Numerous researchers have carried out tests to determine the $\sigma(w)$ curve. The most widely used one probably is that developed by Petersson (1981), who was the first one to carry out stable tensile tests to obtain this curve. Based on the test results, a number of expressions of $\sigma(w)$ have been derived, including linear, bilinear, trilinear, exponential and power functions. Hillerborg *et al.* (1976) proposed a linear softening curve which depends on two parameters: the concrete tensile strength f_t and critical crack width w_c (originally w_1). The disadvantage of linear softening curve is that it over-estimates the strength of cracking concrete. Probably with this regard, Petersson (1981) developed a bilinear softening model, followed by Roelfstra and Wittmann (1986). Bilinear softening curve has been widely accepted as a reasonable approximation although there are debates on the position of the kink point. Trilinear curve is similar to the bilinear one but it stays at the tensile strength for a while before it goes to the bilinear phase. A few exponential curves have also been proposed (Cornelissen *et al.* 1986a, b; Gopalaratnam and Shah 1985). Additionally, Du *et al.* (1992) suggested a softening curve with power law function.

The crack band model for concrete fracture was originally developed by Bažant (1976) and refined by other researchers in more details for sudden cracking (Bažant and Cedolin 1979, 1980, 1983) and strain softening model (Bažant and Oh 1983). Bažant and Oh (1983) modeled the fracture process by a band of uniformly distributed microcracks with a minimum thickness of h_c which exhibits linear strain softening. Fig. 2-24 shows the stress-strain relation for the crack band model. It is assumed of linear relationship in the prepeak stage and nonlinear strain softening. Bažant and Oh (1983) found that the model was rather successful in the same circumstances as it was for the cohesive crack model. The expression of cohesive crack model could be identical to that of crack band model if $h_c\varepsilon^f = w$ is identified.

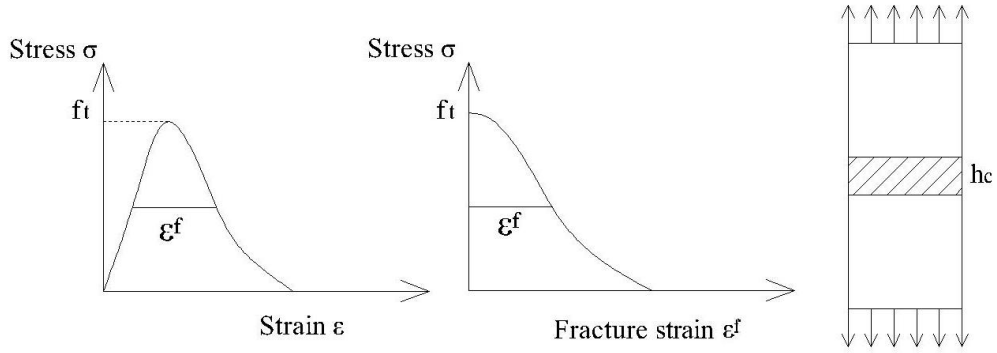

Figure 2-24 Stress-strain relation for crack band model for fracture of concrete (a) stress-strain curve (b) stress-fracture strain curve

When considering strain localization, the total elongation of the bar in Fig. 2-24 can be expressed as

$$\Delta L = \frac{\sigma}{E}\left(L - h_c\right) + \left(\frac{\sigma}{E} + \varepsilon^f h_c\right) = \frac{\sigma}{E} L + \varepsilon^f h_c \tag{2.46}$$

ε^f is called inelastic fracturing strain and $\varepsilon^f h_c$ is the fracturing elongation.

The specific fracture energy G_f can be easily calculated if the softening is assumed to be linear for ease of calculation as $\frac{h_c f_t^2}{2}\left(\frac{1}{E} + \frac{1}{E_t}\right)$ (Shah *et al*. 1995), where h_c can be approximated to be $3d_a$ and d_a is maximum aggregate size. For crack band fracture model, therefore, there are three parameters: tensile strength, initial modulus of elasticity and descending modulus.

2.4.3.3 Effective-elastic Crack Approach (Jenq and Shah)

A two parameter fracture model has been proposed by Jenq and Shah (1985) using effective-elastic approach. This approach models the FPZ by an equivalent elastic crack which is traction free. A notched specimen was loaded to maximum value and then unloaded to obtain the elastic displacement and plastic displacement respectively. Plastic displacement will be omitted and the elastic component will be used to calculate the critical stress intensity factor K_{Ic}^s

and the critical effective elastic crack length a_c. From Eqs. 2.38 and 2.40, K_{Ic}^s and crack mouth opening displacement $CMOD_c^e$ can be expressed as:

$$K_{Ic}^s = \sigma_c \sqrt{\pi a_c}\, g_1\left(\frac{a_c}{b}\right) \tag{2.47}$$

$$CMOD_c^e = \frac{4\sigma_c a_c}{E} g_2\left(\frac{a_c}{b}\right) \tag{2.48}$$

$CMOD_c^e$ and σ_c are measured from three-point bending test while a_c and K_{Ic}^s are derived from the Eqs. 2.47 and 2.48. After obtaining all these parameters, crack tip opening displacement $CTOD_c^e$ can be calculated by

$$CTOD_c^e = CMOD_c^e\, g_3\left(\frac{a_c}{b}, \frac{a_0}{a_c}\right) \tag{2.49}$$

As discussed in 4.2.2, g_1, g_2 and g_3 are dependent on element geometry.

Jenq and Shah (1985) have found that K_{Ic}^s and $CTOD_c^e$ are almost constant and not dependent on structural size. Due to this, they proposed a two parameter fracture model based on K_{Ic}^s and $CTOD_c^e$ ($CTOD_c$ in some literature), as follows.

$$K_I = K_{Ic}^s \tag{2.50}$$

$$CTOD = CTOD_c^e \tag{2.51}$$

It should be pointed out that K_I and $CTOD$ are functions of applied loads, element geometry and crack length from the theory of LEFM, while K_{Ic}^s and $CTOD_c^e$ are material constants.

2.4.4 Fracture Resistance Curves ($\Re$-curves)

$\Re$-curve is expressed as the crack growth resistance as a function of the crack extension, which is usually effective or equivalent crack extension (Bažant and Planas 1998). It is developed due to the fact that the fracture models introduced in the preceding sections 2.4.2 and 2.4.3 are applicable only to the critical situation and not able to provide full mechanical description such as complete crack growth process. Instead of using the fracture criteria discussed before, i.e., Eqs. 2.50 and 2.51, a crack growth rule relating a variable crack growth resistance R to the crack extension Δa (effective or equivalent) is proposed.

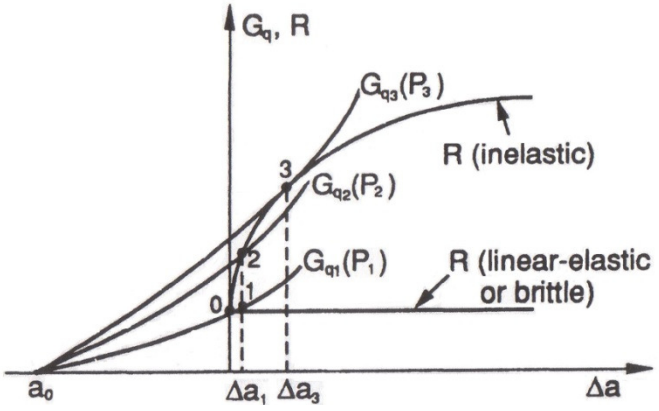

Figure 2-25 Relationships between G_q-curves and $\Re$-curves (Shah *et al.* 1995)

In a quasi-static fracture process, $G_q = \Re$ is used as a fracture criterion, where G_q is a function of applied load and crack length, and $\Re$ is a function of crack extension. It is assumed that $\Re$ is material dependent. Thus, to account for stable crack propagation, the relationship between G_q-curve and $\Re$-curve is schematically drawn in Fig. 2-25. To interpret the crack propagation using G_q-curve and $\Re$-curve, a critical point should be introduced which satisfies:

$$G_q(P, a_0 + \Delta a) = \Re(\Delta a) \tag{2.52}$$

$$\frac{\partial G_q(P, a_0 + \Delta a)}{\partial a} = \frac{\partial \Re(\Delta a)}{\partial a} \tag{2.53}$$

For linear-elastic material, $\Re$ is a material constant and not dependent on crack extention, which means that the propagation of a crack in this material needs no more energy. Therefore, $\Re$-curve is a straight line. G_q-curve starts from the initial crack length a_0 and is subjected to different applied loads P. For a given load P_1, the G_q-curve passes through point 0 which is the intersection point with $\Re$-curve for linear-elastic material. At $G_q = \Re$ point, it means that the crack initiates but the propagation of this crack will lead to catastrophic failure (unstable crack propagation) because any crack extension will result in $G_q > \Re$. For inelastic material, $\Re$ increases monotonically due to the presence of crack arrest mechanisms in the inelastic zone around the crack tip (Shah *et al.* 1995). When increasing applied load from P_1 to P_2, G_q-curve becomes $G_{q2}(P_2)$ and intersects with $\Re$-curve at point 2 where crack extension (Δa_1) occurs. At both point 0 and point 2, $G_q = \Re$ and $\frac{\partial G_q}{\partial a} < \frac{\partial \Re}{\partial a}$ are satisfied which means that stable crack propagation occurs, that is, the crack propagates only when the applied load increases. At point 3, the conditions become $G_q = \Re$ and $\frac{\partial G_q}{\partial a} = \frac{\partial \Re}{\partial a}$. This point is called critical point after which $\frac{\partial G_q}{\partial a} > \frac{\partial \Re}{\partial a}$ indicating unstable crack propagation. However, with the existence of strain softening, applied load can be decreased which leads to $G_q = \Re$ again.

2.5 Numerical modelling of concrete cracking

To predict cracking of either plain or reinforced concrete, FEA seems to be necessary which replaces the solid physical body with an interconnected system of elements leading to approximate solution to structural response (Bažant and Planas 1998; Ngo and Scordelis 1967; Shah *et al.* 1995). These elements are connected at the nodes where the equilibrium of tractions/stresses and compatibility of deformations are required. Even though finite element method is a powerful numerical tool, it has been proven to be difficult to apply to the problem of concrete cracking when the strength of a structure or structural

element is controlled by inelasticity of its materials, e.g., concrete cracking (ACI Committee 446.3R 1997). To deal with the cracks in a body, there are two ways: discrete crack approach and smeared crack approach. Discrete crack approach treats the crack as a "real" crack by introducing discontinuity in the geometry of the body. The crack path should normally be assumed a *priori* and a mesh is arranged so that the path coincides with boundaries between elements (Shah *et al.* 1995). When the crack path is not known in advance, however, remeshing is needed. The smeared crack approach treats the crack not as a "real" one but a continuous medium with altered mechanical properties. There is no displacement discontinuity in the finite elements by this approach. Instead, the mechanical properties of the cracked elements are modified by some deterioration law. Considerable discussions have been made on the advantages and disadvantages on these two crack models (ACI Committee 446.1R 1991; Bažant and Planas 1998; Shah *et al.* 1995). In terms of physical phenomenon, distributed damage or densely distributed parallel cracks can be well represented by smeared crack model, while if only a single crack is present or of interest, discrete crack model is more appropriate. Ideally, however, smeared crack model should be capable of representing the propagation of a single crack with reasonable accuracy (ACI Committee 446.3R 1997).

2.5.1 Smeared crack approach

Rashid (1968) seems to be the first to introduce the concept of smeared crack to finite element analysis. Since then, it has become clear that the smeared crack model is effective to represent the cracks by changing the constitutive properties of the material. The smeared manner means a lot of infinitely small parallel cracks are continuously distributed over finite element, and reduce the material stiffness and strength in the direction normal to the cracks. This method has two typical advantages against discrete crack approach which are computational convenience and more appropriate representations for some physical observations.

To apply the smeared crack model, certain numerical difficulties need to be overcome. These are mainly the strain localization instabilities and spurious

mesh sensitivity of finite element calculations (Bažant and Planas 1998). The nature of these numerical problems is the phenomenon of "strain localization". When cracks or microcracks form, the strain tends to localize in a small region while the other part undergoes much smaller strains. With this phenomenon, the conventional continuum mechanics is no longer applicable because the strain localized band is too small. Therefore, the effort should be put on preventing localization of smeared cracking in arbitrarily small regions. A few methods have been suggested in ACI Committee 446.3R (1997), while the most widely used one is the crack band model proposed by Bažant and his coworkers (Bažant 1976; Bažant and Cedolin 1979, 1980, 1983; Bažant and Oh 1983). The key of the crack band model is that the constitutive relation with strain softening must be associated with a certain characteristic width (minimum threshold) of the crack band as discussed in Section 2.4.3. The crack band model, therefore, is regarded as a relationship between the element size and the constitutive model so that the total energy dissipated will match that of the material being modelled (ACI Committee 446.3R 1997).

2.5.2 Discrete crack approach

Discrete crack model treats a crack as a geometric entity. For elastic materials, LEFM implies that there is stress singularity ahead of the crack tip. For quasi-brittle materials, the stress singularity is removed by introducing the FPZ which experiences strain softening once the peak load is reached. Although LEFM is only applicable to the large concrete structures like dams, the finite element modelling method of LEFM is still relevant before NFM is presented.

2.5.2.1 Numerical application of LEFM

LEFM can be applied to concrete cracking when the FPZ is negligibly small compared with the size of the structure. This is determined by comparing the size of FPZ with the least dimension associated with the crack tip (ACI Committee 446.1R 1991). The FPZ is defined as the surrounding area at a crack tip and its size is identified from the crack tip to the point where the tensile stress just reaches the fracture strength. For a steady state FPZ, the stress reduces to zero at the crack tip and is equal to fracture strength at the other end.

This size of steady state FPZ is a material constant which may be affected by tensile strength and fracture energy of concrete and aggregate size. For normal strength concrete, the size of steady state FPZ ranges from 150mm to 1m (Ingraffea and Gerstle 1985). Illustration of least dimension regarding different cracking conditions is shown in Fig. 2-26. According to ACI Committee 446.1R (1991), when the size of FPZ is smaller than one percent of the least dimension associated with the crack tip, LEFM is applicable to concrete fracture.

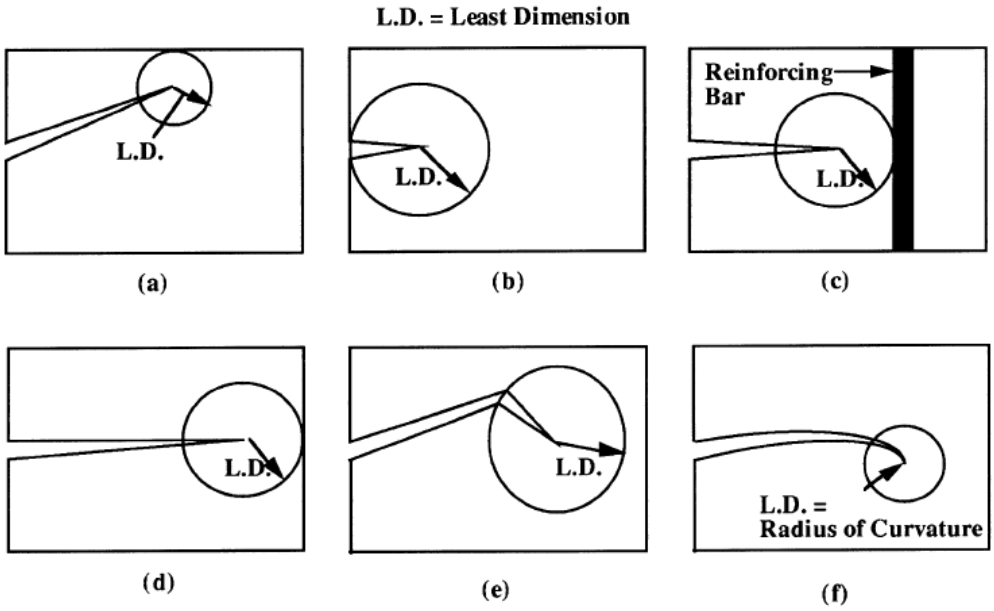

Figure 2-26 Determination of least dimension with different cases of cracking (Gerstle and Abdalla 1990)

For discrete crack propagation by LEFM, the key is to calculate the stress intensity factor. The most accurate approaches are: the J-integral, virtual crack extension, and stiffness derivative methods as they use integrated information. These methods are categorized as energy approaches and can be applied without singularity elements. They will not be discussed herein although there have been a few researchers who have extracted the stress intensity factor by using these methods, such as Bittencourt *et al.* (1992), Rice (1968a, b) and Shivakumar *et al.* (1988). However, these energy methods are not easy to apply to both mix-mode fracture and three-dimension problems. The often used one is displacement correlation technique. This method samples local displacements at various points, and correlates these with the theoretical displacement field associated

with a crack tip (ACI Committee 446.3R 1997). The displacement correlation technique is used with the singularity elements. The singularity elements are of two kinds. One is a special-purpose singular element which includes stress-intensity factor as a degree-of-freedom explicitly. This hybrid element, unfortunately, is not embedded in common displacement-based FE software. The other is displacement-based elements such as Tracey element (Tracey 1971) and the quarter-point quadratic triangular isoparametric element (Henshell and Shaw 1975). Most general FE packages provide 6-nodes triangular elements which can be used as singular quarter-point crack tip elements (ACI Committee 446.3R 1997). Once the stress intensity factor has been calculated using displacement correlation technique with singular elements at the crack tip, the next stage is to consider the fracture criteria as discussed in Chapter 4.

2.5.2.2 Cohesive crack model

Since Hillerborg *et al.* (1976) first proposed the fictitious crack model, it has been widely used in modelling fracture in concrete (Bocca *et al.* 1991; Gerstle and Xie 1992; Ingraffea and Gerstle 1985; Petersson 1981; Planas and Elices 1992). The fictitious crack model, also termed as cohesive crack model (CCM), assumes that the FPZ is long and narrow, and is characterized by a stress-crack opening displacement curve. CCM is normally incorporated into finite element codes by employing interface elements. Goodman *et al.* (1968) seems to be the first to develop the interface element, which was used in rock modelling. Zero-thickness interface elements are usually used to represent the cracks and nonlinear solution is required as the stiffness of the interface element is a nonlinear function of the crack opening displacement. The existing techniques for solving nonlinear problems are still appropriate for those interface elements, such as classic Newton iteration.

The selection of the stiffness of the interface elements is normally a problem. This might be due to the fact that there is no such an interface physically existing thus no suitable values for its mechanical properties. To establish a proper stiffness for the interface elements, it should be noted that the interface must be stiff enough to give exactly the same mechanical behaviour prior to the crack initiation. However, the stiffness cannot be too high to introduce

numerical convergence problems. Some researchers have suggested a few values after they successfully carried out the numerical modelling. Brown *et al.* (1993) advice that the axial stiffness of the interface elements shall be about 50 times that of adjacent concrete elements. Gerstle and Xie (1992) postulate to define the stiffness of the interface by using the stress-crack opening displacement curve, which is based on experimental results. On this curve, they suggest first to find a point on the descending part which has crack opening displacement of 1/20 to 1/30 of the maximum displacement, and then to define the interface stiffness equal to the secant stiffness to that point.

Perhaps the most commonly used approach to determine the direction of a Mode I crack and crack initiation with CCM is based on the criterion that the crack will propagate when the tensile stress exceeds the tensile strength of the material (Gerstle and Xie 1992; Petersson 1981). The direction of the crack propagation will be perpendicular to the maximum tensile principle stress. However, some researchers use energy-based approach to obtain the crack initiation and its direction (Li and Liang 1992; Xie *et al.* 1995).

2.6 Experimental research

It appears certain that the mechanical properties of the quasi-brittle materials after cracking plays an essential role in determining the behaviour of cracked materials. The most commonly used nonlinear fracture models have been discussed in the preceding sections. In these fracture models, some fracture parameters, such as, fracture energy and tensile strength, are regarded to depend on material properties and can only be determined from the experiments. RILEM has set up a number of committees since 1985 to propose the testing recommendations to different fracture models.

2.6.1 RILEM method based on fictitious crack model

As discussed in Section 4.3.2 there are three parameters for Hillerborg fictitious fracture model (HFM) which are: material tensile strength f_t, fracture energy G_F and critical crack separation w_c. RILEM Technical Committee 50-FMC (1985) has proposed a draft recommendation to measure the material fracture energy G_F using three-point bending beam. In addition, based on fictitious crack model, RILEM Technical Committee 162-TDF (2001) has established a procedure to determine the stress-crack opening relationship for both steel fibre reinforced concrete and plain concrete. In this section, the relatively widely accepted testing method based on three-point bending will be reviewed, while the uniaxial tensile testing will be discussed in Section 6.3.

Fig. 2-27 shows the basic testing arrangement of three-point bending. It needs to be noted that the depth of the beam is dependent on the maximum size of aggregate and the notch depth is set to be half of the beam depth. The other geometry arrangement as well as curing requirements can be found in RILEM Technical Committee 50-FMC (1985). The test is performed under displacement control which allows the maximum load to be reached within about 30-60 seconds and keeps increasing to get the post-cracking behaviour. The output is the relationship between the applied load and load point displacement. It should be ensured that the whole beam behaves elastically except for the zone ahead of the crack tip.

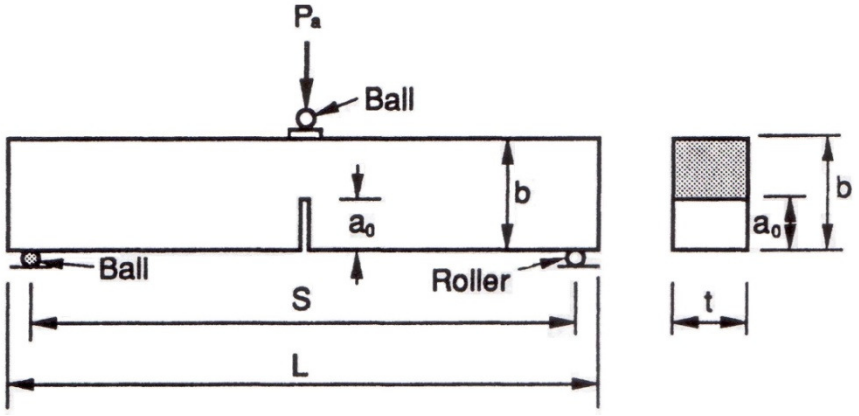

Figure 2-27 Three-point bending test of a notched beam

The fracture energy G_F can be determined from the results obtained from the test. Fig. 2-28 schematically shows the evaluation of the fracture energy, where P_w is the equivalent force introduced by self-weight, P_a is the external applied load which is also the load measured, and the sum of which represents the total force. W_0 is the area below the measured $P_a - \delta$ curve and $W_1 = P_w \delta_0$. As it has been demonstrated by Petersson (1981) W_2 is approximately equal to W_1. The total fracture energy can be expressed as:

$$W_t = W_0 + W_1 + W_2 = W_0 + 2P_w\delta_0 \tag{2.54}$$

Thus the fracture energy $G_F = \dfrac{W_t}{(b-a_0)t} = \dfrac{W_0 + 2P_w\delta_0}{(b-a_0)t}$ (2.55)

Eq. 2.55 is applicable to the case when the loading, beam self-weight and deflection all act downwards.

How to measure the load point displacement, however, is not specified in the RILEM Recommendation. Swartz and Kan (1990, 1991) stated that the measurement of distance between the notch and the reference bar in the middle position is most accurate. The fracture energy obtained in this testing method exhibits size effect as well. A number of researchers have been trying to explain this size effect and pointed out that the unwanted energy absorption outside the fracture zone is one of the most important contributing factors. This unwanted energy absorption may come from hysteresis in the testing equipment, friction of supports, and deformation of bulk material (Shah *et al.* 1995).

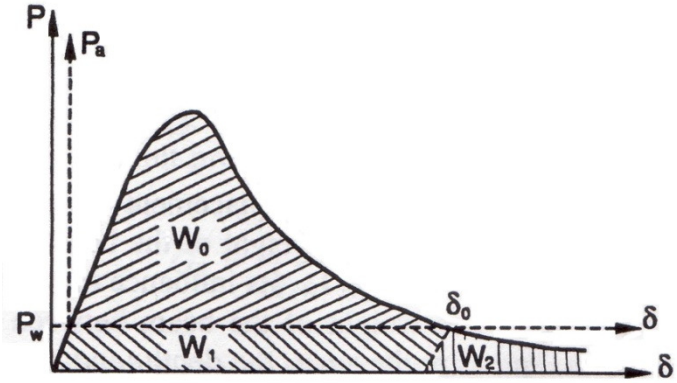

Figure 2-28 Load displacement curve for evaluation of the fracture energy

2.6.2 RILEM method based on two-parameter fracture model

RILEM Technical Committee 89-FMT (1990) proposed a recommendation for determination of fracture parameters (K_{Ic}^{s} and $CTOD_c$) based on Jenq and Shah's fracture model (JSFM) of plain concrete, also using three-point bending tests. The specimen is a notched beam of which the dimension is dependent on the maximum size of aggregate details of which could be found in RILEM report. JSFM requires relatively small specimen in geometry compared with HFM and the span/depth ratio for JSFM is always 4 for different structural size while it is between 8 for small size and 4 for large size for HFM. A closed loop testing equipment should be used in this test with *CTOD* as the feedback signal. Still, displacement control is adopted but different displacement is measured with HFM – separation of crack mouth rather than displacement of loading point. The *CMOD* and the applied load should be recorded continuously and a curve of load-crack mouth opening displacement will be produced in the end. Much lower loading rate than HFM is used in the test which allows the peak load is reached in 5 minutes. The beam will be monotonically loaded to its peak load of which within 95 percent unloading is employed. This is because the *CMOD* in JSFM is elastic crack mouth opening displacement and the plastic part must be removed from the total displacement. Fig. 2-29 shows a typical test arrangement and the load-*CTOD* curve.

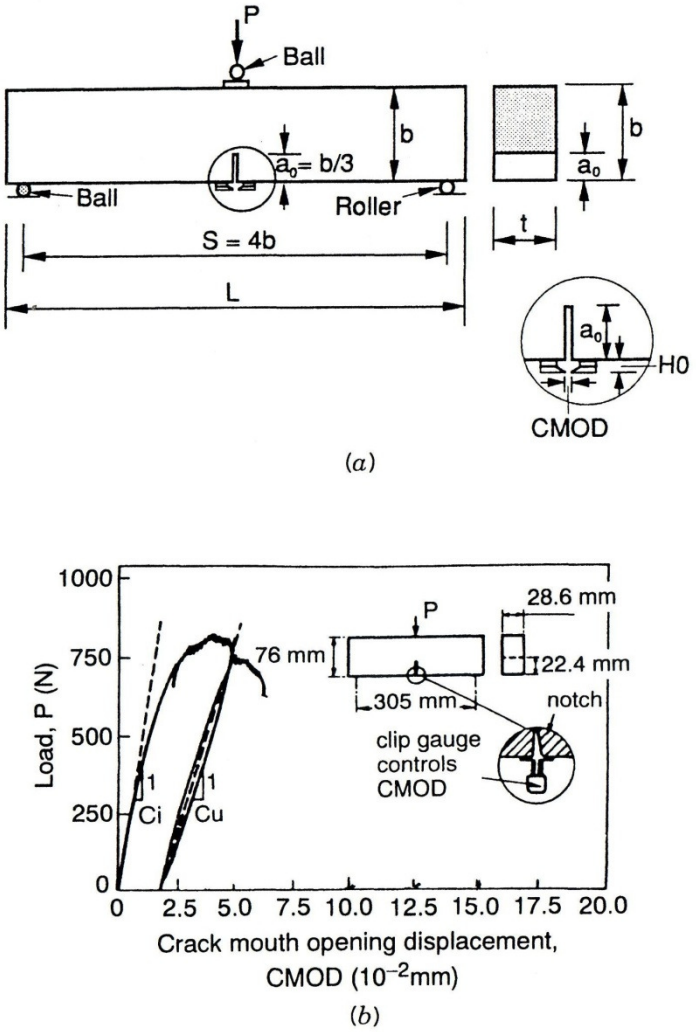

Figure 2-29 A typical load-*CMOD* curve (RILEM Technical Committee 89-FMT 1990)

Jenq and Shah (1985) originated JSFM and determined the fracture parameters from testing results. They related the critical stress intensity factor to the structural geometry, peak load, self weight of the beam, and effective-elastic critical crack length. In addition, the critical crack tip displacement $CTOD_c$, derived from the critical crack mouth displacement $CMOD_c$, is corresponding to the same factors above as well as the modulus of elasticity. The effective-elastic critical crack length and modulus of elasticity can be calculated in terms of the compliances (Ci and Cu) of the load-*CMOD* curve shown in Fig. 2-29. Details of calculations can be found in Jenq and Shah (1985), RILEM Technical Committee 89-FMT (1990) and Shah *et al.* (1995). Different from HFM, self-

weight was not included in the calculations which was explained by Shah *et al.* (1995) it was due to the relatively small structural size. It should be noted that the specimen used cannot be too small as that will increase the portion of plastic critical crack tip opening displacement and easily introduce errors.

2.6.3 RILEM recommendations for uni-axial tension test

RILEM Technical Committee 162-TDF (2001) proposed a recommendation for uniaxial tension test for steel reinforced and plain concrete. Rather than three-point bending test for HFM to determine the curve of applied load and load point displacement, this test is to obtain the stress-crack opening relationship $\sigma(w)$, also called traction-separation relation. The standard test specimen recommended is cylindrical with nominal length of 150mm and circular cross-section with nominal diameter 150mm. The specimen is notched with a circumferential notch with a depth of 15mm+/-1 mm and a width of 2-5mm which shall be cut with a diamond saw.

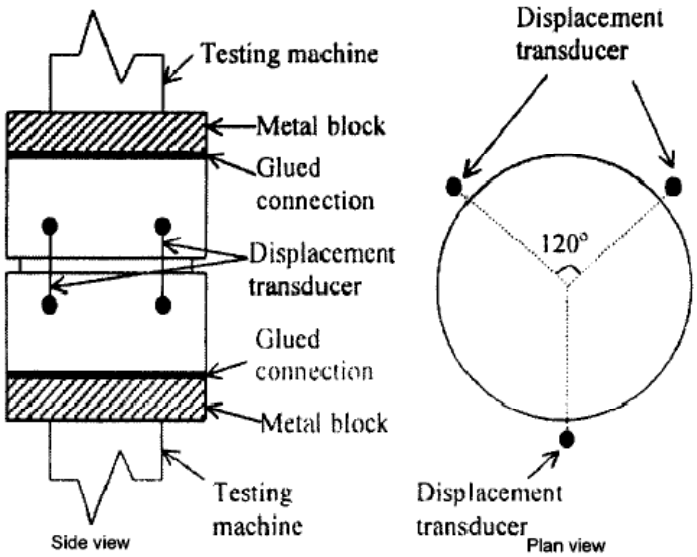

Figure 2-30 test setup for uniaxial tension testing (RILEM TC 162-TDF 2003)

Test setup and instrumentation of this method are shown in Fig. 2-30. The specimen is glued to metal plates which are connected to testing machine – normally bolted. No less than three displacement transducers should be arranged

across the notch at equal distances along the perimeter of the test specimen. The gauge length shall not be larger than 40 mm. RILEM has set a procedure to fix the specimen which, principally, is to make sure the specimen be pulled uniaxially and eliminate pre-stressing which could lead to failure of obtaining stable crack propagation. The signal from the displacement transducers will be used as feedback to control the loading, and the load and corresponding displacement shall be recorded digitally. The required displacement rates are 5 μm / min up to a displacement of 0.1 mm and 100 μm / min until the completion of the test when a displacement of 2 mm is reached. The stress-crack opening relationship can be obtained from interpreting the raw results, shown in Fig. 2-31. The stress σ is calculated from the load P simply by dividing with the cross-section area at the notch. The crack opening w is calculated from the average signal of the displacement transducers ($\overline{\delta}$) by subtracting the average displacement at the peak stress ($\overline{\delta_p}$), neglecting the elastic unloading, as schematically described in Fig. 2-30.

$$w = \overline{\delta} - \overline{\delta_p} \tag{2.56}$$

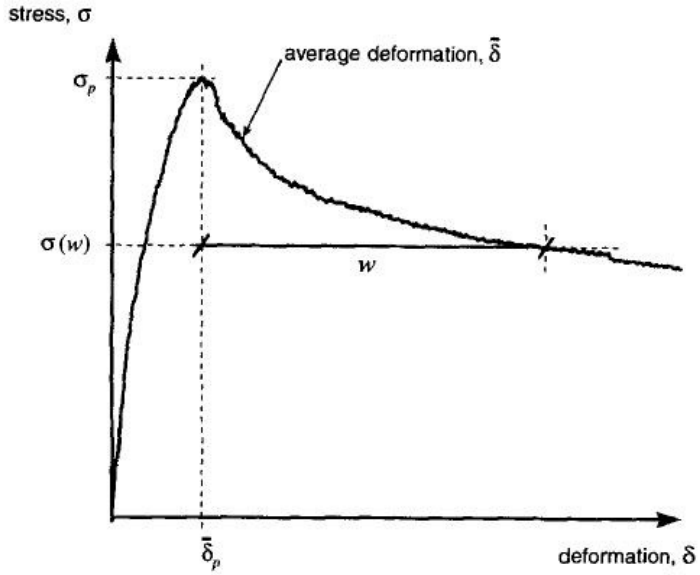

Figure 2-31 typical average stress-deformation relation (RILEM TC 162-TDF 2001)

Prior to the RILEM recommendations for uni-axial tension test, there were a number of researchers, e.g., Gopalaratnam and Shah (1985), who tried to propose a suitable testing method for the uni-axial tension test. Gopalaratnam and Shah (1985) developed a scheme for direct tension test to obtain the post-crack response of plain concrete. They used rectangular prism specimens of dimensions of 76*19(38)*305mm with two notches in the middle. Special wedge-type frictional grips were designed consisting of sliding soft aluminium, steel plates and a layer of serrated gasket rubber (from outside to inside in Fig. 2-32). The grips are vital to this test method as non-uniform distributed pressure could lead to failure of this test. The testing rig is shown in Fig. 2-32. Also illustrated is the closed-loop test scheme. The specimens were tested in an MTS servocontrolled testing machine and were loaded by a constant strain rate. The average elongation across the notch measured using two strain gauge extensometers with length of 13mm was used as a feedback signal to the servocontroller. Additionally, the average elongation for a second gage length of 83mm using two linear variable differential transducers (LVDTs) is recorded as a function of time. Crack widths were measured by 100X microscope. Fig. 2-33 is the typical result obtained for concrete and mortar specimens. The displacements recorded herein refer to those using a gauge length of 83mm and the stresses are calculated by dividing the load with the net cross-sectional area.

Stress-crack width $\sigma(w)$ curve is the focus of this testing and both stress-observed crack width curve and stress-measured crack width are produced in this test. To calculate the crack width from the measured displacement, it is assumed that the crack initiates at the peak load and that the uncracked parts gradually unload with the same modulus as the initial elastic modulus. The difference in displacement between softening curve and unloading curve is the crack width, shown in Fig. 2-34. They have compared the optical crack width and the calculated crack width and it seems they are very close (Fig. 2-34). It should be mentioned that based on the experimental results, they proposed an exponential softening model for stress and crack width relationship, which is,

$$\sigma = \sigma_p \left(e^{-kw\lambda} \right) \tag{2.57}$$

where σ_p is the peak value of tensile stress, k and λ are constants.

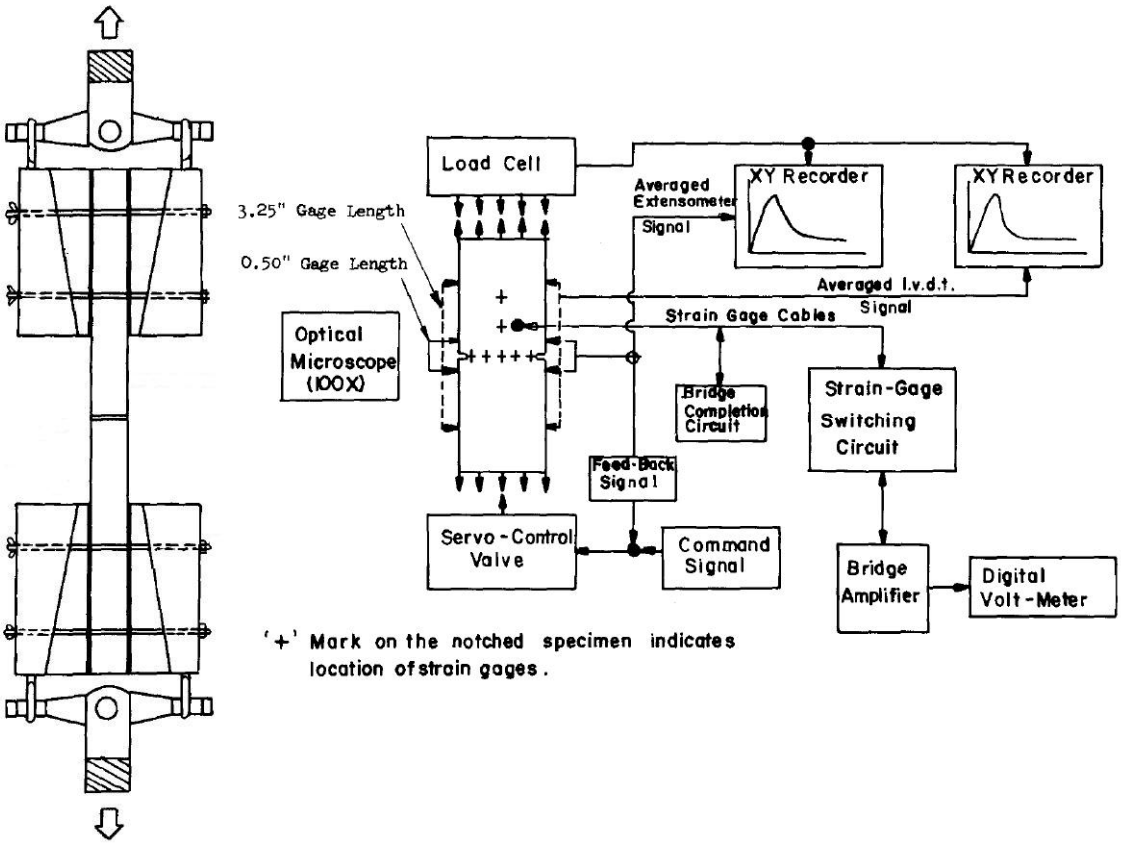

Figure 2-32 test apparatus and closed-loop test scheme (Gopalaratnam and Shah 1985)

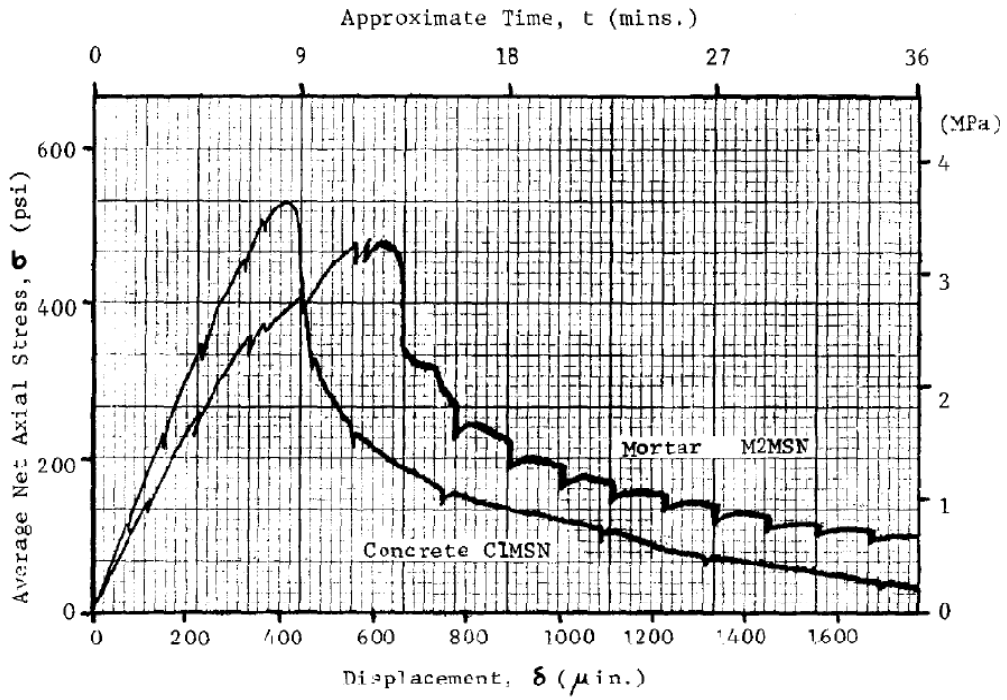

Figure 2-33 typical test results obtained for concrete and mortar (Gopalaratnam and Shah 1985)

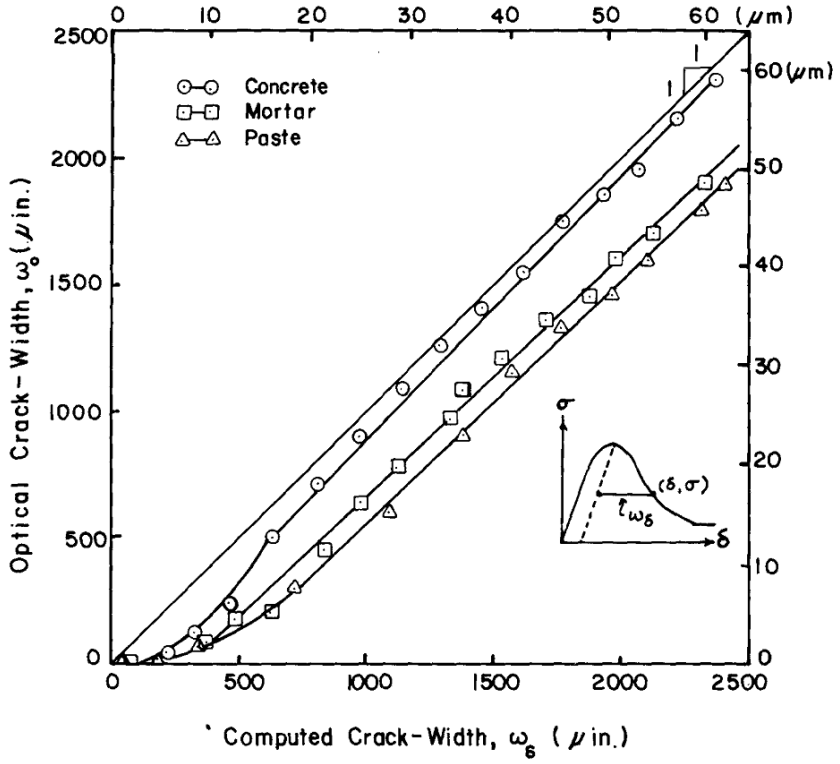

Figure 2-34 Comparison between observed crack width and calculated crack width (Gopalaratnam and Shah 1985)

2.7 Conclusions

In this chapter, the basic knowledge and skills that are required in determining the concrete crack width induced by the combined effects of reinforcement corrosion and applied load has been examined. The state-of-the-art of research in the area of concrete cracking either caused by steel corrosion or applied load as well related topics has been critically reviewed. It has been found that there is a lack of research in the area of prediction of concrete crack width under both the reinforcement corrosion and applied load, by either analytical or numerical means.

CHAPTER 3

DEVELOPMENT OF ANALYTICAL METHOD

3.1 Introduction

Corrosion of reinforcing steel in concrete has been and will continue to be a global problem for RC structures located in chloride and/or carbon dioxide laden environment (Broomfield 1997; Schiessl 1988), causing structural deterioration due to premature concrete cracking and spalling, and leading to ultimate structural collapse. Meanwhile, there are continual demands for greater load for infrastructure, particularly for transport systems (e.g., bridges), energy plants (e.g., power stations) and flood defences. Climate change is also likely to add more loads (e.g., more intense storms) for structures. This combined effects of reinforcement corrosion and applied load highlights the issue of safety and serviceability to all engineers and asset managers responsible for the operation of corrosion affected RC structures.

A review of the most recent research literature in Chapter 2 has shown that little research has been undertaken on corrosion induced crack width of concrete under the reinforcement corrosion and even lesser under the combined effects of corrosion and applied load. As is known, concrete crack width is the criterion that is of the most practical significance for structural design and assessment and of real concern to structural engineers, operators and asset managers responsible for infrastructure. Also as discussed previously, demands on load are likely to increase which, combined with corrosion effect, will escalate concrete cracking. The combined effects justify the need for a thorough investigation on concrete cracking to ensure the serviceability of RC structures.

This Chapter attempts to develop an analytical method for determining the concrete crack width under the combined effects of reinforcement corrosion and applied load. A whole process of concrete cracking under the combined effects is examined. Models for corrosion induced pressure, applied load induced pressure and constitutive relationship of cracked concrete are proposed. In the analysis of stress distribution in concrete, both elastic and fracture mechanics are employed as appropriate. A key contribution of the model is that the degradation of stiffness is related to the fracture property of concrete, i.e., tensile strength and fracture energy. A programme in MatLab is developed to

execute all the computations. Worked examples are provided to illustrate the application of the developed method. This method is further refined according to the results from direct tensile tests, overcoming the limitation of the assumption. A merit of the developed method is that it is directly related to the parameters that are used by practitioners in design and assessment of reinforced concrete structures, such as the corrosion rate, applied load, concrete property and geometry. The developed method can equip the engineers, operators and managers with a useful tool in decision making about the serviceability of the RC structures subject to corrosion and applied load.

3.2 Mathematical formulation

Concrete with an embedded bar subjected to an internal pressure at the interface between the bar and concrete can be modelled as a thick-wall cylinder (Bažant 1979, Pantazopoulou and Papoulia 2001, Tepfers 1979). This is schematically shown in Fig. 3-1(a), where D is the diameter of the bar; d_0 is the thickness of the annular layer of concrete pores at the interface between the bar and concrete; and C is the concrete cover. Usually d_0 is constant once concrete has hardened. The inner and outer radii of the cylinder are $a = D/2 + d_0$ and $b = C + D/2 + d_0$.

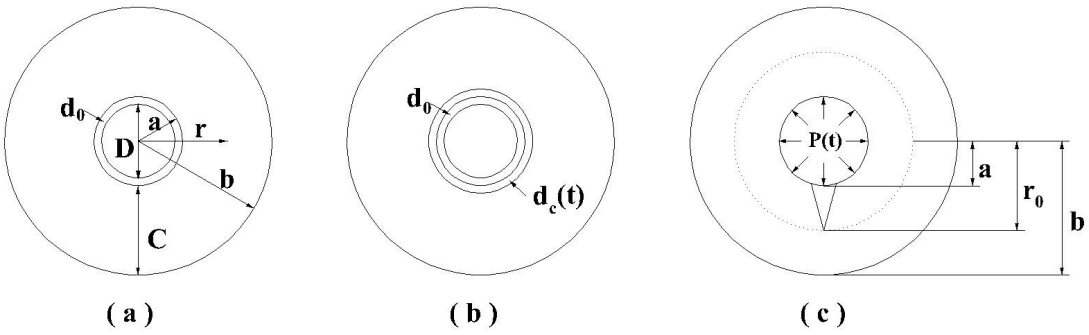

Figure 3-1 Illustration of internal pressure induced concrete cracking process

In this thick-wall cylinder, the internal pressure $P(t)$ is caused by two effects: one is the products of corrosion of the reinforcing steel bar in concrete, which

changes with time and denoted as $P_1(t)$ and the other is the applied load via the transverse (radial) component of the bond stress between the bar and concrete, which is usually sustained and denoted as P_2. The total expansive pressure $P(t)$ can therefore be expressed as:

$$P(t) = P_1(t) + P_2 \tag{3.1}$$

Under this pressure, tangential tensile stresses (or hoop stresses as widely referred to in the literature of mechanics) are developed in the concrete cylinder, which leads to the concrete cracking owning to its low tensile strength. To predict the cracking and importantly the crack width of the concrete cylinder, it is essential to analyse the stress (and strain) distribution in the concrete cylinder using both elastic mechanics (Timoshenko and Goodier 1970) and fracture mechanics (Bažant and Planas 1998; Shah *et al.* 1995), wherever appropriate. This requires the development of the models for both the effects of corrosion products and applied load, and more importantly the material properties of the cracked concrete.

3.2.1 Determination of corrosion-induced expansion

As discussed in the literature review, the corrosion products (mainly ferrous and ferric hydroxides, $Fe(OH)_2$ and $Fe(OH)_3$) occupy a few times more space than the original steel. These corrosion products first fill in the annular pores in concrete around the reinforcing bar, with thickness d_0, but do not produce stresses in concrete. As the corrosion propagates in concrete, a ring of corrosion products forms, the thickness of which is denoted as $d_c(t)$, as shown in Fig. 3-1 (b). According to Liu and Weyers (1998), the total amount of corrosion products $W_{rust}(t)$ can be assumed to distribute annularly around the bar, which can be determined based on three parts: the band of corroded steel, the porous band d_0 and the rust band $d_c(t)$ as in the equation below:

$$W_{rust}(t) = W_s + W_0 + W_c \tag{3.2}$$

where W_s is the amount of rust replacing the corroded steel, W_0 is the amount of rust filling the porous band d_0 and W_c is the amount of rust in the band $d_c(t)$. W_s, W_0 and W_c can be derived respectively from Eq. 3.3 to 3.5.

$$W_s = \alpha_{rust} W_{rust} \frac{\rho_{rust}}{\rho_{st}} \tag{3.3}$$

$$W_0 = \pi \rho_{rust} d_0 D \tag{3.4}$$

$$W_c = \pi \rho_{rust} (D + 2d_0) d_c(t) \tag{3.5}$$

α_{rust} is the ratio of molecular weight of steel to the molecular weight of corrosion products. It varies from 0.523 to 0.622 according to different types of corrosion products (Liu and Weyers 1998). ρ_{rust} is the density of corrosion products.

By substituting Eq. 3.3 – 3.5 into Eq. 3.2, it becomes:

$$\frac{W_{rust}(t)}{\pi}\left(\frac{1}{\rho_{rust}} - \frac{\alpha_{rust}}{\rho_{st}}\right) = D d_c(t) + 2 d_0 d_c(t) + d_0 D \tag{3.6}$$

The quantities $2 d_0 d_c(t)$, compared with $D d_c(t)$ and $d_0 D$, are at least 2 orders of magnitude less and can be neglected. $d_c(t)$ can then be derived as follows:

$$d_c(t) = \frac{W_{rust}(t)}{\pi D}\left(\frac{1}{\rho_{rust}} - \frac{\alpha_{rust}}{\rho_{st}}\right) - d_0 \tag{3.7}$$

$d_c(t)$ in Eq. 3.7 is the corrosion induced expansion to the concrete cylinder under which the stress will be initiated in the cylinder.

In Eq. 3.7, $W_{rust}(t)$ is related to the corrosion rate of the steel rebar and can be expressed as (Liu and Weyers 1998):

$$W_{rust}(t) = \sqrt{2\int_0^t 0.105(1/\alpha_{rust})\pi D i_{corr}(t)dt} \tag{3.8}$$

where i_{corr} is the corrosion current density in $\mu A/cm^2$, which is widely used as a measure of corrosion rate.

The units of the parameters in Eq. 3.2 to 3.8 need to be kept consistent which are specified in Table 3-1.

Table 3-1 Units of the parameters

Parameter	Unit
D/d_0	mm
ρ_{rust}/ρ_{st}	kg/m^3
α_{rust}	n.a.
$W_{rust}/W_s/W_0/W_c$	mg/mm
$d_c(t)$	m
i_{corr}	$\mu A/cm^2$
t	year

3.2.2 Determination of applied load induced expansion

Applied load may cause longitudinal cracks along the reinforcing bar in concrete members due to the transverse component of the bond stress between the deformed bar and surrounding concrete (Tepfers 1979). When subject to pull-out force, the deformed steel bar may slip in two ways (Lutz and Gergely 1967): (a) the ribs can crush the surrounding concrete, shown in Fig. 3-2, and (b) the ribs can split the concrete by wedging action, illustrated in Fig. 3-3. Both

mechanisms are due to the development of the bond stress between the steel bar and surrounding concrete. However, the ribs can split the concrete without crushing it if the surrounding concrete resistance is moderate, as it is for ordinary concrete cover (Tepfers 1979).

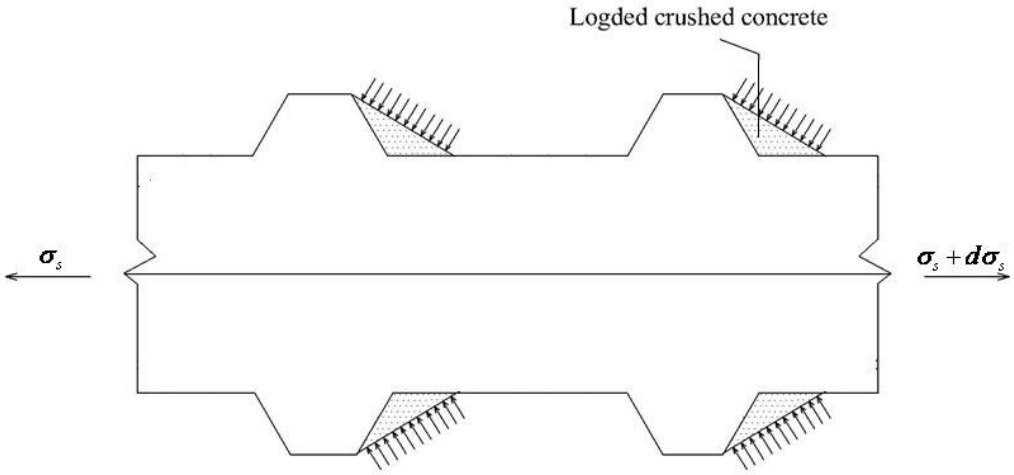

Figure 3-2 Crushing of concrete surrounding deformed steel bar

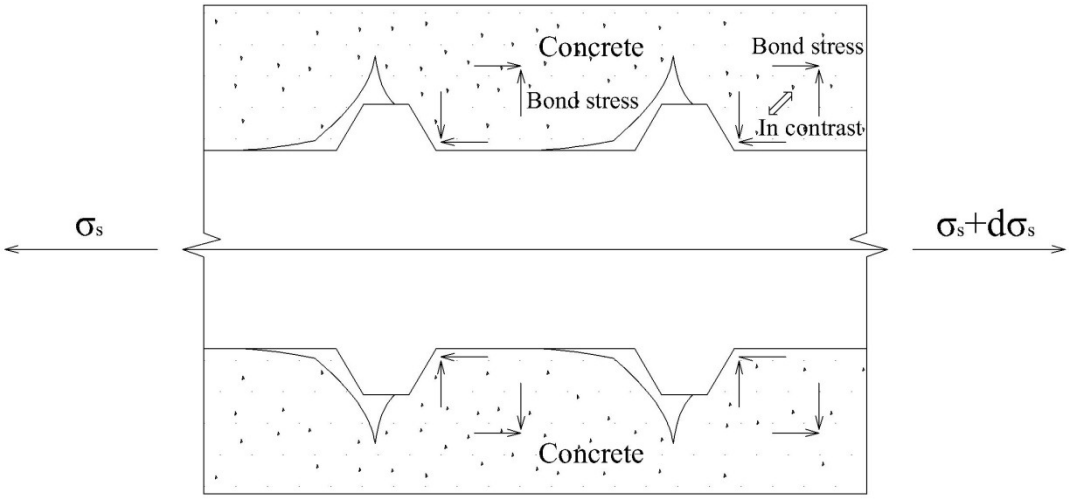

Figure 3-3 Splitting of concrete surrounding deformed steel bar

The bond stress, in an angle θ with respect to the bar axis, is normally expressed as the principal compressive stress. The bond is the grip due to adhesion or mechanical interlock and bearing in deformed bars between the reinforcement and the concrete (Bhatt *et al.* 2006). The bond stress can be divided into two components – transverse (radial) and longitudinal stresses. To determine its

transverse component, the bond stress (longitudinal) needs to be analysed. Considering an element of the reinforcing bar dx (as shown in Fig. 3-2), the longitudinal (shear) bond stress can be expressed from mechanical equilibrium as follows (Tepfers 1979)

$$\tau = \frac{D}{4}\frac{d\sigma_s}{dx} \tag{3.9}$$

where σ_s is the stress in the reinforcing bar due to the applied load. For a given application, i.e., the structure and applied load, σ_s is known.

From the theory of Mohr Circle (see Fig. 3-4), the radial component of the bond stress can be derived as follows

$$P_2 = \frac{\sigma_2 + \sigma_1}{2} - \frac{\sigma_2 - \sigma_1}{2}\cos 2\theta = \sigma_1 \cos^2\theta + \sigma_2 \sin^2\theta \tag{3.10}$$

$$\tau = \frac{\sigma_2 + \sigma_1}{2}\sin 2\theta \tag{3.11}$$

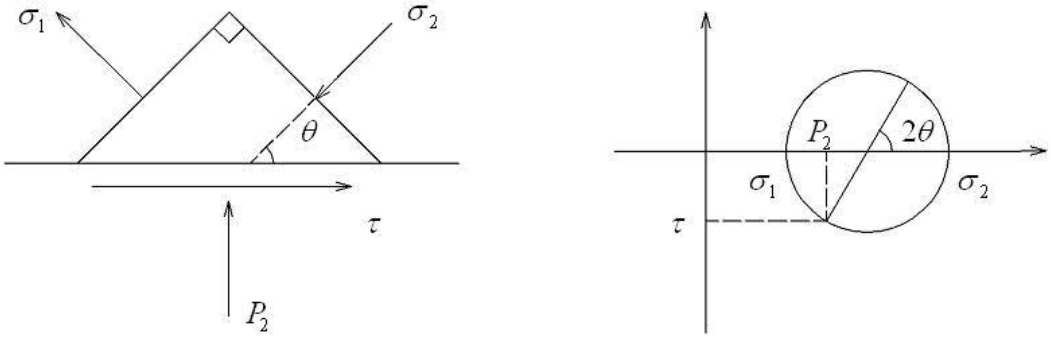

Figure 3-4 Mohr circle for determining P_2 at the interface between the rebar and concrete

where σ_1 is the principal tensile stress and σ_2 is the principal compressive stress.

The angle θ depends on the rib face angle and the remaining chemical bond. It is 45^0 at the beginning of loading, when the principal tensile stress and principal compressive stress are equal in magnitude. Once a crack is initiated, the principal tensile stress decreases to zero and the angle θ may change and the principal compressive stress still develops. The change of θ can only be determined in experiments.

Therefore, when the surrounding concrete has cracked, the radial bond stress component becomes (from Eqs. 3.10 and 3.11):

$$P_2 = \sigma_2 \sin^2\theta = \tau \tan\theta = \frac{D}{4}\frac{d\sigma_s}{dx}\tan\theta \tag{3.12}$$

3.3 Solution to elastic behaviour of uncracked concrete

Under the internal pressure, the concrete cylinder undergoes three stages: no-cracking, partially cracked and completely cracked stages (Li *et al*. 2006). For the uncracked concrete either in the no-cracking phase or in the partially cracked phase, it is of linear elasticity. By taking a finite element out of the uncracked concrete and considering the radial stress equilibrium, the stress components can be expressed as follows (Timoshenko and Goodier 1970).

$$\sigma_\theta(r) - \sigma_r(r) - r\frac{d\sigma_r(r)}{dr} = 0 \tag{3.13}$$

where σ_θ is the tangential/hoop stress, σ_r is the radial stress and r is the distance in the radial direction from the centre point of the steel bar.

For any elastic material, the stress-strain relations in plane state (2D) are:

$$\sigma_\theta(r) = \frac{E_{ef}}{1-\upsilon_c^2}\left(\varepsilon_\theta(r) + \upsilon_c\varepsilon_r(r)\right) \tag{3.14a}$$

$$\sigma_r(r) = \frac{E_{ef}}{1-\upsilon_c^2}\left(\varepsilon_r(r) + \upsilon_c \varepsilon_\theta(r)\right) \tag{3.14b}$$

ε_θ and ε_r are the tangential and radial strain respectively. E_{ef} is the effective modulus of elasticity allowing for the creep effect. υ_c is the Possion's ratio.

Also, the strain components are related to the radial displacement u by compatibility condition. Taking advantage of symmetry, they can be expressed as follows:

$$\varepsilon_\theta(r) = \frac{u(r)}{r} \tag{3.15a}$$

$$\varepsilon_r(r) = \frac{du(r)}{dr} \tag{3.15b}$$

Substituting Eqs. 3.14 and 3.15 into Eq. 3.13, the displacement differential equation for the concrete element is obtained as:

$$\frac{d^2u(r)}{dr^2} + \frac{1}{r}\frac{du(r)}{dr} - \frac{u(r)}{r^2} = 0 \tag{3.16}$$

Since r and $\frac{1}{r}$ are both solutions to Eq. 3.16, the general solution to Eq. 3.16 is:

$$u(r) = c_1 r + \frac{c_2}{r} \tag{3.17}$$

The tangential and radial stresses then become:

$$\sigma_\theta(r) = \frac{E_{ef}}{1-\upsilon_c^2}\left(c_1(1+\upsilon_c) + c_2\frac{1-\upsilon_c}{r^2}\right) \tag{3.18a}$$

$$\sigma_r(r)=\frac{E_{ef}}{1-\upsilon_c^2}\left(c_1(1+\upsilon_c)-c_2\frac{1-\upsilon_c}{r^2}\right) \tag{3.18b}$$

Before corrosion starts in concrete, there is only applied load induced pressure P_2 at the interface between the bar and concrete, under which the concrete cylinder could be either uncracked or partially cracked since the completely cracked case can be designed out. If it is (reasonably) assumed that the concrete is not cracked under the pressure P_2 at the beginning, i.e., $t=0$ the concrete cylinder is considered to be elastically isotropic so that the theory of elasticity can be used to derive the equation for radial displacement *u(r)*, from which the radial stress $\sigma_r(r)$ and tangential stress $\sigma_\theta(r)$ at any point (r) in the cylinder can be determined. By applying the boundary conditions $\sigma_r(a)=-P_2$ and $\sigma_r(b)=0$, the displacement caused by P_2 at $r=a$ can be obtained as $d_p=\frac{a}{E_{ef}}\left(\frac{b^2+a^2}{b^2-a^2}+\upsilon_c\right)P_2$.

Also, the tangential stress in the cylinder can be obtained as follows

$$\sigma_\theta(r)=\frac{a^2P_2}{b^2-a^2}\left(1+\frac{b^2}{r^2}\right) \tag{3.19}$$

Eq. 3.19 is used to check whether the concrete cylinder is: (i) not cracked ($\sigma_\theta(a) < f_t$); and (ii) partially cracked [$\sigma_\theta(a) \geq f_t$ and $\sigma_\theta(b) < f_t$], at the beginning (prior to the initiation of corrosion).

The corrosion induced pressure could not cause concrete cracking at an early stage either. The corrosion induced expansion $d_c(t)$, together with the applied load induced expansion d_p, is the actual displacement boundary condition at $r=a$ for the combined effects. The coefficients c_1 and c_2 of Eq. 3.18, therefore, can be determined.

$$c_1 = \frac{(1-\upsilon_c)a[d_c(t)+d_p]}{(1-\upsilon_c)a^2+(1+\upsilon_c)b^2} \tag{3.20a}$$

$$c_2 = \frac{(1+\upsilon_c)ab^2[d_c(t)+d_p]}{(1-\upsilon_c)a^2+(1+\upsilon_c)b^2} \tag{3.20b}$$

3.4 Solution to inelastic behaviour of cracked concrete

Under the combined effects of two pressures, the concrete cylinder will be cracked with the accumulation of the corrosion products. In the case of partially cracked concrete cylinder, the radial crack divides the cylinder into two co-axial cylinders at a self-equilibrium radius r_0 (which varies between the radii *a* and *b*): (i) the inner cracked cylinder; and (ii) the outer uncracked cylinder, as shown in Fig. 3-1(c). For the outer uncracked concrete cylinder, the theory of elasticity still applies and the radial displacement $u(r)$ as well as the stress components can be expressed in the same form as that for no-cracking stage, but with different coefficients due to different boundary conditions.

$$u(r) = c_3(r_0)r + \frac{c_4(r_0)}{r} \tag{3.21}$$

$$\sigma_\theta(r) = \frac{E_{ef}}{1-\upsilon_c^2}\left(c_3(r_0)(1+\upsilon_c) + c_4(r_0)\frac{1-\upsilon_c}{r^2}\right) \tag{3.22a}$$

$$\sigma_r(r) = \frac{E_{ef}}{1-\upsilon_c^2}\left(c_3(r_0)(1+\upsilon_c) - c_4(r_0)\frac{1-\upsilon_c}{r^2}\right) \tag{3.22b}$$

where the coefficients $c_3(r_0)$ and $c_4(r_0)$ are a function of r_0 since it varies between *a* and *b*.

For inner cracked concrete cylinder, the mechanical properties of concrete have changed due to its cracking. With the assumption of quasi-brittle nature of concrete, concrete will still have strength after its ultimate strength. The

stiffness of concrete is gradually degraded until the complete lose of strength. To account for the residual stiffness and residual stress after the ultimate strength, a damage parameter called stiffness reduction factor α is proposed.

3.4.1 Stiffness reduction factor

In deriving the equations for stresses in the inner cracked concrete cylinder, let it be assumed that the cracks are smeared and uniformly distributed on the circumference of the crack cylinder (Chen and Mahadevan 2007; Pantazopoulou and Papoulia 2001). The cracking makes the concrete an anistropic material, which means the elastic modulus in the radial direction is different from that in the tangential direction. Also assumed is that concrete is a quasi-brittle material, that is, the strength of concrete will steadily decrease after peak stress rather than suddenly drop to zero. To account for the anisotropic behavior of cracked concrete, a tangential stiffness reduction factor α (≤ 1) is proposed and defined as follows (Bažant and Jirasek 2002; Gopalaratnam and Shah 1985)

$$\alpha = \frac{E_r}{E_{ef}} \tag{3.23}$$

where E_r denotes the residual modulus of elasticity of cracked concrete in tangential direction and E_{ef} is the effective modulus of elasticity of intact concrete. The tangential stiffness reduction factor α can be derived from the concept of fracture energy. According to Gopalaratnam and Shah (1985) and Bažant and Planas (1998), a general relationship between the post-crack (residual) stress σ and crack width w of cracked concrete can be expressed as follows

$$\sigma(w) = Ae^{-Bw} \tag{3.24}$$

where A and B are coefficients to be determined for a given concrete and loading conditions. In this study, the $\sigma(w)$ curve from Shah *et al.* (1995) is

adopted as shown in Fig. 3-5 since it has been widely used in stress analysis of cracked concrete.

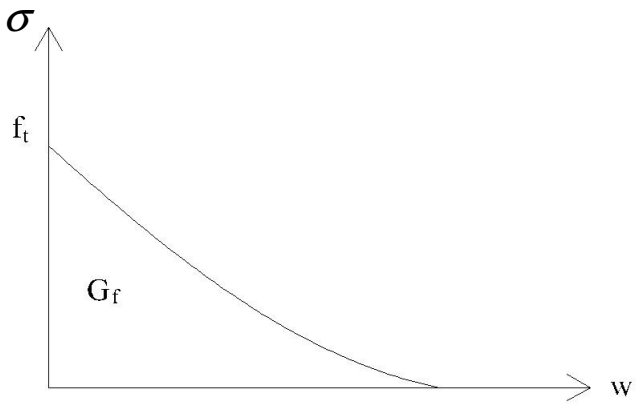

Figure 3-5 Post crack stress and crack width relationship (from Shah *et al*. 1995)

In Fig. 3-5, f_t is the tensile strength of concrete and G_f is its fracture energy. From the initial condition $\sigma(0) = f_t$ and the definition of the fracture energy $\int_0^\infty \sigma(w)dw = G_f$, the coefficients A and B can be determined as $A = f_t$ and $B = \frac{f_t}{G_f}$. Therefore the tangential stiffness reduction factor α, i.e., Eq. 3.23, can be expressed as

$$\alpha = \frac{\sigma / \varepsilon_\theta(r)}{E_{ef}} = \frac{f_t \exp\left(-\frac{f_t}{G_f} w\right)}{E_{ef}\varepsilon_\theta(r)} \tag{3.25}$$

where ε_θ denotes the residual tangential strain of cracked concrete.

Since crack width is determined by the strains as in the general form below

$$w(r) = 2\pi r\left(\varepsilon_\theta(r) - \varepsilon_\theta^{e,m}(r)\right) \tag{3.26}$$

$\varepsilon_\theta^{e,m}(r)$ is the maximum elastic tangential strain at any radius r as illustrated in Fig. 3-6. The tangential stress is assumed to be linear with respect to the tangential strain until the peak stress f_t as in Eq. 3.14a. After f_t the tangential stress decreases while the tangential strain increases. Since elasticity is not assumed to be damaged, the elastic strain will be unloaded with respect to the original modulus of elasticity. Therefore, $\varepsilon_\theta(r) - \varepsilon_\theta^{e,m}(r)$ represents the fracture strain which is used to determine the crack width.

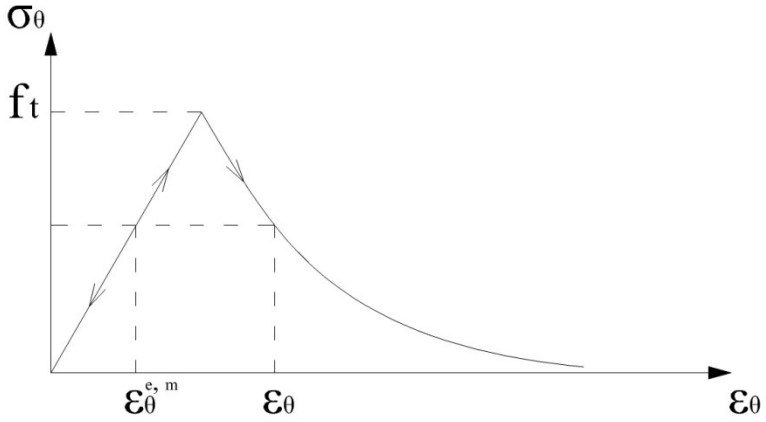

Figure 3-6 Tangential stress and strain relation

By substituting Eq. 3.26 into Eq. 3.25, α becomes

$$\alpha = \frac{f_t \exp\left(-2\pi r \frac{f_t}{G_f}\left(\varepsilon_\theta(r) - \varepsilon_\theta^{e,m}(r)\right)\right)}{E_{ef}\varepsilon_\theta(r)} \tag{3.27}$$

From Eq. 3.27, it can be seen that α is a function of both time and position, that is $\alpha(t,r)$. However, in order to derive an analytical solution, α has to be assumed as constant along the cracked surface in radial direction, to be feasible for an analytical solution. This means that α is only a function of time. Scientific explanations will be provided later in the integration of the differential equation (Eq. 3.30) of the cracked concrete. Under this assumption,

the strains $\varepsilon_\theta(r)$ and $\varepsilon_\theta^{e,m}(r)$ of Eq. 3.27 become average along the cracked surface.

For the cracked concrete, the stress equilibrium Eq. 3.13 and the strain-displacement compatibility Eq. 3.15(a, b) are still applicable. However, the constitutive relation between stress and strain changes due to the anisotropy of the cracked concrete (Pantazopoulou and Papoulia 2001)

$$\sigma_\theta(r)=\frac{\alpha E_{ef}}{1-\upsilon_1\upsilon_2}\left[\varepsilon_\theta(r)+\upsilon_1\varepsilon_r(r)\right] \tag{3.28a}$$

$$\sigma_r(r)=\frac{E_{ef}}{1-\upsilon_1\upsilon_2}\left[\varepsilon_r(r)+\upsilon_2\varepsilon_\theta(r)\right] \tag{3.28b}$$

where υ_1 and υ_2 are the Poisson's ratios in the radial and tangential directions respectively. According to anisotropic requirement $\upsilon_2 E_{ef}=\alpha\upsilon_1 E_{ef}$ (Lekhnitskii 1963) and approximation of $\upsilon_c^2=\upsilon_1\upsilon_2$ (Sheng *et al.* 1991), Eq. 3.28 (a, b) become

$$\sigma_\theta(r)=\frac{E_{ef}}{1-\upsilon_c^2}\left(\alpha\varepsilon_\theta(r)+\sqrt{\alpha}\upsilon_c\varepsilon_r(r)\right) \tag{3.29a}$$

$$\sigma_r(r)=\frac{E_{ef}}{1-\upsilon_c^2}\left(\varepsilon_r(r)+\alpha\upsilon_c\varepsilon_\theta(r)\right) \tag{3.29b}$$

By substituting Eqs.3.15 (a, b) and 3.29 (a, b) into Eq. 3.13, the differential equation for radial displacement $u(r)$ can be obtained as follows

$$\frac{d^2u(r)}{dr^2}+\frac{1}{r}\frac{du(r)}{dr}-\alpha\frac{u(r)}{r^2}+\frac{\nu_c u}{r}\frac{d\sqrt{\alpha}}{dr}=0 \tag{3.30}$$

As mentioned earlier, α is assumed to be independent of r. This is because Eq. 3.30 would not have analytical solution if α is a function of r in which case there are two unknown functions of r. Therefore, Eq. 3.30 becomes

$$\frac{d^2u(r)}{dr^2}+\frac{1}{r}\frac{du(r)}{dr}-\alpha\frac{u(r)}{r^2}=0 \tag{3.31}$$

The solution to Eq. 3.31 can be in the form of (James 1993)

$$u(r)=c_5(r_0)r^{\sqrt{\alpha}}+c_6(r_0)r^{-\sqrt{\alpha}} \tag{3.32}$$

The corresponding radial and tangential stresses are respectively

$$\sigma_\theta(r)=\frac{\alpha E_{ef}}{1-\upsilon_c^2}\left[c_5(r_0)(1+\upsilon_c)r^{(\sqrt{\alpha}-1)}+c_6(r_0)(1-\upsilon_c)r^{(-\sqrt{\alpha}-1)}\right] \tag{3.33a}$$

$$\sigma_r(r)=\frac{\sqrt{\alpha}E_{ef}}{1-\upsilon_c^2}\left[c_5(r_0)(1+\upsilon_c)r^{(\sqrt{\alpha}-1)}-c_6(r_0)(1-\upsilon_c)r^{(-\sqrt{\alpha}-1)}\right] \tag{3.33b}$$

There are six unknowns in Eqs. 3.22 and 3.33 for stresses, i.e., $c_3(r_0)$, $c_4(r_0)$, $c_5(r_0)$, $c_6(r_0)$, r_0 and α. There are two boundary conditions for the concrete cylinder, i.e.,

$$\sigma_r(b)=(1+\upsilon_c)c_3(r_0)-\frac{(1-\upsilon_c)c_4(r_0)}{b^2}=0 \tag{3.34a}$$

$$u(a)=c_5(r_0)a^{\sqrt{\alpha}}+c_6(r_0)a^{-\sqrt{\alpha}}=d_c(t)+d_p \tag{3.34b}$$

and two continuity requirement for the displacement and radial strain at r_0, i.e.,

$$c_3(r_0)r_0+\frac{c_4(r_0)}{r_0}=c_5(r_0)r_0^{\sqrt{\alpha}}+c_6(r_0)r_0^{-\sqrt{\alpha}} \tag{3.35a}$$

$$(1+\upsilon_c)c_3(r_0)-\frac{(1-\upsilon_c)c_4(r_0)}{r_0^2}=\sqrt{\alpha}(1+\upsilon_c)r_0^{(\sqrt{\alpha}-1)}c_5(r_0)-\sqrt{\alpha}(1-\upsilon_c)r_0^{(-\sqrt{\alpha}-1)}c_6(r_0) \tag{3.35b}$$

Two more equations can be derived as follows. Since the tip of the crack is at r_0, the cracking condition requires that (i.e., Eq. 3.22a)

$$\frac{E_{ef}}{1-\upsilon_c^2}\left[(1+\upsilon_c)c_3(r_0)+\frac{(1-\upsilon_c)c_4(r_0)}{r_0^2}\right]=f_t \tag{3.36}$$

Also in Eq. 3.26, the average crack width can be expressed approximately as

$$\overline{w}=2\pi\frac{a+r_0}{2}(\overline{\varepsilon_\theta}-\overline{\varepsilon_\theta^{e,m}}) \tag{3.37}$$

where $\overline{\varepsilon_\theta}$ is the average residual tangential strain of cracked concrete over $[a, r_0]$ and $\overline{\varepsilon_\theta^{e,m}}$ is the average maximum elastic tangential strain of concrete over $[a, r_0]$ which can be obtained as follows

$$\overline{\varepsilon_\theta^{e,m}}=\frac{1}{r_0-a}\int_a^{r_0}\left(\frac{u(r_0)}{r_0}\right)d\xi=\frac{1}{r_0-a}\int_a^{r_0}\left(c_3(\xi)+\frac{c_4(\xi)}{\xi^2}\right)d\xi \tag{3.38}$$

Likewise, the average tangential strain of cracked concrete can be obtained as follows

$$\begin{aligned}\overline{\varepsilon_\theta}&=\frac{1}{r_0-a}\int_a^{r_0}\left(c_5(r_0)\xi^{(\sqrt{\alpha}-1)}+c_6(r_0)\xi^{(-\sqrt{\alpha}-1)}\right)d\xi\\&=\frac{(r_0^{\sqrt{\alpha}}-a^{\sqrt{\alpha}})[c_5(r_0)+c_6(r_0)/(ar_0)^{\sqrt{\alpha}}]}{\sqrt{\alpha}(r_0-a)}\end{aligned} \tag{3.39}$$

Substitution of Eqs. 3.38 and 3.39 into Eq. 3.27 results in

$$\alpha=\frac{f_t\exp\left\{-\frac{\pi f_t(a+r_0)}{G_f}\left[\frac{\left(r_0^{\sqrt{\alpha}}-a^{\sqrt{\alpha}}\right)\left[c_5(r_0)+c_6(r_0)/(ar_0)^{\sqrt{\alpha}}\right]}{\sqrt{\alpha}(r_0-a)}-\frac{1}{r_0-a}\int_a^{r_0}\left(c_3(\zeta)+\frac{c_4(\zeta)}{\zeta^2}\right)d\zeta\right]\right\}}{\frac{E_{ef}\left(r_0^{\sqrt{\alpha}}-a^{\sqrt{\alpha}}\right)\left[c_5(r_0)+c_6(r_0)/(ar_0)^{\sqrt{\alpha}}\right]}{\sqrt{\alpha}(r_0-a)}} \tag{3.40}$$

By simultaneously solving Eqs. 3.34 to 3.36 and 3.40, all six unknown

coefficients, i.e., $c_3(r_0)$, $c_4(r_0)$, $c_5(r_0)$, $c_6(r_0)$, r_0 and α can be determined and accordingly stress distributions in the concrete cylinder. A computer program has been developed for all computations.

3.4.2 Derivation of surface crack width

Eventually, the crack will penetrate to the surface of the concrete cylinder, indicating that the cylinder is completely cracked. In this case, Eq. 3.31 is the governing equation for radial displacement *u(r)* in the concrete cylinder but the solution should be different since the boundary conditions have been changed. Thus, the solution to Eq. 3.31 can be expressed as follows (James 1993)

$$u(r) = c_7 r^{\sqrt{\alpha}} + c_8 r^{-\sqrt{\alpha}} \tag{3.41}$$

where c_7 and c_8 are the coefficients to be determined. The boundary conditions require that

$$c_7(1+\upsilon_c)b^{(\sqrt{\alpha}-1)} - c_8(1-\upsilon_c)b^{(-\sqrt{\alpha}-1)} = 0 \tag{3.42}$$

$$c_7 a^{\sqrt{\alpha}} + c_8 a^{-\sqrt{\alpha}} = d_c(t) + d_p \tag{3.43}$$

Re-arranging Eqs. 3.42 and 3.43 by c_7 and c_8 leads to

$$c_7 = \frac{(1-\upsilon_c)a^{\sqrt{\alpha}}}{(1-\upsilon_c)a^{2\sqrt{\alpha}} + (1+\upsilon_c)b^{2\sqrt{\alpha}}}\left(d_c(t) + d_p\right) \tag{3.44a}$$

$$c_8 = \frac{(1+\upsilon_c)a^{\sqrt{\alpha}}b^{2\sqrt{\alpha}}}{(1-\upsilon_c)a^{2\sqrt{\alpha}} + (1+\upsilon_c)b^{2\sqrt{\alpha}}}\left(d_c(t) + d_p\right) \tag{3.44b}$$

The corresponding average residual tangential strain of cracked concrete $\overline{\varepsilon_\theta}$ can be obtained from Eqs. 3.15a and 3.41 as follows

$$\overline{\varepsilon_\theta} = \frac{1}{b-a}\int_a^b (c_7 r^{(\sqrt{\alpha}-1)} + c_8 r^{(-\sqrt{\alpha}-1)})dr = \frac{(b^{\sqrt{\alpha}} - a^{\sqrt{\alpha}})[c_7 + c_8/(ab)^{\sqrt{\alpha}}]}{\sqrt{\alpha}(b-a)} \tag{3.45}$$

Hence the stiffness reduction factor α becomes

$$\alpha = \frac{f_t \exp\left\{-\frac{\pi f_t (a+b)}{G_f}\left[\frac{\left(b^{\sqrt{\alpha}} - a^{\sqrt{\alpha}}\right)\left[c_7 + c_8/(ab)^{\sqrt{\alpha}}\right]}{\sqrt{\alpha}(b-a)} - \frac{1}{b-a}\int_a^b \left(c_3(\zeta) + \frac{c_4(\zeta)}{\zeta^2}\right)d\zeta\right]\right\}}{\frac{E_{ef}\left(b^{\sqrt{\alpha}} - a^{\sqrt{\alpha}}\right)\left[c_7 + c_8/(ab)^{\sqrt{\alpha}}\right]}{\sqrt{\alpha}(b-a)}} \tag{3.46}$$

By solving Eqs. 3.44a, b and 3.46 simultaneously, c_7, c_8 and α can be obtained. Accordingly, the stress distributions, i.e., $\sigma_r(r,t)$ and $\sigma_\theta(r,t)$ as a function of time at any point (r) in the concrete cylinder, can be determined. Again by assigning $\sigma_\theta(b,t) = f_t$, the surface cracking time t_2 can also be obtained.

Also the tangential strain of concrete at $r = b$, i.e., $\varepsilon_\theta(b)$ can be determined from Eqs. 3.15a and 3.41. Evidently, the crack width on the surface of the concrete cylinder should be

$$w_c = 2\pi b[\varepsilon_\theta(b) - \varepsilon_\theta^{e,m}(b)] \tag{3.47}$$

where $\varepsilon_\theta^{e,m}(b)$ is the maximum elastic strain of concrete at $r = b$ and equal to (Timoshenko and Goodier 1970)

$$\varepsilon_\theta^{e,m}(b) = \frac{f_t - \upsilon_c \sigma_r(b)}{E_{ef}} \tag{3.48}$$

Since $\sigma_r(b) = 0$, the crack width w_c is finally derived as follows

$$w_c = 2\pi b\left[c_7 b^{(\sqrt{\alpha}-1)} + c_8 b^{(-\sqrt{\alpha}-1)} - \frac{f_t}{E_{ef}} \right]$$

$$= \frac{4\pi d_c(t)}{(1-\upsilon_c)(a/b)^{\sqrt{\alpha}} + (1+\upsilon_c)(b/a)^{\sqrt{\alpha}}} + \frac{4\pi a\left[(1+\upsilon_c)b^2 + (1-\upsilon_c)a^2 \right] P_2}{(b^2-a^2)\left[(1-\upsilon_c)(a/b)^{\sqrt{\alpha}} + (1+\upsilon_c)(b/a)^{\sqrt{\alpha}} \right] E_{ef}} - \frac{2\pi b f_t}{E_{ef}}$$

(3.49)

As can be seen the crack width is directly related to corrosion effect ($d_c(t)$ or i_{corr}), the applied load (P_2), the stiffness reduction factor (α), concrete property (f_t, E_{ef}, υ_c) and geometry (*a, b* or *C, D*). Obviously, with the accumulation of corrosion products, i.e. $d_c(t)$, the crack width increases with time. This makes sense both theoretically as shown in Eq. 3.49 and practically as experienced and observed (Andrade *et al.* 1993; Liu and Weyers 1998). It needs to be noted that, due to the random nature of crack occurrence, there may be more than one crack occurring either simultaneously or within a short period of time. In this case, the assumption is that the crack width of all cracks is equal (Molina *et al.* 1993). Thus Eq. 3.49 is still applicable but w_c should be divided equally by the number of cracks. In any event, Eq. 3.49 represents the maximum crack width on the surface of the concrete cylinder, which is conservative in structural assessment.

If the concrete cylinder is partially cracked at the beginning, the initial cracking time is zero, i.e., $t_1 = 0$. This can be checked with Eq. 3.19. In this case the stress analysis starts from the partially cracked concrete cylinder, i.e., Eq. 3.21 which will be illustrated in the worked example to follow.

3.5 Worked examples

Although crack width is analytically derived in Eq. 3.49, the calculation itself is very computationally involved. In this section, an algorithm is developed for all the calculations. A programme written in MatLab is also developed to execute

all the computations and display the results graphically as presented in the example. The computational procedure is shown in Fig. 3-7.

To demonstrate the application of the developed method for crack width, i.e., Eq. 3.49, a numerical example is undertaken on a reinforced concrete beam originally investigated in Li (2003). This beam is taken because it underwent a comprehensive test under the simultaneously corrosion and applied load and hence can provide realistic values of corrosion rate and other related parameters, although the objective of the test was to determine corrosion induced structural strength deterioration. The values of the basic variables of the structure and corrosion are shown in Table 3-2. To investigate both scenarios of the concrete cylinder cracking under the applied load only at the beginning ($t = 0$), i.e., "not cracked" and "partially cracked", two uniformly distributed loads of 40 KN/m and 80 KN/m are considered.

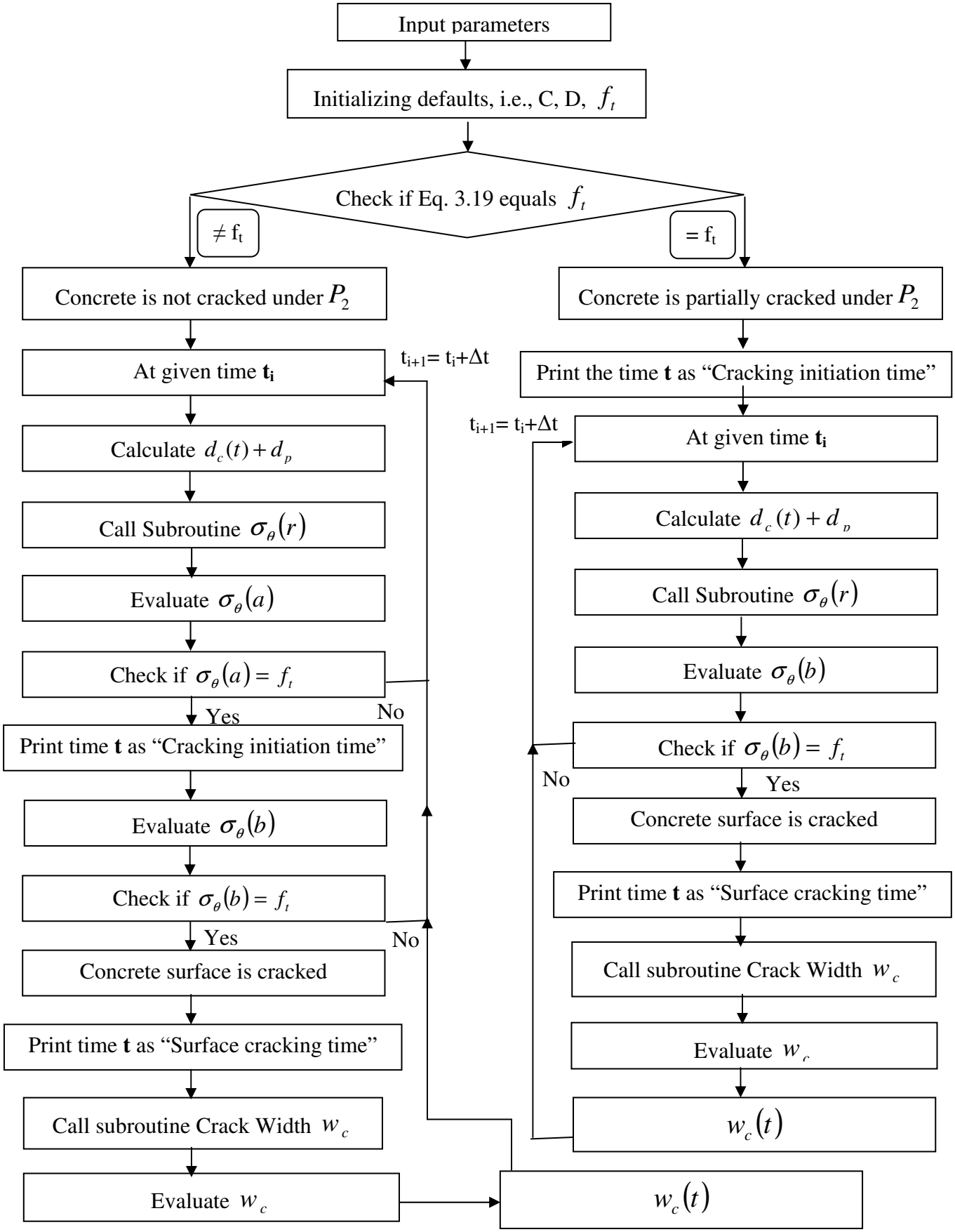

Figure 3-7 Flow chart for computation of concrete crack width

Table 3-2 Values of basic variables used in cracking computation

Symbol	Values	Sources
G_f	0.088 N/mm	Pantazopoulou and Papoulia (2001)
h_0	163 mm	Li (2003)
f_y	400 MPa	Li (2003)
b_1	120 mm	Li (2003)
C	31 mm	Li (2003)
D	12 mm	Li (2003)
d_0	12.5 μm	Liu and Weyers (1998)
E_{ef}	18.82 GPa	Li (2003)
f_t	5.725 MPa	Li (2003)
i_{corr}	$0.3686Ln(t)+1.1305$ μA/cm^2	Li (2003)
α_{rust}	0.57	Liu and Weyers (1998)
ν_c	0.18	Liu and Weyers (1998)
ρ_{rust}	3600 kg/m^3	Liu and Weyers (1998)
ρ_{st}	7850 kg/m^3	Liu and Weyers (1998)

With these values of basic variables, the crack width on the surface of concrete, the expansive pressure and the tangential stiffness reduction factor can be determined using Eqs. 3.49, 3.1 and 3.40 or 3.46 respectively. The results are shown in Figs. 3-8 to 3-10, where "1st Scenario" is for concrete "not cracked" at the beginning of applied load and "2nd Scenario" is for concrete "partially cracked" at the beginning of applied load.

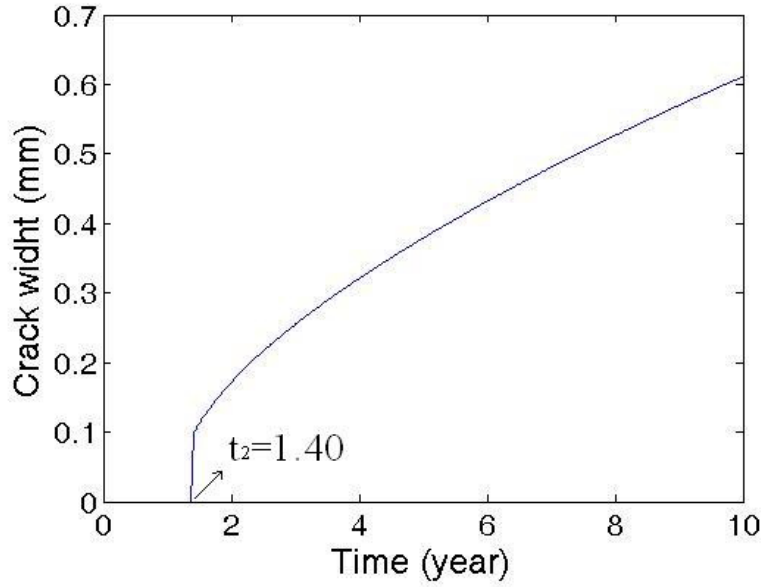

Figure 3-8a Crack width as a function of time for the 1st scenario

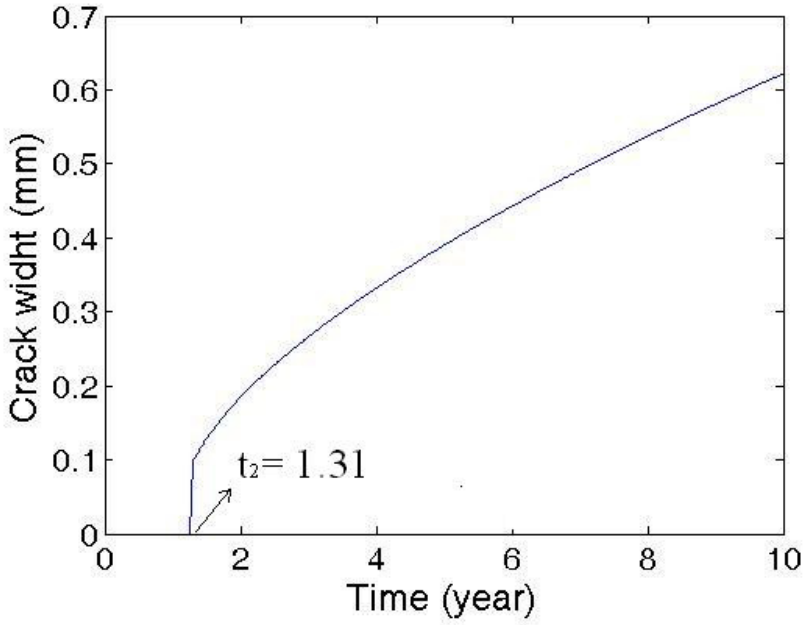

Figure 3-8b Crack width as function of time for the 2nd scenario

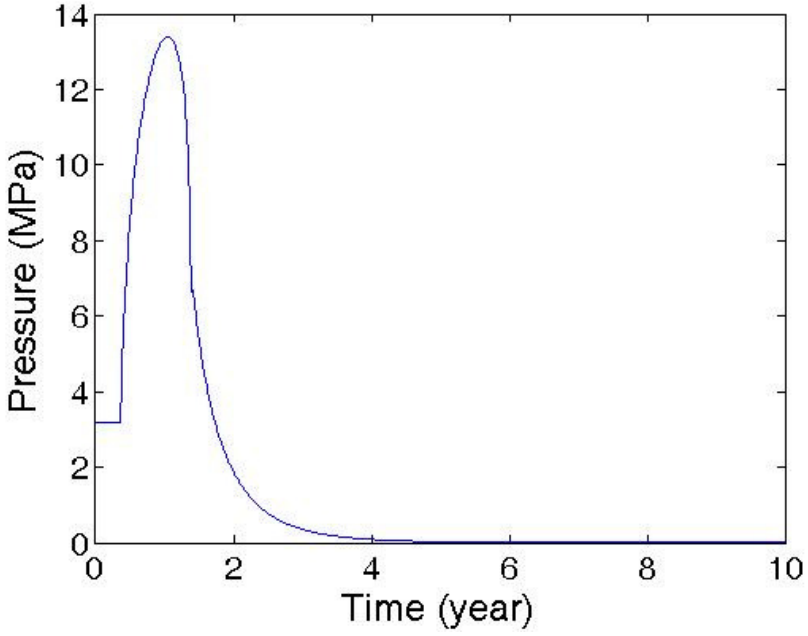

Figure 3-9a Expansive pressure as function of time for the 1st scenario

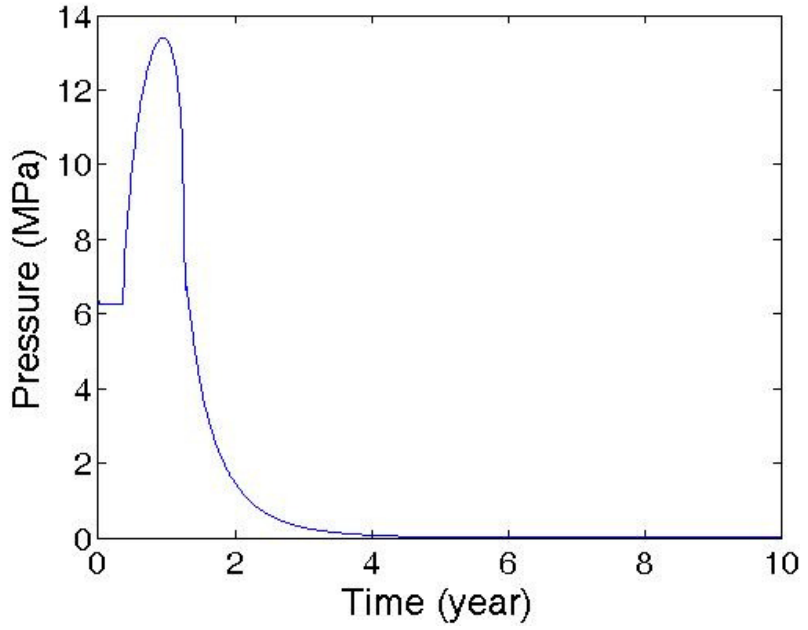

Figure 3-9b Expansive pressure as function of time for the 2nd scenario

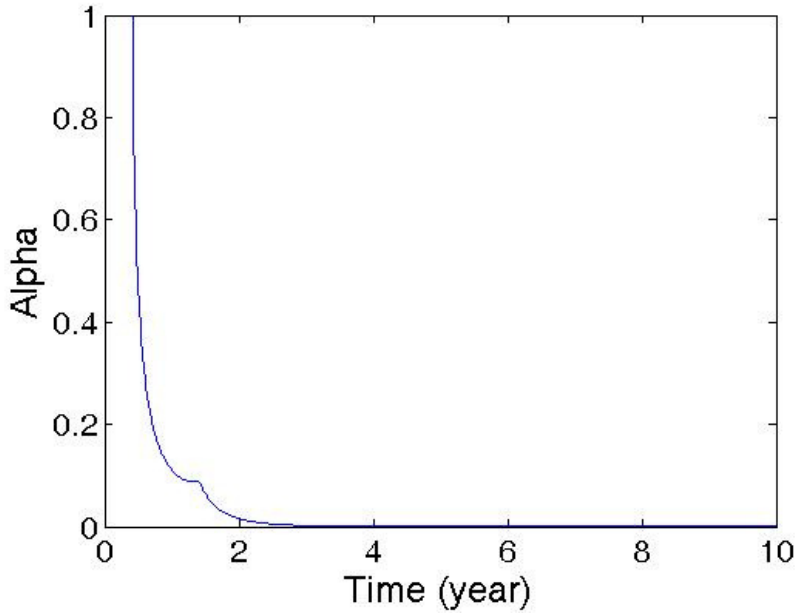

Figure 3-10a Tangential stiffness reduction factor α for the 1st scenario

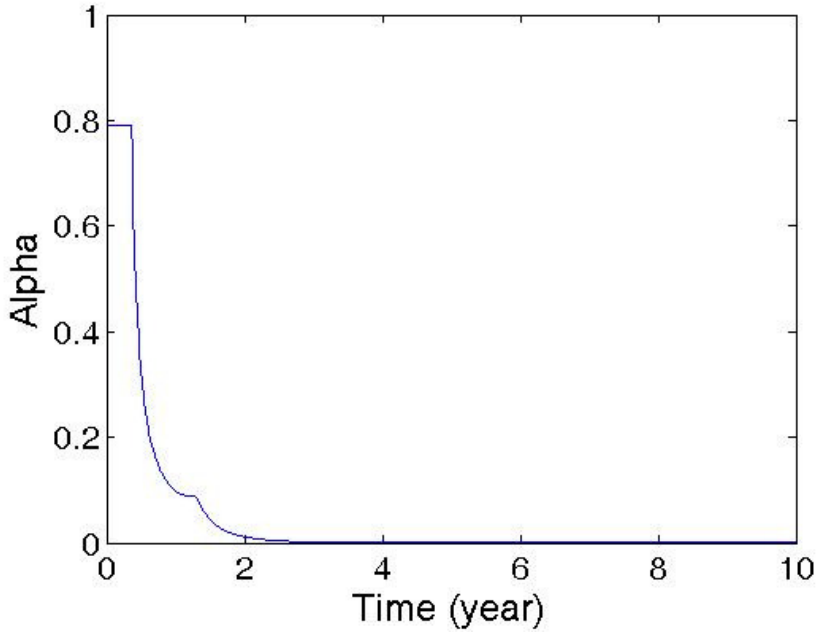

Figure 3-10b Tangential stiffness reduction factor α for the 2nd scenario

As can be seen from Fig. 3-8 the crack width increases with time as expected. At the time that the concrete cylinder is completely cracked, i.e., at time t_2, there is an abrupt increase in crack width, which vindicates the assumption of quasi-brittle concrete. The surface cracking times t_2 are 1.40 year and 1.31 year for 1st and 2nd scenarios respectively. Of particular interest here is that there are

corresponding sudden reduction of both the expansive pressure (P) and the tangential stiffness reduction factor (α) as shown in Figs. 3-9 and 3-10. This indicates the consistency in deriving the crack width based on both isotropic, elastic concrete (i.e., elastic mechanics) and anisotropic, quasi-brittle concrete (i.e., fracture mechanics). In Figs. 3-8 to 3-10, when the applied load is 40 KN/m the initial pressure at $t = 0$ is 3.2 MPa (first scenario) whilst at 80 KN/m (second scenario) it is 6.2 MPa which causes initial cracking in concrete at $t = 0$. In addition the tangential stiffness reduction factor $\alpha = 1$ in the first scenario at $t = 0$ since there is no cracking in concrete whilst in the second scenario the factor drops to about 0.8 since the concrete is cracked $t = 0$. Also noted in Fig 3-8b is that in the second scenario, the crack appears earlier and develops faster which is again expected due to the greater pressure.

3.6 Refinement of the analytical method

In this section, the developed method is further evaluated for the stress deterioration which is characterised by stiffness reduction factor α. The stress-strain curve or the stress-time curve displays a bump during the strain softening phase. This is found to be purely caused by the assumption of α, which is taken as constant along the cracked surface in radial direction. Since α was assumed to be independent of the radius r for a feasible analytical solution as discussed in Section 3.4.1, the real form of α needs to be modified in other means, i.e., experimental results. Direct tensile tests have been carried out to provide evidence for the modification.

3.6.1 Analysis and discussions

Based on the α in Fig. 3-10 in the worked example, the complete tensile stress-tensile strain curve can be obtained which varies at different points of the cylinder. Fig. 3-11 shows the tangential stress at $r = a$ as a function of the tangential strain and time for the 1st scenario.

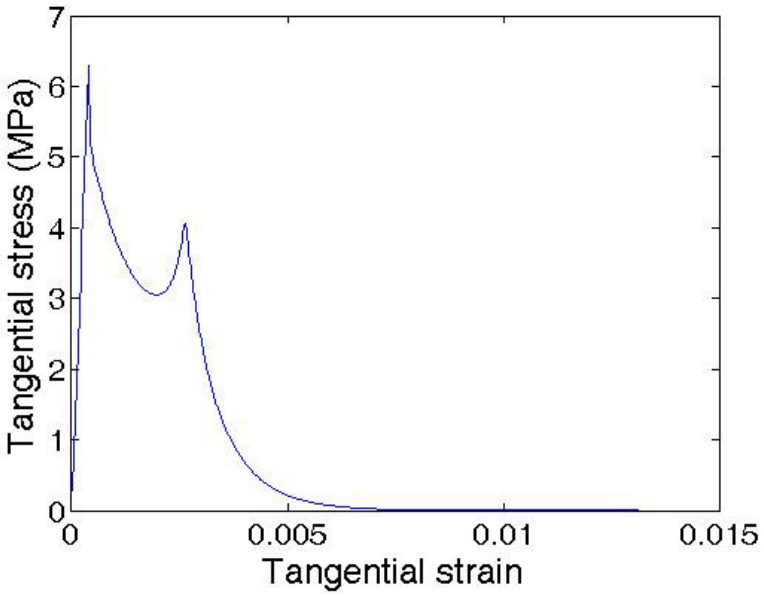

(a) Tangential stress in a function of tangential strain

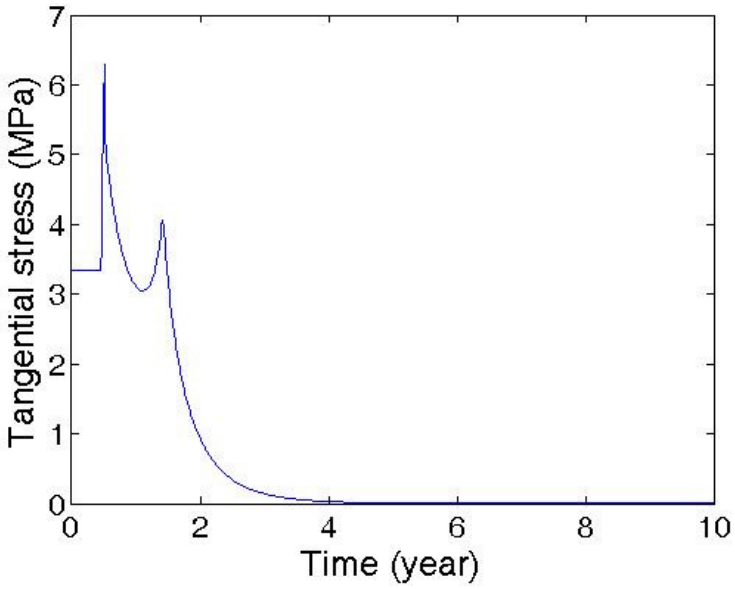

(b) Tangential stress in a function of time

Figure 3-11 Tangential stress at the point of inner boundary ($r = a$)

From the direct tensile tests carried out as part of this research (to be presented in Chapter 5) and the literature, the tensile stress should increase almost linearly to the peak stress and then decrease monotonically towards zero, with the increase of tensile strain. In the Fig. 3-11, however, there is an unexpected phase of stress increase during the descending regime. This stress increase is

induced by the assumption of α, since α is defined to be constant along the cracked surface and is calculated from the average strains along the cracked surface in radial direction. When crack propagates outwards, therefore, the α will less and less reflect the real reduction in stiffness of the element at the point $r = a$. For instance, prior to 1.11 year, the tensile stress decreases with the increase of the tensile strain and the influence of the variation of α is minor. However, after 1.11 year until 1.42 year when the crack reaches the surface, the influence of such a variation on the stress at the point $r = a$ is not minor which is the reason of the stress increase (stress stiffening) at the strain softening stage.

Similar phenomenon is also observed when plotting the tangential stress-strain and tangential stress-time relations for the point at middle position ($r = 0.021m$) as shown in Fig. 3.12. It can be seen that the tangential stress increases linearly until the tensile strength (5.725MPa) at 1.14 years. After that, the tangential stress experiences sudden drop (from 1.14 to 1.15 years), slight increase (from 1.15 to 1.42 years) and finally steadily decrease until completely failure. The sudden decrease at 1.14 years in the tangential stress is induced by α which is 0.0995. It is, therefore, the abrupt decrease in residual modulus of elasticity that causes this immediate large drop of tangential stress.

In order to identify the region of α in relation to time which causes the stress stiffening problem, more points in the cylinder are selected to obtain their tangential stresses and strains for further analysis. It has been found that, although the initiation times of the stress stiffening vary at different positions, the end times of the stress stiffening are all the same – 1.42 years. This is shortly after the surface cracking which takes place at 1.40 years. The reason will be explained in the next page. As for the initiation of the stress stiffening, the earliest time within these different positions is 0.92 year and the position is at $r = 0.012m$. Therefore, from 0.92 year to 1.42 year, the values of α influence the stress stiffening most as illustrated in Figure 3-13.

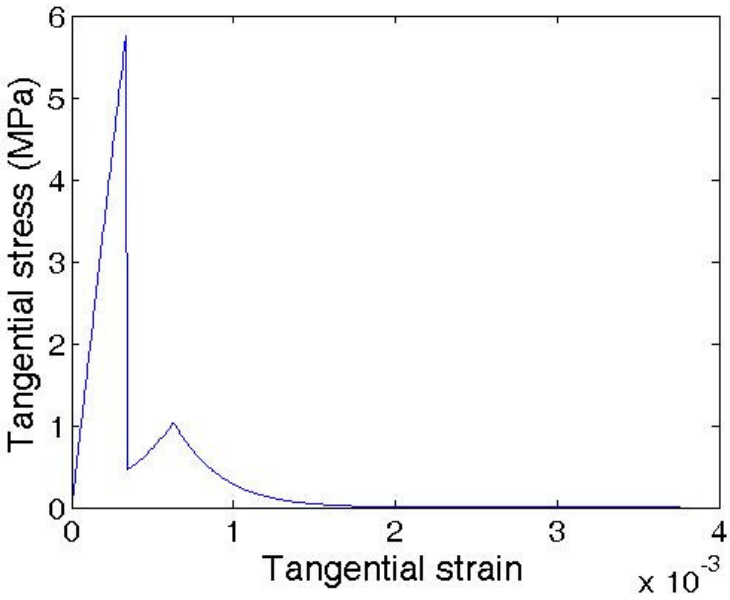

(a) Tangential stress as a function of tangential strain

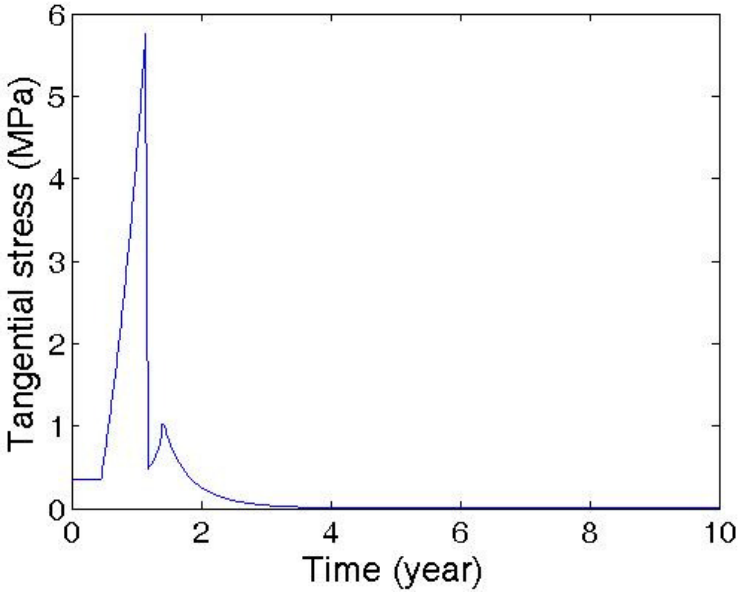

(b) Tangential stress as a function of time

Figure 3-12 Tangential stress of the point at middle position

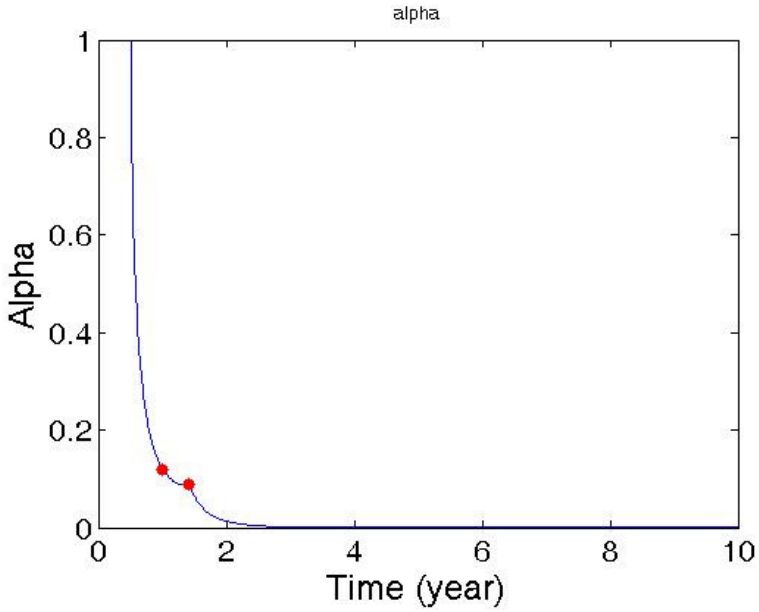

Figure 3-13 The region of α causing the stress stiffening

To quantitatively explain the reason why such values of α make the tangential stress increasing on the strain softening phase, a point in the middle of the cylinder is taken as an example. The tangential stress of a point of cracked concrete can be expressed as a function of tangential strain and radial strain under anisotropic condition as follows:

$$\sigma_\theta = \frac{\alpha E_{ef}}{1-\upsilon_c^{\,2}}\left(\varepsilon_\theta - \frac{\upsilon_c}{\sqrt{\alpha}}\varepsilon_r\right) \tag{3.50}$$

For simplicity the Poisson's effect is neglected with very minor difference in result and the above expression becomes

$$\sigma_\theta = \frac{E_{ef}}{1-\upsilon_c^{\,2}}\alpha\varepsilon_\theta \tag{3.51}$$

Table 3-3 Values of basic variables for the point at $r = 0.021m$

Time (year)	1.15	1.16	1.17	1.18
α	0.0995	0.0984	0.0973	0.0963
$\sigma_\theta\,(MPa)$	0.4624	0.4698	0.4775	0.4856
$\varepsilon_\theta\,(\times 1\text{e-}4)$	3.412	3.479	3.548	3.618

In Eq. 3.51, only α and ε_θ are variables. From 1.15 years to 1.16 years, for instance, tangential strain increases 0.0196 times while α reduces 0.011 times. It means that after the abrupt drop of the tangential stress, the increase in strain is too rapid compared to the degradation of the modulus of elasticity. It also means that the modulus of elasticity supposes to be degraded more for the given strain to actually reflect the strain softening behaviour of concrete rather than stress stiffening of ductile materials, i.e. metal.

It has been identified that the region of α as highlighted in Fig. 3-13 induces the unexpected stress stiffening during strain softening stage. It has also been explained that it is due to the change rates of these values of α with respect to time are too small. Since α is calculated on average along the cracked surface, the reduction in the modulus of Elasticity at the inner boundary compensates for that at the newly cracked point. This is, intrinsically, why there is a range of α causing stress stiffening problem. This analysis will help understand the reason that a bump phenomenon occurs at the strain softening stage of concrete, which is a very common problem during either analytical or numerical modelling of concrete cracking. The bump phenomenon in the numerical model will be discussed separately in next chapter.

3.6.2 Modification of the analytical method

Based on the analysis in preceding section, some modifications to the stiffness reduction factor α are proposed herein so that the assumption of constant α which causes the bump phenomenon in the stress-strain relation can be eliminated. Direct tensile tests are carried out to provide evidence/verification for such modifications. Details of the tests are presented in Chapter 5. Fig. 3-14 shows the relation of the tensile stress σ_t and average displacement δ_a of the three transducers across the crack. As the measure length of the transducers L is fixed, the tensile strain across the crack can be determined as follows

$$\varepsilon_t = \delta_a / L \tag{3.52}$$

If α is also defined in the direct tensile test to account for the reduction of the tensile stress, it can be expressed as follows:

$$\alpha = \frac{\sigma_t}{K_p \delta_a} \tag{3.53}$$

where K_p is the penalty stiffness shown in Fig. 3-14.

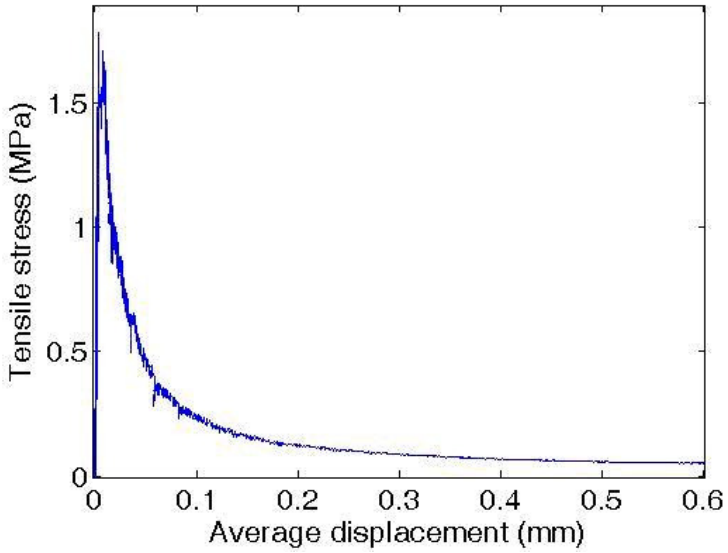

Figure 3-14 Stress-displacement relation from direct tensile tests

With Eqs. 3.52 and 3.53, Fig. 3-14 can be reformulated in terms of α and ε_t as in Fig. 3-15a.

The shapes of the $\alpha - \varepsilon_t$ curves can be compared between those by the analytical method and the direct tensile tests. The difference of the shapes is that there is a "kink" point in the curve from the analytical method while it is smooth in the one from the direct tensile tests. This "kink" point and its convex correspond to the region of α shown in Fig. 3-13.

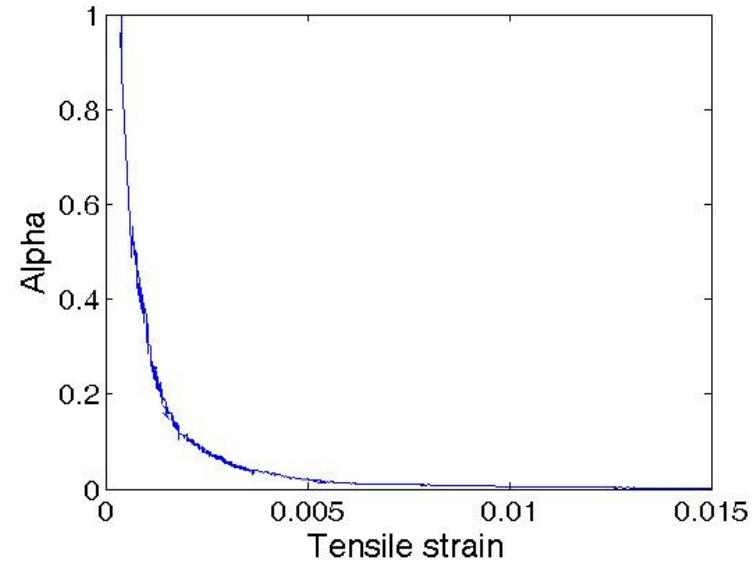

(a) Alpha as a function of tensile strain from direct tensile tests

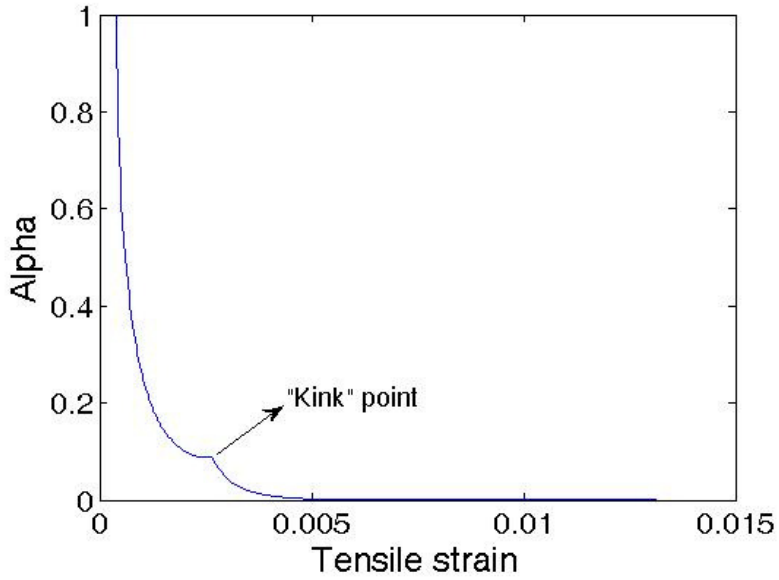

(b) α as a function of tensile strain from analytical method

Figure 3-15 Relation between α and tensile strain for both direct tensile tests and analytical method

However, there are also differences in $\alpha - \varepsilon_t$ curve in Fig. 3-15. The first one is that the $\alpha - \varepsilon_t$ curve from the direct tensile tests is obtained under uniaxial tension but the one from the analytical method is determined under biaxial loading condition. This difference is considered to be small since the effect of

Poisson's ratio is regarded as minor. The other one is that the $\alpha - \varepsilon_t$ curves may not exactly correspond to each other although the shape should be close. This is because both curves are determined by the tensile strength $f_t^{'}$ and the fracture energy G_f. For example, the area under the curve is dependent on G_f. Since these two variables are not identical for those two cases, the values on the curves do not correspond although they might be close.

Based on the range of α that causes tension stiffening as specified in Fig. 3-13 and the experimental evidence that demonstrates the difference in $\alpha - \varepsilon_t$ curve as shown in Fig. 3-15, the $\alpha - t$ curve can be modified and plotted in Fig. 3-16. The curve in red colour is the modified α with the black curve representing the original α. It can be seen from Fig. 3-16 that the two curves are identical for most parts, except a small region from about 0.9 year to about 1.7 years. In this region, α is smoothly decreased and the "kink" point is eliminated which is more realistic as shown from lab tests. With this modification, the effect of assumption of α which is independent of the radius can be compensated.

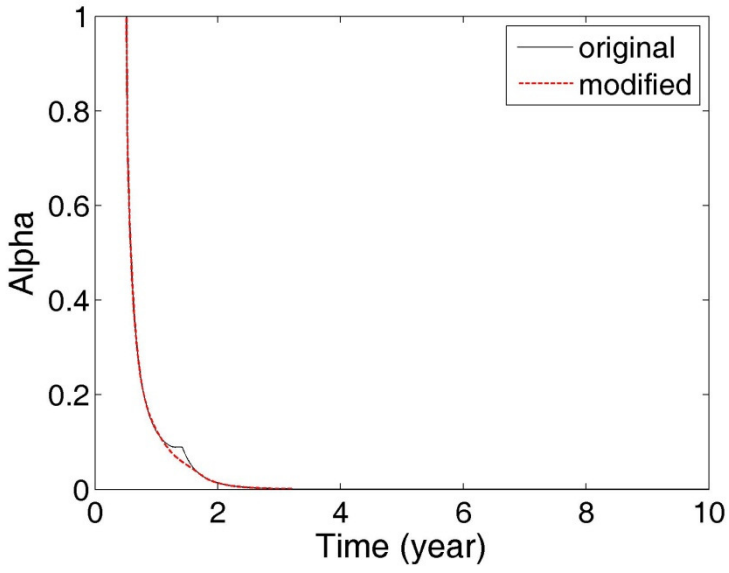

Figure 3-16 Original and modified alpha as a function of time

Based on the improved stiffness reduction parameter α, the tangential stress at $r = a$ is plotted as a function of time and shown in Fig. 3-17, in which the

original α is plotted as well. It can be observed that the tangential stress degradation with the improved α is more reasonable and the stress stiffening problem has mostly been resolved. In addition, the expansive pressure at the inner boundary of the concrete cylinder and the surface crack width, both as a function of time, are calculated with the modified α and shown in Fig. 3-18 and 3-19 respectively.

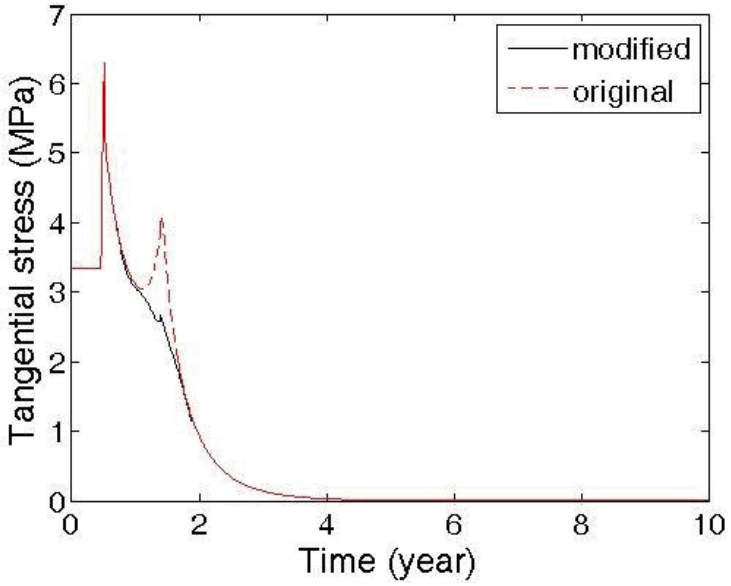

Figure 3-17 Tangential stress as a function of time at $r = \alpha$ (modified and original)

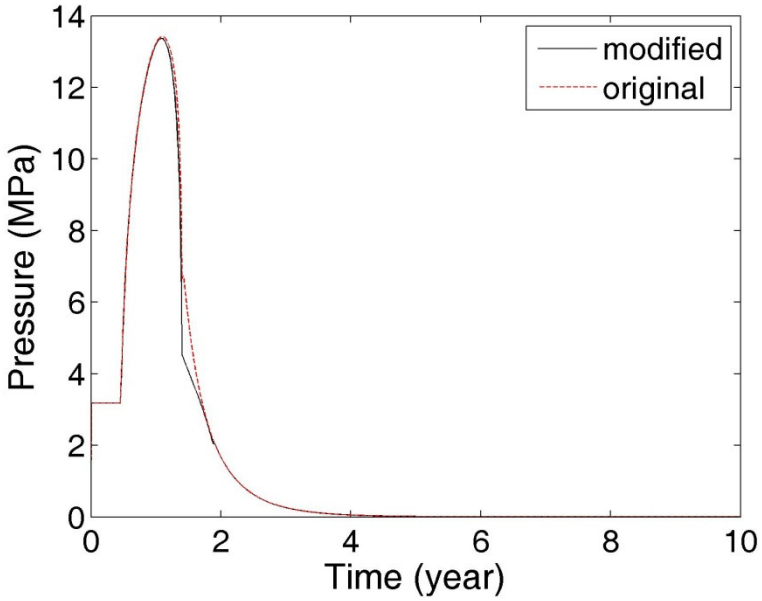

Figure 3-18 Expansive pressure as a function of time for 1st scenario (modified and original)

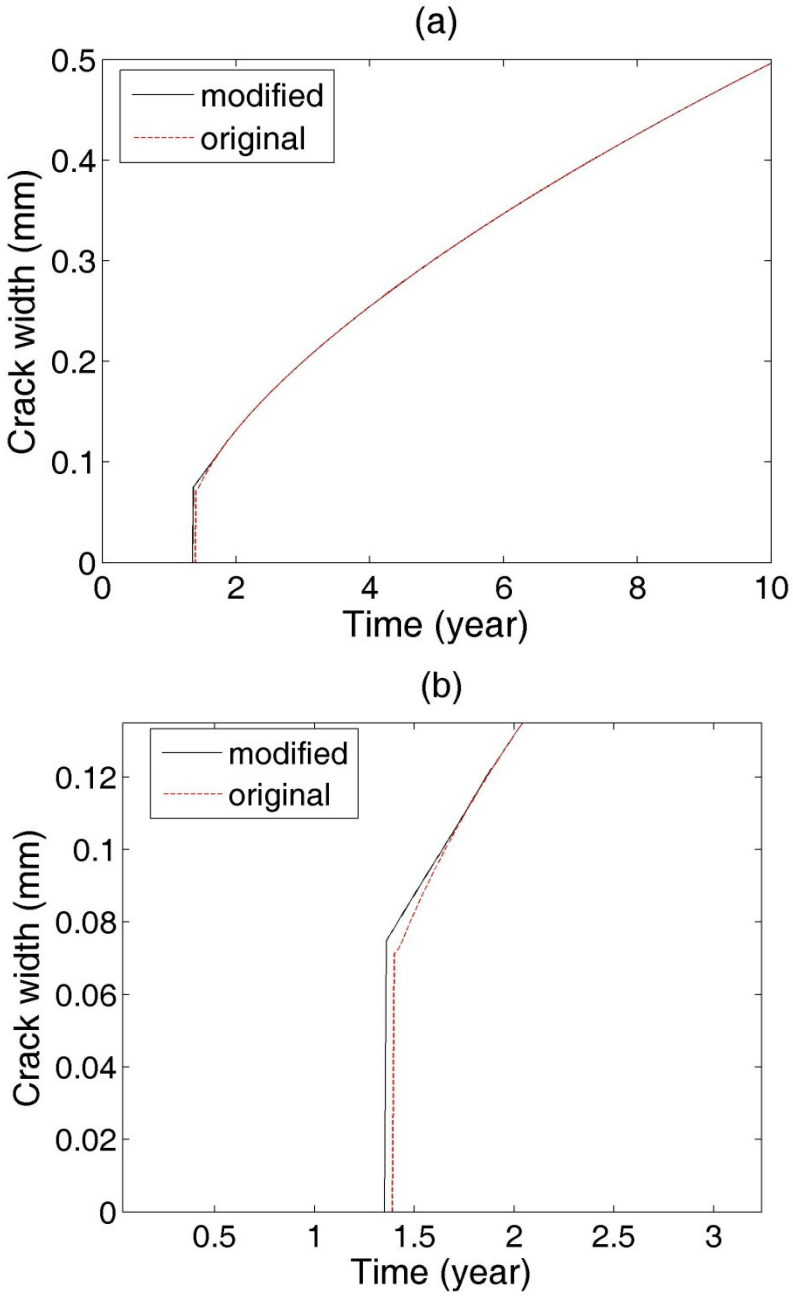

Figure 3-19 Crack width as function of time for 1st scenario (modified and original)

Fig. 3-19a shows the crack width as a function of time from both the original and modified α. Fig. 3-19b illustrates the details of both curves around their surface cracking times. It has been seen from the figures that although the modified α curve well represents the energy release after peak stress and thus significantly improved the stress degradation during the strain softening stage, its overall influence on the crack width is not significant. This is due to the fact

that only a small area under α curve is amended and the magnitude of the change is small. Nevertheless, the modified α does affect the surface cracking time and the crack width at the surface cracking time, i.e., the surface cracking is advanced from 1.40 year to 1.36 year. In addition, the crack width is increased from 0.07mm to 0.075mm as shown in Fig. 3-19b. This is because the value of the modified α is smaller than each of the original values, which means that when the surface is just cracked, the reduction in tangential stress is more and therefore the increase in the tangential strain is more. As shown in Eq. 3.47, the surface crack width depends on the tangential strain $\varepsilon_\theta(b)$ and maximum elastic tangential strain $\varepsilon_\theta^{e,m}(b)$. Since $\varepsilon_\theta^{e,m}(b)$ is the same for both cases, more increase in $\varepsilon_\theta(b)$ with the modified α at the surface cracking time results in more increase in the crack width. Since this modified values of α are around the surface cracking time, smaller values of α lead to less energy required to break the concrete and thus earlier surface cracking time.

3.7 Conclusions

An analytical method to determine the crack width on the surface of reinforced concrete structures under the combined effects of reinforcement corrosion and applied load has been developed in this chapter. In the analysis of stress distributions in cracked concrete, a stiffness reduction factor has been proposed and analytically derived based on the concept of fracture energy. The assumption of a constant reduction factor along the cracked surface in radial direction has been evaluated in terms of the stress-strain relationship. The model of α has then been refined based on experimental evidence. Such a refinement has been proven by reasonable stress-strain relationship produced after the refinement. It can be concluded that the method developed in the study is one of very few theoretical methods that can predict with reasonable accuracy the crack width of reinforced concrete under the combined effects of reinforcement corrosion and applied load. Therefore it can serve as a useful tool for engineers and asset managers in decision-making with regard to the serviceability of corrosion affected concrete infrastructure in operation.

CHAPTER 4

DEVELOPMENT OF NUMERICAL METHOD

4.1 Introduction

Realising the difficulties in developing analytical methods, various attempts have been made to predict concrete cracking based on numerical tools, e.g., Finite Element (FE) software and using facture mechanics (e.g., Hanson and Ingraffea, 2003, Guo *et al.*, 1999, Roesler *et al.*, 2007, Qiao and Chen, 2008). DIANA is a general purpose FE software exclusively designed for analysis of concrete structures. Effects of crack are implemented into its material model by smeared crack approach and facture energy concept. ANSYS is another FE code which is based on smeared crack approach in the modelling of concrete cracking problems. The presence of a crack at an integration point is represented through modification of the stress-strain relation. For plain concrete, the results obtained by using strain softening relation will introduce severe problem of mesh sensitivity. FRANC is a fracture analysis code which treats the crack in a discrete manner. It has interface element to represent the crack and both LEFM and nonlinear fracture models can be applied. This software is designated to simulate static crack propagation which involves user interaction. In this research, ABAQUS is chosen to simulate the cracking of concrete mainly because of two reasons: (1) the implemented cohesive crack model and, (2) excellent solver of nonlinear FEA.

Of considerable research on concrete fracture, most numerical studies concentrate on concrete cracking due to external bending, e.g., beams rather than internal pressure, e.g., corrosion expansion. The full stress-strain/displacement relationship of concrete used in numerical studies, including that after concrete cracking, is obtained from tests of concrete beams with notches in the middle (Qiao and Chen, 2008). For example, Roesler *et al.* (2007) developed a finite element (FE) method based on cohesive crack model to predict the relationship of load and crack mouth opening displacement of concrete beams. A series of tests on geometrically similar beams were carried out to obtain the stress-strain/displacement relationship of concrete. Also Barpi and Valente (2005) simulated the crack propagation in a concrete dam based on FEA and cohesive crack model. As shown in the research literature, little research has been undertaken on numerical modelling of concrete cracking due

to internal pressure such as corrosion induced expansion and almost none on concrete crack width. Given the difficulties in analytical methods and the significant advances in FE techniques, it is well justified that a numerical method be developed to predict corrosion induced concrete crack width over time. Moreover, for accurate numerical analysis, actual material properties of concrete, in particular, the complete tensile stress-strain/displacement relationship, need to be used in the analysis which can only be obtained from accurate experiments, i.e., direct tension tests of concrete rather than on bending tests and splitting tests as most studies did hitherto.

This chapter attempts to develop a numerical method to predict the cracking and crack width for corrosion affected concrete structures under the combined action of corrosion and applied load. Fracture mechanics and finite element techniques are employed in the method. A cohesive crack model for concrete is presented and a finite element model is proposed. A procedure is developed to apply the time-dependent displacement at the inner boundary. Typical numerical problems in nonlinear analysis of concrete cracking, i.e., material nonlinearity, are investigated. An example is then presented to demonstrate the application of the method.

4.2 Cohesive Crack Model

The failure of structures is significantly influenced by the properties of the material used. In terms of tensile stress-elongation relationship, most of engineering materials can be classified into brittle, ductile and quasi-brittle (Shah *et al.,* 1995), which have been reviewed in Section 2.4.1. Different materials used will result in different failure mechanisms of structures and hence different material models should be applied correspondingly. For example, Drucker-Prager Model and Von Mises Model are used for ductile materials. For brittle materials, Griffith model based on linear elastic fracture mechanics is usually applied. Cohesive Crack Model, one of few nonlinear fracture mechanics models, is developed for quasi-brittle materials.

4.2.1 Fracture Process Zone

Concrete is considered as a quasi-brittle material, in which the tensile stress gradually decreases after it reaches the tensile strength while the tensile strain/displacement continues to increase. This behaviour of concrete is called strain softening. The concept of strain softening evolves from plasticity where the post-peak decline of the tensile stress is considered as a gradual decrease of the tensile strength, i.e., softening. Since the softening is related to all the strain components, it is normally called strain softening. The reason of strain softening is that there is an inelastic zone developed ahead of the crack tip which is also referred to as fracture process zone (FPZ) as shown in Fig. 4-1a. When a crack propagates in concrete, the cracked surfaces may be in contact and are tortuous in nature (Mindess and Diamond, 1982), due to various toughening mechanisms such as aggregate bridging, void formation or microcrack shielding (Shah *et al*., 1995). Therefore, the cracked surfaces may still be able to sustain the tensile stress which is characterized by the softening degradation curve. It should be noted that, strictly speaking, FPZ is always surrounded by a nonlinear hardening zone (Bažant and Planas, 1998). For a quasi-brittle material, e.g. concrete, the size of this hardening zone is negligible. For a ductile material, however, the size of the hardening zone is considerably larger than that of the FPZ. Therefore, ductile materials exhibit hardening or perfect yielding behaviour, rather than softening. For a brittle material, these two zones may still present, but their sizes must be vanishingly small.

Cohesive Crack Model (CCM), originally developed by Hillerborg *et al.* (1976), is generally accepted as a realistic simplification for FPZ (Elices *et al*., 2009). CCM assumes that FPZ is long and narrow and is characterized by a stress-displacement curve as typically shown in Fig. 4-1b. In Fig. 4-1a, the shadowed zone from point A to B is FPZ and the area beyond Point B is the true crack where the cracked surfaces are completely separated. In the FPZ, Point A represents the crack initiation point where the tensile stress just reaches the tensile strength $f_t^{'}$. Point B is the so-called crack tip of the true crack where no tensile stress exists. The tensile stress in the FPZ is in a nonlinear function of

the separation (opening) at that point. The CCM is normally incorporated into finite element analysis as an interface when the crack path is known in advance. As the cracking is assumed to occur at the cohesive interface, concrete outside cracking, known as bulk concrete, can be dealt with by linear elastic mechanics. Once crack occurs, the bulk concrete undergoes unloading.

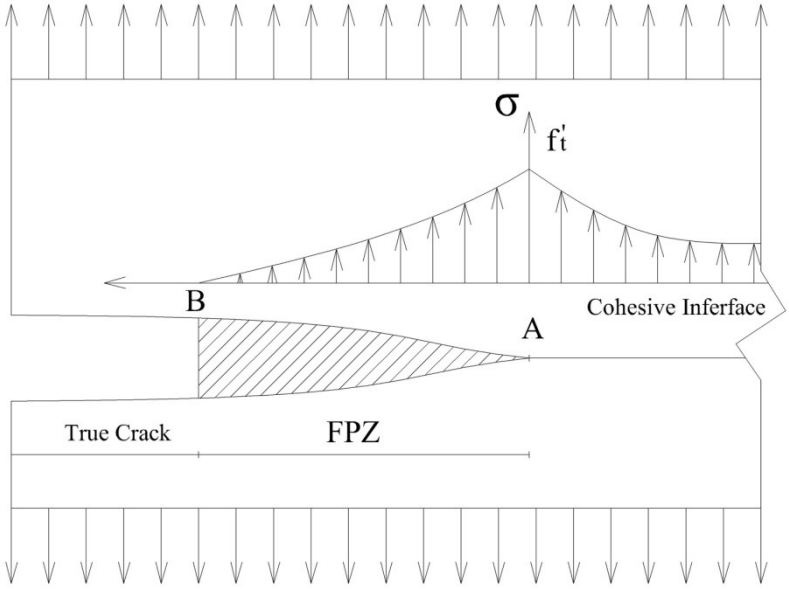

(a) Schematic of mechanism of FPZ

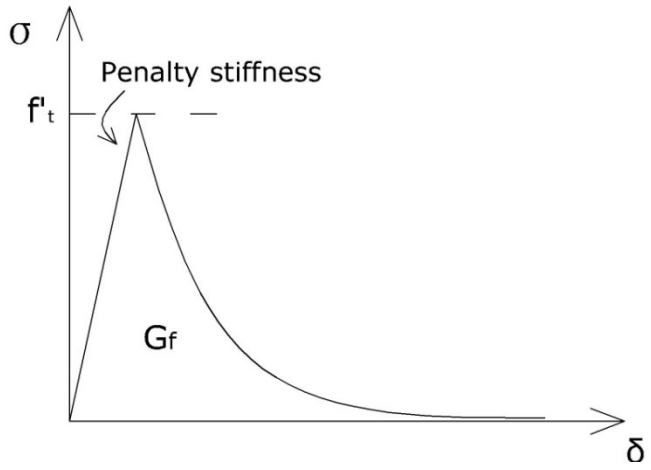

(b) Stress-displacement curve for cohesive material

Figure 4-1 Cohesive crack model

4.2.2 Constitutive Relationship

To describe the constitutive relationship used in the CCM, the phenomenon of strain localization needs to be explained. In general, when a structure/element made of quasi-brittle material is subjected to uniaxial tension and the full stress-elongation curve is obtained, the stress will initially linearly increase followed by nonlinear increase until the peak stress. In this stage, the strain is uniformly distributed throughout the structure. After the peak stress, strains localize into a narrow region which is the cohesive crack. This crack appears somewhere in the structure – either at the weakest area or at the pre-existing crack. Beyond this strain localized area, the structure unloads. This is illustrated in Fig. 4-2a where a concrete cylinder with a notch in the middle is subjected to a pull-out force at two ends. Under this force, the stress will concentrate around the notch where the crack will take place. Once the crack is initiated, the strain will localize to the notch band whilst the other two parts unload. Fig. 4-2b shows relationship of the stress and the elongation of the whole cylinder and the relationship of the stress and the crack width at the notch. w is the crack opening/crack width at the notch. By neglecting the inelastic strain in the loading-unloading cycle (Hillerborg *et al.*, 1976), the total elongation under uniaxial tension δ can be expressed as follows

$$\delta = L\varepsilon + w = L\frac{\sigma}{E} + w \tag{4.1}$$

where ε is the strain of the structure beyond the cohesive crack, L is the original length of the structure in the direction of tension, E is the modulus of Elasticity and σ is the residual stress. In Eq. 4.1, it can be seen that the total elongation consists of the opening of the cohesive crack and the unloaded displacement of the rest of the structure.

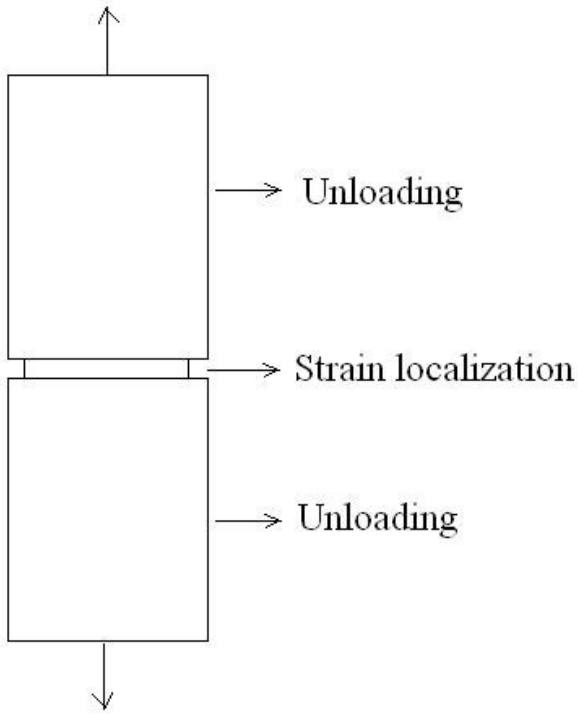

(a) Schematic of strain localization and unloading of a structural element

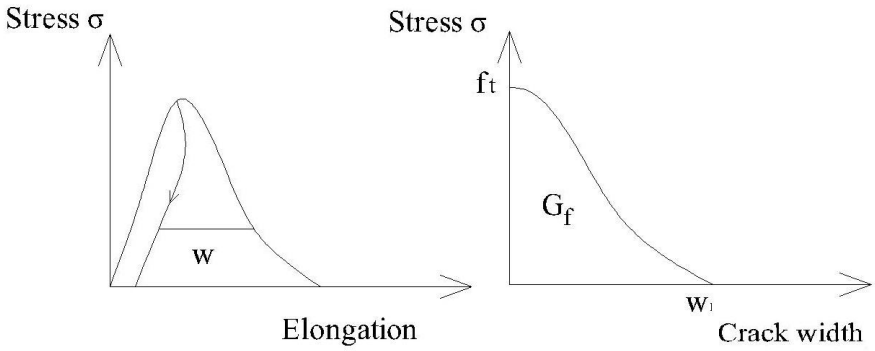

(b) Stress-elongation/crack width relationships

Figure 4-2 Strain localization and unloading of a structural element

Since the FPZ is represented by the cohesive interface and the thickness of the cohesive interface should be very small or zero, a traction-separation law is introduced to describe its stress-displacement relationship as follows:

$$\sigma = f_{T-S}(\delta) \tag{4.2}$$

where f_{T-S} is a nonlinear function, on which a number of researchers have been working to define it, e.g., ACI Committee 446.1R (1991) and Gopalaratnam and Shah (1985). It has been found that with zero thickness, the traction-separation law for the interface provides best estimation for concrete cracking because there is actually no real interface in it. Since δ is related to w, $f_{T-S}(\delta)$ can also be expressed in terms of w. As shown in Fig. 4-1b, there are four parameters to define $f_{T-S}(\delta)$: the elastic stiffness (also called penalty stiffness) K_p, the tensile strength $f_t^{'}$, the fracture energy G_f and the shape of the softening curve. These four parameters will be explained and discussed in details in Section 4.2.3.

Since the crack opening w can be determined via unloading process as shown in Fig. 4-2, the stress-displacement relationship can also be expressed as stress-crack opening relationship. As proposed in the analytical method in Chapter 3, the traction-separation relation for exponential softening curve can be expressed as follows

$$\sigma = f(w) = f_t^{'} \exp\left(-\frac{f_t^{'}}{G_f} w\right) \tag{4.3}$$

Once $f_t^{'}$ and G_f are known, the constitutive relationship for the cohesive interface can be determined.

In the cases that the analytical forms of the softening curve are unknown, i.e., irregular softening shape, the constitutive relationship can be defined by a tabular $\sigma - w$ or $\sigma - \delta$ relations provided in FE package. In this regard, the choice of the numbers of the points selected should be able to reflect the real curve, since linear interpolation is generally adopted in most applications to produce the points between those defined. For example, if the softening curve is linear, only two points are needed to define the curve; however, if the softening curve is of high curvature a number of points are then required and the exact numbers depend on the degree of the curvature. The difficulties (bump phenomenon in stress-displacement curve) in applying this method in ABAQUS will be discussed in details in Section 6.4.

As the cracking is assumed to occur at the interface, concrete outside the cracking zone, known as bulk concrete, can be dealt with by linear elastic mechanics. Once a crack occurs, the bulk concrete undergoes unloading. The stress-strain relationship for the bulk concrete is linear as shown below:

$$\sigma' = E\varepsilon' \tag{4.4}$$

where σ' represents tensile/compressive stress and ε' represents the corresponding strain.

4.2.3 Material Properties

The material parameters of CCM have been defined in Fig. 4-1b which shows the full tensile stress-displacement relation of plain concrete. The term "full" means the tensile stress firstly increases to the tensile strength and then steadily decreases until the tensile strength is completely degraded to zero. The material parameters include the penalty stiffness K_p, the tensile strength f_t', the fracture energy G_f and the shape of the softening curve. These parameters, however, may be substituted by some others, i.e., G_f can be substituted by the failure displacement δ_m which is the displacement when stress drops to zero. The principle is that the parameters are adequate to determine the full stress-displacement curve specified in Fig. 4-1b.

Penalty stiffness K_p: Since $f(w)$ defines only the strain softening after the peak stress f_t', the elasticity of the concrete prior to the peak stress needs to be described separately. The initial response of the cohesive interface is assumed to be linear to be represented by a constant penalty stiffness (K_p) as shown in Fig. 4-1b. The concept of penalty stiffness comes from the elastic stiffness which is obtained by dividing the elastic modulus of the concrete by its thickness. Since cohesive interface is normally very thin or even of zero thickness, the elastic stiffness of the cohesive interface approaches infinitesimally large. This makes sense as the interface should be stiff enough prior to initiation of crack to hold

the two surfaces of the bulk concrete together, leading to the same performance as that of no interface existing. This also meets the condition of CCM which assumes that the energy required to create the new surfaces is vanishingly small compared to that required to separate them (Bažant and Planas, 1998). The reason for this condition is that when the elastic stiffness is large, the displacement at tensile strength is small and thus the energy to create the new surfaces is small. However, the elastic stiffness cannot be too large as it will cause convergence problems due to ill-conditioning of the numerical solver of the FE programmes (ACI Committee 446.3R, 1997). Therefore, the cohesive stiffness becomes a "penalty" parameter (K_p), which controls how easily the cohesive interface deforms elastically. As such this stiffness is large enough to provide the same or close response of intact concrete prior to cracking, but not so large as to cause numerical problems.

Tensile strength $f_t^{'}$: The tensile strength $f_t^{'}$ of concrete material is used as an important index to determine if a cohesive crack is initiated. For Mode I fracture, once the tensile stress at any point of a structure reaches its tensile strength, a crack is initiated and the material of that point starts to degrade. As is known, the tensile strength of concrete can be obtained mainly by three types of tests, which are splitting test, flexural test and direct tensile test. The strengths measured from these tests vary considerably and $f_t^{'}$ must be determined via direct tensile test. This is because, in the splitting and flexural tests, the distributed stresses are not pure tension but involving compression. The strength determined from such tests, therefore, is not truly tensile property of concrete.

Fracture energy G_f: The fracture energy G_f is the energy absorbed per unit area of crack with the unit of N/mm or N/m. It can be regarded as the external energy supply required to create and fully break a unit surface area of cohesive crack (Elices *et al.,* 2002). Therefore, G_f can be calculated as the area under the softening curve shown in Fig. 4-1b and expressed as follows

$$G_f = \int_0^{\delta_m} f_{T-S}(\delta) d\delta \tag{4.5}$$

Since the entire stress-displacement curve $f_{T-S}(\delta)$ is regarded as a material property, G_f is also a material parameter which is independent of structural geometry and size. G_f is used as an energy balance which controls stable crack propagation, that is, a crack will propagate when the strain energy release rate is equal to G_f.

There is another material parameter which is related to G_f and used to evaluate the brittleness of the material. This is called characteristic length l_{ch}, expressed as follows

$$l_{ch} = \frac{EG_f}{f_t^{'}} \tag{4.6}$$

l_{ch} is an parameter which can be used to estimate the brittleness of given concrete. Since G_f, $f_t^{'}$ and E are all material properties and definite once the concrete is harden, l_{ch} is treated as a material index of brittleness. To measure the brittleness of material, the larger the l_{ch} the less brittle the material. Moreover, l_{ch} is proportional to the length of FPZ which is in the order of $0.3 l_{ch}$ to $0.5 l_{ch}$ according to Shah *et al.* (1995). It is noted that the length of FPZ is termed as the distance from the point just at complete separation to the point where crack is just initiated. It is illustrated in Fig. 4-1a as the distance from B to A.

Shape of softening curve**:** The cohesive crack initiation is followed by strain softening, which can be represented by a range of forms, e.g., linear, bilinear and non-linear softening. Without knowing the shape of the softening curve, it is difficult to determine the entire stress-displacement curve. Although some researchers have suggested that the exact shape of the softening curve is less important than the values of fracture energy for certain cases (Elices *et al.*,

2002), the shape of the softening curve is important in predicting the structural response and the local fracture behaviour, i.e. the crack width is particularly sensitive to the shape of the softening curve (Shah *et al*., 1995).

As reviewed in the literature in Chapter 2, a number of researchers have been working on deriving the analytical forms of the softening curve due to realizing its importance to the fracture behaviour of concrete structures. The analytical form of exponential softening curve has been derived in Chapter 3 which is recalled in Eq. 4.3.

4.3 Finite Element Modelling

To quantify the cracking of either plain or reinforced concrete, there have always been technical difficulties in solving a set of usually high order differential equations that govern the geometric/mechanical behaviour of concrete (ACI Committee 446.3R, 1997). A numerical approach seems to be the only viable option. There are two approaches in numerical solutions: one is boundary element method and the other finite element method. It has been observed that the second method has attracted considerably more research effort (Bažant and Planas, 1998, Ngo and Scordelis, 1967, Shah *et al*., 1995). In this study, a commercial FE software package ABAQUS (version 6.8) is used for numerical computations. ABAQUS is a suite of powerful engineering simulation programs, based on the finite element method, that can solve problems ranging from relatively simple linear analyses to the most challenging nonlinear simulations (Dassault Systèmes Simulia Corp. 2008). ABAQUS has a relatively broad library of elements and material models that can be employed to simulate a variety of problems. Most importantly, it performs well for nonlinear analysis. Moreover, it uses the open source scripting language Python for scripting and customization which enables the users to develop their own elements or materials if needed. ABAQUS mainly has two solvers which are Standard and Explicit. ABAQUS/Standard is a general purpose solver using traditional implicit integration scheme, i.e., Newton-Raphson method (also known as Newton's method), to solve a system of equations at each "increment" of an analysis. ABAQUS/Explicit is a special purpose solver using an explicit

dynamic finite element formulation, which is primarily designed for dynamic problems although it can be applied to quasi-static analysis for certain cases. In this study, the FE model is resolved in ABAQUS/Standard. Before being submitted to the solver, the FE model is established in ABAQUS/CAE (Computer Aided Engineering). ABAQUS/CAE is an interactive and graphical environment where the FE model can be created with ease.

4.3.1 Model Formation

To apply the cohesive process zone model to the software, an interface element is created as shown in Fig. 4-3. This 4 nodes cohesive interface element has two stress components – normal stress in direction 1 and shear stress in direction 2. There are no other stresses because the thickness in direction 1 is infinitesimally small.

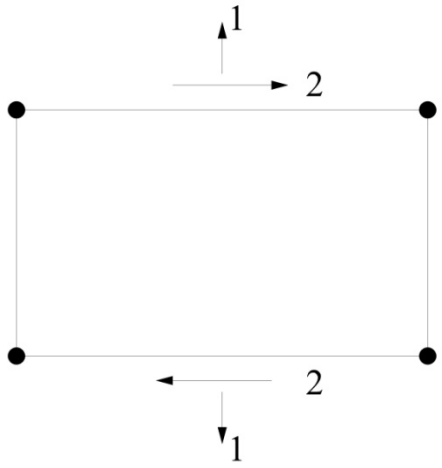

Figure 4-3 Local directions for two-dimensional cohesive element

This cohesive interface element will have linear elastic behaviour prior to peak load followed by the initiation and evolution of damage, i.e., cracking. The elastic constitutive relationship between the nominal stresses and nominal strains is described as follows:

$$\sigma = \begin{Bmatrix} \sigma_1 \\ \sigma_2 \end{Bmatrix} = \begin{bmatrix} E & 0 \\ 0 & G \end{bmatrix} \begin{Bmatrix} \varepsilon_1 \\ \varepsilon_2 \end{Bmatrix} \tag{4.7}$$

where σ_1 and σ_2 are the normal stress in direction 1 and shear stress in direction 2 respectively, G is the shear modulus in plane state (in 2D), and ε_1 and ε_2 are the corresponding strains of σ_1 and σ_2. It should be noted that, theoretically speaking, the stiffness of the cohesive element should equal E/h, where h is the geometric thickness of the cohesive element. However, as the concept of "penalty" is introduced in aforementioned discussion, K_p does not always equal E/h. It should also be mentioned that in addition to geometric thickness h there is a theoretic thickness h_t of the cohesive element, which is the thickness used in calculation. Thus taking h_t as 1 will lead to the strain of the cohesive element equal to the displacement. Moreover, h_t and h can be adjusted together to determine the geometric thickness of the cohesive interface. For instance, the real interface is very thin but needs to be modelled larger for the purpose of visibility. In this case, h is increased but h_t has to be decreased to the same proportion.

As discussed earlier, for concrete with embedded reinforcing steel bar, it is widely accepted to be modelled as a thick-wall cylinder (Pantazopoulou and Papoulia, 2001, Tepfers, 1979). Fig. 4-4 shows the geometry of the cylinder as well as the placement of cohesive interface. Rebar is not physically modelled. The geometry of the cylinder is defined as the same as in the analytical method, e.g. inner radius a and outer radius b. It is assumed that only one crack will initiate and propagate from the inner boundary of the cylinder to the outer boundary. However, this crack represents the total cracks in a way that the total crack width can be divided by the number of the cracks, as widely employed in smeared crack model. Since the mechanical behaviour along the longitudinal direction is the same and the length in the longitudinal direction is much larger than the geometry in the transverse direction, this cylinder is modelled as a plane strain problem. For FEA, two elements are employed in this study: 4 nodes cohesive interface element as discussed earlier for the cohesive interface, and 4 nodes bilinear plane strain quadrilateral element for the bulk concrete. Reduced integration is used for the plane strain element because the accuracy of the bulk concrete is not an issue herein. As a result, the damage evolution of the

cohesive element is combined with the elastic deformation of the bulk concrete in the global response.

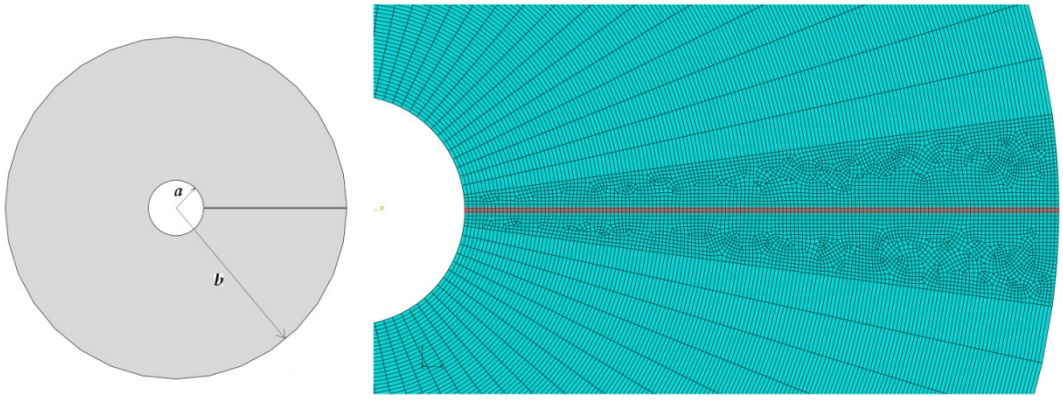

Figure 4-4 Geometry of the FE model and the mesh around the cohesive interface

Additionally, very fine mesh is used in the cohesive interface and its surrounding bulk concrete. The thickness of the cohesive interface is 0.2mm and the inner radius and outer radius are 6mm and 37mm respectively. Since the cohesive interface should only accommodate a single layer of cohesive elements due to traction-separation law, the element size of the cohesive element is chosen as 0.2mm. The region around the cohesive interface will have stress concentration during the cracking process of the cohesive elements which should have the same element size as the cohesive element. The other area of the bulk concrete is in pure linear elasticity and has no concentration of stress, therefore, much coarser mesh can be applied. It has been tried on this selected mesh size to ensure that the convergence is not the problem due to the mesh size.

For meshing the cohesive elements, attention should be paid to the *stack direction* which is the isoparametric direction along which the top and bottom faces of a cohesive element are stacked (Dassault Systèmes Simulia Corp. 2008). For example, in Fig. 4-3, direction 1 is the stack direction along which the traction-separation law is applied. This direction must be set the same as the sweep direction when generating the mesh. If they are not identical, i.e. in this model, the results will show that the cohesive elements will be subjected to compression. These results will therefore be invalid.

4.3.2 Application of loads

The cylinder is subjected to a uniformly distributed pressure at the inner boundary, i.e., the corrosion induced pressure and applied load induced pressure. For brittle and ductile materials, pressure/force can be directly applied to the boundary. However, for strain softening materials, only displacement can be used as boundary condition. In the analytical method, as the crack is assumed to be smeared over the cylinder and thus the corrosion and applied load induced expansion (displacement) is uniformly distributed along the inner boundary. In the numerical method, however, the expansion cannot be just uniformly distributed due to the introduction of the cohesive interface. The reason is that if the radial displacement is applied uniformly in a solar coordinate system (also called cylindrical coordinate system in ABAQUS), there will be a component in the normal direction (direction 1 in Fig. 4-3) of the 1st cohesive element at the inner boundary because of its finite geometric thickness, which is illustrated in Fig. 4-5. The component can only be waived if the cohesive elements are geometrically modelled as zero thickness, which will lead to the expansion in Fig. 4-5 in horizontal direction. Making the geometric thickness be zero, however, is not possible. Such a displacement component results in dramatically large stress since the stiffness of the cohesive elements are much larger than the surrounding bulk concrete. This does not make sense as the displacement causing the cohesive element to deform does not come from the surrounding bulk concrete but from the applied displacement. It is also not reasonable because the assumption of the CCM is that the thickness of its element is negligibly small and thus any load cannot be applied in the normal direction to the thickness. Moreover, during elastic development prior to the damage initiation, the deformation of the cohesive element is supposed to be much smaller than the other elements. Uniformly applying the displacement leads to the same deformation for both cohesive elements and bulk concrete elements.

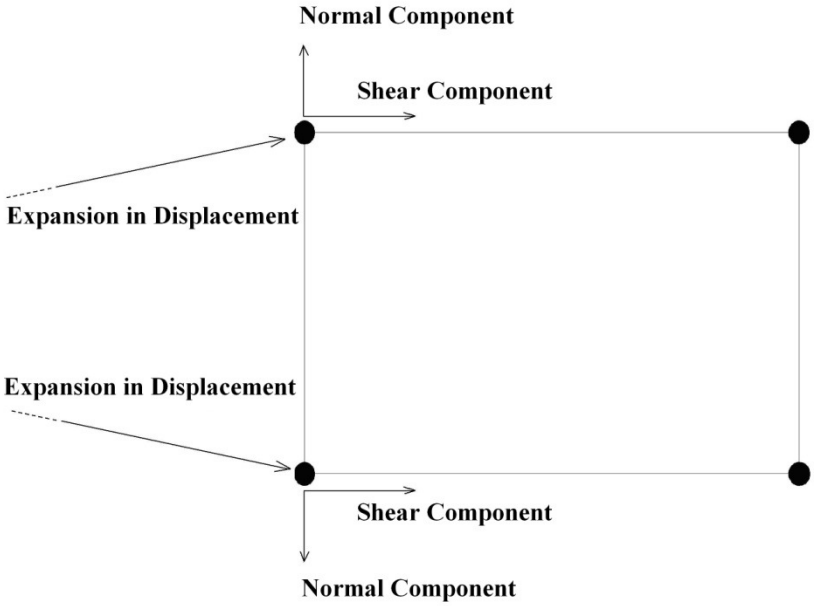

Figure 4-5 Stresses of the 1st cohesive element under uniform load distribution

Due to the fact that the displacement (normal component) cannot be directly applied to the 1st cohesive element, the displacement is applied in two coordinate systems in this study. The displacement applied to the cohesive element is defined in direction of x-axis in rectangular coordinate system, and the displacement applied to the other part of the inner boundary is defined in radial direction in cylindrical coordinate system, as shown in Fig. 4-6. With this arrangement, the geometric thickness of the cohesive element needs to be very small. This arrangement eliminates the normal component of the displacement on the 1st cohesive element and approximately reserves the shear component of the displacement (shown in Fig. 4-5). Since the thickness of the cohesive element is extremely small, the shear component of the uniformly distributed displacement can be considered the same as the distributed displacement itself. Under this arrangement, the traction of the cohesive element comes from the deformation of the whole cylinder and there is no artificial displacement added to the normal direction of the cohesive element.

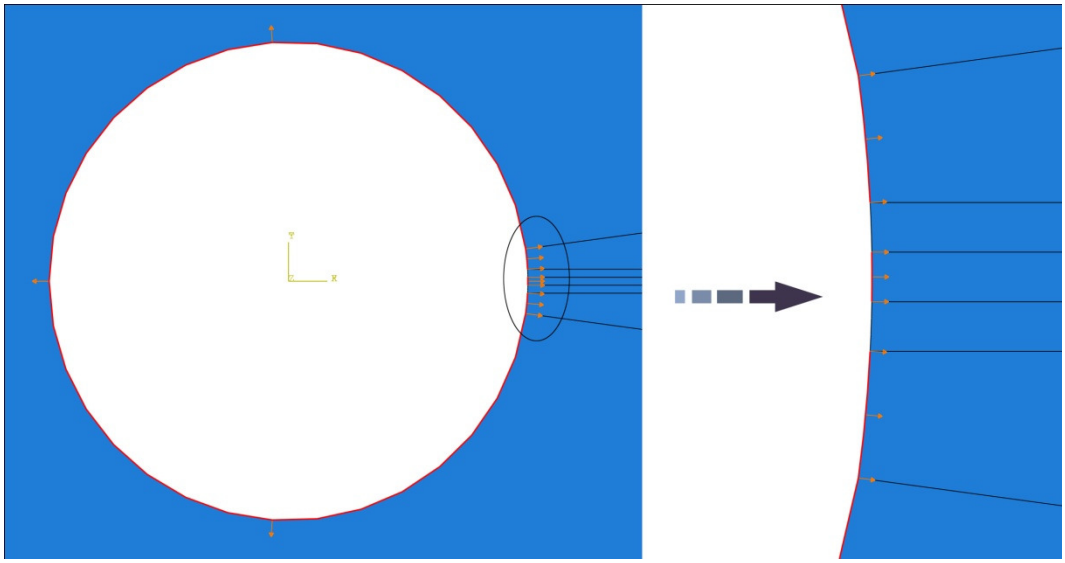

Figure 4-6 Loading arrangements at the inner boundary

Stable crack propagation can be treated as a quasi-static problem. Since the elastic behaviour and the inelastic response of the concrete have different requirements of incremental size to converge, it is better to apply the loading in two steps – the first step for elastic development only and the second step for the damage evolution. It should be emphasized that the incremental size for the second step has to be small enough to ensure quasi-static feature when the crack propagates.

In addition to the direction of the loading, how to make the magnitude of the loading time-dependent in the FEA is of particular concern. As it is well known in FEA, the load (can be either force or displacement) is usually divided into a number of increments which are applied to the FE model in sequences. Correspondingly, the simulation is split up into a number of time increments and the nonlinear solution path is then followed. The term "time" herein is proposed for incrementation and does not directly have physical meaning. Since the displacement at the inner boundary of the cylinder under both corrosion and applied load is a function of the service time, as shown in Fig. 4-7, the application of the displacement to the numerical method has to be real time dependant. Fig. 4-7 illustrates the inner displacement development under both effects during 10 years service time. It is produced based on the 1st scenario in the analytical method (see Section 3.5) where the concrete is not cracked at the

beginning of the applied load. At the start ($t = 0$), the displacement is 1.25e-3 mm and it is kept constant until $t = 0.46$ years. The displacement then steadily increases until about 0.08 mm at 10 years.

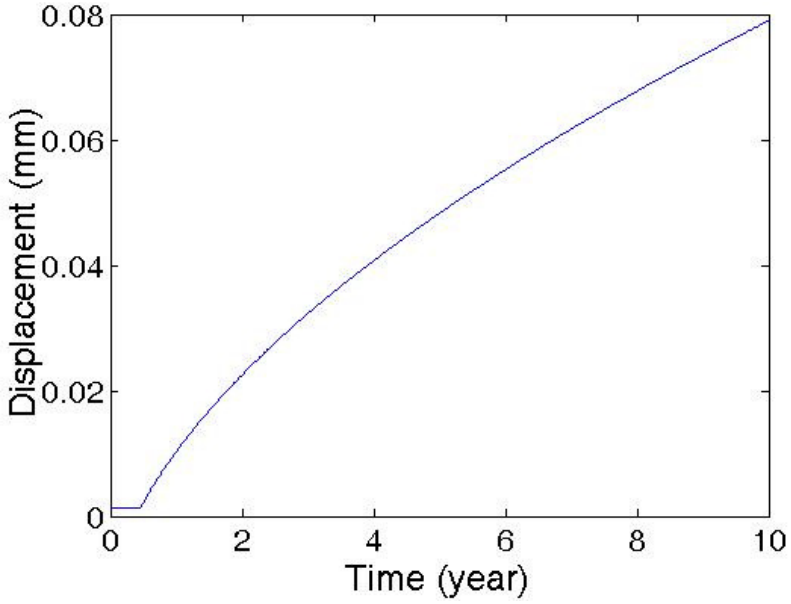

Figure 4-7 Internal expansion (displacement) as function of service time

By default in ABAQUS, the displacement as well as other types of loading changes linearly with the incremental time in a step. Nonlinear time-varied displacement needs to be separately defined in *amplitude*. *Amplitude* is where in ABAQUS the magnitude of the loading in a step can be specified as a function of step time. There are a few pre-existing options to identify the amplitude curve, i.e. periodic curve and exponential decay curve. However, the most general purpose one is the tabular definition method. To use this method, it is a good practice to set 1.0 as step time and 1.0 as the ultimate magnitude of displacement of the same step, and use the exact values of time and displacement of Fig. 4-7 in the *amplitude* definition. For the nonlinear curve, the more points entered the closer the amplitude curve is generated to the real time-varied displacement.

To implement the time dependent displacement of Fig. 4-7 in ABAQUS (can also be other FE packages), a procedure is developed as follows

- Set 3 analysis steps with the first 2 for the elastic analysis and the 3rd for the inelastic analysis.

- Determine at which level of displacement the cylinder goes to inelasticity. This can be done by carrying out a few trial runs. It is assumed herein that at 1.2e-2 mm displacement the cylinder starts to inelastically deform.

- In Step 1, set the displacement at 1.25e-3 mm. Allocate 1 increment for this step as the whole cylinder is in pure elastic state.

- In Step 2, set the displacement at 1.0e-2 mm. It is not suggested to use exactly 1.2e-2 mm. This step is also an elastic analysis. In Fig. 4-7 for displacement from 1.25e-3 mm to 1.0e-2 mm, make 5 points and input their values of time and displacement in the amplitude curve. For the increment size, use 1.0 as the initial increment size, 1.0e-5 as the minimum increment size and automatic generation of increment size based on computational efficiency.

- In Step 3, set the displacement at 8.0e-2 mm. From displacement of 1.0e-2 mm to 8.0e-2 mm, make 20 points and input their values of time and displacement in the amplitude curve. For the increment size, use 1.0e-2 as the initial increment size, 1.0e-5 as the minimum increment size and automatic generation of increment size.

4.3.3 Damage Criteria

Crack initiation marks the beginning of degradation or damage of concrete at a point. Crack is assumed to initiate when the maximum nominal tensile stress reaches the tensile strength of the concrete for the Mode I fracture – opening mode (see Chapter 2 for the descriptions of all three fracture modes), expressed as follows

$$\langle \sigma_1 \rangle = f_t^{'} \tag{4.8}$$

where $\langle \sigma_1 \rangle = \begin{cases} \sigma_1 & for \quad \sigma_1 > 0 \\ 0 & for \quad \sigma_1 < 0 \end{cases}$

The operation $\langle \sigma_1 \rangle$ is to ensure that a crack will not initiate under compression.

After cracking is initiated, the cohesive element is damaged and the normal stress of this element softens in a manner as defined (e.g., Fig. 4-1b). The failure of the element is governed by the softening curve. To calculate the residual stress after its peak/cracking stress, a damage parameter D is introduced and defined as follows:

$$\sigma = (1 - D)\sigma_u \tag{4.9a}$$

$$\sigma_u = K_p \delta \tag{4.9b}$$

where σ_u is the undamaged stress as shown in Fig. 4-8.

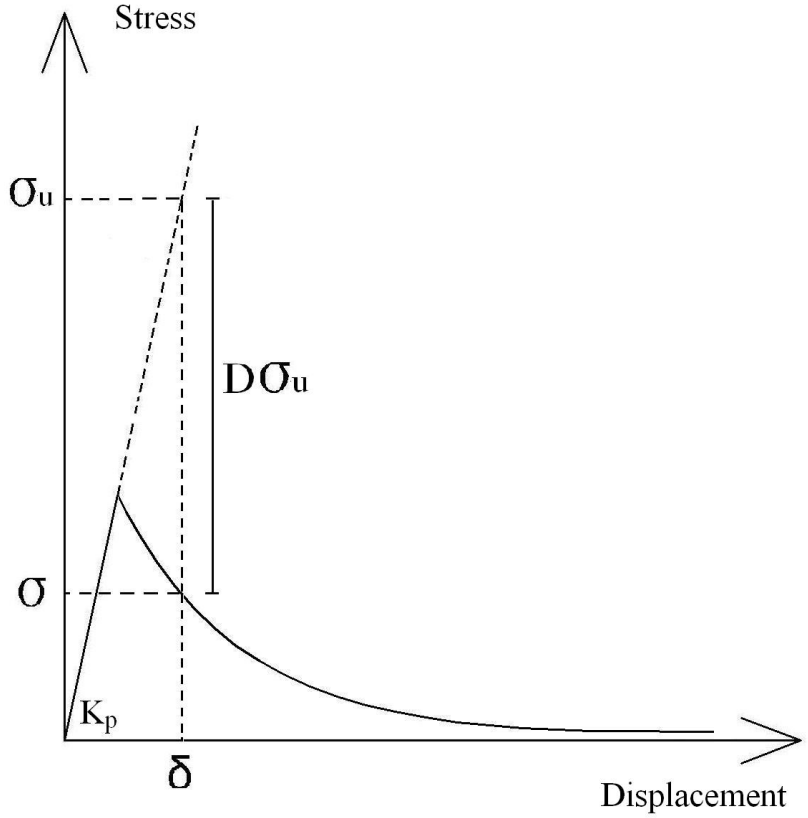

Figure 4-8 Determination of residual stress in terms of damage parameter D

To prevent mesh sensitivity in FE analysis, the damage evolution has to be based on displacement or energy rather than strain. This means the crack opening is not dependant on the strain of the element but the opening distance of the element. Therefore, as the distance between the nodes is used as a crack measure rather than a change in strain (which depends on the element length) the mesh dependency is significantly reduced.

Although ABAQUS has the capability to allow users to develop their own subroutines for the failure criteria, it is believed that the existing ones, i.e. displacement or energy criteria, are sufficient for concrete cracking problems. For example, if the softening shape is known as linear or exponential, the fracture energy criteria can be used. If the softening shape is, however, bilinear or cannot be described in an analytical form, the criteria based on tabular effective displacement can be applied. It should be noted that the effective displacement δ_{ef} is expressed as follows

$$\delta_{ef} = \sqrt{\delta_1^2 + \delta_2^2} \tag{4.10}$$

where δ_1 is the displacement of the cohesive element in the normal direction (direction 1 in Fig. 4-3) and δ_2 is the displacement of the cohesive element in the shear direction (direction 2 in Fig. 4.3). They are equal to ε_1 and ε_2 respectively when the theoretical thickness of the cohesive element is set as 1.0. Because δ_2 is considerably smaller than δ_1 in this problem, it is a convention that in this thesis the effective displacement of the cohesive element equals to the normal displacement.

Taking energy damage evolution criteria for example, when the strain energy release rate reaches the fracture energy of the material, the cohesive element completely fails. To evaluate the damage of the cohesive element and obtain the residual stress, D is calculated as follows:

$$D = \frac{G_r}{G_f - G_e} = \frac{\int_{\delta_0}^{\delta_r} f_{T-S}(\delta) d\delta}{G_f - \frac{f_t \delta_0}{2}} \tag{4.10}$$

where G_r is the energy release rate after peak stress, G_e is the elastic energy release rate prior to peak stress. The relationship of these energy parameters is illustrated in Fig. 4-9.

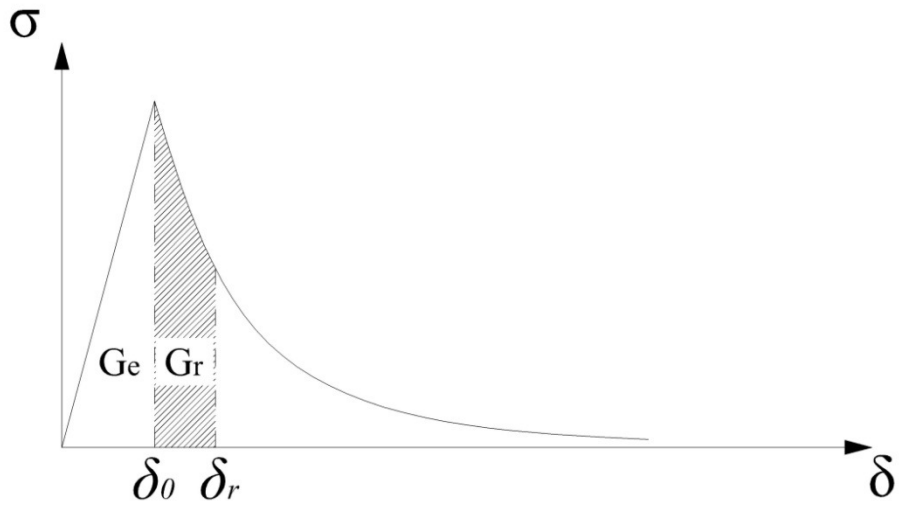

Figure 4-9 Illustration of various energy release rates

To use energy damage evolution criteria, G_f and $f_{T-S}(\delta)$ need to be known. ABAQUS automatically generates a relation of $D-\delta$ with Eq. 4.10. The relation of $\sigma-\delta$ is then determined with Eq. 4.9. To use tabular effective displacement damage evolution criteria, however, the whole $D-\delta$ curve is known by manually specifying a number of points. The points between these defined points are interpolated automatically and linearly. Insufficient defined points may lead to stress stiffening in the strain softening stage. Therefore, although the inputs in defining the material constitutive properties for both criteria are different, the methods in interpreting the inputs are identical – they both employ $D-\delta$ to produce the constitutive relation $\sigma-\delta$.

4.4 Nonlinear Analysis

For mechanical analysis, there are mainly three types of nonlinearity, resulting from geometry, material and boundary conditions. Geometric nonlinearity applies to the problems of large strain, small strain but finite displacement, large rotation, etc. No matter which type of the geometric nonlinearities it falls to, to consider nonlinear geometry, the equilibrium equations in FEA must be formulated based on the deformed geometry rather than the original geometry. Material nonlinearity, simply speaking, is that the relation between the stress and strain is not linear. The material can be of nonlinear elasticity, plasticity, viscoelasticity or creep. Concrete is a nonlinear material which has strain softening behaviour. The strain softening makes the nonlinear analysis even more difficult to deal with because the degradation of the stiffness usually introduces severe convergence problem. This will be discussed in details in Section 4.4.2. Boundary condition nonlinearity is normally introduced by the change of the boundary conditions, i.e., boundary is free to move in the beginning but then fixed. Contact problems usually involve boundary condition nonlinearity. This research does not involve boundary condition nonlinearity. Each kind of these nonlinearities has its own nonlinear term in the governing equation (as discussed in Section 4.4.1), which controls the analysis in a nonlinear manner.

4.4.1 Fundamentals of Nonlinear FEA

In an FEA, it always comes to solving a series of simultaneous algebraic equations in the form as follows

$$[K]\{u\}=\{R\} \tag{4.11}$$

where $[K]$ is the global stiffness matrix, $\{u\}$ is the vector of global nodal displacements and $\{R\}$ is the vector of global nodal forces. In the linear analysis, $[K]$ is unique. For nonlinear analysis, however, $[K]$ is a variable and related to stresses or displacements. For both linear and nonlinear analysis, $[K]$

is assembled by the local element stiffness matrix, as in the form of (Jiang *et al.*, 2005)

$$[K]=\sum_{n}[K_r]=\sum_{n}\int[B]^T[D_r][B]dV \tag{4.12}$$

where $[K_r]$ is the stiffness matrix of the local elements, $\sum_{n}[\ ]$ is assemblage operator that assembles the stiffness matrix of local elements into the global stiffness matrix, and $[B]$ is the geometric matrix which relates the displacements of the nodes to the strains of the elements and is shown as follows

$$[\varepsilon]=[B][\delta] \tag{4.13}$$

$[D_r]$ in Eq. 4.12 is the constitutive matrix of the material which can be expressed as follows

$$[\sigma]=[D_r][\varepsilon] \tag{4.14}$$

For linear materials, $[D_r]$ is a constant. For nonlinear materials, $[D_r]$ is a function of the stresses as shown below

$$[D_r]=f\{[\sigma]\} \tag{4.15}$$

In Eqs. 4.11 to 4.15, Eq. 4.11 expresses the stiffness equilibrium, Eq. 4.13 represents the geometric relations, Eq. 4.14 and 4.15 are the constitutive relations. These three relations – equilibrium (Eq. 4.11), geometric relation (Eq. 4.13) and constitutive relation (Eq. 4.14 and 4.15) are the basis of the nonlinear analysis. Nonlinearity can be caused by material, geometry and boundary conditions. If one of these three nonlinearities is present, the analysis is regarded as nonlinear. For this study, only material nonlinearity is considered.

ABAQUS/Standard employs the Newton's method to solve the nonlinear equations. Since $[K]$ is variable and may depend on internal stress or displacement, a nonlinear solution is not as straightforward as solving a single system of equations, i.e., in the linear analysis. In the Newton's method, a load is divided into a number of *increments* and added to the structure in sequences. During each increment, the global stiffness matrix is calculated and the approximate equilibrium configuration is obtained. It usually takes a few iterations to get the analysis converged in an increment. An iteration is an attempt made to determine an equilibrium solution in an increment. The maximum number of iterations that is allowed in an increment by default is 16. If the converged results are still not accessible after 16 iterations, the increment size will be reduced to ¼ of current one and continue to iterate with another 16 times allowance. On the other hand, if in two consecutive increments the solution can be both achieved with 5 iterations, in the 3rd increment, the increment size will be increased to 150%. Since it may take a long time for nonlinear analysis to achieve a successful solution in every increment, the knowledge of FE theory and mechanics is essential to grasping how ABAQUS deals with the incrementation and how it can be adjusted to achieve the final solution.

4.4.2 Material Nonlinearity

From Eqs. 4.14 and 4.15, it can be seen that the constitutive matrix $[D_r]$ is not a constant but a function of stresses. This is where the material nonlinearity comes from and can be schematically shown in Fig. 4-1b where the slopes of the curve at any point formulate the stiffness matrix $[D_r]$. As the slope gradually inclines after the peak stress, $[D_r]$ is dependant on the stress at the same point. In nonlinear analysis, $[D_r]$ cannot be generated in a single attempt. Instead, the solution is divided into a number of increments within each one of which the total load is split into smaller portions. In each increment, it is to calculate a displacement correction for the cylinder subjected to a small load increment until the end of the solution. It may take several iterations to obtain the converged results during each increment. The displacement will be corrected in

every increment and the final displacement will be obtained in the last increment.

$[D_r]$ can also be a function of displacements in displacement loading cases, especially for strain softening problems. This is because in the iterations, the solution is obtained by applying the specified displacements gradually rather than the loads. For strain softening behaviour, the typical problem is that $[D_r]$ will not be always positive which will cause severe convergence difficulties. There are a few methods or techniques that can be used to overcome this. Viscous regularization is one of them and will be discussed in the next section.

As aforementioned, the tensile stress-displacement relationship (Fig. 4-1b) is used for the material property of the cohesive elements in the current study. This will mainly control the cracking behaviour. Apart from the cohesive elements, all the other elements are assumed linearly elastic. To implement the material property of Fig. 4-1b into ABAQUS, there are a few approaches depending on the purposes. The implementation of elastic behaviour is always the same, with specification of the penalty stiffness and tensile strength. Penalty stiffness is supposed to be as large as possible, but without introducing computing difficulties. For the damage evolution process, however, it depends on the failure criteria to be adopted. As elaborated in the preceding section of cohesive process zone, for concrete cracking problems, two damage evolution criteria are available which are based on fracture energy and inelastic effective displacement respectively. The effective displacement δ_e is defined as follows

$$\delta_e = \sqrt{\delta_1^2 + \delta_2^2} \tag{4.16}$$

where δ_1 and δ_2 are the displacement along the normal and shear direction of the cohesive element respectively. Since for opening mode fracture (Mode I) the shear stress and displacement are considerably less than the normal ones, the effective displacement can be approximately regarded as the same as the normal displacement. The inelastic effective displacement means the total effective

displacement minus the effective displacement at maximum tensile stress where the material is assumed to start to deform inelastically.

The fracture energy based damage evolution criteria and the inelastic effective displacement based criteria are theoretically equivalent to each other because the area under $\sigma - \delta$ is the fracture energy. The difference lies in the fact that the inelastic effective displacement criteria can define the exact shape of softening curve – not just linear or exponential. This does help when the descending softening curve has a long tail as low grade concrete may exhibit. To input a specific material property for the cohesive element with inelastic effective displacement damage evolution criteria, the relationship between the damage parameter D and the corresponding inelastic effective displacement needs to be defined. This will then be transformed automatically to the stress-displacement relation using Eq. 4.9.

4.4.3 Viscous Regularization

Convergence is usually a problem in the execution of FE programmes for materials exhibiting softening behaviour for implicit schemes as in most FE programmes. Also, when a material is damaged, e.g., concrete is cracked, sudden dissipation of energy will make the computation more dynamical while the quasi-static analysis is expected. The difference between the quasi-static and dynamical analysis is if the crack can be stably propagated. An artificial viscosity is therefore used to overcome the convergence difficulties by making the stiffness matrix of the material positive. This viscosity regularizes the traction-separation law by modifying the stiffness reduction variable D as follows

$$\dot{D}_v = \frac{D - D_v}{\mu} \tag{4.17}$$

where μ is the viscosity parameter which can be specified in the property of cohesive element and D_v is the viscous stiffness degradation variable. Once μ and D are known, D_v can be determined.

A small viscosity value μ helps improve the rate of convergence without compromising results. When viscosity is introduced to the model, D is not referred to any more but D_v is referred to. The material stiffness matrix is then modified.

4.5 Worked Example

As a demonstration of the application of the developed numerical method and techniques in FEA, the example used in Li (2003) is taken for numerical solutions using ABAQUS, a commercial FE package. This example has been described in Section 3.5 of the analytical method. In this example the combined corrosion induced and applied load induced pressure is taken as loading. This loading is applied to the concrete in the form of displacement rather than pressure, due to the strain softening behaviour as explained previously. Fig. 4-7 shows the displacement applied to the concrete as a function of service time which can be calculated analytically using classic mechanics. The difference between these two examples from the analytical method (Section 3.5) and the numerical method (Section 4.5) is that the constitutive relations (full stress-displacement curve) used are not identical. In this example, the stress-displacement relationship is taken from the direct tensile test. The motivation for such a variation of constitutive relation in these two examples is to demonstrate that the proposed numerical solution has general applications. Nevertheless, the same constitutive relations will be used and the results from the analytical and numerical methods will be compared in Chapter 6.

The values of the basic variables used in the numerical solution are listed in Table 4-1. To calculate the effective modulus of elasticity, the creep coefficient is taken as 2.0. Since the cohesive element size is of 0.0002 m and the theoretical thickness of the cohesive element is 1, the elastic stiffness of the

cohesive interface is 35250 GPa (5000 E_{ef}). However, due to the value is too large, the penalty stiffness is taken as 14100 GPa (2000 E_{ef}). The time-dependant internal displacement is applied to the concrete cylinder according to the procedures proposed in Section 4.3.2. As a result, Fig. 4-7 is implemented into the FEA as the boundary displacement condition.

Table 4-1 Values of basic variables used in the example

Description	Symbol	Values	Sources
Inner radius	a	6mm	Li (2003)
Outer radius	b	37mm	Li (2003)
Effective modulus of Elasticity	E_{ef}	7.05GPa	Experiment
Poisson's ratio	ν_c	0.18	Li (2003)
Tensile strength	$f_t^{'}$	1.7MPa	Experiment
Fracture energy	G_f	65N/m	Experiment

The constitutive stress-displacement relation is obtained from the direct tensile test on concrete. As discussed in Section 4.4.2, the stress-inelastic effective displacement curve can be plotted in Fig. 4-10.

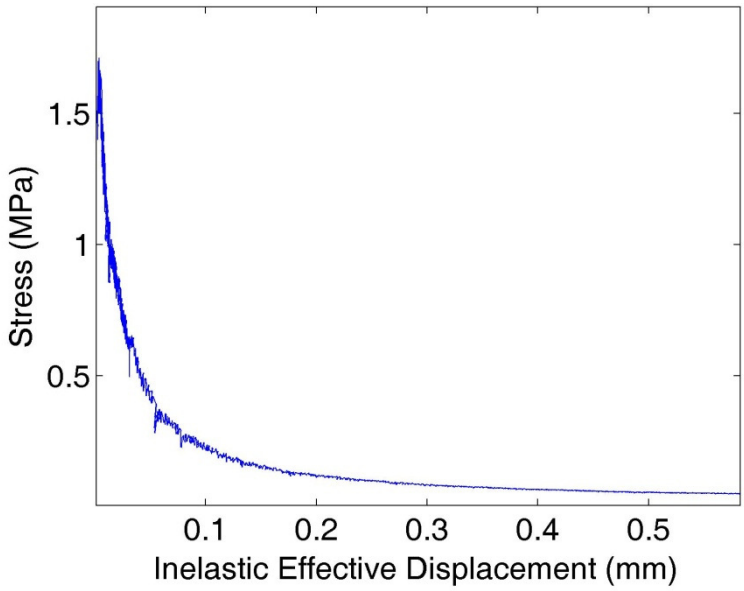

Figure 4-10 Constitutive relation for CCM in this example

Since the analytical form of the softening shape in Fig. 4-10, i.e. exponential, cannot be accurately determined, it is more appropriate to use the tabular effective displacement damage evolution criteria. To use it, Fig. 4-10 needs to be technically transformed into D-inelastic effective displacement curve, as shown in Fig. 4-11.

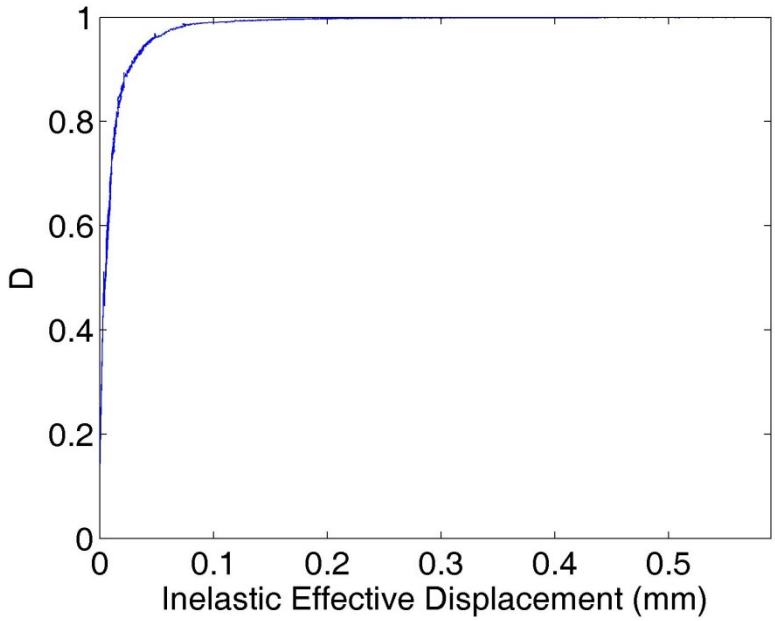

Figure 4-11 Damage parameter D as a function of inelastic effective displacement

It is not straightforward to properly establish a model for crack width of concrete and successfully run it in ABAQUS. To accomplish that needs comprehensive understanding of CCM and sufficient knowledge of FEA. It is therefore well justified to produce a step-by-step procedure to demonstrate how to apply the proposed method. The procedure to determine the concrete crack width under combined reinforcement corrosion and applied load is as follows

I. Define and build the geometry. As specified in Section 4.3.1, the concrete with embedded reinforcing steel bar can be modelled as a thick-wall cylinder. The inner radius of the cylinder should equal to the radius of the steel bar and the distance between the inner and outer boundaries of the cylinder should be the size of concrete cover.

II. Partition the cylinder. Three layers of the same size are partitioned with the middle layer representing the cohesive interface (shown in red in Fig. 4-12). Another two areas are also partitioned for the purpose of transition of mesh. The partitions are schematically shown in Fig. 4-12.

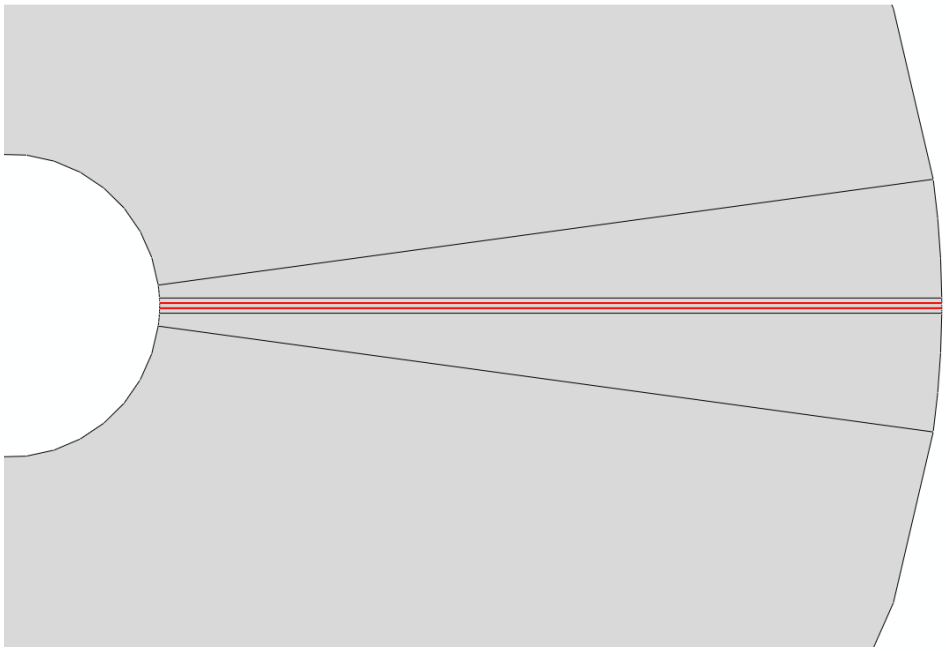

Figure 4-12 Partitions of the cylinder concrete

III. Establish the material model. There are two material models for this problem, which are used for cohesive interface and bulk concrete respectively. To define the material property of the cohesive interface, there are three components: linear elastic behaviour (Eq. 4.7), crack initiation criterion (Eq. 4.8) and damage evolution criteria (Section 4.3.3). To define the material property of the bulk concrete which is all of the cylinder except the cohesive interface, only linear elasticity needs to be identified including Young's modulus and Poisons' ratio.

IV. Obtain the fracture parameters for the cohesive interface used in previous step from experiments. The ideal experiments are direct tensile tests as discussed Chapter 5. A stress-displacement curve or a stress-crack opening curve needs to be obtained from the test. The fracture parameters can then be determined based on Section 4.2.3.

V. Assign the material properties to the entity (cylinder) and create an *instance*. *Instance* is an assembly of the *parts*. The assembling is to define a global coordinate system since every *part* is created in its own coordinate system. There are two options for the *instance* type which are *mesh on part* and *mesh on instance*. For this study it does not make much difference to choose any of the two options because the cylinder is constructed by using 1 *part*.

VI. Define the steps for analysis. There are 3 steps to be identified and an exclusive procedure has been developed in Section 4.3.2. Additionally, several output parameters need to be identified in the "field output request" or by modifying the KEYWORDS in the input file. It depends on how the user would prefer to establish the model. In this study, besides the default output parameters, i.e. stress, strain etc., the output parameters for the cohesive element need to be specified. These parameters are MAXSCRT, SDEG and STATUS. For example, MAXSCRT is the variable indicating whether the crack initiation criterion (Eq. 4.8) for the cohesive element has been satisfied. SDEG and STATUS are the variables expressing the damage extent and status of the cohesive element respectively, more descriptions of which can be found in ABAQUS manual.

VII. Define the load. An original method has been developed in Section 4.3.2 to implement the time-dependent displacement curve in Fig. 4-7 to ABAQUS. There should be 3 pairs of boundary conditions to match the 3 analysis steps, as shown in Fig. 4-13. Moreover, there is an important operation which is to deactivate the boundary conditions defined in previous analysis steps, i.e., BC-2 is created in analysis step 2 but is inactive in analysis step 3. If it is not deactivated, the error message below will be present when checking the data or submitting the job. The error message informs that two displacement boundary conditions have been added to the same nodes, i.e., two displacements of 1e-4m and 1e-5m are added to a node simultaneously.

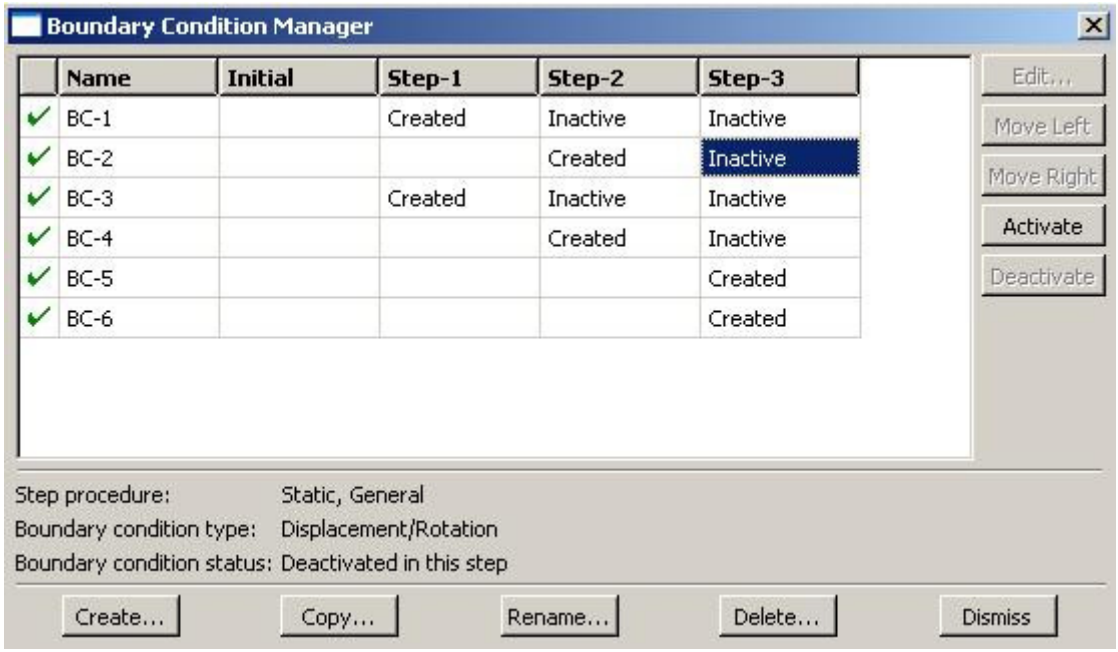

Figure 4-13 Adding boundary conditions in ABAQUS

Error: 81 nodes have dof on which velocity/displacement/acceleration/base motion etc. constraints are specified simultaneously. The nodes have been identified in node set ErrNodeBCRedundantDof.

VIII. Mesh the *instance*. Before generating the mesh, there are 3 things need to be accomplished which are as follows

- Define the element shape and meshing technique. It is suggested to use Quadrilateral element rather than Triangular element. For the meshing techniques, as the same as most FE softwares, ABAQUS has 3 options which are free, structured and sweep. For the cohesive layer and the adjacent two layers, sweep technique is adopted. For the two fan-shaped areas next to the 3 layers, free technique is used. For the rest of the *instance*, sweep technique is employed. It should be noted that for cohesive layer, the sweep path needs to follow the *stack direction* as discussed in Section 4.3.1, when specifying sweep technique. In Fig. 4.14, the red arrow at the right of the cylinder shows the direction of the sweep path.

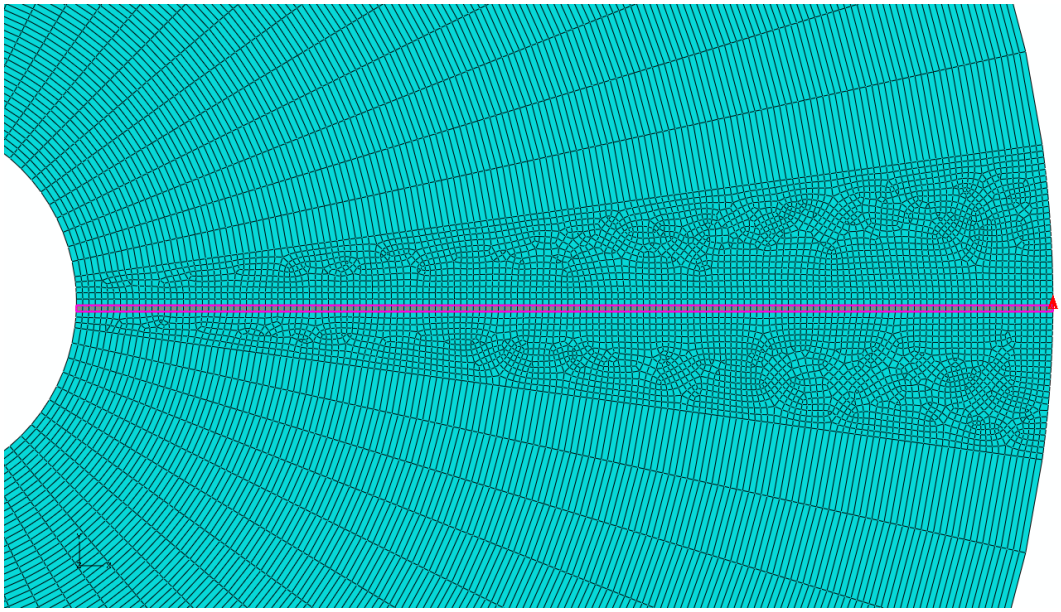

Figure 4.14 Direction of the sweep path at the cohesive interface

- Choose the element type. Two elements are chose for the two materials – cohesive interface and bulk concrete. A 4-node bilinear plane strain quadrilateral element (CPE4R) is adopted for the bulk concrete and a 4-node two-dimensional cohesive element (COH2D4) is employed for cohesive interface. In the options of the cohesive element, the viscosity can be specified.

- Set seeds on the edges of all the regions of the *instance*. The seeds are the potential nodes of the elements. It should be noted that for the mesh to be generated by sweep technique, the numbers of the seeds at the two edges which are normal to the sweep direction need to be identical. In addition, the seeds of the cohesive interface and its adjacent two layers should have the same numbers of the seeds.

IX. Create a job and submit the job to the solver of ABAQUS/Standard. Open the *Monitor* that is shown in Fig. 4-15 to observe the progress of the increment generation.

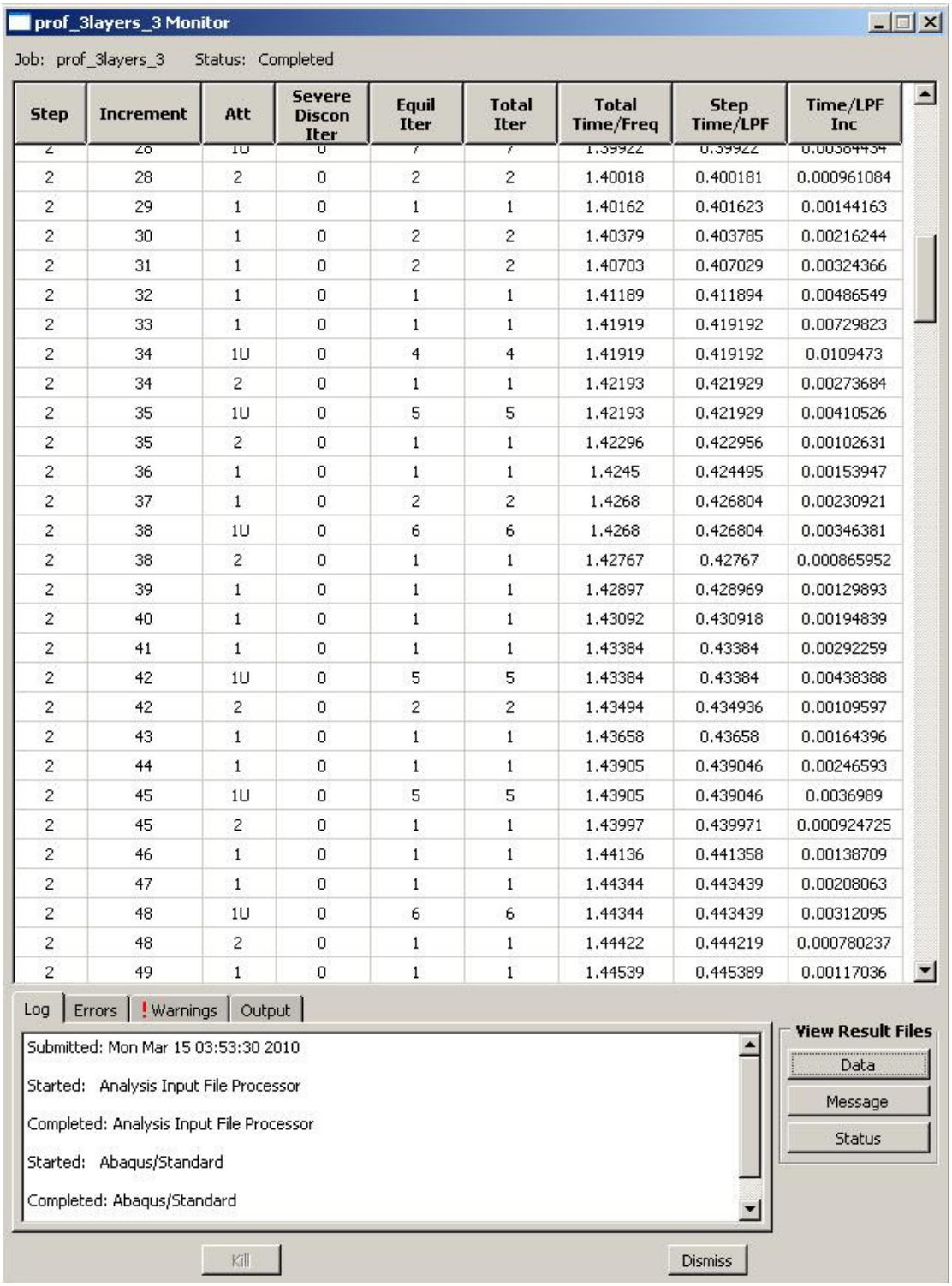

Figure 4-15 Monitor of progress of the solution

X. Review the results. Once the job has been successfully executed, a result file is generated. The results can be visualized by opening the *name*.odb file in the module of Visualization. All the default output parameters, i.e.

stress, strain and deformation, together with the defined output parameters at every increment can be obtained.

XI. Determine the crack width. The crack width can be obtained by plotting *L22* of the surface cohesive element under polar coordinate system as a function of the step time. *L22* is the logarithmic strain in tangential direction under polar coordinate system. Since the theoretical thickness of the cohesive element is 1.0, *L22* is equal to the tangential displacement of the cohesive element. By removing the cracking displacement, the crack width as a function of time is attained.

With the values of the variables in Table 4-1 and damage evolution in Fig. 4-11, and by following the procedure proposed above, the tensile (hoop/tangential) stress distribution can be determined and plotted in Fig. 4-16, with the increase of loading. It can be seen from Fig. 4-16a that the tensile stress in the cylinder is uniformly (circumferentially) distributed at the low level of loading where the whole cylinder is in elasticity. This is because although the present of the cohesive interface makes the structure nonsymmetric, uniformly applied loads should result in uniformly distributed stress in elastic stage. The uniform distribution of stress also verifies the arrangement of loading in Section 4.3.2. However, it may be noted that the stress distribution in Fig. 4-16a is not perfectly uniform, due to the slight variation of distribution of applied loads. Fig. 4-16a, b, c, d show the stress distributions under increasing stages of loading history with Fig. 4-16d the final stage. It can be seen that under a small load, e.g. Fig. 4-16a, the crack is not yet initiated and thus the whole cylinder is purely elastic. Since the penalty stiffness of the cohesive element implies the same response as no cohesive element is introduced in the elastic stage, the tangential stresses at the points with the same radius are approximately identical, as shown in Fig. 4-16a. Once any one of the cohesive elements is cracked, inelastic behaviour is included in the global response and symmetry of stress distribution is perturbed, as shown in Fig. 4-16 b, c and d.

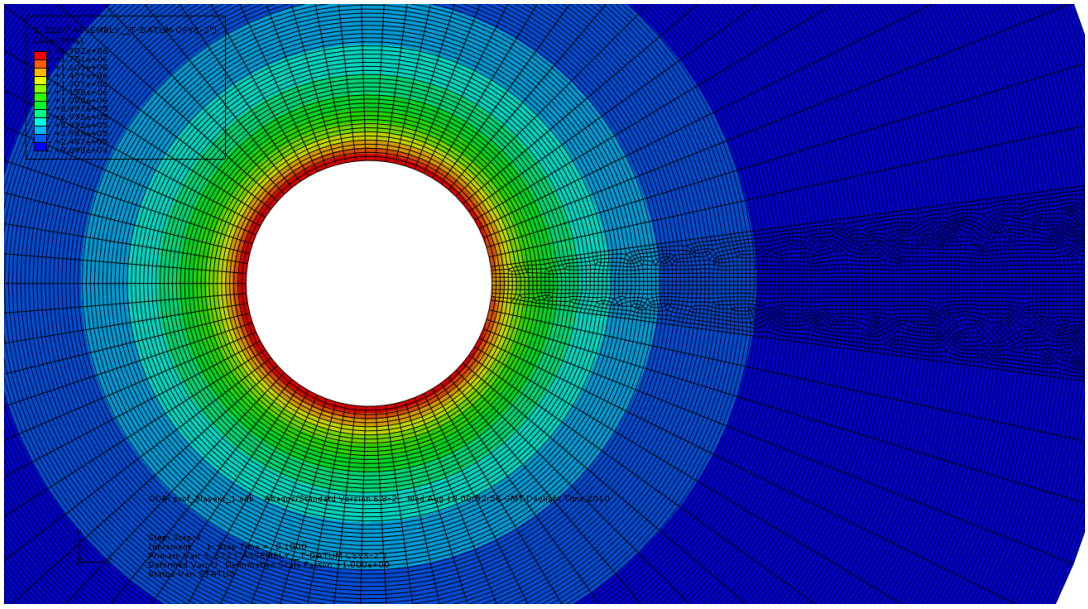

(a) 1% of the displacement at 10 years

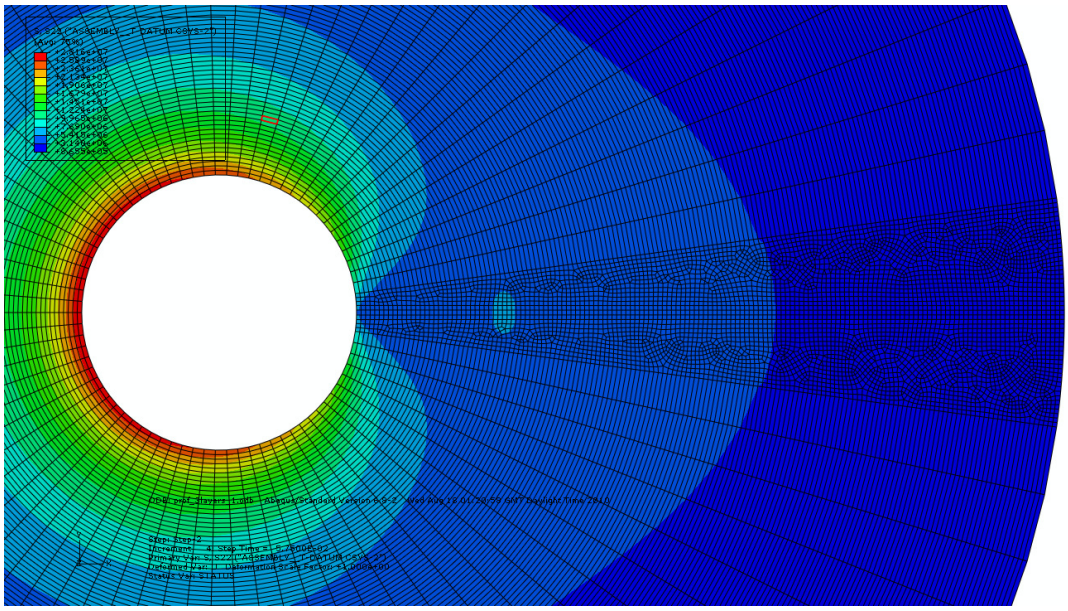

(b) 15% of the displacement at 10 years

Figure 4-16 Tangential stress distributions with increasing loading

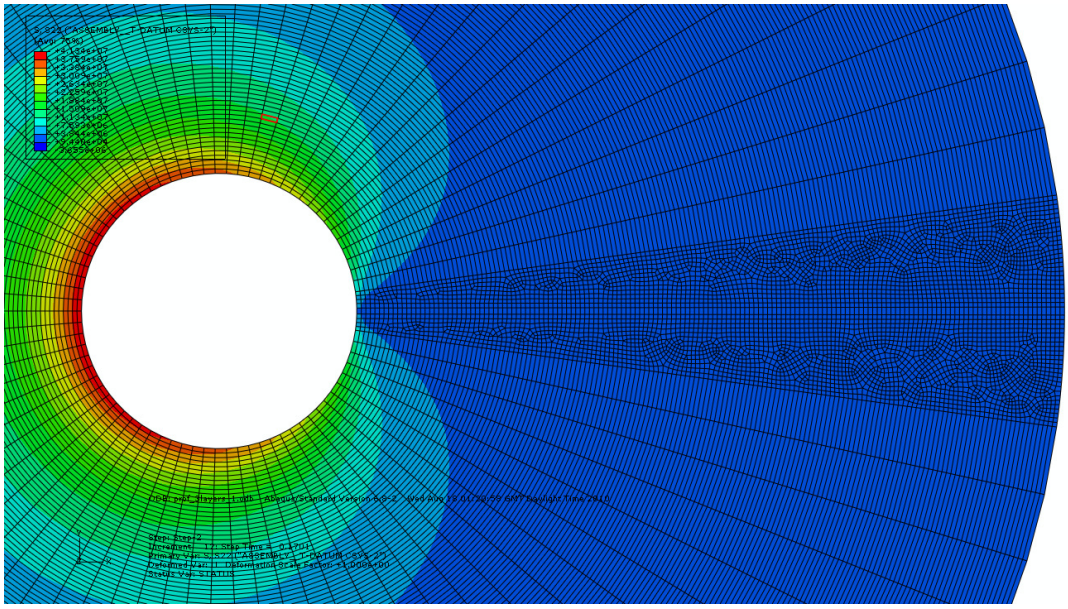

(c) 30% of the displacement at 10 years

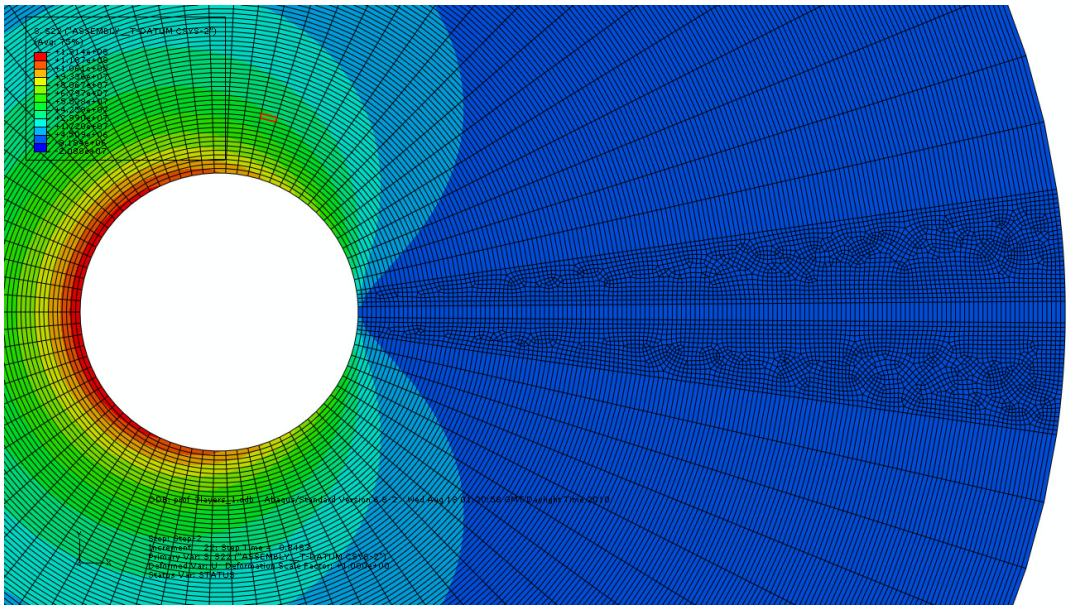

(d) 90% of the displacement at 10 years

Figure 4-16 Tangential stress distributions with increasing loading

To make the crack visible, the nodes of the cohesive elements need to be edited and share the same coordinates in y-axial. As a result, the cohesive interface will become a line. Fig. 4-17 shows the tangential strain distributions in the cylinder with the increase of the loading. Since the theoretical thickness of the cohesive element is 1.0 which means the tangential strain of the cohesive element is equal to its tangential displacement. Therefore, Fig. 4-17 also shows

the displacement/deformation of the cohesive interface (which visibly becomes a line).

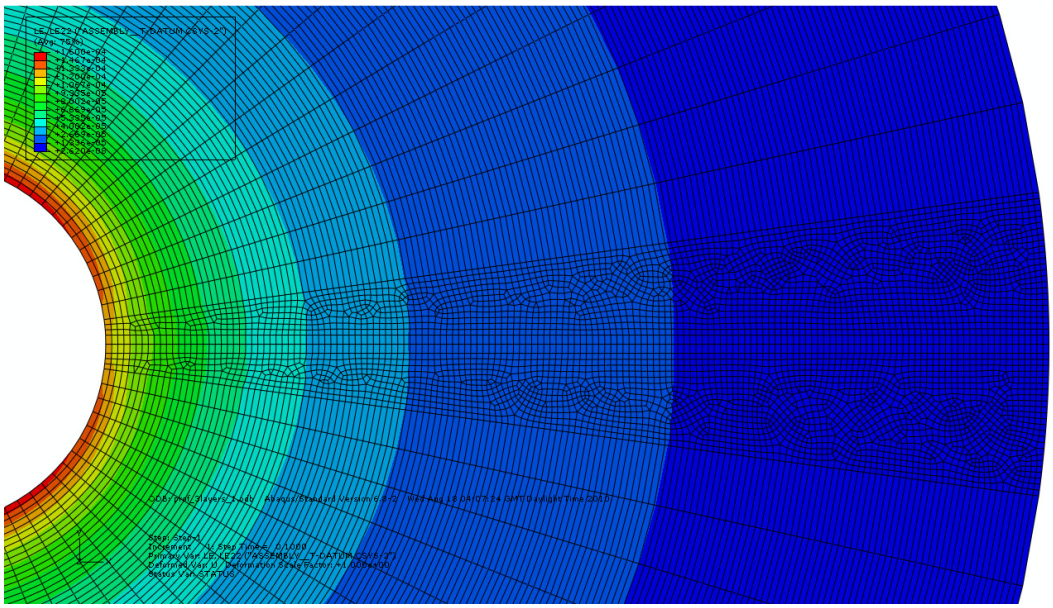

(a) 1% of the displacement at 10 years

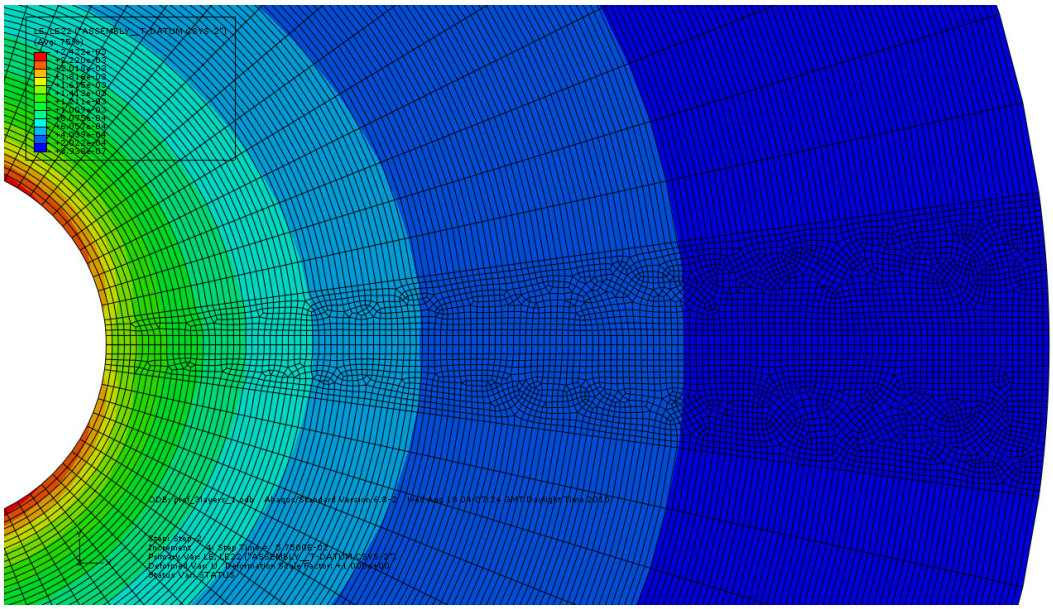

(b) 15% of the displacement at 10 years

Figure 4-17 Tangential strain distributions with increasing loading

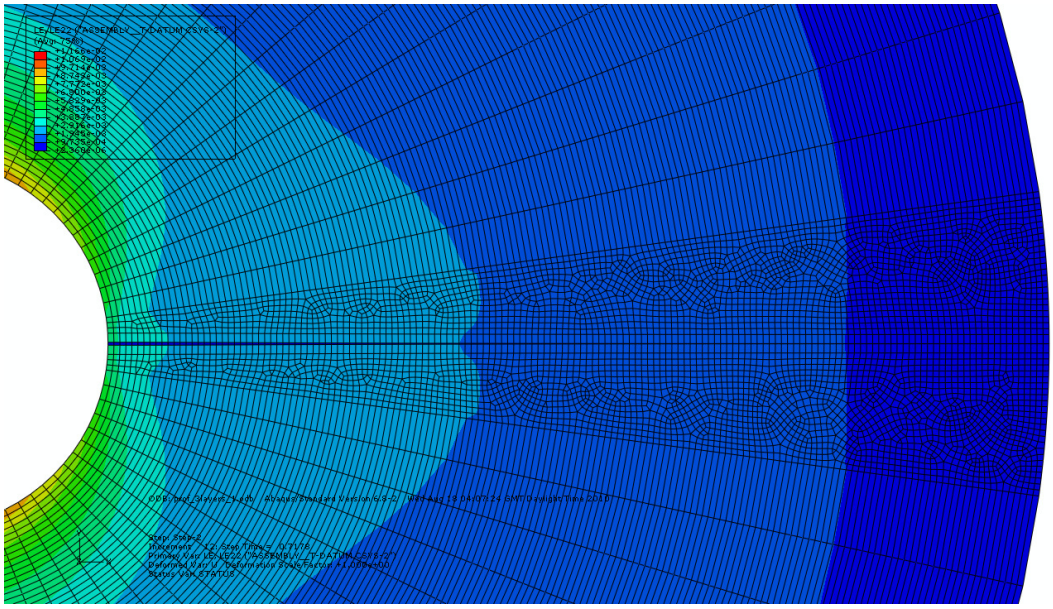

(c) 70% of the displacement at 10 years

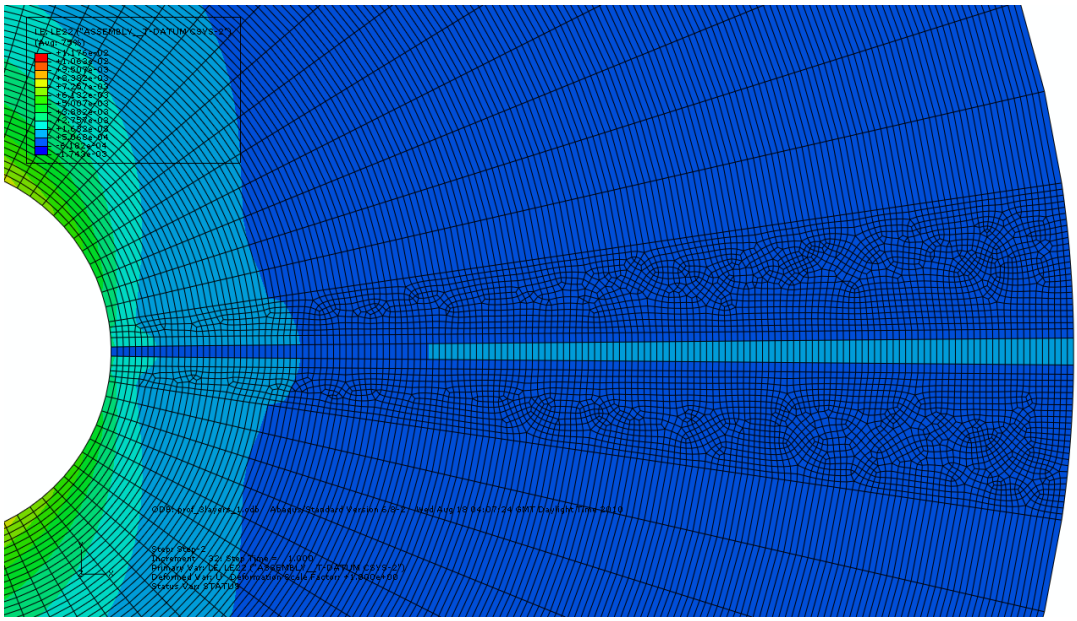

(d) 100% of the displacement at 10 years

Figure 4-17 Tangential strain distributions with increasing loading

As shown in Fig. 4-10 concrete can still have tensile stress (although may be very small) at large tensile displacement and the cohesive elements do not fail even under very large load as illustrated in Fig. 4-16d or Fig. 4-17d. The status of failure of cohesive element is expressed in a parameter SDEG in ABAQUS. The values of SDEG are in the range of 0 to 1.0, with 0 representing no damage of the cohesive element and 1.0 corresponding to complete failure of the cohesive element. For the purpose of visualization of the crack propagation, it

can be adjusted to set the maximum value of SDEG as 0.95 for the complete failure of the cohesive element. It needs to be noted that the adjustment of SDEG is purely for visualization and the real calculation can successfully run until SDEG is 1. Fig. 4-18 then shows the crack propagation at the cohesive interface.

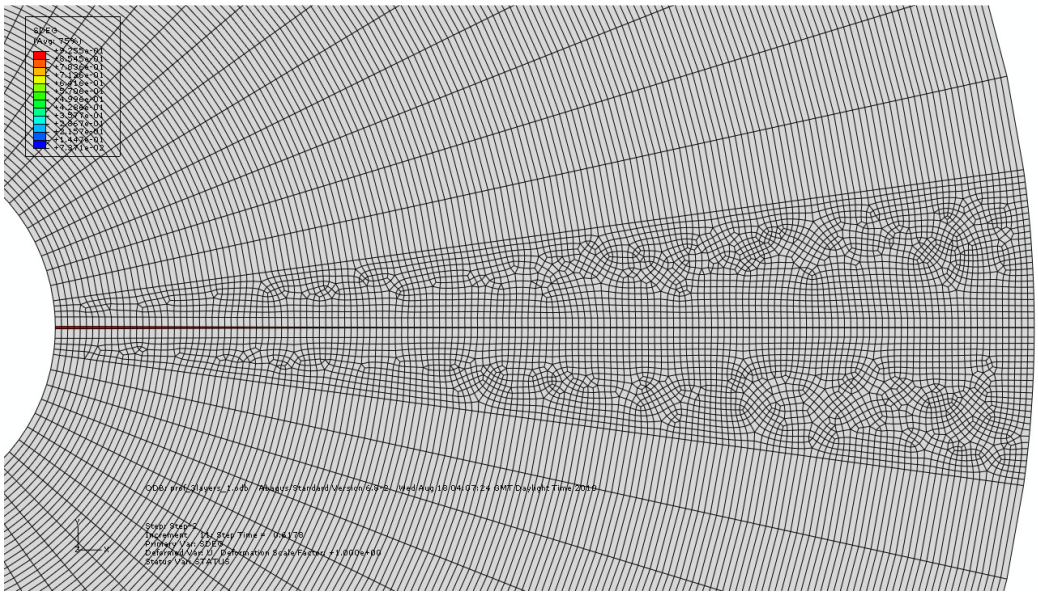

(a) 65% of the displacement at 10 years

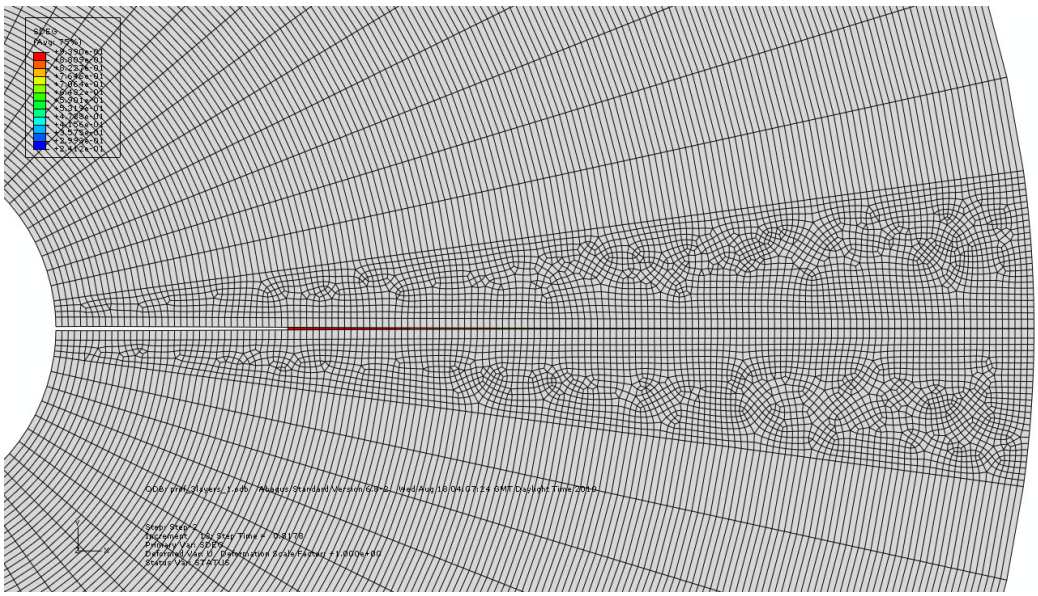

(b) 82% of the displacement at 10 years

Figure 4-18 Schematic of crack propagation

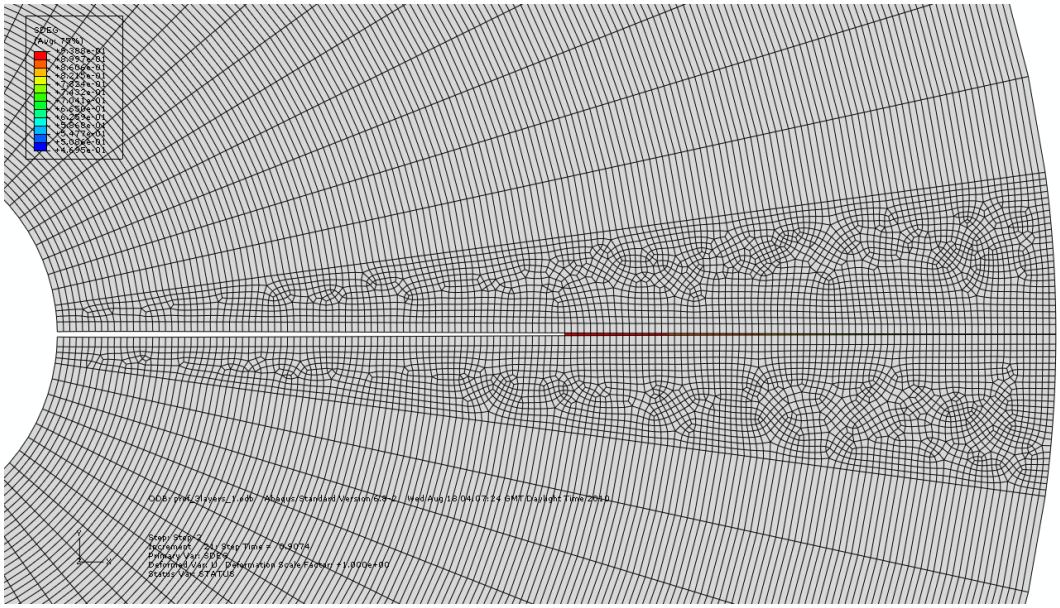

(c) 91% of the displacement at 10 years

Figure 4-18 Schematic of crack propagation

The crack finally approaches the outer boundary of the cylinder (surface). Since the theoretical thickness of the cohesive element is set to be 1.0, the strain of the cohesive element is equal to its displacement. Upon removing the elastic displacement from the total displacement of the last cohesive element at the outer boundary of the cylinder, the surface crack width can be expressed in a function of time, shown in Fig. 4-19.

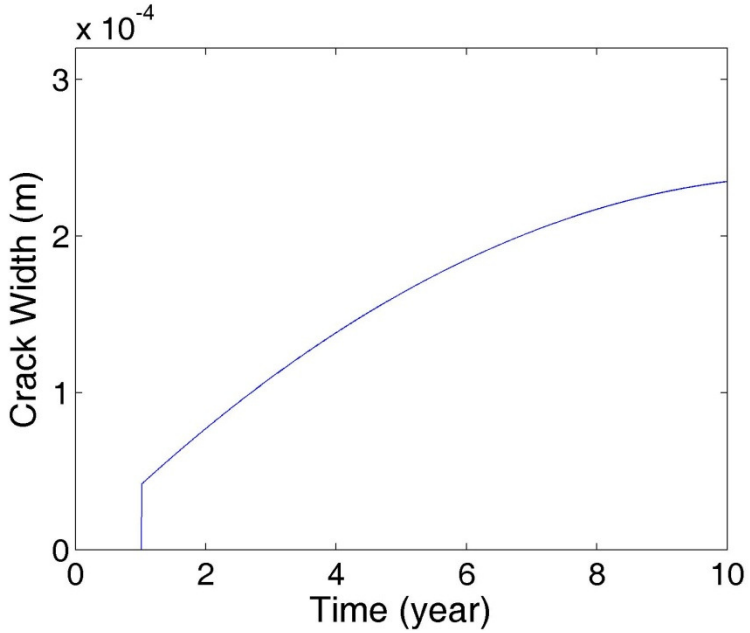

Figure 4-19 Crack width as a function of time

In Fig. 4-19, it can be seen that the surface crack width increases with time. The abrupt increase in the crack width corresponds to rapid decrease of tensile stress in the element as shown in Fig. 4-10. After about 4 years, the increase of the crack width is steady and seems to approach certain value after about 7 years. This is due to the steady decrease of the tensile stress with respect to continuously increasing displacement (long tail of the stress-displacement curve in Fig. 4-10). At 10 years, the crack width reaches about 0.23mm.

4.6 Conclusions

A numerical method to predict concrete cracking and crack width for concrete structures subjected to corrosion and applied loads has been developed. This method is based on fracture mechanics and finite element techniques. Cohesive crack model has been employed to represent the fracture process zone of concrete whose constitutive relationship at the cohesive interface is characterised by a traction-separation law. The displacement at the inner boundary of the cylinder has been applied in two coordinate systems which are Cartesian coordinate system and cylindrical coordinate system. It has been found that this arrangement of loading negligibly alters the uniformity of stress distribution in the elastic stage. Numerical problems, caused by strain softening of concrete, have been discussed and the solutions have been proposed. In addition, the boundary conditions have been arranged in two coordinate systems to avoid stress singularity around the cohesive element at the inner boundary. To demonstrate the application of the numerical method, a worked example has been carried out. It has been found that the stress-displacement relation used for cohesive material is vital in accurately predicting the crack width. It can be concluded that the developed method can be used to predict the crack width.

CHAPTER 5

CONSTITUTIVE RELATIONSHIP OF CONCRETE

5.1 Introduction

The application of nonlinear fracture mechanics to predict concrete cracking requires the information about the softening properties of concrete. These properties, characterized by the tensile strength and stress-displacement/crack width curve, can only be determined from experiments. Evidently, the more accurate this information is determined, the more accurate the prediction is. There are other test methods, e.g., BRE Digest 451 (2000), for concrete tensile strength. The purpose of the test is however, different from the method employed in this study, as is outlined in RILEM TC 162-TDF (2000). The BRE method is only to obtain the ultimate tensile strength whilst the RILEM method is to obtain the full stress-strain curve. Such as the testing methods are difference, i.e., the BRE specimens are not notched whilst the RILEM ones have notches. The BRE method employs either force or displacement at the ends of the specimens as the control of loading whilst the RILEM measures the displacement across the notch and use it as a feedback signal to control loading. For Mode I (opening) fractures, there are mainly three types of experiments, which are flexural test, splitting test and direct tensile test. Flexural test is generally a three-point bending test of concrete beam with a notch at the bottom as shown in Fig. 5-1. The concrete beam is subjected to a central load under which a crack will initiate at the notch and propagate towards the loading position. RILEM TC 162-TDF (2000) proposed a test guidance for a bending beam to determine the fracture parameters. A possible problem for using bending test is that the specimen size is relatively large and influence of the self weight on the fracture energy needs to be carefully estimated. Therefore, some researchers developed a compact three-point bending test – splitting test (also known as wedge splitting test) as shown in Fig. 5-2. So far there is no test standard proposed for the splitting test. However, it is a reliable test method verified by a number of researchers, i.e., Bruhwiler and Wittmann (1990), Kumar and Barai (2009) and Yang *et al*. (1997). Both of these two methods are easy to handle in normal laboratory conditions and have thus attracted most of the research interests. However, since both methods incur a non-uniform state of stress along the crack, there are doubts as to whether the fracture parameters such as tensile strength and fracture energy measured from bending and splitting

tests are truly tensile properties of concrete (Van Mier and Van Vliet, 2002). In this regard, RILEM TC 162-TDF (2001) proposed a recommendation for direct tensile test, also called uniaxial tensile test for concrete, to obtain the complete stress-displacement/crack width curve. Based on this curve, the tensile strength and fracture energy can be obtained. The direct tensile test is considered as the ideal test method to determine the Mode I fracture property of either steel reinforced or plain concrete.

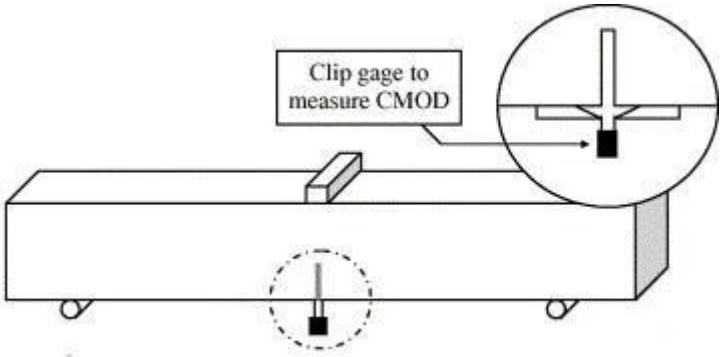

Figure 5-1 Typical specimen and testing arrangement for three-point bending test

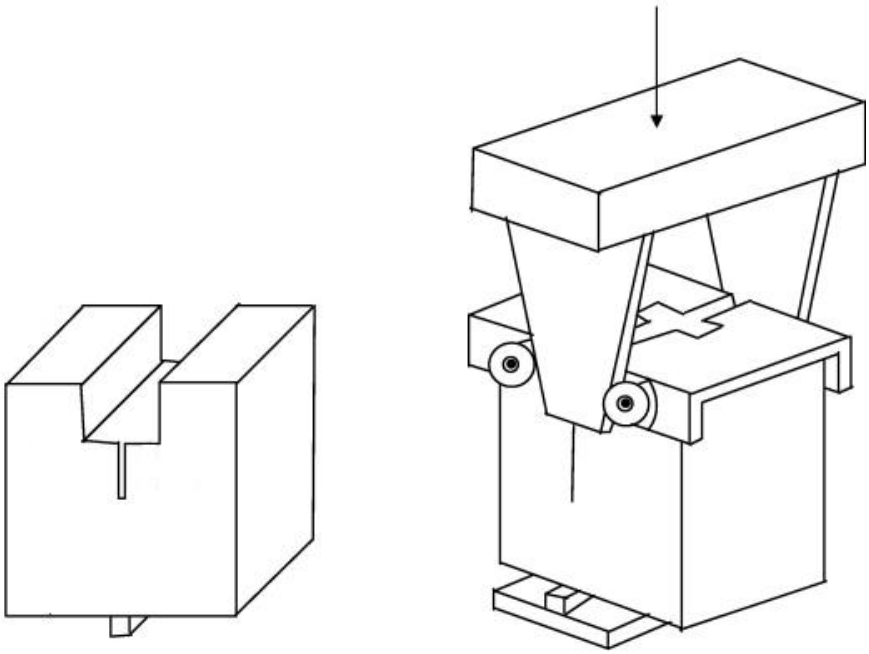

Figure 5-2 Typical specimen and testing arrangement for wedge splitting test

This chapter will present a test programme to determine the real fracture properties of plain concrete, i.e., the complete stress-displacement curve, under uniaxial tension. It will start with materials used, design and casting of specimen, test set-up and the test procedure. The results from the direct tensile tests will be then presented and analysed, followed by the discussions and suggestions on how to carry out this kind of test to achieve accurate fracture properties. The chapter finalises with conclusions.

5.2. Test programme

The programme follows the standard proposed by RILEM TC 162-TDF (2001). Two test variables, i.e., water-cement ratio and maximum size of coarse aggregate, were selected since from literature review, these two variables are the most significant factors that affect the fracture properties of concrete. Two values were selected for each variable in mixture design for concrete. With this, four (2×2) mix proportions were calculated and four batches of concrete were made. For each batch of concrete, six specimens were cast, with a total of 4×6= 24 specimens for test. The tests were carried out on the servo-hydraulic testing machine with three linear variable differential transducers in the Structural Laboratory at the University of Greenwich. In addition to the test recommendation of RILEM TC 162-TDF (2001), a simple procedure was developed to overcome practical problems typically encountered in conducting direct tensile tests.

5.2.1 Materials used

In this test, Portland cement of Type II/B-V 32.5 N was used. This is a class of Portland-fly ash cement which consists of 65-79% by mass clinker and 21-35% siliceous fly ash with a strength class of 32.5 N. Sea-dredged sand was used for fine aggregate and crushed limestone with max sizes of 10mm and 20mm was used for coarse aggregate, as shown in Fig. 5-3. Sieve analysis was performed for grading and determination of oversize and undersize aggregate. The sieve sizes used were 75.0, 50.0, 37.5, 20.0, 10.0, 5.00, 2.36, 1.18mm and 600, 300,

and 150μm. Before undertaking the sieve analysis, the aggregate sample was air-dried in order to avoid lumps of fine particles being classified as large particles. For the calculation of the mix design, percentage of the sand passing 600μm sieve was used. The results of the grading of sand are listed in Table 5-1. According to BS EN 13139 (2002), the size of the sand is classified as 0/4 mm in terms of d/D designation. Normal tap water from the lab was used for mix the concrete.

(a) Maximum size of 10mm (b) Maximum size of 20mm

Figure 5-3 Coarse aggregate

Table 5-1 Results of grading for the sand

Sieve size	Mass retained (g)	Percentage retained	Cumulative percentage passing	Cumulative percentage retained
10.0 mm	0	0.0	100	0.0
4.75 mm	6	1.20	98.80	1.20
2.36 mm	48	9.64	89.16	10.84
1.18 mm	68	13.65	75.50	24.50
600 μm	142	28.51	46.99	53.01
300 μm	138	27.71	19.28	80.72
150 μm	74	14.86	4.42	95.58
< 150 μm	24	4.42	0.0	100

5.2.2 Preparation of specimens

There were two test variables in the experiments: water-cement ratio and maximum size of coarse aggregate. Two water-cement ratios of 0.45 and 0.56 and two maximum sizes of coarse aggregate of 10mm and 20mm were used. Therefore, there are four batches altogether, the mix proportion of which are shown in Table 5-2. Batches 1 and 3 are the mix proportions recommended by RILEM (2001) while the mix proportions for Batches 2 and 4 were calculated based on BRE (1997). For the batches 2 and 4, a realistic smaller water-cement ratio (than Batches 1 and 3) was chosen as 0.45. Following the procedures outlined in BRE (1997), the proportions of fine and coarse aggregates can be determined. In the Table 5-2, the mix proportion is by weight in the order of cement, fine aggregate, coarse aggregate and water. For each batch 6 specimens were cast.

Table 5-2 Mix proportions for concrete

Batch No.	Source	Mix Proportion	Max Size of Aggregate(mm)	No of Specimens
1	RILEM	1:2:2.5:0.56	10	6
2	Designed	1:1.27:2.57:0.45	10	6
3	RILEM	1:2:2.5:0.56	20	6
4	Designed	1:1.27:2.57:0.45	20	6

To mix the fresh concrete thoroughly and consistently, the concrete mixer, shown in Fig. 5-4 was used. Cylindrical specimens were produced by the mould (shown in Fig. 5-5) with nominal length of 150mm and nominal diameter of 150mm. All the moulds were applied with the mould oil at the inner surface before casting. The oil formed a tenacious oily film on the mould surface that prevented rusting of mould and the released agents which prevented concrete clinging to the moulds. The specimens were then compacted on the vibrating

table in the laboratory. The entire compacted specimens were left for at least 24 hours in the room temperature of about 20^0-22^0 C.

Figure 5-4 Concrete mixer

Figure 5-5 Cylindrical mould used in the experiments

Curing controls the rate and extent of moisture loss from the concrete during cement hydration to ensure a high degree of hydration. The specimens were cured in water tank located in the laboratory under the temperature of 20^0C. After 28 days of curing, all of the specimens were taken out of the water tank and notched. A circumferential notch was cut off each specimen with depth of 15mm and width of 2-5mm at the middle of the cylinder by electric saw, as shown in Fig. 5-6.

Figure 5-6 Work platform for notching the specimen

After notching, the specimens were glued to two steel plates at the two ends respectively. The adhesive used in this test was Sikadur ®-31 CF Normal, a 2-part epoxy adhesive. The colour of part A is white and part B is dark grey which gives a mixture of concrete grey. Part A and B were mixed together (in a ratio of 2:1 by weight or volume – approximately equivalent) for at least 3 minutes until the mixture became smooth and a uniform grey colour. This adhesive is designed for use at temperatures between +10ºC and 30 ºC. The tests took place in the season of autumn/winter and the temperature of testing environment was kept at about +10ºC. Under this temperature, the tensile strength of the adhesive was 14-20 MPa which is sufficient for this test. Once the gluing process was completed, a small load was applied on the glued specimens overnight to ensure the strength of the adhesive was achieved as shown in Fig. 5-7.

Figure 5-7 Applying small loads on the glued concrete specimen.

5.2.3 Test procedure

Open-loop tests are normally used to determine the maximum load but only to certain approximate values (Van Mier and Van Vliet, 2002). To obtain stable post-peak response, a servo-controlled (closed-loop) testing machine was employed. It works in a way that the displacement across the notch was recorded as the feedback signal to control the loading. In this experiment, the servo-hydraulic Dartec testing machine, equipped with an electronic system for data acquisition, was used, as shown in Fig. 5-8. Double plates were used at both ends of the specimen in order to ensure the uniform stress distribution in the concrete specimens. One plate was glued to the specimen and bolted to the other plate which was connected to the platen of the machine. Both ends were clamped to the testing machine and were parallel to each other, to avoid rotation of the specimen. Three linear variable differential transducers (LVDTs) were fixed around the circumference of the specimen as shown in Fig. 5-9 to record the displacements and send the average of them to the control system. Three LVDTs were arranged at equal distances along the perimeter of the cylinder to ensure the uniform displacement. The loading rates applied were 0.005mm/min up to a displacement of 0.1mm and 0.1mm/min until the completion of the test.

Figure 5-8 Setup of direct tensile test

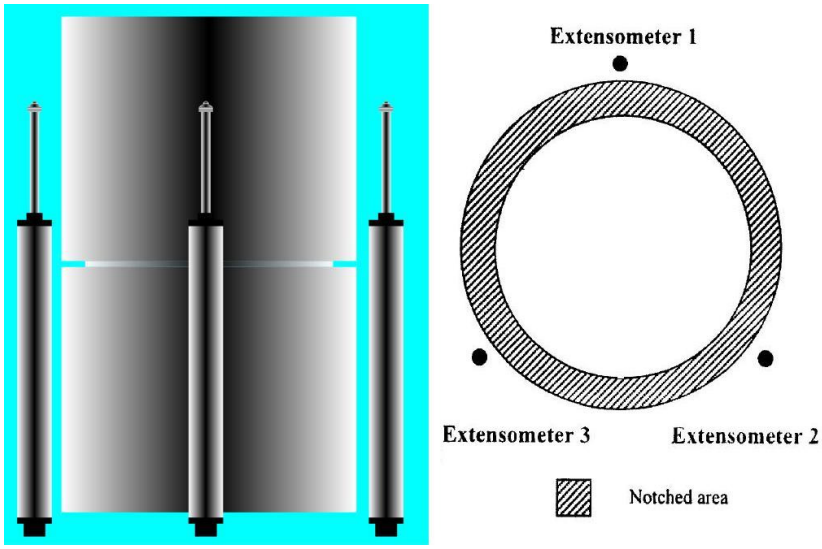

Figure 5-9 Illustration of the specimen and arrangement of LVDTs

The success of the test, i.e., to obtain a full stress and displacement curve, considerably depends on whether the loading chain (specimen and loading platen) can be perfectly aligned. If the alignment was not straight, there would be an eccentricity added to the specimen which would result in a bending moment. Therefore, the specimen will not be in pure tension. The eccentricity can occur either at the beginning of the test or at the cracking of the specimen. In the latter case, it can only be relied on the stiffness of the testing rig. In the former case, however, pre-loading was carried out before the test to eliminate eccentricity. The methodology was:

I. to apply a small load under loading control, and check if the three readings from the three transducers are the same;

II. to increase the load slightly to see if all the three transducers have the same increase;

III. if two "yes" from the steps I and Π, then switch to displacement control and continue;

IV. if there is a "no" from either step I or Π, unload it and calibrate the testing setup, then try the procedures again until it is "yes".

5.3 Results and analysis

In this section, the results from the direct tensile tests of concrete are presented. Some tests were very successful, i.e., a complete stress-displacement curve obtained, but some were less successful, i.e., the softening part was not obtained. Successful tests were mainly from the specimens with water-cement ratio of 0.56. Discussions on the results and their variations due to specimen size and testing conditions are then provided. It is followed by the suggestions on how to effectively conduct the direct tensile tests of concrete.

5.3.1 Results

The servo-controlled system in the testing machine is automatically operated by the computer as shown in Fig. 5-10. The main outputs of the test are the "Current Load" and "Transducers Average" from which the stress-displacement curve can be produced as shown below. A sample of raw data from the data logger is shown in Table 5-3.

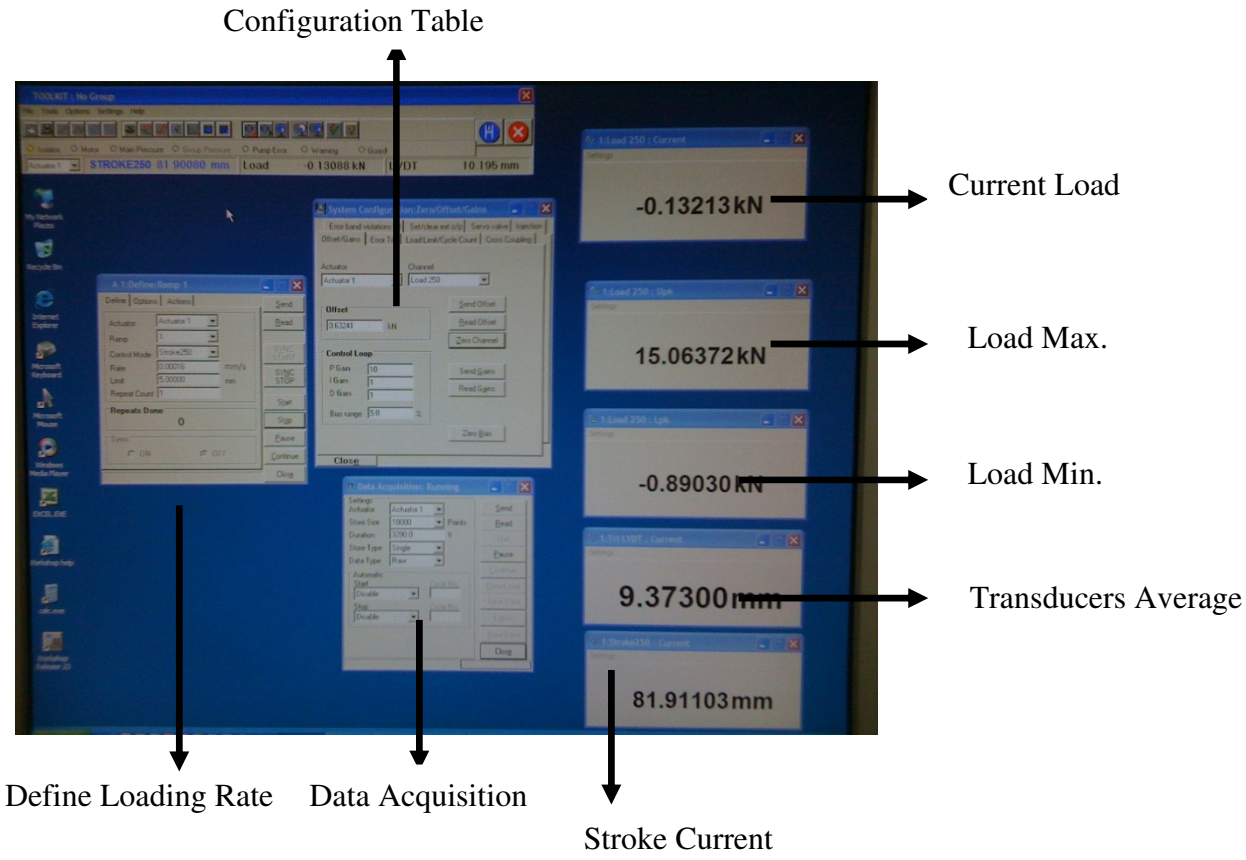

Figure5-10 Control system in the testing machine

Table 5-3 A sample of raw data from the testing system

Time (Min:Sec)	Load (KN)	LVDT1 (mm)	LVDT2 (mm)	LVDT3 (mm)	Average LVDT (mm)
06:48.5	0.004	0	0	0.002	0.000667
06:49.0	0.004	0	0	0.002	0.000667
06:49.5	0.018	0	0	0.002	0.000667
06:50.0	0.027	0	0	0.002	0.000667
06:50.5	0.069	0	0	0.002	0.000667
06:51.0	0.396	0	0	0.002	0.000667
06:51.5	0.606	0	0	0.002	0.000667
06:52.0	0.995	0	0	0.002	0.000667
06:52.5	0.888	0.001	0	0.002	0.001
06:53.0	1.118	0	0	0.002	0.000667
……	……	……	……	…….	……
07:01.0	-2.228	0.001	0.001	0.002	0.001333
07:01.5	-2.183	0.001	0	0.002	0.001
07:02.0	-2.027	0.001	0.001	0.002	0.001333
07:02.5	-1.993	0.001	0.001	0.002	0.001333
07:03.0	-2.38	0.001	0	0.002	0.001
07:03.5	-2.364	0.001	0.001	0.002	0.001333
07:04.0	-2.402	0.001	0.001	0.002	0.001333
07:04.5	-3.776	0.001	0.001	0.002	0.001333
07:05.0	-4.727	0.001	0.001	0.002	0.001333
07:05.5	-5.167	0.001	0.001	0.002	0.001333
07:06.0	-5.36	0.001	0.001	0.002	0.001333
07:06.5	-5.402	0.001	0.001	0.002	0.001333
07:07.0	-5.225	0.001	0.001	0.002	0.001333
07:07.5	-5.111	0.001	0.001	0.002	0.001333
07:08.0	-4.881	0.001	0.001	0.002	0.001333
07:08.5	-5.069	0.001	0.001	0.002	0.001333

For specimens with maximum size of coarse aggregate of 10mm and water-cement ratio of 0.56, the relationship of the stress and the average displacement across the notch is shown in Fig. 5-11. Fig. 5-11 is produced based on the average values of data from these successful tests (3 out of 6 specimens were successfully tested). The points on the three successful curves with same values in the X-axis (displacement) were selected and their values in the Y-axis (stress) were averaged. In the cases that the X-axis values were not the same for the three curves, linear interpolation was used to obtain the points which shared the same X-axis values on the three curves. The results from the other 3 specimens were not used due to the effect of eccentricity and hence sudden failure at the peak load as shown typically in Fig. 5-12. It has been observed that for tests with eccentricity effect, the specimen suddenly broke into two parts when the tensile stress approaching the peak stress of concrete. Obviously, the linear descending curve in Fig. 5-12 cannot reflect the real fracture behaviour and thus is not useful. Similar curves to Fig. 5-12 have been obtained for the other batches.

As illustrated in Fig. 4-1b, the area under this curve is fracture energy G_f (N/mm) and the slope of the elastic part of the curve prior to peak load is penalty stiffness. Since cracks were initiated from the notch, Fig. 5-11 can be reformulated to the stress-crack width curve as shown in Fig. 5-13, by neglecting the elastic unloading. Fig. 5-13 can be used as material inputs in the nonlinear fracture models, i.e. cohesive crack model, to quantify the value of energy dissipation. The curve of $\sigma(w)$ influences the prediction of the structural response considerably and the local fracture behaviour, i.e. the crack opening displacement, is particularly sensitive to $\sigma(w)$ (Shah *et al*., 1995).

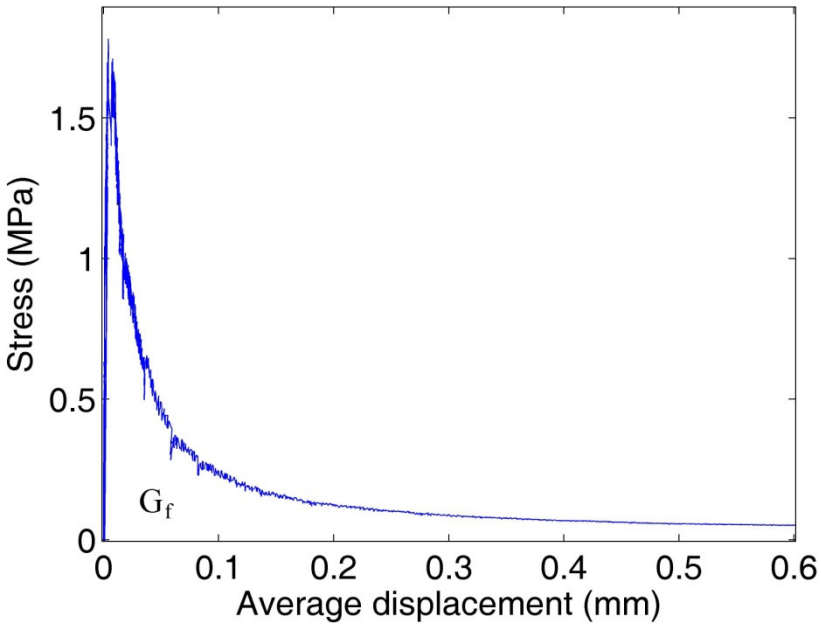

Figure 5-11 Stress-displacement curve with softening curve

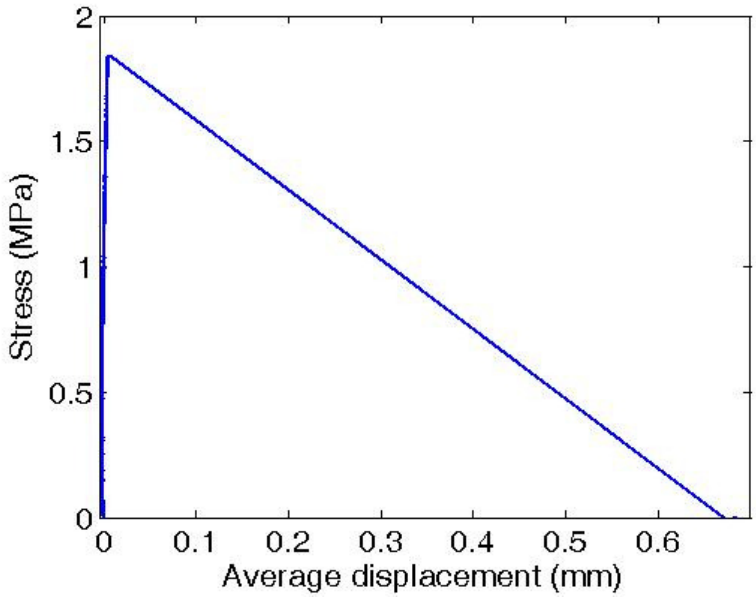

Figure 5-12 Stress-displacement curve without softening curve

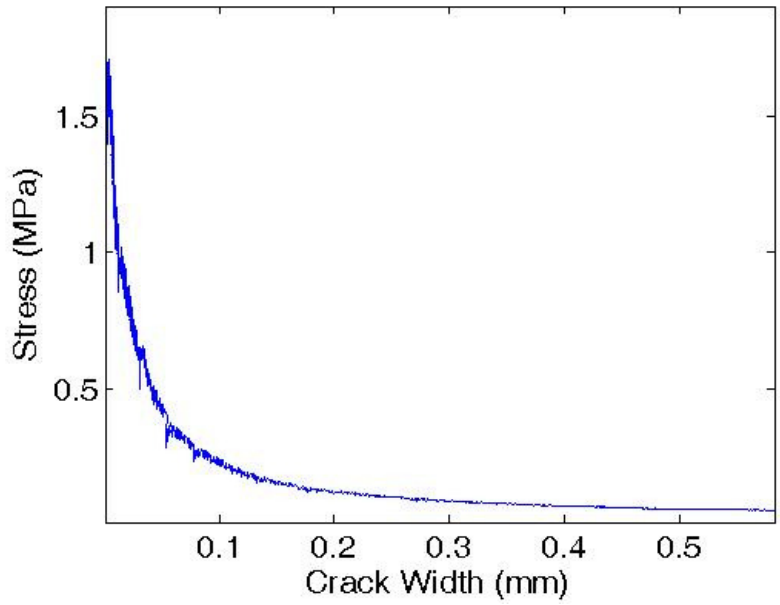

Figure 5-13 Stress-crack width curve

5.3.2 Discussions

It can be seen from Fig. 5-11 that after the stress reaches the peak value, it decreases rapidly at the initial stage (until the displacement of about 0.07mm). This means a small increase in displacement leads to a significant decrease in stress. Also the energy required for crack propagation, i.e., the area under the curve in Fig. 5-11, is little for such magnitude of decrease of stress, which reflects the brittle nature of the concrete. After displacement 0.07mm, the curve becomes flatter and for an increment of displacement, the drop of stress is much less. This stage shows that concrete is a quasi-brittle material. In some literature, e.g. Barpi and Valente (2005), the softening curve is modelled by a bilinear shape. Moreover, Roesler *et al.* (2007) proposed two fracture energy terms to represent these two phases of energy dissipation.

There have been some augments that the fracture parameters such as $f_t^{'}$ and G_f are not material properties but depend on the specimen size and testing conditions. However, a more widely accepted view is that the dependency of the specimen size is due to the fact that concrete is a heterogeneous material and the dependency of the testing conditions come from the susceptibility of

eccentricity in direct tensile tests. Due to the heterogeneous nature, the fracture properties of concrete vary at different points in concrete. This heterogeneity may induce stress/strain gradient in the specimen when load is applied. This also explains why the fracture energy is constant for specimens with large size. In addition, the measured fracture parameters are affected by the testing conditions, such as, rate of loading, alignment of loading chain etc. However, these two sources of dependency can be eliminated by employing a standard testing method and using standard specimens. For this purpose, RILEM developed a standard for direct tensile tests of concrete, e.g. RILEM TC 162-TDF (2001). The fracture parameters measured from the experiments following RILEM TC 162-TDF (2001) are regarded as the material properties. Moreover, the procedure proposed in Section 5.3.3 to eliminate the eccentricity induced during the testing, is effective and can work as a supplement to the standard test method.

5.3.3 Suggestions

It is well known that direct tensile test is very difficult because it is a precise test and largely relies on the testing equipments and skills of technicians. To obtain reliable results, some technical problems have to be solved as follows:

- It is important to align the specimens and the loading platen. Non-perfect alignment may result in eccentricity when load is applied. The presence of eccentricity leads to the stress gradient along the notched surface which makes the results measured not exact uniaxial. The alignment can be achieved in the preloading stage, by observing the readings from the three transducers and adjusting the loading chain. If the readings are the same or with a small variation, it can be assumed that the whole system is properly aligned.
- Secondary flexure must be avoided. Secondary flexure is a flexure when a bending moment is developed by eccentricity which is induced during loading. There are a number of sources that may introduce secondary flexure, e.g., the specimens are not properly manufactured. For example, if the concrete specimen has clear difference in strength at different sides,

a crack will be initiated from the weak side rather than simultaneously from all sides. Cracking at one side makes the deformation of the specimen not uniformly distributed along the notched surface. Additionally, a steep decrease in the stress just after the peak stress, as shown in Fig. 5-4a, can cause secondary flexure. This is because brittle nature makes the crack propagation more dynamic rather than quasi-static in concrete.

In addition to technical problems mentioned above, it should be noted that the testing rig must be stiff enough. This is crucial to obtain stable crack propagation since the scale of deformation of concrete in tension is very small. Employing three transducers to send feedback signal to the servo-controlled system is another important measure. Only by satisfying these requirements, the results can be obtained or the results obtained from the tests are useful.

5.4 Conclusions

In this chapter, a programme of direct tensile tests of plain concrete has been presented. Three linear variable differential transducers are used to ensure the average displacement across the notch is used as feedback signal to the control system. A complete stress-displacement curve of plain concrete is obtained from the tests and the stress-crack width curve as well as the fracture energy is then calculated. It has been proven that the plain concrete still has residual strength after its peak stress. It has also been observed that the steep decrease of stress reflects the brittle nature of concrete at crack initiation and the flatter decrease of stress represents the quasi-brittle nature of concrete. It has been found difficult to obtain successful test results, i.e., a complete stress-displacement curve, and the difficulties have been evaluated. It has been suggested that a simple procedure is developed to eliminate the problem of non-perfect alignment of the specimen. It can be concluded that once all the requirements of RILEM TC 162-TDF (2001) are satisfied, the results obtained can represent the real material property of concrete and can be used as fracture parameters in the nonlinear fracture mechanics models both analytically and numerically.

CHAPTER 6

ANALYSIS AND DISCUSSIONS

6.1 Introduction

The crack width of concrete induced by reinforcement corrosion and applied load has been derived analytically and numerically in Chapters 3 and 4. As a means of verification, it is necessary to compare the results from both methods. With the use of the same inputs, i.e., same material properties, same corrosion and applied load, and same boundary conditions, the two sets of results are comparable. The only possible instinctive difference between the methods is that the analytical method assumes the crack smeared and uniformly distributed in the concrete cylinder, whilst the numerical method uses the discrete crack approach. However, these two approaches of dealing with cracks are theoretically equivalent to each other as explained in Bažant and Planas (1998). After the methods are verified, a parametric study is conducted to investigate the effects of various factors that affect the cracking and crack growth. This includes a comprehensive range of factors, i.e., material factors, geometric factors, external factors (such as corrosion and applied load) and numerical techniques. A parametric study is useful for engineers or analysts, from the practical perspective, if the relationships between the assessment criteria, i.e. crack width, and the design and external factors, i.e. geometry and corrosion rate, need to be established. Discussions on the results and suggestions for the analytical and numerical modelling are also provided.

6.2 Verifications of developed methods

It has been demonstrated that the analytical and numerical methods can both be used to determine the crack width of concrete under combined reinforcement corrosion and applied load. To verify both methods, the results obtained from each should be comparable, when the same inputs, such as material properties and loading conditions, are applied. In this section, the analytical and numerical methods are first compared in material models including the failure criteria, and loading conditions, prior to the comparison in the results.

6.2.1 Comparison of material models and failure criteria

Since concrete is a quasi-brittle material, the tensile stress initially increases up to the tensile strength of the concrete and then decreases until the strength is deteriorated to zero, with constant increase of the tensile strain/displacement. Both methods treat the material property as two parts: linear elasticity prior to peak stress and inelastic behaviour (strain softening) after peak stress. For the linear elastic behaviour in the analytical method, Eq. 3.14 (a and b) describes the stress-strain relationships in the radial and tangential directions. It is based on Timoshenko's theory of elasticity (Timoshenko and Goodier, 1970) and applies to the numerical method also. In the numerical method, Young's modulus E and Poisson's ratio υ_c are necessary to define the elastic behaviour, the way of which is the same as expressed in Eq. 3.14. Thus, in essence both methods are the same in material models.

For the inelastic behaviour after the peak stress, both methods employ damage parameters to account for the degradation of material stiffness, i.e., α in the analytical method and D in the numerical method. It has been found that α and D are theoretical equivalent to each other. The relationship between these two damage parameters is shown as follows

$$D = 1 - \alpha \tag{6.1}$$

α and D are respectively calculated from Eqs. 3.27 and 4.10. They both relate to the fracture energy G_f and the tensile strength $f_t^{'}$. The only possible difference is that α is dependent on the tensile strain and cannot be directly user-specified while D can be either determined by the displacement of the cohesive element or manually defined by users. The use of displacement rather than strain in the constitutive model of numerical method is because the application of strain to measuring the crack width will introduce severe problem of mesh sensitivity, however, it can be used without any problem in analytical method.

The residual tensile stress in concrete by either analytical or numerical method is calculated in terms of α or D. Fig. 6-1 shows the schematic of the residual tensile stress in terms of α, if an undamaged stress σ_u beyond the peak stress is selected. Since α is defined as E_r / E_{ef} as formulated in Eq. 3.23, the residual stress σ can be expressed as follows

$$\sigma = \alpha\sigma_u = \alpha E_{ef}\varepsilon_\theta(r) \tag{6.2}$$

Recall the calculation of the residual stress in the numerical method as shown in Fig. 6-2. The residual stress is dependent on the penalty stiffness, displacement and damage parameter D. With all these three parameters known, the residual stress can be obtained as follows

$$\sigma = (1-D)\sigma_u = (1-D)K_p\delta \tag{6.3}$$

where K_p is the penalty stiffness and δ is the displacement.

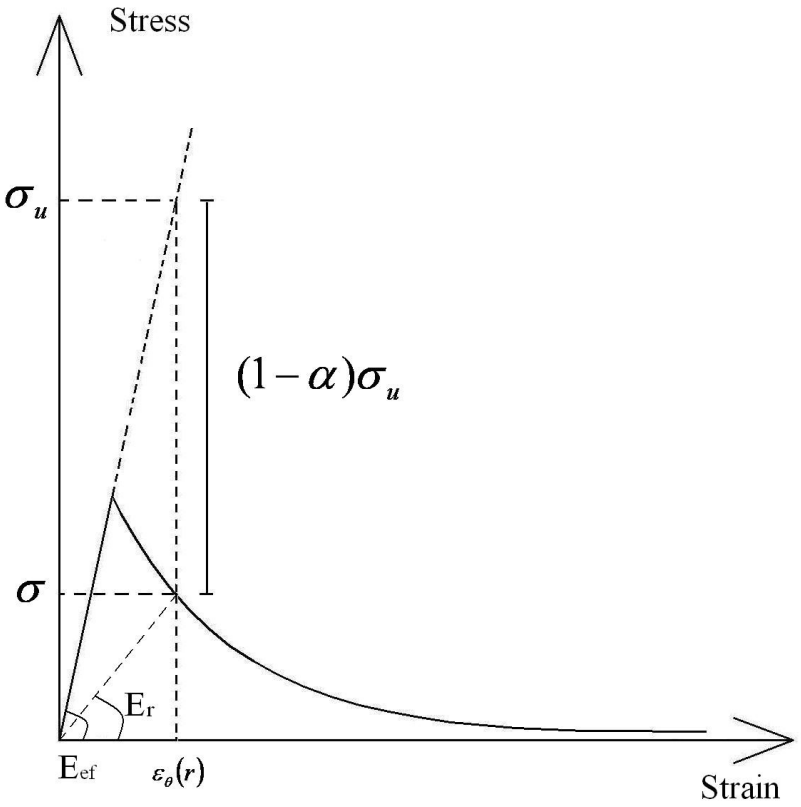

Figure 6-1 Determination of the residual tensile stress in terms of α

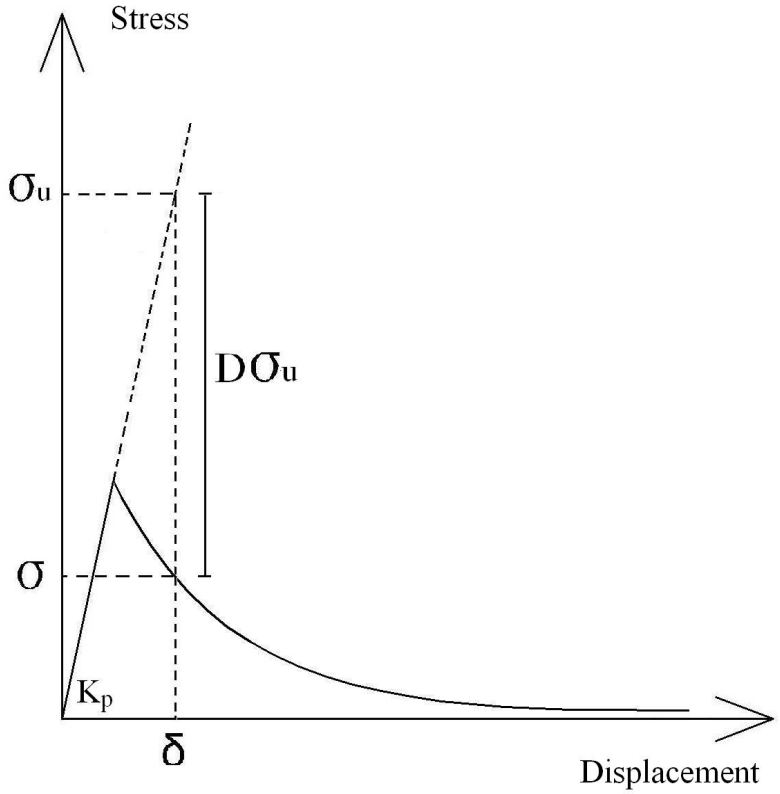

Figure 6-2 Determination of the residual tensile stress in terms D

It is, therefore, reasonable to suggest that the material models in both of the analytical and numerical methods are comparable. The failure criteria for both of the analytical and numerical methods consist of two parts: crack initiation and damage evolution at a point of material and of an element respectively. The crack initiation criteria are exactly identical for both methods that is a crack will initiate once the tensile stress at a material point or of an element reaches the tensile strength of the material. The control equations are Eqs. 3.36 and 4.8 for the analytical and numerical methods respectively. As for the damage evolution, α changes from 1 to 0 and D varies from 0 to 1 which represent the degree of damage. Between the values of 1 – 0 or 0 – 1, damage is considered to have occurred but there is still stiffness or stress existing to maintain at a point or of an element not to be completely separated.

6.2.2 Comparison of loading conditions

The smeared crack approach is adopted in the analytical method which means the property of concrete including cracks is uniformly smeared over the circumference of the concrete cylinder. The mechanical property of the cylinder, therefore, is the same at any points of the material. If the load is uniformly applied to the inner boundary of the cylinder, the results, i.e., the tangential stress or strain, should with no doubt be the same at all the points of the same radius. In the numerical method, however, the discrete crack approach is used which alters the distribution of the material property of the concrete cylinder. More precisely, the discrete crack approach divides the cylinder into a cohesive interface and the rest as bulk concrete. These two parts have different mechanical properties and thus the results cannot be uniformly distributed in a polar coordinate system even though the load is uniformly applied to the inner boundary of the concrete cylinder.

As discussed in Section 4.3.2, uniformly distributed displacement in the numerical method will lead to dramatically large stress in the cohesive elements. More importantly, a cohesive element is primarily intended to model the bonded interfaces where the interface thickness is negligibly small. In this case, the displacement cannot be directly applied to the cohesive elements. For this reason, a method on how to arrange the load has been proposed in Section 4.3.2. Although the loading conditions are different for the analytical and numerical methods, they are more technical rather than fundamental. Therefore, the variation in the results must be minor.

To prove that the loading conditions in the analytical and numerical methods do not vary the results, the elastic response of the numerical method is obtained. Although the displacement cannot be evenly applied to the inner boundary of the cylinder, the proposed arrangement of the displacement should also lead to uniform (or relatively uniform) distribution of the tangential/hoop stress and radial stress, during elastic stage. Fig. 6-3 shows the contour of the nodal tangential stress. It can be seen that the placement of the cohesive interface and the application of the displacement do not alter the symmetry of the distribution

of the tangential stress. The colour bands represent the contour of tangential stress. It shows that the elements with the same radius have the same magnitude of stress. The symmetry will not be altered until the cohesive element is cracked. To achieve the uniformity of stress distribution, the penalty stiffness is the control parameter. For this purpose, a parametric study on penalty stiffness will be carried out in the following section where the effect of penalty stiffness on the uniformity of stress distribution can be obtained.

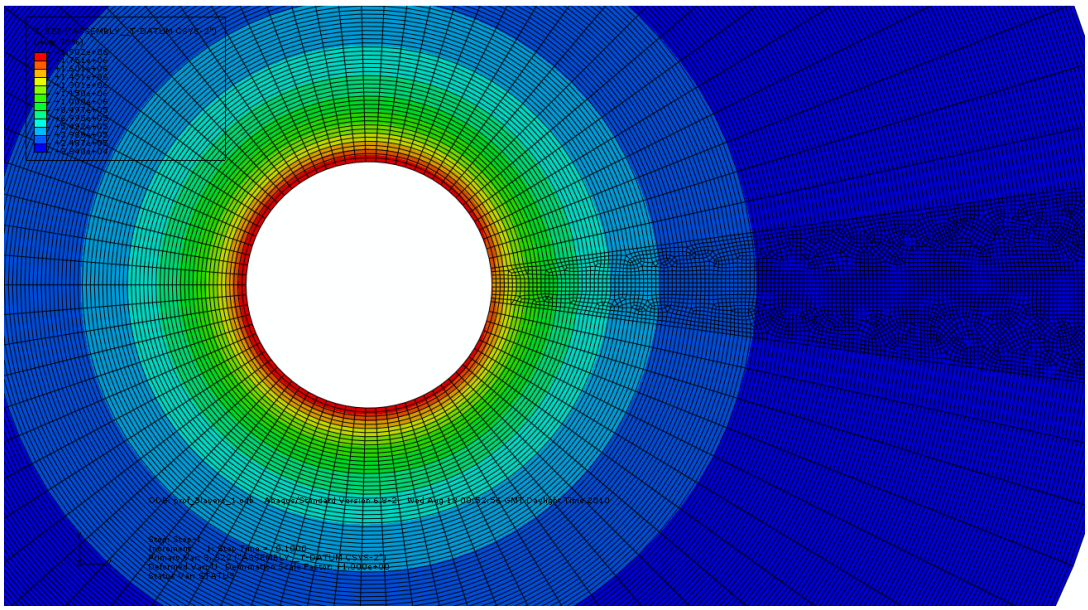

Figure 6-3 Contour of the nodal tangential stress at elastic stage

6.2.3 Comparison of results

It has been demonstrated that the material model including the failure criteria and boundary conditions are comparable for both analytical and numerical methods in the preceding sections. By using the same inputs as listed in Table 6-1, the results of concrete crack width from both methods can be compared, which are shown in Fig. 6-4. The values of input variables are taken simply mainly from Li (2003) and Liu and Weyers (1998) for demonstration purpose. It can be seen that the numerical results are in good agreement with the analytical results. The crack width from both results increases with time as expected. The crack initiation times obtained from both methods are shown in Table 6-2. It can be seen that the difference is quite small – 1.7%. The crack initiation time

reflects the end of pure elasticity and start of development of inelasticity. The surface cracking times are 1.38 years and 1.49 years for analytical and numerical methods respectively, shown in Table 6-3. At the time of surface cracking, there is an abrupt increase in crack width which in essence reflects the quasi-brittle nature of concrete. This means for a newly crack point there is a sudden decrease in its stiffness. The abrupt increases of the crack width obtained from both methods are compared in Table 6-4. The average difference in crack width between two methods is about 4% within 10 years and the maximum difference occurs at about 2.5 years which is 12%. Such a difference is mainly caused by the assumption of constant α.

Table 6-1 Values of basic variables used for comparison

Description	**Symbol**	**Values**	**Sources**
Inner radius	a	6mm	Li (2003)
Outer radius	b	37mm	Li (2003)
Effective modulus of Elasticity	E_{ef}	18.82GPa	Li (2003)
Poisson's ratio	ν_c	0.18	Li (2003)
Tensile strength	$f_t^{'}$	5.725MPa	Li (2003)
Fracture energy	G_f	120N/m	Pantazopoulou and Papoulia (2001)
Corrosion current density	i_{corr}	$0.3686\ln(t)+1.13$	Li (2003)
Coefficient related to corrosion products	α_{rust}	0.57	Liu and Weyers (1998)
Density of corrosion products	ρ_{rust}	3600kg/m^3	Liu and Weyers (1998)
Density of steel	ρ_{st}	7850kg/m^3	Liu and Weyers (1998)

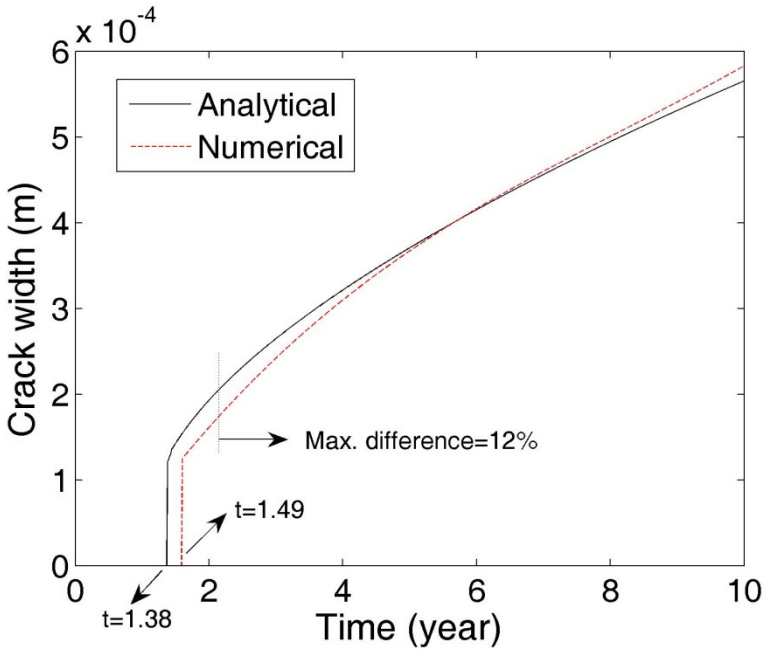

Figure 6-4 Crack widths as a function of time by both methods

Table 6-2 Comparison of time to inner boundary cracking t1

Method	Time to inner boundary cracking, years	Difference, %
Analytical	0.57	—
Numerical	0.58	1.7

Table 6-3 Comparison of time to surface cracking t2

Method	Time to surface cracking, years	Difference, %
Analytical	1.38	—
Numerical	1.49	7.9

Table 6-4 Comparison of the crack width at the time of surface cracking

Method	Crack width at the time of surface cracking, m	Difference, %
Analytical	1.21	—
Numerical	1.23	1.6

It has been observed that the results obtained from the analytical and numerical methods agree with each other very well except for the time to surface cracking which has a difference of 7.9%. The variation in the time to surface cracking could be because of a few reasons, such as, introduce of viscosity in the numerical method, different loading conditions and the assumption of α in the analytical method. The effect of loading conditions is considered as negligibly small since it has little effect on the elastic stage. The introduction of viscosity in the numerical method can significantly improve the convergence. However, it can also slightly vary the results depending on how small the value it is used. A parametric study on the effect of viscosity will be presented in the following section. Moreover, the stiffness reduction factor α is assumed to be constant along the cracked surface of the concrete cylinder in the redial direction which can be another possible reason.

6.3 Parametric study

One of the advantages of both the analytical and numerical methods is that the effect of contributing factors on crack width can be studied with relative ease. Based on literature review of Chapter 2, several important factors are selected to investigate their effects on the crack width, which range from the external factors, i.e. corrosion and applied load, to internal factors, i.e. concrete property and geometry. The effects of numerical techniques, i.e. viscosity, on the results are also investigated.

6.3.1 Effect of corrosion rate on crack width

Corrosion rate affects the pressure exerted on the inner boundary of the concrete cylinder. Effect of corrosion rate on crack width is examined by using 4 different corrosion rates – 0.5, 1, 5 and 10μA/cm^2, as shown in Fig. 6-5. Constant corrosion rate is assumed. It can be seen that the corrosion rate i_{corr} affects both cracking and crack development. The cracking time is quite sensitive to corrosion rate when it is smaller than 1 μA/cm^2, but almost insensitive once it is greater than 5 μA/cm^2. On the other hand, the crack width is affected by corrosion rate considerably over time. As is known, i_{corr} can only be determined on-site. Accurate measurement of i_{corr}, therefore, is necessary to the prediction crack width.

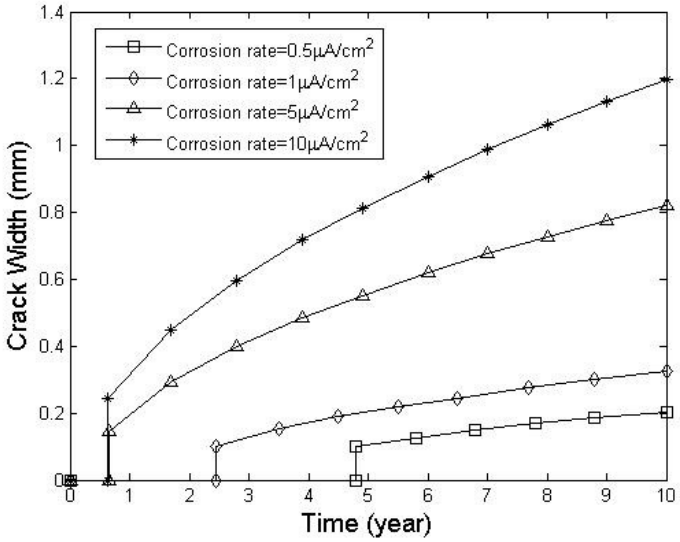

Figure 6-5 Effect of corrosion rate i_{corr} on crack width

6.3.2 Effect of applied load on crack width

Evidently, applied load also affects the pressure exerted on the inner boundary of the concrete cylinder. Three levels of applied loads (1, 2 and 3) are used to obtain the crack width, which are load-free, 1st scenario and 2nd scenario respectively. Recall the 1st scenario and 2nd scenario which assume the inner boundary of concrete cylinder is not cracked and cracked respectively. The

crack width curves are shown in Fig. 6-6. It can be observed that as the applied load increases, the crack appears earlier and develops faster. For the example of applied load 1, 2 and 3, the surface cracking times are 1.5, 1.4 and 1.3 respectively. As for the initial (abrupt) crack growth, the differences are minor. For the long term development of crack width, i.e., from 2 to 10 years, the trends of the three levels of applied load are identical. This demonstrates that the constant applied load (sustained load) does not significantly affect the long term crack growth.

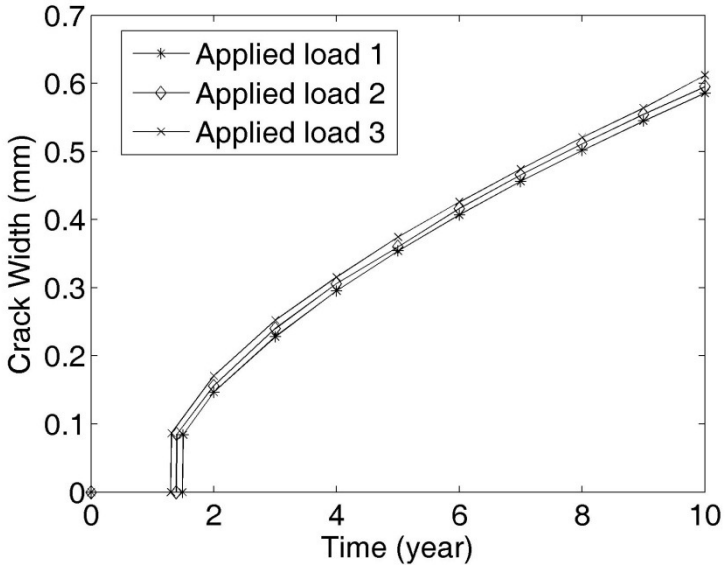

Figure 6-6 Effect of applied load on crack width

6.3.3 Effect of concrete property on crack width

Concrete property, i.e. concrete tensile strength, is a design variable that may affect the fracture property of concrete. In both of the analytical and numerical methods, the concrete tensile strength $f_t^{'}$ is used as a criterion of crack initiation. The effect of the tensile strength $f_t^{'}$ on crack width is shown in Fig. 6-7. In the figure, crack widths of 3 levels of tensile strength, i.e. 3MPa, 4MPa and 5MPa, are produced. It can be seen that an increase of $f_t^{'}$ proportionally delays the time to surface cracking. Also, the tensile strength $f_t^{'}$ affects the time to surface cracking more than crack width growth. In addition, the initial (abrupt) crack

growth is considerably affected by $f_t^{'}$. This has proven that the higher the strength of the concrete, the more brittle the structure is. It has also been found that the variation of $f_t^{'}$ does not alter the long-term crack growth.

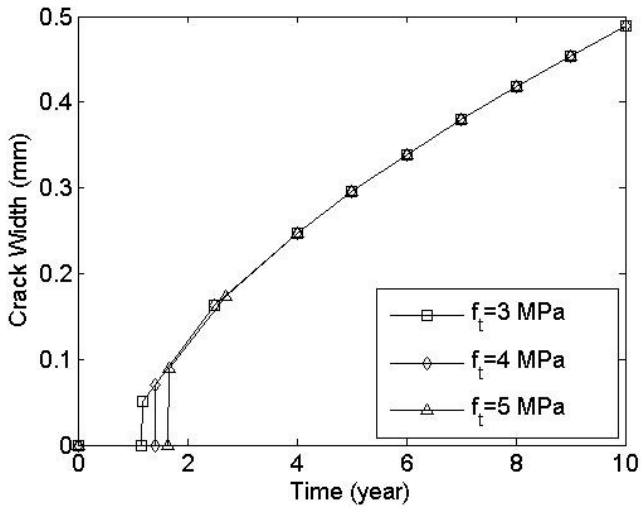

Figure 6-7 Effect of concrete tensile strength $f_t^{'}$ on crack width

6.3.4 Effect of geometry on crack width

The geometry herein corresponds to the sizes of the reinforced rebar and the concrete cover. Concrete cover is known as a physical barrier of the reinforcement to prevent the ingress of aggressive agents, i.e. chlorides. The geometry of the reinforced concrete can be represented by the ratio of concrete cover to reinforced rebar diameter C/D which is schematically shown in Fig. 3-1. The crack widths obtained from 3 geometries, i.e. C/D=2, C/D=3 and C/D=4, are then shown in Fig. 6-8. It indicates that in Fig. 6-8 the geometry represented by C/D significantly affects the surface cracking time. The surface cracking time is postponed from about 1.5 years to 2.8 years when C/D is increased from 2 to 4. The same as the tensile strength, the geometry as represented by C/D does not vary the long-term crack growth.

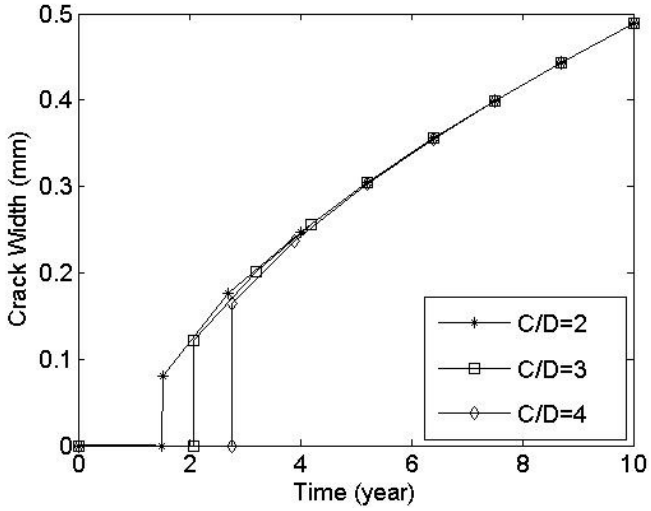

Figure 6-8 Effect of cover to bar diameter ratio C/D on crack width

6.3.5 Summary of the effects affecting crack width

A wide range of factors that affect the concrete crack width have been investigated, such as, corrosion rate, applied load, concrete property and geometry. These factors affect the crack width in different ways – some affects the surface cracking time, some affects the crack width (abrupt) at the time of surface cracking, etc. This section will summarize the effects of these factors on different stages of the crack width.

The time to surface cracking is an important index to show when the concrete structure/element will have the first crack on its surface. Amongst these factors, corrosion rate seems to be the most sensitive one to the time to surface cracking, followed by geometry, concrete tensile strength and applied load, which are shown in Table 6-5. It can be seen from Table 6-5 that applied load does not have significant effect on the time to surface cracking, with only 0.07 times change of the time to surface cracking for 2 times change of applied load.

Table 6-5 Effects on the time to surface cracking

Name of factors	Change of factors	Change of time to surface cracking
Corrosion rate	Increase to 2 times	Reduce to 1/2
C/D	Increase to 2 times	Increase to 1.87 times
Tensile strength $f_t^{'}$	Increase to 1.67 times	Increase to 1.5 times
Applied load	Increase to 2 times	Reduce to 0.93

For the long-term crack growth, only corrosion rate has significant effect on it. For instance, the crack width at 10years can be changed from 0.2mm up to 1.2mm for the corrosion rate from 0.5μA/cm^2 to 10μA/cm^2. Additionally, applied load seems to slightly affect the long-term crack width with the same magnitude change of crack width for different years. The geometry and concrete property have been found to have little influence on the long-term crack development.

6.3.6 Effect of viscosity on the results of crack width

As discussed, the results of materials exhibiting softening behaviour and degradation of stiffness will normally have severe convergence problems. A common numerical technique to solve the convergence difficulty is to employ a small viscosity value to regularize the constitutive equations, which has been presented in 4.4.3. Fig. 6-9 shows the effect of the viscous regularization on the predicted concrete crack width with three viscosity values used. Visco5e-4, Visco1e-3 and Visco5e-3 represent viscosity values of 5e-4, 1e-3 and 5e-3 respectively. The analytical result is also plotted in Fig. 6-9 for comparison. Smaller viscosity values, i.e. 1e-4, have been used but no converged results have been obtained. It can be seen from Fig. 6-9 that the viscosity value of 5e-4 matches best with the analytical results. Higher viscosity values provide better convergence, i.e., easier to converge and less increments required, but also affect the results more than the lower values of viscosity. Therefore, the viscosity coefficient should be kept as small as it can make the analysis be

converged. In this example, the appropriate value of viscosity coefficient is considered as 5e-4.

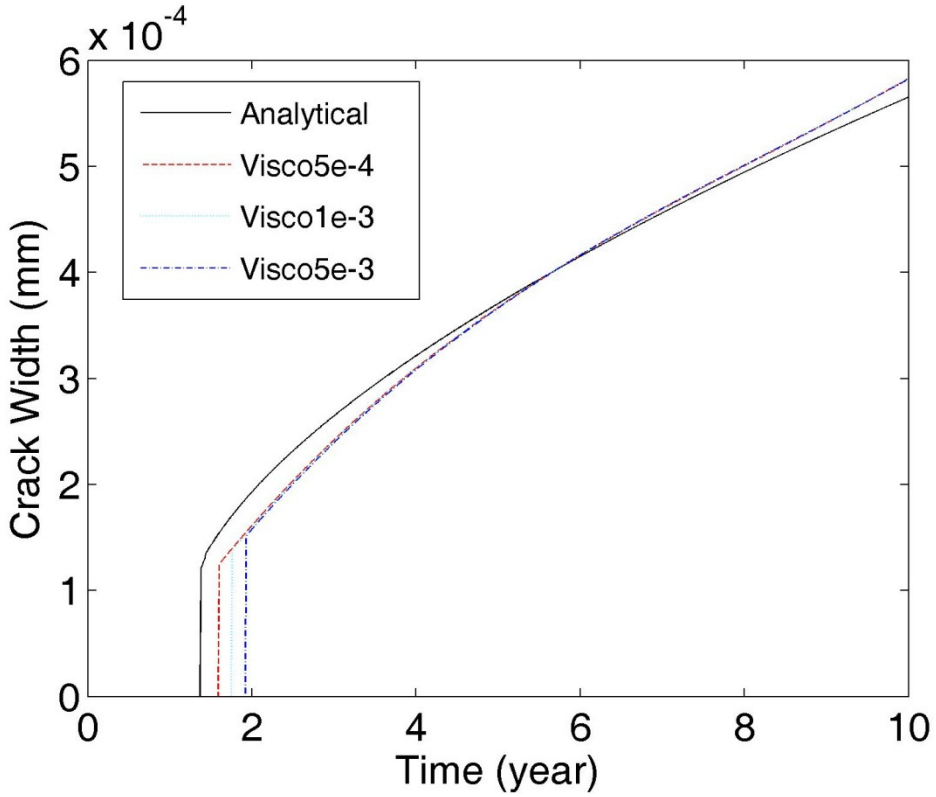

Figure 6-9 Effect of viscous regularization on the predicted concrete crack width

6.3.7 Effect of penalty stiffness on the results of crack width

Penalty stiffness is the cohesive stiffness as shown in Fig. 4-1b which controls how easily the cohesive interface deforms elastically. To investigate its effect on the results of concrete crack width, three values of penalty stiffness are employed and the results are shown in Fig. 6-10. Penalty1, Penalty2 and Penalty3 represent the values of penalty stiffness of 14100 GPa, 7050 GPa and 3525 GPa respectively. 14100 GPa was used in the worked example in Chapter 4. It can be seen that smaller penalty stiffness makes the surface cracking time earlier. There might be confusion herein that the penalty stiffness controls the elasticity of the cohesive elements but it does affect the concrete crack width which is mainly controlled by the inelastic behaviour of the cohesive elements. This can be explained by using Fig. 4-8 that the calculation of the residual

tensile stress is dependent on the undamaged stress σ_u which is determined by the penalty stiffness. Therefore the energy required to break a unit cohesive surface (fracture energy) is influenced by the penalty stiffness. It thus explains why the early stage of cracking, i.e., surface cracking initiation, is sensitive to the change of penalty stiffness. However, the long-term development of crack width seems not affected by the penalty stiffness. The reason for that could be the long-term development of crack width is considerably influenced by the tail of the stress-displacement curve as shown in Fig. 4-8. The tail of the curve is, however, negligibly affected by the penalty stiffness.

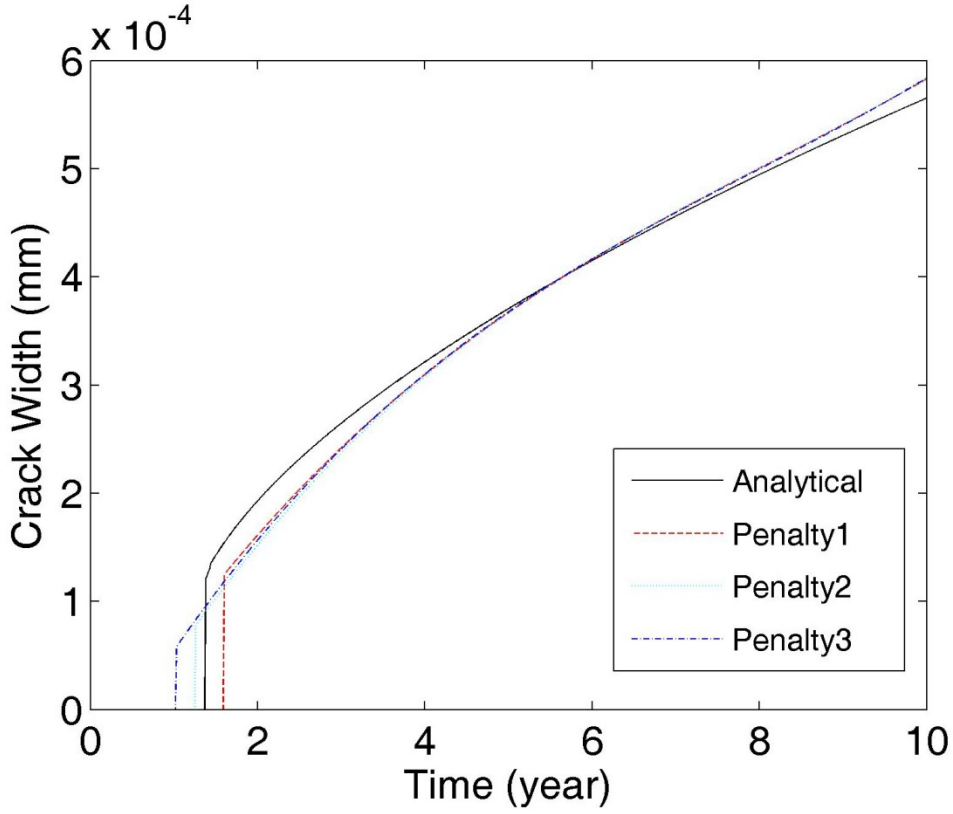

Figure 6-10 Effect of penalty stiffness on predicted concrete crack width

Figs. 6-11 to 6-13 show the tangential stress distributions during elastic stage for the three cases: Penalty1, Penalty2 and Penalty3. As discussed, there is no analytical equation to directly calculate the penalty stiffness. The determination of the penalty stiffness should be based on the requirements proposed in Section 4.2.3. To test whether the value of the penalty stiffness is reasonable or appropriate, the tangential stress distribution during elastic stage needs to be

produced. Ideally, the tangential stress should be uniformly distributed throughout the cylinder prior to the start of the inelastic behaviour. Therefore, the distribution in Fig. 6-11 is ideal, i.e., very uniform; the distribution in Fig. 6-12 is reasonably accepted with minor non-uniformity but the one in Fig. 6-13 cannot be accepted since non-uniformity of distribution of tangential stress is not negligible.

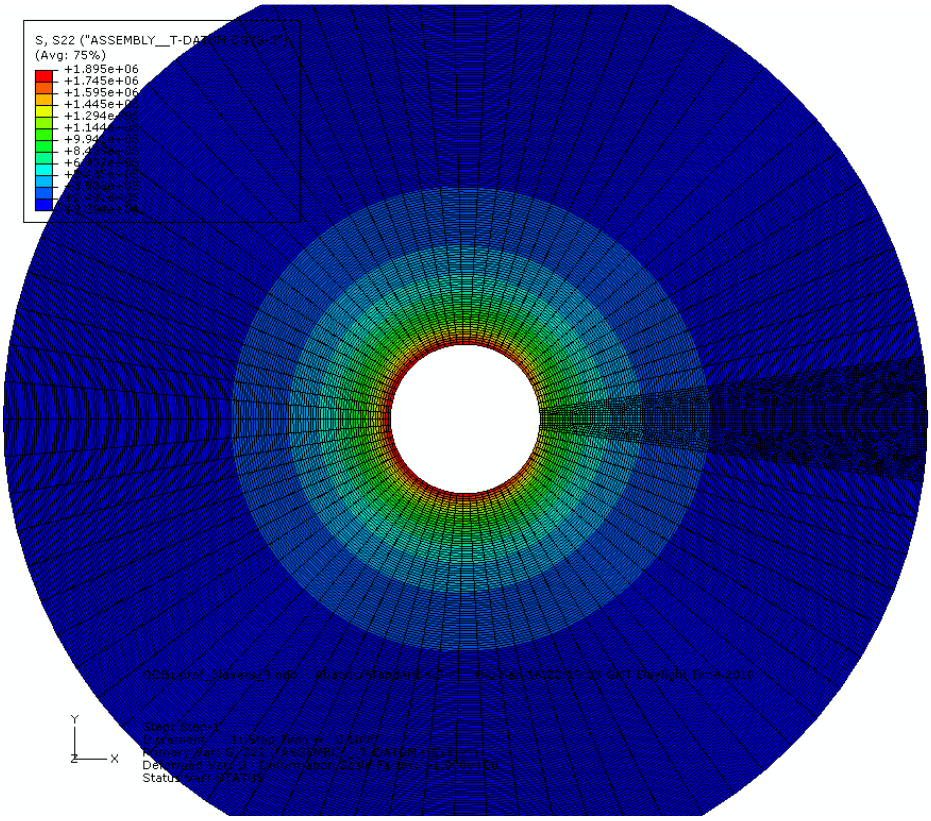

Figure 6-11 Tangential stress distribution (elasticity) for Panalty1

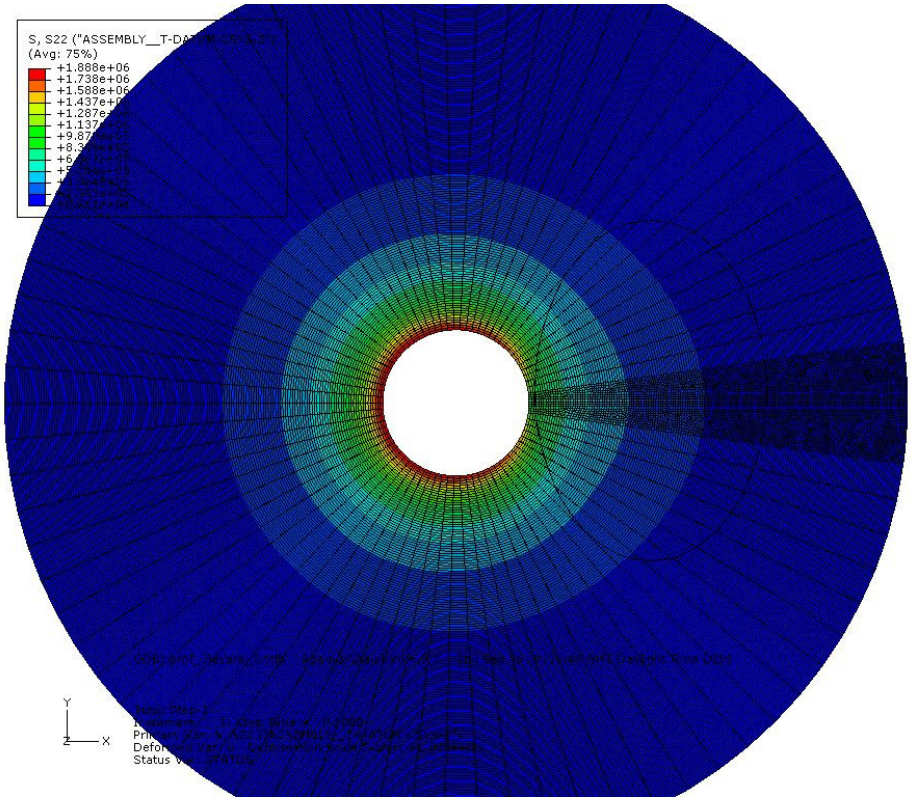

Figure 6-12 Tangential stress distribution (elasticity) for Panalty2

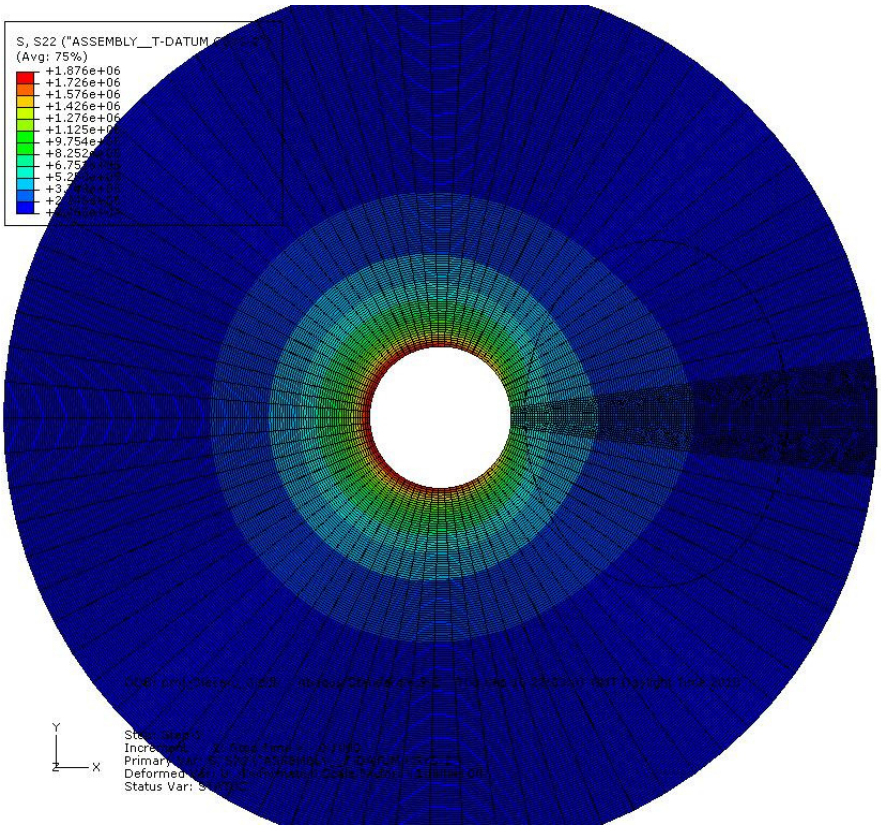

Figure 6-13 Tangential stress distribution (elasticity) for Panalty3

6.4 Observations and discussions

During the calculation and analysis of results, it has been noted that there is a common problem for both the analytical method and the numerical method. That is, there might be a “bump” in the stress-strain/displacement curve, as shown in Fig. 6-14 and 6-15. These two figures are produced respectively from the analytical method and numerical method. The bump phenomenon shows that the tensile stress increases even after its peak stress whilst the tensile strain/displacement continues to increase. However the correct form or the most accepted form of strain softening of plain concrete should be that the tensile stress gradually decreases with the increase of the tensile strain or displacement. The reason for the bump phenomenon in the analytical method has been explained in Section 3.6.1 and this section will focus on the interpretation of phenomenon in the numerical method.

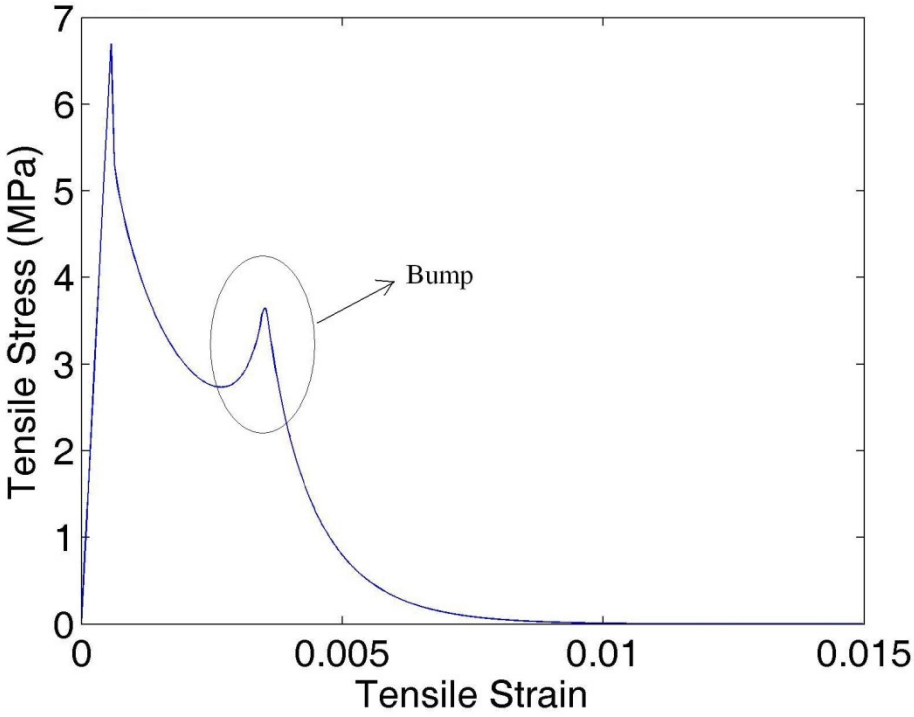

Figure 6-14 Bump phenomenon in the stress-strain curve

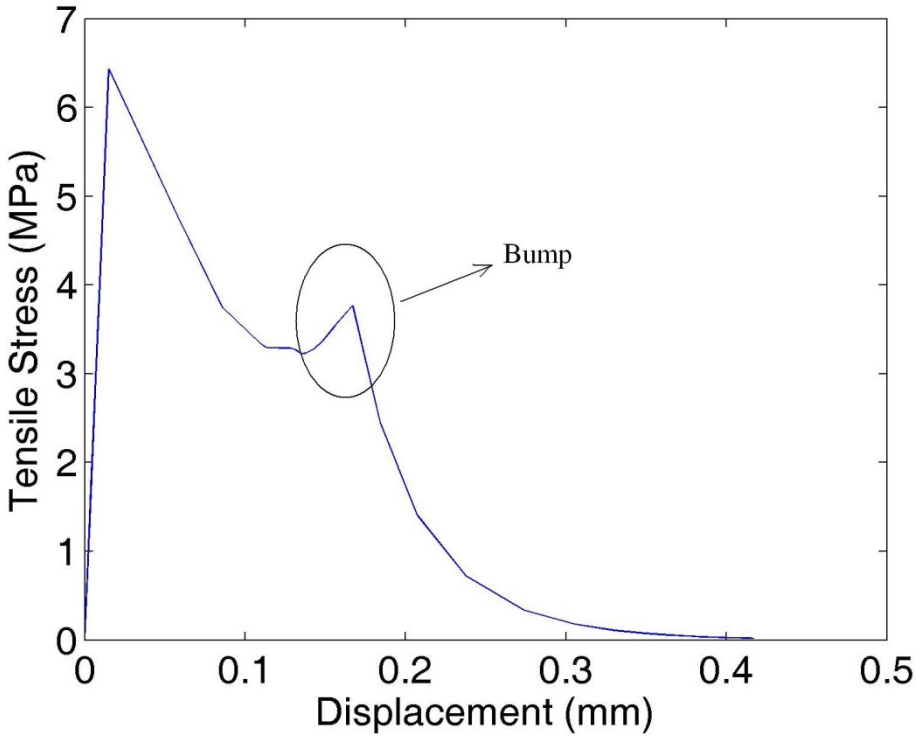

Figure 6-15 Bump phenomenon in the stress-displacement curve

If the damage evolution criterion is defined based on the displacement, a relationship between the damage parameter and the corresponding displacement after cracking initiation, i.e. ($D-\delta_{in}$), needs to be implemented in the material model of ABAQUS. ABAQUS will then automatically transform the relation of ($D-\delta_{in}$) to the residual stress – displacement ($\sigma-\delta$) relation. The displacement after cracking initiation δ_{in} is expressed as follows

$$\delta_{in} = \delta - \delta_0 \tag{6.4}$$

where δ_0 is the displacement at the peak stress.

As shown in Section 4.3.3, the equations on determining the residual stress σ and the undamaged stress σ_u are as follows

$$\sigma = (1-D)\sigma_u \tag{6.5}$$

$$\sigma_u = K_p \delta \tag{6.6}$$

With Eqs. 6.4 – 6.6 the points specified in terms of $D - \delta_{in}$ can be converted into $\sigma - \delta$. As an example, Table 6-6 shows the results of $\sigma - \delta$ converted from $D - \delta_{in}$ for two given points (A and B) in the stress-displacement curve, i.e., Fig. 6-2, by assuming δ_0 and K_p are 4.06e-7m and 14100GPa respectively.

Table 6-6 Results of conversion from $D - \delta_{in}$ to $\sigma - \delta$

Point	D	δ_{in} (m)	σ (MPa)	δ (m)
A	0.2	5e-9	4.63	4.11e-7
B	0.4	2e-8	3.60	4.26e-7

It has been observed that with the increase of displacement from 4.11e-7m to 4.26e-7m, the stress decreases from 4.63MPa to 3.60MPa as expected. For the points between A and B, however, ABAQUS will interpolate and this is where the bump phenomenon usually occurs. To elaborate it, a point between A and B is interpolated as follows.

The point is linearly interpolated in terms of D and δ_{in} and is shown as follows

$$D = 0.2 + \frac{0.4 - 0.2}{(2e-8) - (5e-9)} \delta_{in} \tag{6.7}$$

The relationship between the stress σ and displacement δ of the point interpolated can be obtained by substituting Eqs. 6.4, 6.6 and 6.7 into Eq. 6.5 as follows

$$\sigma = K_p (0.8 + 1.33e7\delta_0)\delta - 1.33e7 K_p \delta^2 \tag{6.8}$$

As seen in Eq. 6.8, σ is in a quadratic relationship with δ for the points to be interpolated between two given points, although the inputs, i.e. $D - \delta_{in}$ is linearly

interpolated. The quadratic relationship between σ and δ can result in the bump phenomenon. This is because for the linear relationship between D and δ_{in}, D always increases when δ_{in} increases, whilst for the quadratic relationship between σ and δ as shown in Eq. 6.8, σ may increase or decrease when δ increases. Such a method to implement the material data makes the simulation not straightforward and gives rise to acquiring as accurate material property as possible. Minor deviation in the material inputs could lead to the bump phenomenon and incorrect results. Therefore, it is suggested to obtain more reliable and accurate material property in the numerical modelling and use sufficient numbers of points to precisely reflect the trend of very nonlinear/bended stress-displacement curve.

6.5 Conclusions

The analytical method has been compared with the numerical method as a means of verification in the aspects of material models, failure criteria, application of loads and final results. It has been found that material models and failure criteria used in both methods are equivalent and that the loading condition in the numerical method which is slightly different from that of analytical method results in almost the same elastic response as that of the analytical method. A parametric study has been carried out ranging from the external factors, i.e. corrosion rate and applied load, to internal factors, i.e., concrete property and geometry. It has been found that the effect of numerical techniques, i.e. penalty stiffness and viscosity parameter in particular, has also been investigated. It has been found that the penalty stiffness and viscosity parameter considerably affect the crack width at surface cracking time and proper values need to be used to accurately predict the crack width. Finally, a problem encountered in both analytical and numerical modelling – bump phenomenon – has been examined and solution to eliminate the problem has been found. It can be concluded that either analytical or numerical methods can be employed to predict the concrete crack width under combined reinforcement corrosion and applied load with similar precision.

CHAPTER 7

CONCLUSIONS AND FUTURE WORK

7.1 Conclusions

The following conclusions can be drawn from this study:

1. An analytical method and a numerical method have been developed in this study to predict the concrete crack width under combined effects of reinforcement corrosion and applied load. The results produced by these two methods have been found comparable as demonstrated in the examples. It has been shown that the difference in the time to inner boundary cracking is 1.7%, the difference in the time to surface cracking is 7.9% and the difference in the crack width at the time of surface cracking is 1.6%.

2. In the analytical method, a model of the tangential stiffness reduction factor α has been developed based on the strains and material property, i.e., fracture energy and tensile strength of concrete. It has been shown that the concrete crack width under the combined effects is a function of the corrosion effect ($d_c(t)$ or i_{corr}), the applied load (P_2), concrete property ($G_f, f_t^{'}, E_{ef}, \upsilon_c$) and geometry (*a, b* or *C, D*) of the cylinder. Amongst these factors, the corrosion effect is time dependent and the others are constants.

3. Since the assumption of the constant stiffness reduction factor α along the cracked surface causes "bumps" in the stress-strain relationship, the α is modified based on the actual data of complete stress-displacement curve from the direct tensile tests on concrete. The modification has been proven to well represent the energy release after peak stress and as a result, the "bump" phenomenon is eliminated. Nevertheless, the overall influence of the modification on the crack width is not significant.

4. In the numerical method, a model of cohesive interface is used to represent the crack in concrete induced by the combined effects. The cohesive elements are damaged with strain softening in outward order

which means the crack propagates from the inner boundary to the outer boundary. The crack width is related to the geometry (*a, b* or *C, D*) of the cylinder, concrete property, including that of cohesive interface ($f_t^{'}, E_{ef}, \upsilon_c, K_p, G_f$), corrosion effect $d_c(t)$ and the applied load P_2. A step-by-step procedure has been developed to demonstrate how to apply the developed numerical method. The procedure can serve as a manual for e.g., engineers, asset managers etc. in determining the concrete crack width under both reinforcement corrosion and applied load.

5. The displacement at the inner boundary of the cylinder has been applied in two coordinate systems which are Cartesian coordinate system and cylindrical coordinate system. It has been found that this arrangement of loading negligibly alters the uniformity of stress distribution in the elastic stage. Moreover, a real time-dependent displacement has been added in the finite element model.

6. The effect of viscosity coefficient on the results for crack width has also been investigated. Of three values of viscosity coefficient used, the result with viscosity of 5e-4 has been found to best match the analytical results. The penalty stiffness has been found to affect the results on crack width as well. The more appropriate value of penalty stiffness has been found to be 14100 GPa in this study from which the results best match the analytical results.

7. A programme of direct tensile tests for plain concrete has been undertaken which involves a servo-controlled testing machine, three linear variable differential transducers and a control system. A complete stress-displacement curve for plain concrete is obtained. It has been observed that the steep decrease of the stress reflects the brittle nature of concrete at crack initiation and the flatter decrease of stress represents the quasi-brittle nature of concrete. It has been found difficult to obtain successful test results, i.e., a complete stress-displacement curve, and the difficulties have been found to be mainly the non-perfect alignment of

the specimen and the loading platens and secondary flexure occurred during loading. A simple procedure has been proposed in this study to effectively avoid some of these technical difficulties except for the secondary flexure which relies on the stiffness of the testing equipment.

8. It has been found that the predicted surface cracking time is very sensitive to corrosion rate when it is smaller than 1 μA/cm^2, but almost has no effect once it is greater than 5 μA/cm^2. When the corrosion rate is smaller than 5 μA/cm^2, the decrease of the surface cracking time is approximately proportional to the increase of the corrosion rate. The surface cracking time are also sensitive to the geometry as represented by C/D and concrete property as represented by the tensile strength $f_t^{'}$. When C/D and $f_t^{'}$ are increased by 2 times and 1.67 times respectively, the time to surface cracking is increased to 1.87 times and 1.5 times respectively.

9. It has been found that, for the predicted long-term crack growth, only corrosion rate amongst the factors investigated has significant effects. The predicted crack width increases from 0.2mm to 1.2mm at the time of 10 years if the corrosion rate increases from 0.5μA/cm^2 to 10μA/cm^2. Moreover, the applied load only slightly affects the predicted long-term crack width with the proportional increase of crack width over time. The geometry and concrete property have been found to have little influence on the predicted long-term crack development.

7.2 Recommendations for future work

1. In the analytical method for the concrete crack width under the combined effects, a model of stiffness reduction factor α is introduced to account for the residual stiffness of the concrete in tangential direction after the concrete is cracked. Evidently, α is based on the tangential strains, i.e., strain after cracking and cracking strain, at the cracked point.

Strictly speaking, α should vary along the radius of the cylinder because the stress (tangential) varies along the radius of the cylinder when the concrete cylinder is subject to internal pressure. This is formulated in the differential equation (Eq. 3.30) where the last term is the first derivative of $\sqrt{\alpha}$ with respect to the radius r. If α is a function of the radius r, it is almost impossible to derive an analytical solution to Eq. 3.30. Further research is needed with this regard either to derive an analytical equation or develop numerical solution with sufficient accuracy.

2. The corrosion-induced pressure is assumed to be uniformly applied to the concrete cylinder. However, in reality, corrosion may be initiated from one side of the reinforcing bar (e.g. bottom) and the corrosion products at one side, e.g. bottom, of the rebar would be much more than those of other side, e.g., on top. This would lead to non-uniform pressure on the concrete. Further research is needed to consider non-uniform corrosion induced pressure for both analytical and numerical solutions.

3. The developed analytical method for predicting the crack width only considers two effects, i.e., reinforcement corrosion induced volume increase and applied sustained load. In the real world, other factors, such as weathering, freeze-thaw, chemical attack, mechanical overloading will affect the crack width to certain extent. Further research is needed to consider these factors in both methods.

4. One possible shortcoming of the numerical method is that the crack path has to be known *a priori*. If in any case, although may be uncommon due to the advancement of mechanics, that the crack path cannot be pre-defined, the applicability of the developed numerical method is limited. In these cases, the developed numerical method can be extended by employing a recently developed theory called Extended Finite Element Method (XFEM) which allows cracking occurring everywhere without pre-defining it. This can be a good topic for future research.

5. Although the developed methods have been verified with each other numerically or analytically, and partially verified by experimental results, it is desirable to validate the predicted crack width directly from data produced from physical tests, either in the laboratory or in field. Therefore, further research is needed to either carry out experiments in laboratory (under corrosive environment) or collect data of crack width on-site.

REFERENCES

Abrams, D. A., 1919, *Design of Concrete Mixtures*, Structural Materials, Research laboratory, Lewis Institute, Bulletin 1, ISBN 111314761X, Chicago.

ACI 318-02, 2001, "Building Code Requirements for Structural Concrete and Commentary", *American Concrete Institute*, Farmington Hills, Mich.

ACI 363R-92, 1992, "Report on High-Strength Concrete", *American Concrete Institute*, Farmington Hills, Mich.

ACI Committee 222, 1985, "Corrosion of Metals in Concrete", *American Concrete Institute*, Farmington Hills, Mich.

ACI Committee 224, 2001, "Control of Cracking in Concrete Structures", *American Concrete Institute*, Farmington Hills, Mich.

ACI Committee 446.1R, 1991, "Fracture Mechanics of Concrete: Concepts, Models and Determination of Material Properties", *American Concrete Institute*, Farmington Hills, Mich.

ACI Committee 446.3R, 1997, "Finite Element Analysis of Fracture in Concrete Structures", *American Concrete Institute*, Farmington Hills, Mich.

Alexander, K., 1959, "Strength of the Cement Aggregate Bond", *Journal of American Concrete Institute*, V.56, No.5, 377-390.

Al Khalaf, M. N. and Page, C. L., 1979, "Steel/Mortar Interface: Microstructural Features and Modes of Failure", *Cement and Concrete Research*, 9, 197-208.

Andrade, C., Molina, F. J. and Alonso, C., 1993, "Cover Cracking as A Function of Rebar Corrosion: Part I – Experiment Test", Materials *and Structures*, V. 26, pp. 453-464.

Ann, K. Y. and Song, H., 2007, "Chloride Threshold Level for Corrosion of Steel in Concrete", *Corrosion Science 49*, 4113-4133.

Anstice, D. J., Page, C. L. and Page, M. M., 2004, "The Pore Solution of Carbonated Cement Pastes", *Cement and Concrete Research* 35, 377-383.

Anyeung, Y., 2001, *Bond Properties of Corroded Reinforcement with and without Confinement*, PhD Thesis, New Brunswick Rutgers, The State University of New Jersey.

Arya, C. and Newman, J. B., 1990, "Problem of Predicting Risk of Corrosion of Steel in Chloride Contaminated Concrete", *Proceedings of the Institution of Civil Engineers*, Part 1 88, 875-888.

Avram, C., Facaoaru, I., Filimon, I., Mirsu, O. and Tertea, I., 1981, *Developments in Civil Engineering 3: Concrete Strength and Strains*, Elsevier Scientific Publishing Co.

ASTM C 867, 1991, *Standard Test Method for Half-cell Potentials of Uncoated Reinforcing Steel in Concrete*, American Society for Testing and Materials, Philadelphia, PA.

ASTM C 903, 2007, *Standard Specification for Liquid Membrane-Forming Compounds for Curing Concrete,* American Society for Testing and Materials, Philadelphia, PA.

ASTM C 1218, 1999, *Standard Test Method for Water-soluble Chloride in Mortar and Concrete*, American Society for Testing and Materials, Philadelphia, PA.

Attiogbe, E. K. and Darwin, D., 1987, "Submicrocracking in Cement Paste and Mortar", *ACI Material Journal*, V. 84, No. 6, pp. 491-500.

Bamforth, P. B., 1999, "The Derivation of Input Data for Modelling Chloride Ingress From Eight-Year UK Coastal Exposure Trials", *Magazine of Concrete Research*, V.51, No.2, pp.89-96.

Bamforth, P. B., Price, W. F. and Emerson, M., 1997, "An International Review of Chloride Ingress into Structural Concrete", *Contractor Report 359*, Transport Research Laboratory, UK, pp.128.

Barenblatt, G. I., 1962, "The Mathematical Theory of Equilibrium of Cracks in Brittle Fracture", *Adv. Appl. Mech.,* 7, 55-129.

Barnes, B. D., Diamond, S. and Dolch, W. L., 1978, "Contract Zone between Portland Cement Paste and Glass Aggregate", *Cement and Concrete Research*, V.8, No.2, 233-244.

Barpi, F. and Valente, S., 2005, "Lifetime Evaluation of Concrete Structures Under Sustained Post-Peak Loading", *Engineering Fracture Mechanics* **72**, 2427-223.

Bažant, Z. P., 1976, "Instability, Ductility and Size Effect in Strain-Softening Concrete", *Journal of Engineering Mechanics Division, ASCE*, 102, 331-344.

Bažant, Z. P., 1979, "Physical Model for Steel Corrosion in Concrete Sea Structures - Theory", *Journal of Structure Division*, ASCE, V. 105, No. ST6, pp. 1137-1153.

Bažant, Z. P. and Cedolin, L., 1979, "Blunt Crack Band Propagation in Finite Element Analysis", *Journal of Engineering Mechanics Division, ASCE*, 105, 297-315.

Bažant, Z. P. and Cedolin, L., 1980, "Fracture Mechanics of Reinforced Concrete", *Journal of Engineering Mechanics Division, ASCE*, 106, 1257-1306.

Bažant, Z. P. and Cedolin, L., 1983, "Finite Element Modeling of Crack Band Propagation", *Journal of Structural Engineering, ASCE*, 109, 69-92.

Bažant, Z. P. and Jirasek, M., 2002, "Nonlocal Integral Formulations of Plasticity and Damage: Survey and Process", *Journal of Engineering Mechanics*, ASCE, V. 128, No. 11, pp. 1119-1149.

Bažant, Z. P. and Oh, B. H., 1983, "Crack Band Theory for Fracture of Concrete", RILEM, *Material and Structures*, 16, 155-177.

Bažant, Z. P. and Planas, J., 1998, *Fracture and Size Effect in Concrete and Other Quasibrittle Materials*, CRC Press, ISBN 084938284x, pp. 640.

Bažant, Z. P. and Prat, P. C., 1988, "Effect of Temperature and Humidity on Fracture Energy of Concrete", *Journal of American Concrete Institute*, V. 84, 262-271.

Beaudoin, J. J. and Ramachandran, V. S., 1992, "A New Perspective on the Hydration Characteristic of Cement Phases", *Cement and Concrete Research*, 22, No.4, 689-694.

Bentur, A., Diamond, S and Berke, A. S., 1997, *Steel Corrosion in Concrete: Fundamentals and Civil Engineering Practice*, E &FN Spon, ISBN 0419225307, London, UK, pp.201.

Bhargava, K., Ghosh, A. K., Mori, Y. and Ramanujam, S., 2006, "Model for Cover Cracking Due to Rebar Corrosion in RC Structures", *Engineering Structures* **28**, 1093-1109.

Bhatt, P. MacGinley, T. J. and Choo, B. S., 2006, *Reinforced Concrete: Design Theory and Examples*, Taylor & Francis, ISBN 0415307961, pp. 686.

Bier, T., 1987, "Influence of Type of Cement and Curing on Carbonation Progress and Pore Structure of Hardened Cement Pastes", *MRS Symposium Proceedings*, Volume 85, 123-134.

Bittencourt, T. N., Barry, A. and Ingraffea, A. R., 1992, "Comparison of Mixed-Mode Stress Intensity Factors Obtained Through Displacement Correlation, J-Integral Formulation, and Modified Crack-Closure Integral", *Fracture Mechanics: Twenty Second Symposium*, ASTM STP 1131, American Society for Testing and Materials, Philadelphia, V. 2, 69-82.

Bocca, P., Carpinteri, A. and Valente, S., 1991, "Mixed Mode Fracture of Concrete", *International Journal in Solid Structures*, V. 27, No. 9, 1139-1153.

Bogue, R H, 1955, *Chemistry of Portland Cement*, New York, Reinhold, ISBN B002EPKSYW, pp. 572.

BRE 1997, *Design of Normal Concrete Mixes*, Building Research Establishment, 2nd Edition, ISBN 1860811728, UK.

BRE Digest 444 – Part 1, 2000, *Corrosion of Steel in Concrete: Durability of Reinforced Concrete Structures*, Building Research Establishment, ISBN 9781860813603, UK.

BRE Digest 444 – Part 2, 2000, *Corrosion of Steel in Concrete: Investigation and Assessment*, Building Research Establishment, ISBN 1860813610, UK.

BRE Digest 444 – Part 3, 2000, *Corrosion of Steel in Concrete: Protection and Remediation*, Building Research Establishment, ISBN 1860813623, UK.

BRE Digest 451, 2000, *Tension Tests for Concrete*, Building Research Establishment, ISBN 1860814387, UK.

BRE Digest 455, 2001, *Corrosion of Steel in Concrete: Service Life Design and Prediction*, Building Research Establishment, ISBN 18608414719, UK.

British Standard 1881-124, 1988, *Testing concrete – methods for analysis of hardened concrete*, British Standards Institute, ISBN 0580166171, London UK.

Broek, D., 1986, *Elementary Engineering Fracture Mechanics*, 4th Edition, ISBN 9024726565, Martinus Nijhoff, Dordrecht, pp. 540.

Broomfield, J. P., 1997, *Corrosion of Steel in Concrete: Understanding, Investigating and Repair,* E&FN Spon, ISBN 0419196307, London.

Brown, C. J., Darwin, D. and McCabe, S. L., 1993, "Finite Element Fracture Analysis of Steel-Concrete Bond", *SM Report No.36*, University of Kansas Centre for Research, Lawrence, Kansas.

Bruhwiler, E. and Wittmann, F. H., 1990, "The Wedge Splitting Test, A New Method of Performing Stable Fracture Mechanics Tests", *Engineering Fracture Mechanics*, V. **35**, No. 1/2/3, pp. 117-125.

BS EN 13139, 2002, *Aggregates for Mortar*, British Standard Institute, ISBN 0580397726, London UK.

Canadian Standards Association A23.3-94, 1994, "Design of Concrete Structures", Canadian Standards Association, Rexadle, Ontario, Canada, pp. 220.

Castellot, M. and Andrade, C., 2008, "Modelling the Carbonation of Cementitious Matrixes by Means of the Unreacted-Core Model, UR-CORE", *Cement and Concrete Research*.

Chen, Z. J., 2004, *Effect of Reinforcement Corrosion on the Serviceability of Reinforced Concrete Structures*, MSc Thesis, Department of Civil Engineering, University of Dundee, UK, pp. 168.

Chen, D. and Mahadevan, S., 2007, "Cracking Analysis of Plain Concrete under Coupled Heat Transfer and Moisture Transport Process", *Journal of Structural Engineering*, ASCE, V. 133, pp. 400-410.

Clear, K. C., 1989, "Measuring Rate of Corrosion of Steel in Field Concrete Structures", *Transportation Research Record*, Transportation Research Board, Washington, DC.

Colotti, V. and Spadea, G., 2004, "An analytical Model for Crack Control in Reinforced Concrete Elements under Combined Forces", *Cement and Concrete Composites*, 27, (4), pp. 503-514.

Cook, R. F., Fairbanks, C. J., Lawn, B. R. and Mai, Y. W., 1987, "Crack Resistance by Interfacial Bridging: Its Role in Determining Strength Characterization", *Journal of Materials Research*, Vol. 2, No. 3, pp. 345-356.

Cordon, W. A. and Gillespie, H. A., 1963, "Variables in Concrete Aggregates and Portland Cement Paste which Influence the Strength of concrete", *Journal of American Concrete Institute*, V. 60, Issue 8, 1029-1052.

Cornelissen, H. A. W., Hordijk, D. A. and Reinhardt, H. W., 1986a, "Experimental Determination of Crack Softening Characteristics of Normal Weight and Lightweight Concrete", *Heron*, 31, 2, 45-56.

Cornelissen, H. A. W., Hordijk, D. A. and Reinhardt, H. W., 1986b, "Experiments and Theory for the Application of Fracture Mechanics to Normal and Lightweight Concrete", In *Fracture Mechanics and Fracture Energy of Concrete*, Wittmann, F. H. ed., Elsevier, Amsterdam, 565-575.

Coronelli, D., 2002, "Corrosion Cracking and Bond Strength Modelling for Corroded Bars in Reinforced Concrete", *ACI Structural Journal*, V.99, No.3, pp.267-276.

Cox, B. N. and Marshall, D. B., 1994, "Concepts in the Fracture and Fatigue of Bridged Cracks", *ACTA Metallurgica et Materialia*.

Crank, J., 1975, *The Mathematics of Diffusion*, Oxford Science Publications, 2nd Edition, ISBN 0198533446, USA, pp. 424.

Currie, R. J., 1986, "Carbonation Depths in Structural-Quality Concrete", *Building Research Establishment Report*, pp. 19, Watford, UK.

Dagher, H. J. and Kulendran, S., 1992, "Finite Element Modelling of Corrosion Damge in Concrete Structures", *ACI Structural Journal*, V.89, No.6, pp.699-708.

Dassault Systèmes Simulia Corp., 2008, *ABAQUS User's Manual*, Version 6.8, Providence, RI, USA.

Desayi, P. and Krishnan, S., 1964, "Equation for the Stress-Strain Curve of Concrete", *Journal of American Concrete Institute*, V.61, Issue 3, 345-350.

Diamond, S., 1976, "C/S Mole Ratio of C-S-H Gel in a Mature C_3S Paste as Determined by EDXA", *Cement and Concrete Research*, 6, No.3.

Diamond, S., 1986, "Microstructures of Cement Paste in Concrete", *Proceedings of 8th International Congress on the Chemistry of Cement*, V.1, Finep, Brazil, 122-147.

Du, J., Yon, J. H., Hawkins, N. M., Arakawa, K. and Kobayashi, A. S., 1992, "Fracture Process Zone for Concrete for Dynamic Loading", *ACI Material Journal*, Vol. 89, No. 3, 310-323.

Dugdale, D. S., 1960, "Yielding of Steel Sheets containing Slits", *J. Mech. Phys. Solids*, 8, 100-108.

Elices, M., Guinea, G. V., Gomez, J. and Planas, J., 2002, "The Cohesive Zone Model: Advantages, Limitations and Challenges", *Engineering Fracture Mechanics* **69**, 137-163.

Elices, M., Rocco, C. and Rosello, C., 2009, "Cohesive Crack Modeling of A Simple Concrete: Experimental and Numerical Results", *Engineering Fracture Mechanics* **76**, Issue 10, 1398-1410.

Eurocode 0 BS EN 1990:2002, *Basis of Structural Design*, British Standards Institute, ISBN 9780580713743, London UK.

Eurocode 2 BS EN 1992-1-1:2004, *Design of Concrete Structures – Part 1-1: General Rules and Rules for Buildings*, British Standards Institute, ISBN 0580208982, London UK.

Eurocode 2 BS EN 206-1:2000, *Concrete – Part 1: Specification, Performance, Production and Conformity*, British Standards Institute, ISBN 0580368823, London UK.

Fang, C., Lundgren, K., Plos, M. and Gylltofy, K., 2006, "Bond Behaviour of Corroded Reinforcing Steel Bars in Concrete", *Cement and Concrete Research*, 36, pp. 1931-1938.

Federal Highway Administration, 1997, *The Status of the Nation's Highway Bridges: Highway Bridge Replacement and Rehabilitation Program and National Bridge Inventory*, Thirteenth Report to the United States Congress, Washington, D. C.

Fontana, M. G., 1986, *Corrosion Engineering*, 3rd Edition, McGraw-Hill Inc, ISBN 0070214638, pp. 556.

Fu, X. and Chung, D. D. L., 1997, "Effect of Corrosion on the Bond Between Concrete and Steel Rebar", *Cement and Concrete Research*, 27 (12), pp. 1811-1815.

Galloway, J. W. and Harding, H. M., 1976, "Elastic Moduli of a Lean and A Pavement Quality Concrete Under Uniaxial Tension and Compression", *Materials and Structures*, 9, No.49, 13-18.

Gerstle, W. H. and Abdalla, J. E., 1990, "Finite Element Meshing Criteria for Crack Problems", *Fracture Mechanics: Twenty-First Symposium,* ASTM STP 1074, American Society for Testing and Materials, Philadelphia, 509-521.

Gerstle, W. H. and Xie, M., 1992, "FEM Modelling of Fictitious Crack Propagation in Concrete", *Journal of Engineering Mechanics*, ASCE, V. 118, No. 2, 416-434.

Gonzalez, J. A., Andrade, C. and Alonso, C., 1995, "Comparison of Rates of General Corrosion and Maximum Pitting Penetration on Concrete Embedded Steel Reinforcement", *Cement and Concrete Research*, V. 25, No. 2, pp. 257-264.

Goodman, R. E., Taylor, R. L. and Brekke, T. L., 1968, "A Model for the Mechanics of Jointed Rock", *J. Soil Mech. And Found. Div.,* ASCE, V. 94, No. 3, 637-659.

Gopalaratnam V. S. and Shah, S. P., 1985, "Softening Response of Plain Concrete in Direct Tension", *Journal of American Concrete Institute*, 82, 3, 310-323.

Goto,Y., 1971, "Cracks Formed In Concrete Around Deformed Tension Bars", *ACI Journal Proceedings*, V. 68, Issue 4, April, pp. 244-251.

Griffith, A. A., 1921, "The Phenomena of Rupture and Flow in Solids", *Philos. T. Roy. Soc.* A, 221, 163-197.

Guo, X. H, Tin-Loi, F. and Li, H., 1999, "Determination of Quasibrittle Fracture Law for Cohesive Crack Models", *Cement and Concrete Research* **29**, 1055-1059.

Hanson, J. H. and Ingraffea, A. R., 2003, "Using Numerical Simulations to Compare the Fracture Toughness Values for Concrete from the Size-Effect, Two-Parameter and Fictitious Crack Models", *Engineering Fracture Mechanics* **70**, 1015-1027.

Hausmann, D. A., 1967, "Steel Corrosion in Concrete: How Does It Occur", *Materials and Protection* 6.

Henshell, R. D. and Shaw, K. G., 1975, "Crack Tip Finite Elements are Unnecessary", *International Journal of Numerical Methods in Engineering*, V. 9, 495-507.

Higgins, D. D. and Bailey, J. E., 1976, "Fracture Measurements on Cement Paste", *Journal of Materials Science*, Vol. 11, No. 11, pp. 1995-2003.

Hillerborg, A., Modeer, M. and Petersson, P. E., 1976, "Analysis of Crack Formation and Crack Growth in Concrete by Means of Fracture Mechanics and Finite Elements", *Cement and Concrete Research*, Vol. 6, Issue 6, 773-781.

Hognestad, E., 1951, *A Study of Combined Bending and Axial Load in Reinforced Concrete Members*, Univerisity of Illinois Engineering Experimental Station, Bulletin Series No 399, pp.128.

Horne, A. T. Richardson, I. G. and Brydson, R. M. D., 2007, "Quantitative Analysis of the Microstructure of Interfaces in Steel Reinforced Concrete", *Cement and Concrete Research*, 37, 1613-1623.

Hsu, T. T. C. and Slate, F. O., 1963, "Tensile Bond Strength between Aggregate and Cement Paste or Mortar", *Journal of American Concrete Institute*, V.60, No.4, 465-486.

Hsu, T. T. C., Slate, F. O., Sturman, G. M. and Winter, G., 1963, "Microcracking of Plain Concrete and the Shape of the Stress-Strain Curve", *Journal of American Concrete Institute*, V.60, 209-224.

Hu, J. and Stroeven, P., 2004, "Properties of the Interfacial Transition Zone in the Model Concrete", *Interface Science*, V.12, 389-397.

Ingraffea, A. R. and Gerstle, W. H., 1985, "Non-Linear Fracture Models for Discrete Crack Propagation", *Application of Fracture Mechanics to Cementitious Composites*, NATO-ARW, S. P. Shah, ed., 247-285.

Irwin, G. R., 1957, "Analysis of Stresses and Strains Near the End of A Crack Traversing A Plate", *Journal of Applied Mechanics, ASME,* 24, 361-364.

Ishida, T. and Mackawa, K., 2001, "Modelling of PH Profile in Pore Water Based on Mass Transport and Chemical Equilibrium Theory", *JSCE 37*.

James, G., 1993, *Advanced Modern Engineering Mathematics*, Addison Wesley, ISBN 0130454257, pp. 901.

Jenq, Y. S. and Shah, S. P., 1985, "Fracture Toughness Criterion for Concrete", *Engineering Fracture Mechanics*, Vol. 21, pp. 1055-1069.

Jiang J., Lu, X. and Ye, L., 2005, *Finite element analysis of concrete structures*. Tsinghua University Press, Chinese Language, ISBN 730210350, Beijing, pp. 386.

Jones, D. A., 1992, *Principles and Prevention of Corrosion*, Prentice Hall, ISBN 0133599930, Macmillan, United States of America, pp. 572.

Kachanov, M., 1986, "Interaction of a Crack with Some Microcrack Systems", *Fracture Toughness and Fracture Energy of Concrete*, Elsevier Science, Amsterdam, pp. 3-10.

Karin, L., 2002, "Modelling the Effect of Corrosion on Bond in Reinforced Concrete", *Magazine of Concrete Research*, V. 54, I. 3, pp. 165-173.

Kay, T., 1992, *Assessment and renovation of concrete structures*, Longman Scientific & Technical, ISBN 0470218649, England, pp. 224.

Keesler, R. J. and Power, R. G., 1988, "Corrosion of Epoxy Coated Rebars-Keys Segmental Bridge-Monroe County", *Report No. 88-8A*, Florida Department of Transportation, Material Office, Corrosion Research Laboratories, Gainesville, FI.

Kobayashi, A. S., Hawkins, N. M. and Bradt, R. C., 1991, "Fracture Process Zone in Concrete and Ceramics: A Matter of Scaling", *Toughening Mechanics in Quasi-Brittle Materials*, pp. 35-46.

Kosaka, Y., Tanigawa, Y. and Ota, F., 1975, "Effect of Coarse Aggregate on the Fracture Behaviour of Concrete", *Journal of Architectural Institute of Japan*, No.228, 1-22.

Kumar, A. Roy, D. M. and Higgins, D. D., 1987, "Diffusion through Concrete", *Concrete*, 31-32.

Kumar, S. and Barai, S. V., 2009, "Determining Double-K Fracture Parameters of Concrete for Compact Tension and Wedge Splitting Tests Using Weight Function", *Engineering Fracture Mechanics*, V. **76**, I. 7, pp. 935-948.

Larbi, L. A., 1993, "Microstructure of the Interfacial Zone around Aggregate Particles in Concrete", *Heron*, 38, No.1, pp 69.

Lekhnitskii, S. G., 1963, *Theory of Elasticity of an Anisotropic Elastic Body*, Holden-Day, ISBN B000O8UNXC, San Francisco, Calif., pp. 404.

Lew, H. S. and Reichard, T. W., 1978a, "Mechanical Properties of Concrete at Early Ages", *Journal of American Concrete Institute*, 75, No.10, 553-542.

Lew, H. S. and Reichard, T. W., 1978b, "Prediction of Strength of Concrete from Maturity", in *Accelerated Strength Testing*, ACI SP-56, 229-248.

Li, C. Q., 2000, "Corrosion Initiation of Reinforcing Steel in Concrete Under natural Salt Spray and Service Loading – Results and Analysis", *ACI Material Journal*, V. 97, No.6, pp. 690-697.

Li, C. Q., 2001, "Initiation of Chloride-Induced Reinforcement Corrosion in Concrete Structural Members - Experimentation", *ACI Structural Journal*, V.98, No.4, pp. 502-510.

Li, C. Q., 2003, "Life-Cycle Modelling of Corrosion-Affected Concrete Structures: Propagation", *Journal of Structural Engineering*, ASCE, V. 129, No. 6, pp. 753-761.

Li, C. Q., 2005, "Time Dependent Reliability Analysis of the Serviceability of Corrosion Affected Concrete Structures", *International Journal of Materials and Structural Reliability*, V. 3, No. 2, pp. 105-116.

Li, C. Q., Melchers, R. E. and Zheng, J. J., 2006, "Analytical Model for Corrosion-Induced Crack Width in Reinforced Concrete Structures", *ACI Structural Journal* **103**, No. 4, 479-487.

Li, C. Q. and Zheng, J. J., 2007, "Closed-Form Solution for Predicting Elastic Modulus of Concrete", *ACI Material Journal*, V. 104, No. 5, pp. 539-546.

Li, C. Q., Zheng, J. J., Zhou X. Z. and McCarthy, M. J., 2003, "A Numerical Method for the Prediction of Elastic Modulus of Concrete", *Magazine of Concrete Research*, V. 55, No. 6, pp. 497-506.

Li, G., Zhao, Y. and Pang, S., 1999, "Four-Phase Sphere Modeling of Effective Bulk Modulus of Concrete", *Cement and Concrete Research*, V.29, 839-845.

Li, Y. N. and Liang, R. Y., 1992, "Stability Theory of Cohesive Crack Model", *Journal of Engineering Mechanics*, ASCE, V. 118, No. 3, 587-603.

Liu, Y. and Weyers, R. E., 1998, "Modeling the Time-to Corrosion Cracking in Chloride Contaminated Reinforced Concrete Structures", *ACI Materials Journal*, V.95, No.6, Nov.-Dec.

Lo, T. K., Tang, W. C. and Nadeem, A., 2007, "Comparison of Carbonation of Lightweight Concrete with Normal Weight Concrete at Similar Strength Levels", *Construction and Building Materials*, 2007.

Longford, P. and Broomfield, J., 1987, "Monitoring the Corrosion of Reinforcing Steel", *Construction Repair*, 1 (2), 32-6.

Lutz, L. A. and Gergeley, P., 1967, "Mechanics of bond and Slip of deformed bars in concrete", *ACI Journal Proceedings*, V. 64, I. 11, pp. 711-721.

Lutz, M. P., Monteiro, P. J. M. and Zimmerman, R. W., 1997, "Inhomogeneous Interfacial Transition Zone Model for the Bulk Modulus of Mortar", *Cement and Concrete Research*, V.27, No.7, 1113-1122.

Lydon, F. D. and Balendran, R. V., 1986, "Some Observations on Elastic Properties of Plain Concrete", *Cement and Concrete Research*, 16, No.3, 314-324.

Maaddawy, T. E., Soudki, K. and Topper, T., 2005, "Analytical Model to Predict Nonlinear Flexural Behaviour of Corroded Reinforced Concrete Beams", *ACI Structural Journal*, V. 102, No. 4, pp. 550-559.

Mangat, P. S. and Molloy, B. T., 1992, "Factors Influencing Chloride-Induced Corrosion of Reinforcement in Concrete", *Material and Structures* ***25***, pp. 404-411.

Maslehuddin, M., Allam, I. M., Al-Sulaimani, G. J., Al-Mana, A. I., Abduljauwad, S. N., 1990, "Effect of Rusting of Reinforcing Steel on Its Mechanical Properties and Bond with Concrete" *ACI Material Journal*. 87 (5), pp. 496-502.

Mattsson, 1996, *Basic Corrosion Technology for Scientists and Engineers*, Ashgate Publishing, 2nd Edition, ISBN 1861250118, Bournemouth, UK, pp. 204.

Mehta, P. K., 1977, "Effect of Cement Composition on Corrosion of Reinforcing steel in concrete", *ASTM Special Technical Publications*, American Society for Testing and Materials, Issue 629, pp. 12-19.

Mehta, P. K. and Monteiro, P. J. M., 1993, *Concrete: Structure, Properties and Materials*, Prentice-Hall Inc., 2nd Edition, ISBN 0131756214, Englewood Cliffs, New Jersey, pp. 496.

Melchers, R. E. and Li, C. Q., 2006, "Phenomenological Modelling of Reinforcement Corrosion in Marine Environments", *ACI Material Journal*, V. 103, No. 1, pp. 25-32.

Mindess, S. and Diamond, S., 1982, "The Cracking and Fracture of Mortar", *Materials and Structures*, Vol. 15, No. 86, pp. 107-113.

Mitsui, K. Li, Z., Lange, D. A. and Shah, S. P., 1994, "Relationship between Microstructure and Mechanical Properties of the Paste-Aggregate Interface", Journal *of American Concrete Institute*, V.91, No.1, 30-39.

Molina, F.J., Alonso, C., and Andrade, C., 1993, "Cover cracking as a function of rebar corrosion: Part 2 – Numerical model", *Materials and Structures*, **26**, pp.

532 – 548.

Mondal, P., Shah, S. P. and Marks, L. D., 2008, "Nanoscale Characterization of Cementitous Materials", *Journals of American Concrete Institute*, V.105, No.2, 174-179.

Moreau, M., 1973, "Contribution to the Study of Adhesion between the Hydrated Constituents of Artificial Portland Cement and Embedded Steel", *Revenue Mater.*, 674, 4-17.

Murakami, Y., 1987, *Stress Intensity Factors Handbook*, Pergamon, 1st Edition, ISBN 0080348092, New York, pp. 8.

Neville, A. M., 1995, *Properties of concrete*, 4th Edition, Pearson Education Limited, England, ISBN 0582230705, pp. 844.

Ngala, V. T., 1997, "Effect of Carbonation on Pore Structure and Diffusional Properties of Hydrated Cement Pastes", *Cement Concrete Research*, 27, 995-1007.

Ngo, D. and Scordelis, A. C., 1967, "Finite Element Analysis of Reinforced Concrete Beams", *Journal of American Concrete Institute*, Vol. 64, No. 3, 152-163.

Noghabai, K., 1996, "Environmental Effects on Bond in Reinforced Concrete Structures", *Durability of Building Materials and Components*, Proceedings of the 7th International Conference, Stockholm, Sweden, pp.605-614.

Odler, I. and Rossler, M., 1985, "Investigations on the relationship between porosity, structure and strength of hydrated Portland cement pastes", *Cement and Concrete Research*, 15, No. 2, pp. 320-330.

Ohgishi, S., Ono, H., Takatsu, M. and Tanahashi, I., 1986, "Influence of Test Conditions on Fracture Toughness of Cement Paste and Mortar", in Proceedings

of *Fracture Toughness and Fracture Energy of Concrete*, Netherlands, pp. 281-290.

Oliver, W. C. and Pharr, G. M., 1992, "An Improved Technique for Determining Hardness and Elastic Modulus Using Load and Displacement Sensing Indentation Experiments", *Journal of Materials Research*, 7, 1564-1579.

Orchard, D. F., 1979, *Concrete Technology: Properties of Materials*, Applied Science Publishers LTD, 4th Edition, ISBN 0853347948, England, pp. 487.

Otsuki, N., Miyazato, S., Diola, N. B. and Suzuki, H., 2000, "Influences of Bending Crack and Water-Cement Ratio on Chloride-Induced Corrosion of Main Reinforcing Bars and Stirrups", *ACI Materials Journal*, 97, (4), pp. 454 – 465.

Page, C. L., 1975, "Mechanism of Corrosion Protection in Reinforced Concrete Marine Structures", *Nature*, 258, pp. 514-515.

Page, C. L. and Treadaway, K. W. J., 1982, "Aspects of the Electro-chemistry of Steel in Concrete", *Nature*, V.297, pp. 109-115.

Page, C. L, Short, N. R., Holden, W. R. and Materials Research Group, 1986, "The Influence of Different Cements on Chloride-Induced Corrosion of Reinforcing Steel", *Cement and Concrete Research*, V. 16, Issue 1, pp. 79-86.

Pantazopoulou, S. J. and Papoulia, K. D., 2001, "Modeling Cover Cracking Due To Reinforcement Corrosion in RC Structures", *Journal of Engineering Mechanics* **127**, ASCE, No. 4, pp. 342-351.

Papadakis, V. G., Fardis, M. N., and Vayenas, C. G., 1992, "Effect of composition, environment factors and cement-lime mortar coating on concrete carbonation", *Materials and Structures*, 25, No. 149, pp. 293-304.

Parrott, L. J., 1987, "A review of carbonation in reinforced concrete", *Cement and Concrete Association*, Wexham Springs, pp. 369.

Parrott, L. J., 1994, "A Study of Carbonation-Induced Corrosion", *Magazine of Concrete Research,* **46**, No. 166, pp. 23-28.

Patel, R. G., Killoh, D. C., Parrott, L. J. and Gutteridge, W. A., 1988, "Influence of Curing at Different Relative Humidities Upon Compound Reactions and Porosity of Portland Cement Paste", *Materials and Structures*, 21, No.123, 192-197.

Petersson, P. –E., 1981*, Crack Growth and Development of Fracture Zone in Plain Concrete and Similar Materials*, Report No.TVBM-1006, Division of Building Materials, Lund Institute of Technology, Lund, Sweden.

Petre-Lazar, I. and Gerard, B., 2000, "Mechanical Behaviour of Corrosion Products formed at the steel – Concrete Interface", Testing and Modelling, *Proceedings EM2000, Fourteenth Engineering Mechanics Conference*, ASCE, Austin, Texas, USA.

Planas, J. and Elices, M., 1992, "Asymptotic Analysis of A Cohesive Crack: 1. Theoretical Background", *International Journal of Fracture*, V. 55, No. 2, 153-178.

Pourbaix, M., 1974, "Application of Electrochemistry in Corrosion Science and in Practice", *Corrosion Science*, 14, 25-83.

Pourbaix, M., translated by Frankin, J. A., 1966, *Atlas of electrochemical equilibria in aqueous solutions*. Pergamon Press, 1st Edition, ISBN 0915567989, New York, pp. 644.

Powers, T. C., 1947, "A Discussion of Cement Hydration in Relation to the Curing of Concrete", *Proc. of Highw. Res. Bd.*, 27, 178-188.

Power, T. C. and Brownyard, T. L., 1947, "Studies of Physical Properties of Hardened Portland Cement Paste", *Proceedings of the American Concrete Institute*, Vol. 43.

Pressler, E. E., Brunauer, S., Kantro, D. L. and Weise, C. H., 1961, "Determination of the Free Calcium Hydroxide Contents of Hydrated Portland Cements and Calcium Silicates", *Analytical Chemistry*, V.33, No. 7.

Qiao, P. and Chen, Y., 2008, "Cohesive Fracture Simulation and Failure Modes of FPR-Concrete Bonded Interfaces", *Theoretical and Applied Fracture Mechanics* **49**, 213-225.

Raina, V. K., 1995, *Concrete Bridges: Inspection, Repair, Strengthening, Testing and Load Capacity Evaluation*, Tata McGraw-Hill Publishing Company, ISBN 0074623494, pp. 493.

Ramesh, G., Sotelino, E. D. and Chen, W. F., 1996, "Effect of Transition Zone on Elastic Moduli of Concrete Materials", *Cement and Concrete Research*, V.26, No.4, 611-622.

Rashid, Y. R., 1968, "Ultimate Strength Analysis of Prestressed Concrete Pressure Vessels", *Nuclear Engineering and Design*, V. 7, 334-344.

Rice, J. R., 1968a, "A Path independent Integral and the Approximate Analysis of Strain Concentrations by Notches and Cracks", *Journal of Applied Mechanics, ASME,* 35, 379-386.

Rice, J. R., 1968b, "Mathematical Analysis in the Mechanics of Fracture", In *Fracture – An Advanced Treatise*, Volume 2, H. Liebowitz, ed., Academic Press, New York, 191-308.

Riggs, O. L., Sudbury, J. D., and Hutchinson, M., 1960, *Corrosion*, 16, 94-98.

RILEM Technical Committee 50-FMC, 1985, "Determination of the Fracture Energy of Mortar and Concrete by Means of Three-Point Bend Tests on Notched Beams", *Material and Structures*, Vol. 18, No. 4, 285-290.

RILEM Technical Committee 89-FMT, 1990, "Determination of the Fracture Parameters (K_{Ic}^{s} and $CTOD_c$) of Plain Concrete Using Three-Point Bend tests", *Material and Structures*, Vol. 23, 457-460.

RILEM Technical Committee 162-TDF, 2000, "Test and Design Methods for Steel Fibre Reinforced Concrete. Bending Test. Recommendations", *Material Structures* ***33****,* pp. 3-5.

RILEM Technical Committee 162-TDF, 2001, "Test and Design Methods for Steel Fibre Reinforced Concrete. Uniaxial Tensile Test for Steel Fibre Reinforced Concrete. Recommendations", *Material and Structures* **34**, pp. 3-6.

Roberts, M. B., Atkins, C., Hogg, V. and Middleton, C., 2000, "A Proposed Empirical Corrosion Model for Reinforced Concrete", *Structures and Buildings*, V. 140, No. 1, pp. 1-11.

Roelfstra, R. E. and Wittmann, F. H., 1986, "A Numerical Method to Link Strain Softening with Fracture in Concrete", in *Fracture Toughness and Fracture Energy in Concrete*, edited by Wittmann, F. H., Elsevier Science, Amsterdam, 163-175.

Roesler, J., Paulino, G. H., Park, K. and Gaedicke, C., 2007, "Concrete Fracture Prediction Using Bilinear Softening", *Cement and Concrete Composites* **29**, 300-312.

Roy, D. M. and Gouda, G. R., 1973, "Porosity-Strength Relation in Cementitious Materials with Very High Strengths", *Journal of American Ceramic Society*, 53, No 10, 549-550.

Sagues, A. A., Moreno, E. I. and Andrade, C., 1997, "Evolution of pH During In-Situ Leaching in Small Concrete Cavities", *Cement and Concrete Research*, V.27, No.11, pp. 1747-1759.

Schiessl, P., 1988, *Corrosion of Steel in Concrete*, Report of the TC60-CSC RILEM, Chapman and Hall, London.

Schiessl, P. and Raupach, M., 1990, "Influence of Concrete Composition and Microclimate on the Critical Chloride Content in Concrete", in: Page, C. L., Treadaway, K. W. J., and Bamforth, P. B. (Eds), "Corrosion of Reinforcement in Concrete", Elsevier Applied Science, London UK.

Scrivener, K. L., Bentur, A. and Pratt, P. L., 1988, "Quantitative Characterization of the Transition Zone in High-Strength Concrete", *Advances in Cement Research*, V.1, No.4, 230-237.

Scrivener, K. L., Crumbie, A. K. and Laugesen, P., 2004, "The Interfacial Transition Zone (ITZ) between Cement Paste and Aggregate in Concrete", *Interface Science*, V.12, 411-421.

Sersale, R., Cioffi, R., Frigione, G. and Zenone, F., 1991, "Relationship between Gypsum content, porosity and strength of cement", *Cement and Concrete Research*, 21, No. 1, 120-126.

Shah, S. P. and Slate, F. O., 1968, "Internal Microcracking, Mortar-Aggregate Bond, and the Stress Strain Curve of Concrete", *International Conference on the Structure of Concrete,* William Clowes and Sons, Ltd., London.

Shah, S. P., Swartz, S. E. and Ouyang, C., 1995, *Fracture Mechanics of Concrete: Applications of Fracture Mechanics to Concrete, Rock, and Other Quasi-brittle Materials*, John Wiley & Sons, Inc., ISBN 0471303119, New York, USA, pp. 552.

Shah, S. P. and Winter, G., 1968, “Inelastic Behavior and Fracture of Concrete”, *Symp. On Causes, Mechanism, and Control of Cracking in Concrete*, ACI SP-20, 5-28.

Sheng, J. M., Wang, Z. Z. and Jiang, J. J., 1991, *Finite Element Methods for Reinforced Concrete and Limit Analysis of Plates and Shells*, Tsinghua University Press, Chinese language, ISBN 7302012393, Beijing, China, pp. 510.

Shivakumar, K. N., Tan, P. W. and Newman, J. C., 1988, “A Virtual Crack-Closure Technique for Calculating Stress Intensity Factors for Cracked Three-Dimensional Bodies”, *International Journal of Fracture*, V. 36, R43-R50.

Song, H. and Kwon S., 2007, “Permeability Characteristics of Carbonated Concrete Considering Capillary Pore Structure”, *Cement Concrete Research*, 909-915.

Su, Z, Bijen, J. M. J. M. and Larbi, J. A., 1991, “Influence of Polymer Modification on the Adhesion of Cement Pastes to Aggregate”, *Cement and Concrete Research*, V.21, No.5, 727-736.

Sun, Z., Garboczi, E. J. and Shah, S. P., 2007, “Modeling the Elastic Properties of Concrete Composites: Experiment, Differential Effective Medium Theory, and Numerical Simulation”, *Cement and Concrete Composites*, V.29, 22-38.

Swartz, S. E. and Kan, Y. C., 1990, “Effect of Support Conditions on Fracture Energy Measurements for Concrete Beam”, in *Proceeding of Fracture Behaviour and Design of Materials and Structures*, EMAS Publishers, London, pp. 660-666.

Swartz, S. E., and Kan, Y. C., 1991, “On the Validity of Indirect Measurement of the LPD for SEN Concrete Beams”, in *Proceedings of Fracture Process in Concrete, Rock and Ceramics*, E&FN SPON, London, pp. 771-778.

Tada, H., Paris, P. C. and Irwin, G. R., 1985, *The Stress Analysis of Cracks Handbook*, 2nd Edition, Paris Productions, ISBN 9994878808, St. Louis, MO.

Taylor, M. A. and Broms, B. B., 1964, "Shear Bond Strength between Coarse Aggregate and Cement Paste or Mortar", *Journal of American Concrete Institute, Proceedings*, V.61, 939-957.

Tepfers, R., 1979, "Cracking of Concrete Cover Along Anchored Deformed Reinforcing Bars", *Magazine of Concrete Research* **31**, No. 106, 3-12.

Thomas, D. E., 1996, "Chloride Threshold in Marine Concrete", *Cement and Concrete Research*, V. 26, No.4, pp. 513-519.

Timoshenko, S. P. and Goodie, J. N., 1970, *Theory of elasticity*, MagGraw-Hill Book Co, 3rd Edition, ISBN 0070647208, Singapore, pp. 608.

Tracey, D. M., 1971, "Finite Elements for the Determination of Crack Tip Elastic Stress Intensity Factors", *Engineering Fracture Mechanics*, V. 3, 255-265.

Trtik, P. and Bartos, P. J. M., 1999, "Micromechanical Properties of Cementitious Composites", *Material and Structures*, 32, 388-393.

Tuutti, K., 1982, *Corrosion of Steel in Concrete*, Swedish Cement and Concrete Research Institute, Stockholm, Sweden, 17-21.

Ueda, T., Sato, Y., Kakuta, Y. & Kameya, H. 1998, "Analytical Study on Concrete Cover Cracking due to Reinforcement Corrosion", *Concrete Under Severe Condition 2,* Proceedings of an Int. Conf., Tromso, Norway, pp. 678 – 687.

Van Mier, J. G. M. and Van Vliet, M. R. A., 2002, "Uniaxial Tension Test for the Determination of Fracture Parameters of Concrete: State of The Art", *Engineering Fracture Mechanics* **69**, pp. 235-247.

Verbeck, G. J., 1955, "Harden Concrete-Pore Structure", *ASTM*, Special Technical Publication, No.169.

Vidal, T., Castel, A. and Francois, R., 2007, "Corrosion Process and Structural Performance of A 17 Year Old Reinforced Concrete Beam Stored in Chloride Environment", *Cement and Concrete Research*, 37, 1551-1561.

Walsh, P. F., 1976, "Crack Initiation in Plain Concrete", *Magazine of Concrete Research*, **28**, pp. 37-41.

Wang, J., Liu, B., Xie, S. and Wu, Z., 1986, "Improvement of Paste-Aggregate Interface by Adding Silica Fume", *Proceedings of 8th International Congress on Chemistry of Cement,* V.3, Finep, Brazil, 460-465.

Ward, M. A., Neville, A. M. and Singh, S. P., 1969, "Creep of Air-Entrained Concrete", *Magazine of Concrete Research*, 21, No.69, 205-210.

Wilkins, N. J. M. and Lawrence, P. F., 1980, "Concrete in the Oceans: Fundamental Mechanics of Corrosion of Steel Reinforcements in Concrete Immersed in Sea Water", *Technical Report 6*, CIRIA/UEG Cement and Concrete Association, Slough, UK.

Winslow, D. and Liu, D., 1990, "The Pore Structure of Paste in Concrete", *Cement and Concrete Research*, 20, No.2, 227-284.

Wittmann, F. H., Roelfstra, P. E., Mihashi, H., Huang, Y. Y., Zhang, X. H, and Nomura, N., 1987, "Influence of Age of Loading, Water-Cement Ratio and Rate of Loading on Fracture Energy of Concrete", *Materials and Structures*, V. 20, 103-110.

Xie, M.; Gerstle, W. and Rahulkumar, P., 1995, "Energy-based Automatic Mixed-Mode Crack Propagation Modelling", *Journal of Engineering Mechanics*, ASCE, V. 121, No. 8, 914-923.

Yang, S., Tang, T., Zollinger, D. G. and Gurjar, A., 1997, "Splitting Tension Tests To Determine Concrete Fracture Parameters by Peak Load Method", *Advn. Cem. Bas. Mat*., **5**, pp. 18-28.

Yuan, Y. S., Ji, Y. S. and Shah, S. P., 2007, "Comparison of Two Accelerated Corrosion Techniques for Concrete Structures", *ACI Structural Journal*, V.104, I.3, pp. 344-347.

Yue, L. and Shuguang, H., 2001, "The Microstructure of the Interfacial Transition Zone between Steel and Cement Paste", *Cement and Concrete Research*, 31, 385-388.

Zimbelmann, R., 1987, "Method for Strengthening the Bond between Cement Stone and Aggregate", *Cement and Concrete Research*, V.17, No.4, 651-660.

Zhu, W. and Bartos, P. J. M., 1997, "Assessment of Interfacial Microstructure and Bond Properties in Aged GRC Using A Novel Microindentation Method", *Cement and Concrete Research*, 27, 1701-1711.

Zhu, W. and Bartos, P. J. M., 2000, "Application of Depth-Sensing Microindentation Testing to Study of Interfacial Transition Zone in Reinforced Concrete", *Cement and Concrete Research*, 30, 1299-1304.

APPENDIX A

ACRONYMS

Acronyms	Meaning
CCM	Cohesive Crack model
FPZ	Fracture Process Zone
HFM	Hillerborg Fictitious Fracture Model
ITZ	Interfacial Transition Zone
JSFM	Jenq and Shah's Fracture Model
LEFM	Linear Elastic Fracture Mechanics
NFM	Nonlinear Fracture Mechanics
$CMOD$	Crack Mouth Opening Displacement
$CMOD_c$	Critical Crack Mouth Opening Displacement
$CTOD$	Crack Tip Opening Displacement
$CTOD_c$	Critical Tip Opening Displacement

APPENDIX B

CODE IN MATLAB FOR ANALYTICAL SOLUTION

```
%%% This program is for determination of concrete crack width ↙
under
%%% combined effects of reinforcement corrosion and applied ↙
load.
clc;
clear all;
close all;

%input parameters
        ec=56.46e9;
        creep = 2.0;
        eff=ec/(1.+creep);
        vc=0.18;
        ft= 5.725e6;
        d=0.012;
        d0=12.5e-6;
        r0=d/2.+d0;
        c = 0.031;
        nt = 1;
        Gf=88;
        pi=22/7;
        gama = 2.*pi*r0*ft/Gf;

%initial value
        b(nt) = c+(d+2*d0)/2.;
        it=0.01;
        alpha=1.0;
        r2=r0;
        r=r0;
        t2=0;

%find time t1
    for i=1:1000
        t=it*(i-1);
        if(t <= 0.05)
            xx = 0.05;
            xicor=0.3686*log(xx)+1.1305;
        else
            xx = t;
            xicor=0.3686*log(xx)+1.1305;
        end
        aicorr = xicor;
        y=st(r0,r2,b,r0,t,alpha,vc,eff,t2,aicorr,nt,d,d0);
        if(y < ft)
            continue
        else
            t1=t;
            disp('time to crack initiation ...') ,t1
            disp('press any key to continue')
            pause
            break
        end
    end %time t1 loop

    alphamin=alpha;
```

```
    m=1;
    xp(1)=r0;
    yp(1)=dt(r0,d,eff,vc,b,nt,t,aicorr,d0)/r0;

%find time t2
    for j=1:1001
        t=it*(j-1);
        tt(j) = t;
        if(t == 0)
            xicor = 0;
        elseif(t <= 0.05)
            xx = 0.05;
            xicor=0.3686*log(xx)+1.1305;
        else
            xx = t;
            xicor=0.3686*log(xx)+1.1305;
        end
        aicorr = xicor;

        if(ds(t,aicorr,d,d0) <= 0)
            alphat(j) = alphamin;
            continue
        end
%        sta=st(r0,r2,b,r0,t,alpha,vc,eff,t2,aicorr,nt,d,d0);↙
%%%tangential pressure at r=a
%        stb=st(r0,r2,b,b,t,alpha,vc,eff,t2,aicorr,nt,d,d0);↙
%%%tangential pressure at r=b
        y1=p(r0,r2,b,t,alpha,vc,eff,t2,aicorr,nt,d,d0);↙
%pressure
        rk=b(nt);
        y2=wc(r0,r2,b,rk,t,alpha,eff,vc,t1,xp,yp,m,t2,aicorr,nt,↙
d,d0,ft);   %crack width
        y3=alphamin;     %alpha
        y4=dc(t,aicorr,d,d0);
        y5=dt(r0,d,eff,vc,b,nt,t,aicorr,d0);
        y6=dp(r0,d,eff,vc,b,nt);
%        stat(j)=sta;                %%%tangential pressure at↙
r=a
%        stbt(j)=stb;                %%%tangential pressure at↙
r=b
        pressurep2=p2(d);
        pressuret(j) = y1/1e6;
        crackwidtht(j) = y2*1000;
        alphat(j) = y3;
        corrosiondis(j)=y4*1000;
        combineddis(j)=y5*1000;
        loadingdis(j)=y6*1000;
        checkwct = (crackwidtht(j)-0.30);

        y7=st(r0,r2,b,r0,t,alpha,vc,eff,t2,aicorr,nt,d,d0);
        y8=stra(r0,r2,b,r0,t,alpha,eff,vc,t1,t2,aicorr,nt,d,d0,↙
ft);
        strsa(j)=y7/1e6;
        strna(j)=y8;
```

```
        rmid=0.021;
        y9=st(r0,r2,b,rmid,t,alpha,vc,eff,t2,aicorr,nt,d,d0);
        y10=stra(r0,r2,b,rmid,t,alpha,eff,vc,t1,t2,aicorr,nt,d,↙
d0,ft);
        strsmid(j)=y9/1e6;
        strnmid(j)=y10;

        rgiven1=0.012;
        y11=st(r0,r2,b,rgiven1,t,alpha,vc,eff,t2,aicorr,nt,d,↙
d0);
        y12=stra(r0,r2,b,rgiven1,t,alpha,eff,vc,t1,t2,aicorr,nt,↙
d,d0,ft);
        strsgiven1(j)=y11/1e6;
        strngiven1(j)=y12;

        r2t(j)=r2;


        if (crackwidtht(j) > 0.300) & (crackwidtht(j) < 0.3005)
            disp('time to critical limit crack width ...') ,t
            disp('crack width ...'),crackwidtht(j)
            disp('press any key to continue')
            pause
        end

        if(t <= t1)
            continue
        end
        if(r ~= b(nt))
            rtt = equa(r0,r2,b,r,t,alpha,vc,eff,ft,t2,aicorr,nt,↙
d,d0); %%%
            r=rtt;
            if(r == r2)
                continue
            end
            m=m+1;
            xp(m)=r;
            r2=r;
            sa=sqrt(alpha);
            del=(1.-vc^2)*(1.-sa)*(r0/r2)^sa/r2^2-(1.+vc)*((1.-↙
vc)+sa*(1.+vc))*(r2/r0)^sa/r2^2 +(1.-vc^2)*(1.-sa)*(r2/r0)^sa/b↙
(nt)^2 -(1.-vc)*((1.+vc)+sa*(1.-vc))*(r0/r2)^sa/b(nt)^2;
            c3=-2.*(1.-vc)*sa/r2/b(nt)^2*dt(r0,d,eff,vc,b,nt,t,↙
aicorr,d0)/del;
            c4=-2.*(1.+vc)*sa/r2*dt(r0,d,eff,vc,b,nt,t,aicorr,↙
d0)/del;
            c5=-(1.-vc)/r2^sa*dt(r0,d,eff,vc,b,nt,t,aicorr,d0)*↙
((1.+vc)*(sa-1.)/r2^2 +((1.+vc)+sa*(1.-vc))/b(nt)^2)/del;
            c6=-(1.+vc)*r2^sa*dt(r0,d,eff,vc,b,nt,t,aicorr,d0)*↙
((1.-vc)*(sa-1.)/b(nt)^2+((1.+vc)*sa+(1.-vc))/r2^2)/del;
            yp(m)=c3+c4/r2^2;
            strain=(r2^sa-r0^sa)*(c5+c6/(r0*r2)^sa)/(sa*(r2-↙
r0));
            if(m == 2)
                strainc=(yp(1)+yp(2))/2.;
```

```
            else
                strainc=(yp(1)*(xp(2)-xp(1))+yp(m)*(xp(m)-xp(m-↙
1)))/2./(r2-r0);
                for ii=2:m-1
                    strainc=strainc+yp(ii)*(xp(ii+1)-xp(ii-1))↙
/2./(r2-r0);
                end
            end
            alpha1=ft*exp(-gama*(strain-strainc)^1.01)/↙
(strain*eff);
            if(alpha1 < alphamin)
                alphamin=alpha1;
                alpha=alpha1;
            end
        else
             if((t2 ~= 0) & (t > t2))
                sa=sqrt(alpha);
                c7=(1.-vc)*r0^sa*dt(r0,d,eff,vc,b,nt,t,aicorr,↙
d0)/((1.-vc)*r0^(2.*sa)+(1.+vc)*b(nt)^(2.*sa));
                c8=(1.+vc)*r0^sa*b(nt)^(2.*sa)*dt(r0,d,eff,vc,b,↙
nt,t,aicorr,d0)/((1.-vc)*r0^(2.*sa)+(1.+vc)*b(nt)^(2.*sa));
                strain=(b(nt)^sa-r0^sa)*(c7+c8/(r0*b(nt))^sa)/↙
(sa*(b(nt)-r0));
             else
                 t2=t;
                 disp('time to surface cracking ...') ,t2
                 disp('press any key to continue')
                 pause
                 sa=sqrt(alpha);
                 c7=(1.-vc)*r0^sa*dt(r0,d,eff,vc,b,nt,t,aicorr,↙
d0)/((1.-vc)*r0^(2.*sa)+(1.+vc)*b(nt)^(2.*sa));
                 c8=(1.+vc)*r0^sa*b(nt)^(2.*sa)*dt(r0,d,eff,vc,↙
b,nt,t,aicorr,d0)/((1.-vc)*r0^(2.*sa)+(1.+vc)*b(nt)^(2.*sa));
                 strain=(b(nt)^sa-r0^sa)*(c7+c8/(r0*b(nt))^sa)/↙
(sa*(b(nt)-r0));     %eqn.(57):3rd
             end
             if(m == 2)
                strainc=(yp(1)+yp(2))/2.;
             else
                strainc=(yp(1)*(xp(2)-xp(1))+yp(m)*(xp(m)-xp(m-↙
1)))/2.0/(b(nt)-r0);
                for ii=2:m-1
                    strainc=strainc+yp(ii)*(xp(ii+1)-xp(ii-1))↙
/2./(b(nt)-r0);
                end
             end
             alpha1=ft*exp(-gama*(strain-strainc)^1.01)/↙
(strain*eff);
             if(alpha1 < alphamin)
                 alphamin=alpha1;
                 alpha=alpha1;
             end
         end
    end %time t2 loop
```

```
    figure(1)
    plot(tt,crackwidtht)
    xlabel('time (year)')
    ylabel('crack widht (mm)')

    figure(2)
    plot(tt,pressuret)
    xlabel('time (year)')
    ylabel('pressure (MPa)')

    figure(3)
    plot(tt,alphat)
    xlabel('time (year)')
    ylabel('alpha')

 %%%The following are subroutines%%%

function ddc=dc(t,aicorr,d,d0)
       if (ds(t,aicorr,d,d0)< d0)
           ddc=0;
       else
           ddc=ds(t,aicorr,d,d0)-d0;
       end
return


function dst = ds(t,aicorr,d,d0)
        pi=22/7;
        ar=0.57;
        d= d*1000;
        d0=d0;
        rost=7850; %kg/m3
        rorust=3600;
        wrust=sqrt(2.*0.105/ar*pi*d*aicorr*t);
        dst=wrust/(pi*d)*(1./rorust-ar/rost);
        %pause
return


function u=dp(r0,d,eff,vc,b,nt)
      u=r0*p2(d)/eff*(vc+(b(nt)^2+r0^2)/(b(nt)^2-r0^2));
return


function ddt=dt(r0,d,eff,vc,b,nt,t,aicorr,d0)
   if(dc(t,aicorr,d,d0)<=0)

       ddt=dp(r0,d,eff,vc,b,nt);
   else
       ddt=dp(r0,d,eff,vc,b,nt)+dc(t,aicorr,d,d0);
   end
return


function rt = equa(r0,r2,b,r,t,alpha,vc,eff,ft,t2,aicorr,nt,d,↙
```

```
d0)
%find distance r from inner radius
        x1=r2;
        y1=ff(r0,r2,b,x1,t,alpha,vc,eff,ft,t2,aicorr,nt,d,d0);
        if(y1 >= 0)
             rt = r2;
             return
        end

        x2=b(nt);
        y2=ff(r0,r2,b,x2,t,alpha,vc,eff,ft,t2,aicorr,nt,d,d0);
        if(y2 <= 0)
            rt = b(nt);
            return
        end

        x3=(x1+x2)/2.;
        y3=ff(r0,r2,b,x3,t,alpha,vc,eff,ft,t2,aicorr,nt,d,d0);
        if(abs((x2-x1)/x3) <= 0.0001)
            rt = x3;
            return
        end

        while (abs((x2-x1)/x3) >= 0.0001)
            if((y1*y3) < 0)
                x2=x3;
                y2=y3;
                x3=(x1+x2)/2.;
                y3=ff(r0,r2,b,x3,t,alpha,vc,eff,ft,t2,aicorr,nt,↙
d,d0);
            else
                x1=x3;
                y1=y3;
                x3=(x1+x2)/2.;
                y3=ff(r0,r2,b,x3,t,alpha,vc,eff,ft,t2,aicorr,nt,↙
d,d0);
            end
        end
        rt = x3;
return


function fft = ff(r0,r2,b,r,t,alpha,vc,eff,ft,t2,aicorr,nt,d,d0)
       fft = ft - st(r0,r2,b,r,t,alpha,vc,eff,t2,aicorr,nt,d,↙
d0);
return


function pt = p(r0,r2,b,t,alpha,vc,eff,t2,aicorr,nt,d,d0)
    pt = -sr(r0,r2,b,r0,t,alpha,vc,eff,t2,aicorr,nt,d,d0);
return


function pp2=p2(d)
   fc=20e6;
```

```
   fy=400e6;
   As=0.452e-3;
   B=0.12;
   cita=pi/4;
   L=3;
   h0=0.163;
   w=0;
   x=0;
   pp2=tan(cita)*d/4./(h0-fy*As/(2.*fc*B))/As*(w*L/2.-w*x);
return


function srt = sr(r0,r2,b,r,t,alpha,vc,eff,t2,aicorr,nt,d,d0)
    if(r2 == r0)
        c1=(1.-vc)*r0*dt(r0,d,eff,vc,b,nt,t,aicorr,d0)/((1.-vc)↙
*r0^2+(1.+vc)*b(nt)^2);
        c2=(1.+vc)*r0*b(nt)^2*dt(r0,d,eff,vc,b,nt,t,aicorr,d0)/↙
((1.-vc)*r0^2+(1.+vc)*b(nt)^2);
        srt=eff/(1.-vc^2)*((1.+vc)*c1-(1.-vc)/r^2*c2);
        return
    end
    if((r2 > r0) & (r2 < b(nt)))
        if(r > r2)
            sa=sqrt(alpha);
            del=(1.-vc^2)*(1.-sa)*(r0/r2)^sa/r2^2-(1.+vc)*((1.-↙
vc)+sa*(1.+vc))*(r2/r0)^sa/r2^2+(1.-vc^2)*(1.-sa)*(r2/r0)^sa/b↙
(nt)^2-(1.-vc)*((1.+vc)+sa*(1.-vc))*(r0/r2)^sa/b(nt)^2;
            c3=-2.*(1.-vc)*sa/r2/b(nt)^2*dt(r0,d,eff,vc,b,nt,t,↙
aicorr,d0)/del;
            c4=-2.*(1.+vc)*sa/r2*dt(r0,d,eff,vc,b,nt,t,aicorr,↙
d0)/del;
            srt=eff/(1.-vc^2)*((1.+vc)*c3-(1.-vc)*c4/r^2);
            return
        else
            sa=sqrt(alpha);
            del=(1.-vc^2)*(1.-sa)*(r0/r2)^sa/r2^2-(1.+vc)*((1.-↙
vc)+sa*(1.+vc))*(r2/r0)^sa/r2^2+(1.-vc^2)*(1.-sa)*(r2/r0)^sa/b↙
(nt)^2-(1.-vc)*((1.+vc)+sa*(1.-vc))*(r0/r2)^sa/b(nt)^2;
            c5=-(1.-vc)/r2^sa*dt(r0,d,eff,vc,b,nt,t,aicorr,d0)*↙
((1.+vc)*(sa-1.)/r2^2+((1.+vc)+sa*(1.-vc))/b(nt)^2)/del;
            c6=-(1.+vc)*r2^sa*dt(r0,d,eff,vc,b,nt,t,aicorr,d0)*↙
((1.-vc)*(sa-1.)/b(nt)^2+((1.+vc)*sa+(1.-vc))/r2^2)/del;
            srt=eff/(1.-vc^2)*sa*(c5*(1.+vc)*r^(sa-1.)-c6*(1.-↙
vc)*r^(-sa-1.));
            return
        end
    else
        sa=sqrt(alpha);
        c7=(1.-vc)*r0^sa*dt(r0,d,eff,vc,b,nt,t,aicorr,d0)/((1.-↙
vc)*r0^(2.*sa)+(1.+vc)*b(nt)^(2.*sa));
        c8=(1.+vc)*r0^sa*b(nt)^(2.*sa)*dt(r0,d,eff,vc,b,nt,t,↙
aicorr,d0)/((1.-vc)*r0^(2.*sa)+(1.+vc)*b(nt)^(2.*sa));
        srt=eff*sa/(1.-vc^2)*(c7*(1.+vc)*r^(sa-1.)-c8*(1.-vc)*r^↙
(-sa-1.));
        return
```

```
    end
return


function stt = st(r0,r2,b,r,t,alpha,vc,eff,t2,aicorr,nt,d,d0)
    if(r2 == r0)
        c1=(1.-vc)*r0*dt(r0,d,eff,vc,b,nt,t,aicorr,d0)/((1.-vc)↙
*r0^2+(1.+vc)*b(nt)^2);
        c2=(1.+vc)*r0*b(nt)^2*dt(r0,d,eff,vc,b,nt,t,aicorr,d0)/↙
((1.-vc)*r0^2+(1.+vc)*b(nt)^2);
        stt=eff/(1.-vc^2)*((1.+vc)*c1+(1.-vc)/r^2*c2);  %eqn↙
(10):3rd
        return
    end
    if((r2 > r0) & (r2 < b(nt)))
        if(r >= r2)
            sa=sqrt(alpha);
            del=(1.-vc^2)*(1.-sa)*(r0/r2)^sa/r2^2-(1.+vc)*((1.-↙
vc)+sa*(1.+vc))*(r2/r0)^sa/r2^2  +(1.-vc^2)*(1.-sa)*(r2/r0)^sa/b↙
(nt)^2 -(1.-vc)*((1.+vc)+sa*(1.-vc))*(r0/r2)^sa/b(nt)^2;
            c3=-2.*(1.-vc)*sa/r2/b(nt)^2*dt(r0,d,eff,vc,b,nt,t,↙
aicorr,d0)/del;
            c4=-2.*(1.+vc)*sa/r2*dt(r0,d,eff,vc,b,nt,t,aicorr,↙
d0)/del;
            stt=eff/(1.-vc^2)*((1.+vc)*c3+(1.-vc)/r^2*c4);
        else
            sa=sqrt(alpha);
            del=(1.-vc^2)*(1.-sa)*(r0/r2)^sa/r2^2-(1.+vc)*((1.-↙
vc)+sa*(1.+vc))*(r2/r0)^sa/r2^2  +(1.-vc^2)*(1.-sa)*(r2/r0)^sa/b↙
(nt)^2 -(1.-vc)*((1.+vc)+sa*(1.-vc))*(r0/r2)^sa/b(nt)^2;
            c5=-(1.-vc)/r2^sa*dt(r0,d,eff,vc,b,nt,t,aicorr,d0)*↙
((1.+vc)*(sa-1.)/r2^2+((1.+vc)+sa*(1.-vc))/b(nt)^2)/del;
            c6=-(1.+vc)*r2^sa*dt(r0,d,eff,vc,b,nt,t,aicorr,d0)*↙
((1.-vc)*(sa-1.)/b(nt)^2+((1.+vc)*sa+(1.-vc))/r2^2)/del;
            stt=eff*sa^2/(1.-vc^2)*(c5*(1.+vc)*r^(sa-1.)+c6*(1.-↙
vc)*r^(-sa-1.));
            return
        end
    else   %never happen for r>b
        sa=sqrt(alpha);
        c7=(1.-vc)*r0^sa*dt(r0,d,eff,vc,b,nt,t,aicorr,d0)/((1.-↙
vc)*r0^(2.*sa)+(1.+vc)*b(nt)^(2.*sa));
        c8=(1.+vc)*r0^sa*b(nt)^(2.*sa)*dt(r0,d,eff,vc,b,nt,t,↙
aicorr,d0)/((1.-vc)*r0^(2.*sa)+(1.+vc)*b(nt)^(2.*sa));
        stt=eff*sa^2/(1.-vc^2)*(c7*(1.+vc)*r^(sa-1.)+c8*(1.-vc)↙
*r^(-sa-1.));
        return
    end
return


function strain = stra(r0,r2,b,r,t,alpha,eff,vc,t1,t2,aicorr,nt,↙
d,d0,ft)
    if(r2 == r0)
        c1=(1.-vc)*r0*dt(r0,d,eff,vc,b,nt,t,aicorr,d0)/((1.-vc)↙
```

```
*r0^2+(1.+vc)*b(nt)^2);
        c2=(1.+vc)*r0*b(nt)^2*dt(r0,d,eff,vc,b,nt,t,aicorr,d0)/↙
((1.-vc)*r0^2+(1.+vc)*b(nt)^2);
        strain=c1+c2/r^2;
        return
    end
    if((r2 > r0) & (r2 < b(nt)))
        if(r >= r2)
            sa=sqrt(alpha);
            del=(1.-vc^2)*(1.-sa)*(r0/r2)^sa/r2^2-(1.+vc)*((1.-↙
vc)+sa*(1.+vc))*(r2/r0)^sa/r2^2  +(1.-vc^2)*(1.-sa)*(r2/r0)^sa/b↙
(nt)^2 -(1.-vc)*((1.+vc)+sa*(1.-vc))*(r0/r2)^sa/b(nt)^2;
            c3=-2.*(1.-vc)*sa/r2/b(nt)^2*dt(r0,d,eff,vc,b,nt,t,↙
aicorr,d0)/del;
            c4=-2.*(1.+vc)*sa/r2*dt(r0,d,eff,vc,b,nt,t,aicorr,↙
d0)/del;
            strain=c3+c4/r^2;
        else
            sa=sqrt(alpha);
            del=(1.-vc^2)*(1.-sa)*(r0/r2)^sa/r2^2-(1.+vc)*((1.-↙
vc)+sa*(1.+vc))*(r2/r0)^sa/r2^2  +(1.-vc^2)*(1.-sa)*(r2/r0)^sa/b↙
(nt)^2 -(1.-vc)*((1.+vc)+sa*(1.-vc))*(r0/r2)^sa/b(nt)^2;
            c5=-(1.-vc)/r2^sa*dt(r0,d,eff,vc,b,nt,t,aicorr,d0)*↙
((1.+vc)*(sa-1.)/r2^2+((1.+vc)+sa*(1.-vc))/b(nt)^2)/del;
            c6=-(1.+vc)*r2^sa*dt(r0,d,eff,vc,b,nt,t,aicorr,d0)*↙
((1.-vc)*(sa-1.)/b(nt)^2+((1.+vc)*sa+(1.-vc))/r2^2)/del;
            strain=c5*r^(sa-1.)+c6*r^(-sa-1.);
            return
        end
    else   %never happen for r>b
        sa=sqrt(alpha);
        c7=(1.-vc)*r0^sa*dt(r0,d,eff,vc,b,nt,t,aicorr,d0)/((1.-↙
vc)*r0^(2.*sa)+(1.+vc)*b(nt)^(2.*sa));
        c8=(1.+vc)*r0^sa*b(nt)^(2.*sa)*dt(r0,d,eff,vc,b,nt,t,↙
aicorr,d0)/((1.-vc)*r0^(2.*sa)+(1.+vc)*b(nt)^(2.*sa));
        strain=c7*r^(sa-1.)+c8*r^(-sa-1.);
        return
    end
return


function wct = wc(r0,r2,b,r,t,alpha,eff,vc,t1,xp,yp,m,t2,aicorr,↙
nt,d,d0,ft)
        pi = 22/7;
        m;
    if((t < t1) | (r > r2))
        wct=0.;
        return
    end
    %for i=1:m-1
    %    if((r < xp(i)) | (r > (xp(i+1))))
    %        continue
     %   else
    %        ii=i;
    %    end
```

```
   % end
    %strainc=yp(ii)+(yp(ii+1)-yp(ii))/(xp(ii+1)-xp(ii))*(r-xp↙
(ii));
    straine=(st(r0,r2,b,r,t,alpha,vc,eff,t2,aicorr,nt,d,d0)-↙
vc*sr(r0,r2,b,r,t,alpha,vc,eff,t2,aicorr,nt,d,d0))/eff;

    if(r2 < b(nt))
        sa=sqrt(alpha);
        del=(1.-vc^2)*(1.-sa)*(r0/r2)^sa/r2^2-(1.+vc)*((1.-vc)↙
+sa*(1.+vc))*(r2/r0)^sa/r2^2+(1.-vc^2)*(1.-sa)*(r2/r0)^sa/b(nt)↙
^2-(1.-vc)*((1.+vc)+sa*(1.-vc))*(r0/r2)^sa/b(nt)^2;
        c5=-(1.-vc)/r2^sa*dt(r0,d,eff,vc,b,nt,t,aicorr,d0)*((1.↙
+vc)*(sa-1.)/r2^2+((1.+vc)+sa*(1.-vc))/b(nt)^2)/del;
        c6=-(1.+vc)*r2^sa*dt(r0,d,eff,vc,b,nt,t,aicorr,d0)*((1.-↙
vc)*(sa-1.)/b(nt)^2+((1.+vc)*sa+(1.-vc))/r2^2)/del;
        strain=c5*r^(sa-1.)+c6*r^(-sa-1.);
        wct=2.*pi*r*(strain-straine);
        return
    else
        sa=sqrt(alpha);
        c7=(1.-vc)*r0^sa*dt(r0,d,eff,vc,b,nt,t,aicorr,d0)/((1.-↙
vc)*r0^(2.*sa)+(1.+vc)*b(nt)^(2.*sa));
        c8=(1.+vc)*r0^sa*b(nt)^(2.*sa)*dt(r0,d,eff,vc,b,nt,t,↙
aicorr,d0)/((1.-vc)*r0^(2.*sa)+(1.+vc)*b(nt)^(2.*sa));
        strain=c7*r^(sa-1.)+c8*r^(-sa-1.);
        wct=2.*pi*r*(strain-straine);
        return
    end
return
```